Carbon Nanotube-based Solar Cells

by

LePing Yu

Thesis
Submitted to Flinders University
for the degree of

Doctor of Philosophy

College of Science and Engineering

7th May 2018

Supervisor: Prof. Joe Shapter,
Co-supervisor: Prof. David Lewis

Table of contents

Summary

Due to the excellent optoelectronic properties of carbon nanotubes, they are considered one of the most promising materials for transparent conducting electrodes for application in future photovoltaics. In the majority of this Thesis, p-type CNT-based transparent conducting films are used to form a heterojunction solar cell with n-type Si.

Several strategies are used to enhance the performance of such devices. Firstly, it is shown that a hybrid film made of CNTs and the conducting polymer, polyaniline, can improve the properties of the heterojunction by separating electron-hole pairs more efficiently. Secondly, a grid design of front metal electrode dramatically reduces the internal series resitance of the CNT based transparent films and thus improves the efficiency of the devices. Thirdly, the application of an organic interlayer, spiro-OMeTAD, can improve the exciton separation efficiency by suppressing the recombination of separated holes and electrons, and thus decreasing the reverse saturation current caused from the electrons tunnelling from Si to CNT based films. Fourthly, different approaches, including the incorporation of AgNWs with CNT based network and p-type doping of the transparent films, are used to improve the optoelectronic properties and/or the charge carrier density, which reveals that the hybridisation of CNT based transparent conducting film with AgNWs is the best way to improve the optoelectronic properties while the increase in the charge carrier density by p-type dopants is more important in improving the performance of heterojunction solar cells. Fifthly, a textured Si surface is applied instead of a planar Si substrate, in which the surface reflection is reduced and the intimate contact area between CNT based electrodes and Si surface is improved and both effects contribute to a higher output of photocurrent.

Though the best performing solar cell in this Thesis is above 13 %, which is one of the highest values in the literature, the non-ideal long-term stability of the devices is an issue (the oxidation of the silicon always ruins the performance of the solar cells over the course of a few days) to be addressed before commercialisation. One potential way to solve this problem is to create a different solar cell structure which contains two layers of SWCNTs of different chiral species as the light absorbing active layers (without

Si layer). Thus, at the end of this Thesis, more than 15 single chiral species have been separated by two different methods, gel chromatography and aqueous two phase extraction, for future fabrication of a new type of solar cell.

Declaration

I certify that this Thesis does not incorporate without acknowledgment any material previously submitted for a degree or diploma in any university; and that to the best of my knowledge and belief it does not contain any material previously published or written by another person except where due reference is made in the text.

LePing Yu

Acknowledgements

First I would thank my supervisor Professor Joe Shapter and Professor David Lewis for their advice and assistance throughout the whole PhD project. I also would like to give a special thank you to Dr. Cameron Shearer, Mr. Tom Grace, Dr. Daniel Tune, Dr. Munkhbayer Batmunkh, Dr. Mahnaz Dadkhah Dr. Christopher Gibson, and Dr. Lachlan Larsen for their guidance and all the questions they answered for me in the last a few years at Flinders University. In addition, thanks to Professor Amanda Ellis' groups for providing some materials required in this project. Finally, thanks to my parents for giving me life and my wife Rong being supportive and always for your love.

List of Figures

List of Tables

List of abbreviations (in order of appearance)

Abbreviations	Definitions
TCFs	transparent conducting films
LCDs	liquid crystal displays
OLEDs	organic light-emitting diode
TCOs	transparent and conductive doped metal oxides
ITO	indium tin oxide
PET	polyethylene terephthalate
FTO	fluorine-doped tin oxide
NPs	nanoparticles
CNTs	carbon nanotubes
SWCNTs	single-walled carbon nanotubes
DWCNTs	double-walled carbon nanotubes
MWCNTs	multiwalled carbon nanotubes
AFM	atomic force microscopy
SEM	scanning electron microscope
DOS	density of states
ssDNA	single-stranded deoxyribonucleic acid
CVD	chemical vapour deposition
FCCVD	floating catalyst chemical vapour deposition
DMF	N,N-Dimethyformamide
NMP	N-methyl-2-pyrrolidone
DCE	dichloroethane

DMSO	dimethyl sulfoxide
CSA	chlorosulfonic acid
SDS	sodium dodecyl sulphate
LB	Langmuir−Blodgett
PDMS	polydimethylsiloxane
PMMA	poly(methyl methacrylate)
EPD	electrophoretic deposition
DEP	dielectrophoresis
APTES	3-aminopropyltriethoxysilane
PS-b-PAA	poly(styrene-block-acrylic acid)
PC	polycarbonate
F4TCNQ	tetrafluorotetracyano-p-quinodimethane
OA	triethyloxonium hexachloroantimonate
TFSI	bis-(trifluromethanesulfonyl)imide
F4-TCNQ	(2,3,5,6-tetrafluoro-7,7,8,8-tetracyanoquinodimethane)
TEM	transmission electron microscope
AgNPs	silver nanoparticles
AgNWs	silver nanowires
PEDOT:PSS	(3, 4-ethylenedioxythiophene)-poly-(styrenesulfonate)
PANI	polyaniline
APS	ammonium persulphate
LUMO	lowest unoccupied molecular orbital
DC	direct current
HTL	hole-transporting layer

EML	emitting layer
ETL	electron-transporting layer
PEN	**polyethylene naphthalate**
RMS	root mean square
FLGs	few-layer graphene sheets
IPCE	incident photon-to-current efficiency
EQE	external quantum efficiency
MCE	mixed cellulose ester
eGaIn	gallium indium eutectic
IQE	internal quantum efficiency
PCE	power conversion efficiency
FF	fill factor
ATP(E)	aqueous two-phase (extraction)
DOC	sodium deoxycholate
SC	sodium cholate
PEG	polyethylene glycol
PAM	polyacrylamide
DX	dextran
PVP	polyvinylpyrrolidone
spiro-OMeTAD	2,2',7,7'-tetrakis(N,N'-di-p-methoxyphenylamine)-9,9'-spirobifluorene
GO	graphene oxide
tBP	4-tert-butylpyridine
Li-TFSI	lithium bis(trifluoromethylsulphonyl)imide

List of Publications

1. Yu, L.; Grace, T.; Batmunkh, M.; Dadkhah, M.; Shearer, C.; Shapter, J. Insights into Chemical Doping to Engineer the Carbon Nanotube/Silicon Photovoltaic Heterojunction Interface. *J. Mater. Chem. A* **2017**. 5, 24247-24256.
2. Yu, L.; Grace, T.; Pham, H. D.; Batmunkh, M.; Dadkhah, M.; Shearer, C.; Sonar, P.; Shapter, J. Application of Hole-Transporting Materials as the Interlayer in Graphene Oxide/Single-Wall Carbon Nanotube Silicon Heterojunction Solar Cells. *Aust. J. Chem.* **2017**. 70, 1202-1211.
3. Yu, L.; Batmunkh, M.; Grace, T.; Dadkhah, M.; Shearer, C.; Shapter, J. Application of a Hole Transporting Organic Interlayer in Graphene oxide/Single walled Carbon Nanotube-Silicon Heterojunction Solar Cells. *J. Mater. Chem. A* **2017**. 5, 8624-8634.
4. Yu, L.; Grace, T.; Jazi, M. D.; Shearer, C.; Shapter, J. Optimization of the Metal Front Contact Design for Single-Walled Carbon Nanotube-Silicon Heterojunction Solar Cells. *Solar RRL* **2017**. 1600026.
5. Yu, L.; Shearer, C.; Shapter, J. Recent Development of Carbon Nanotube Transparent Conductive Films. *Chem. Rev.* **2016**. 116, 13413-13453.
6. Yu, L.; Tune, D.; Shearer, C.; Grace, T.; Shapter, J. Heterojunction Solar Cells Based on Silicon and Composite Films of Polyaniline and Carbon Nanotubes. *IEEE J. Photovolt* **2016.** 6, 688-695.
7. Yu, L.; Tune, D.; Shearer, C.; Shapter, J. Heterojunction Solar Cells Based on Silicon and Composite Films of Graphene Oxide and Carbon Nanotubes. *ChemSusChem* **2015.** 8, 2940-2947.
8. Yu, L.; Tune, D.; Shearer, C.; Shapter, J. Implementation of Antireflection Layers for Improved Efficiency of Carbon Nanotube-Silicon Heterojunction Solar Cells. *Sol. Energy* **2015**. 118, 592-599.
9. Yu, L.; Tune, D. D.; Shearer, C. J.; Shapter, J. G. Application of polymer interlayers in silicon–carbon nanotube heterojunction solar cells. *ChemNanoMat* **2015**. 1, 115-121.
10. Bat-Erdene, M; Batmunkh, M.; Shearer, C.; Tawfik, S.; Ford, M.; Yu, L.; Sibley, A.; Slattery, A.; Quinton, J.; Gibson, C.; Shapter, J. Efficient and Fast Synthesis of Few-layer Black Phosphorus Flakes via Microwave-assisted Liquid-phase Exfoliation, *Small Methods* **2017.**
11. Bat-Erdene, M; Batmunkh, M.; Tawfik, S.; Fronzi, M.; Ford, M.; Shearer, C.; Yu, L.; Dadkhah, M.; Gascooke, J.; Gibson C.; Shapter, J. Efficiency Enhancement of

Single-walled Carbon Nanotube-silicon Heterojunction Solar Cells Using Microwave-exfoliated Few-layer Black Phosphorus, *Adv. Funct. Mater.* 2017.
12. Shearer, C.; Yu, L.; Fenati, R.; Sibley, A.; Quinton, J.; Gibson, C.; Ellis, A.; Andersson, G.; Shapter, J. Adsorption and Desorption of Single-Stranded DNA from Single-Walled Carbon Nanotubes. *Chem-Asian J.* 2017. 12, 1625-1634.
13. Batmunkh, M.; Shrestha, A.; Gao, G.; Yu, L.; Zhao, J.; Biggs, M. J.; Shearer, C.; Shapter, J. Sulfur-Doped Graphene with Iron Pyrite (FeS2) as an Efficient and Stable Electrocatalyst for the Iodine Reduction Reaction in Dye-Sensitized Solar Cells. *Solar RRL* 2017. 1, 1700011.
14. Grace, T.; Yu, L.; Gibson, C.; Tune, D.; Alturaif, H.; Al Othman, Z.; Shapter, J. Investigating the Effect of Carbon Nanotube Diameter and Wall Number in Carbon Nanotube/Silicon Heterojunction Solar Cells. *Nanomaterials* 2016. 6, 52.
15. Gao, G.; Yu, L.; Vinu, A.; Shapter, J. G.; Batmunkh, M.; Shearer, C. J.; Yin, T.; Huang, P.; Cui, D. Synthesis of Ultra-Long Hierarchical ZnO Whiskers in a Hydrothermal System for Dye-Sensitised Solar Cells. *RSC Adv.* 2016. 6, 109406-109413.

- Chapter 1 contains parts of publication 5.
- Chapter 2 contains parts of publication 1, 3, 4, 5 and 6.
- Chapter 3 contains parts of publication 6.
- Chapter 4 contains parts of publication 4.
- Chapter 5 contains parts of publication 3.
- Chapter 6 contains parts of publication 1.

Chapter 1 Introduction

This Chapter has been published as “Recent Development of Carbon Nanotube Transparent Conductive Films” in Chemial Reviews in 2016.

Yu, L.; Shearer, C.; Shapter, J. Recent Development of Carbon Nanotube Transparent Conductive Films. Chem. Rev. 2016. 116, 13413-13453.

Summary

Transparent conducting films (TCFs) now play an important role in many personal electronic devices. Because of the excellent optoelectronic properties, transparent and conductive doped metal oxides are widely applied in current industry and the production processes have been built on the mature understanding of various materials. However, they have limited compatibility with large-scale production (such as roll-to-roll manufacturing) for flexible electronic devices that will be important the near future. A great number of studies have revealed the unique physical, chemical and optoelectronic properties of carbon nanotubes, which make them a potential alternative to doped metal oxides. A detailed analysis of carbon nanotube based transparent conducting films is summarised in this Chapter, including various fabrication methods, chemical doping effects, and hybridisation with other materials. Insights into the optoelectronic properties of the films as well as the potential applications, such as photovoltaics, touch panels, liquid crystal displays and organic light emitting diodes are provided. In addition, both the merits and shortcomings of carbon nanotube transparent conducting films are analysed.

1.1 Overview

Recently, the market for commercial optoelectronic devices, including touch panels, liquid crystal displays (LCDs), photovoltaics and organic light-emitting diodes (OLEDs), has expanded significantly and thus the requirement for transparent conducting films is increasing rapidly.[1] The consumption of TCFs has been led by the LCD industry for years with sales of approximately USD 1.5 billion in 2014.[2] The commercial market of TCFs in the touch panel industry was almost USD 1 billion in 2012, with an anticipated number of USD 5 billion by 2019.[3] A similar market size exists in thin film solar cells whose sales was over 15 billion in 2017.[4]

The most popular and well-studied materials in the field of industrial TCFs are transparent and conductive doped metal oxides (TCOs)[5-9] that can be both p-type[10] and n-type[11] semiconductors. Indium tin oxide (ITO), consisting of tin oxide (SnO_2) and indium oxide (In_2O_3), is the most well-known example and has the best performance among different kinds

of TCOs.[12] However, there are still several issues for ITO though it has excellent optoelectronic properties with a low sheet resistance (R_{sheet} or R_s), ranging from 10 to 100 Ω sq^{-1} at high transmittance (T) above 85 %:[13] (a) The cost and scarcity of indium which accounts for 75 % of the total mass of ITO.[14] (b) Brittleness as demonstrated by cracking under low strain[15] which results in performance degradation upon cyclic bending.[16] Attempts have been made to overcome the ceramic nature by laminating ITO onto a flexible substrate, e.g. polyethylene terephthalate (PET), or by controlling the ratio of indium and tin. The fact is that these methods result in extra manufacturing costs and/or poorer optoelectronic performances.[17] (c) Limited lifespan: the diffusion of indium into the active layer of photovoltaics and OLEDs occurs under certain circumstances, and the corrosion of ITO takes place after being exposed to traces of adhesives and acids in the environment.[18-20] (d) High production costs: different processes have been developed to fabricate ITO films, such as screen printing,[21] molecular beam epitaxy,[22] magnetron sputtering,[23] sol-gel techniques,[24] and pulsed laser deposition,[25] but most of these techniques either consume significant amount of energy due to high-temperature processing steps or cause the waste of raw materials by inefficient deposition.[26] Other alternative doped TCOs, including fluorine-doped tin oxides (FTOs), have similar issues as ITO.

Due to these existing issues for TCOs, researchers have been looking for alternative organic-based materials. When the electrical conductivity of a variety of commonly used polymers, including polypyrrole and polythiophene, was improved by the addition of chemical dopants (such as diamine green black[27] and chromotropic acid disodium salts[28]), conducting polymers attracted attention as an alternative to TCOs. Compared to TCOs, the flexibility and simple preparation processes are two most attractive properties of conducting polymer based TCFs.[29-32] However, the instability of their electrical properties when exposed to different stresses including humidity, UV light, and high-temperature environments is the major challenge for large-scale commercialisation.[33-38] Besides, a noticeable blue/green colour exists in thicker films,[39] which limits their application in display panels.

Another potential TCF material is metallic nanostructures, such as metal films, conducting grids, and metallic nanowires, all of which have been shown to provide better optoelectronic properties than TCOs when on certain plastic substrates.[40-57] However, a hazy appearance

often occurs with these metallic structures, which might be beneficial to various photovoltaics but not compatible with display applications.[58] Metallic nanoparticles (NPs), commonly made from silver, have a similar cost to indium, indicating that there is little financial advantage to apply metallic NPs. Furthermore, the chemical, thermal, and aging stability of TCFs made from metallic NPs is one major concern, and many reports show fast degradation of the electronic properties.[59-61]

It is a revolutionary time for materials scientists because there are a wide range of existing materials considered as potential suitable alternatives to TCFs, but none of these is currently suitable for large-scale, long-term commercial manufacturing. Due to the continuous development of new products reliant on TCFs (such as annually upgrading smart mobile phones), the expense of materials, performance, and the cost of manufacture will continue to be concerns in this burgeoning market. Thus, research into a novel generation of materials for TCFs is required. Compared to TCOs and other options, carbon nanotubes (CNTs) have a series of merits including the abundance of original material (carbon), excellent inherent optoelectronic properties with high flexibility, ease of solution-based processing at room temperature, physical and chemical stability, and a wide spectral range of transmittance with a neutral color.[62] In this Chapter, the properties of CNTs will be summarised first, followed with a list of the requirements for TCFs, and then several preparation and modification methods of the CNT-based TCFs with an emphasis on their optoelectronic properties will be presented, and it will finish with a summary of their applications focusing on photovoltaics, touch panels, liquid crystal displays, and organic light-emitting diodes.

1.2 Properties of CNT TCFs

1.2.1 Properties of CNTs

CNTs were firstly known as carbon nanofibers or graphite whiskers during the 1950s, which then have been the subject of much research since the discovery of their atomic structure by Iijima in 1991.[63] A single-walled carbon nanotube (SWCNT) is similar to a rolled up, single sheet of two-dimensional graphene while the carbon atoms remain in the sp^2 hybridised network.[64] As a result, CNTs have different electronic properties changing from the zero

bandgap semimetal of graphene to a mixture of metallic and semiconducting materials depending on the rolling angle because of the curvature-induced misalignment of p orbitals in the carbon network.[65] SWCNTs can be described completely, except for their length, by the chiral vector (**C**) and **C** is created by choosing two carbon atoms on a single graphene sheet, in which one of the two carbon atoms is chosen as the origin (Figure 1.1 (a)). The chiral vector is directed from the origin to the other carbon atom on the sheet and is defined by Equation 1.1,

$$\mathrm{C} = \mathrm{n}\mathrm{a}_1 + \mathrm{m}\mathrm{a}_2 \qquad \text{Equation 1.1}$$

As shown in Figure 1.1 (a), where n and m are integers, and $\mathbf{a_1}$ and $\mathbf{a_2}$ are the unit chiral vectors of the planar graphene lattice (which originate at the same position as **C**). The nanotube diameter, d_t, can be calculated from the chiral vector by the following Equation 1.2,[66]

$$d_t = \frac{C}{\pi} \qquad \text{Equation 1.2}$$

Equation 1.3 shows the relationship between the electronic properties of the SWCNTs and chiral vectors, n and m; if

$$|\mathrm{n} - \mathrm{m}| = 3\mathrm{q} \qquad \text{Equation 1.3}$$

where if q is an integer, the SWCNTs will be a metal species; otherwise, they will be semiconducting species.[67] The angle between **C** and the nearest zigzag of C−C bonds is specified as the chiral angle, θ ($0° \leqslant \theta \leqslant 30°$), which determines the wrapping pattern of CNT. When θ equals 30°, the SWCNTs (n, n) are known as “armchair” and the SWCNTs (n, 0) are “zigzag” if θ is 0°. SWCNTs are called chiral species when θ is between 0 and 30° (Figure 1.1 (b), with zigzag and armchair structures shown in red).

Therefore, supposing that all chiral species have the same probability of growth, one-third of the CNTs are metallic with two-thirds semiconducting formed in a typical nonselective synthesis.[68] The energy band gap (E_g, in eV) of the semiconducting species is linked to the diameter of the SWCNT, [69] as shown in Equation 1.4, 1.5, and 1.6:

$$\tilde{\nu}_{\mathrm{g}}\ (\mathrm{mod}\ 1) = \frac{1 \times 10^{-7}\ \mathrm{cm}^{-1}}{157.5 + 1066.9\mathrm{d_t}} - 771\ \mathrm{cm}^{-1}\frac{[\cos(3\theta)]^{1.374}}{\mathrm{d_t}^{2.272}} \qquad \text{Equation 1.4}$$

$$\tilde{\nu}_g \,(\mathrm{mod}\ 2) = \frac{1\times10^{-7}\ \mathrm{cm}^{-1}}{157.5 + 1066.9 d_t} + 347\ \mathrm{cm}^{-1}\frac{[\cos(3\theta)]^{0.886}}{d_t^{2.129}} \qquad \text{Equation 1.5}$$

$$E_g = \frac{hc\tilde{\nu}_g}{1.6022\times10^{-19}\mathrm{J}} \qquad \text{Equation 1.6}$$

where h is Planck's constant (6.626×10^{-34} m^2 kg s^{-1}), c is the speed of light (3×10^8 m s^{-1}), and $\tilde{\nu}_g$ (mod 1) is applicable when the remainder of (n − m)/3 is 1, and otherwise $\tilde{\nu}_g$ (mod 2) is applicable.

CNTs can also be classified by the number of shells (n_{shell}) with SWCNTs (n_{shell} = 1), double-walled CNTs (DWCNTs, n_{shell} = 2), and multi-walled CNTs (MWCNTs, $n_{shell} \geqslant 3$), as shown in Figure 1.1 (c). The structural stability of DWCNTs is higher than that of SWCNTs, and the band structure of DWCNTs is not affected by the interaction between different layers, with the potential barrier determined by the chirality pairs.[70] Individual MWCNTs with small diameters (d_t < 10 nm) perform like an SWCNT, and the interaction between adjacent shells is negligible.[71] For MWCNTs with large diameters (d_t >10 nm), they behave like metals.[72] Quasi-ballistic conduction exists in all shells, and thus electron transport happens in all the shells of an MWCNT.[73] In terms of TCF applications, the most important transport properties of CNTs have been well-studied. Some of the main properties of CNTs are listed in Table 1.1 with comparisons to other regular or traditional materials.[74-76] Among these, the excellent electrical conductivity is the most critical property which provides a solid foundation to fabricate conducting transparent thin films. In addition, the amazing thermal and mechanical properties broaden its application in the industry as TCF material. However, it is worth pointing that most of these attractive properties are highly anisotropic (along its axial direction), which causes some challenges for real practical application.[77]

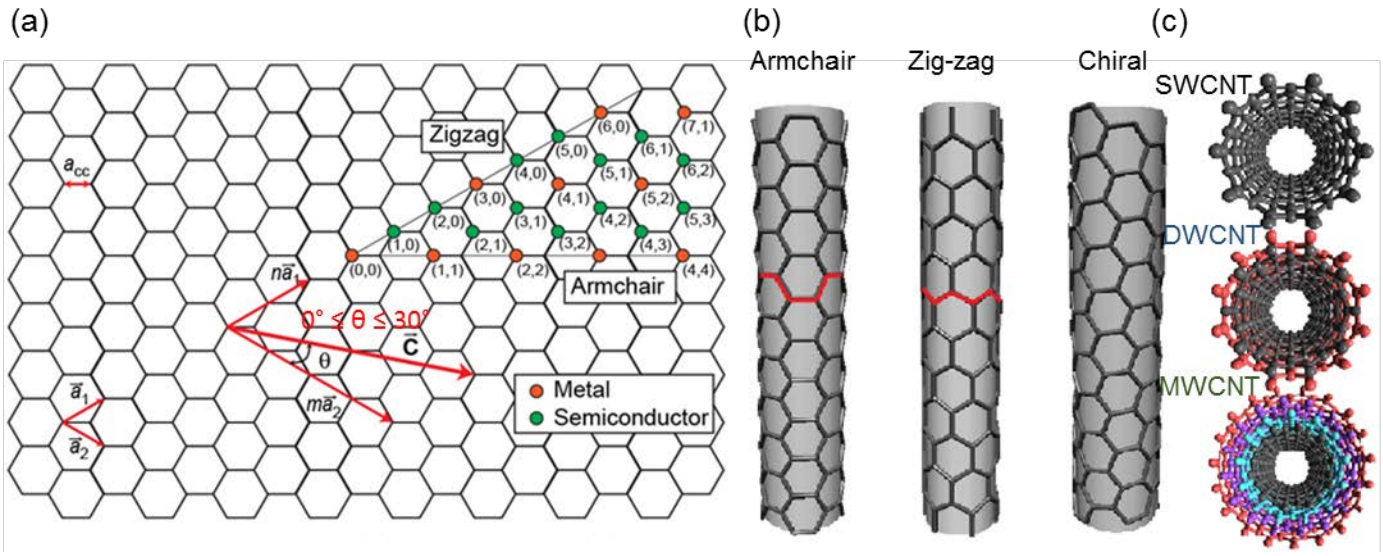

Figure 1.1 (a) A single layer graphene sheet demonstrating that the chiral vector C and electronic properties of SWCNTs are affected by different values of the integers. (b) The appearance of the SWCNTs is dependent on the direction of the chiral vector C, including armchair, zig-zag and chiral structure. (c) "Ball and Stick" schematic of single-walled CNT (SWCNT), double-walled CNT (DWCNT), and multi-walled CNT (MWCNT) (Images are Made Using Nanotube Modeller (www.jcrystal.com)).

Table 1.1 Summary of Properties of CNTs

Property	Value	Remarks
Intrinsic mobility	Exceeding 10^5 cm^2 V^{-1} s^{-1} for individual CNT at room temperature and the value decreases with the decrease in the diameter[78-79]	Almost 100 times higher than that of silicon at 300 K with dopant concentration at 10^{17} cm^{-3} [80-82]
Free carriers concentration	~ 10^{17} cm^{-3} [83-84]	Lower than that of graphene (~ 10^{20} cm^{-3}) , TCOs (~ 10^{21} cm^{-3}) and most of metals (such as ~ 10^{22} cm^{-3} for silver) [85-86]
Current carrying capacity	Exceeding 10^9 A cm^{-2} for individual CNT[87]	1000 times higher than copper [88]
Electrical conductivity	10^4 - 10^6 S cm^{-1} [89-92]	Close to that of some metals, such as mercury[93-94]
On/Off current ratios	Higher than 10^5 [95-97]	1000 times higher than a bilayer structure at room temperature [98]
Thermal conductivity	Up to 3500 W m^{-1} K^{-1} [99-101]	About 1500 W m^{-1} K^{-1} higher than that of diamond [102-103]
Young's modulus	1-2 TPa [104-110]	Comparable to that of a single crystal diamond at room temperature [111]
Fracture stress	50 GPa [112-114]	~ 50 times larger than that of steel wires after density normalization [115-116]
Surface area	1600 m^2 g^{-1} [117-118]	Higher than that of activated carbon (1200 m^2 g^{-1}) [119-120]

1.2.2 Characterisation and requirements of TCFs

1.2.2.1 Figure of merit of TCFs

The requirement for an ideal transparent conducting film contains two points: a very low sheet resistance (or high conductivity) and a very high transmission across a wide range of wavelengths. Practically, a 4-point probe (sometimes 2-point conductivity probe) is applied to measure R_{sheet} while the transmittance is estimated by the UV−Vis-NIR absorbance spectrum of the TCF. In fact, there is a trade-off between these two factors (R_{sheet} and T). Thus, in order to compare the properties of TCFs among different studies, the two major parameters must be combined. Though there are a few proposals, the most commonly used is the ratio of DC electrical conductivity (σ_{DC}) and optical conductivity (σ_{OP}).[121]

De et al. firstly proposed this approach which is useful in evaluating the overall performance of CNT TCFs from different groups, as is shown in Equation 1.7 which is rearranged as Equation 1.8,[122]

$$T = \left(1 + \frac{1}{2R_{sheet}} \cdot \sqrt{\frac{\mu_0}{\varepsilon_0}} \cdot \frac{\sigma_{OP}(\lambda)}{\sigma_{DC}}\right)^{-2} \qquad \text{Equation 1.7}$$

$$\frac{\sigma_{DC}}{\sigma_{OP}(\lambda)} = \frac{1}{2R_{sheet}} \frac{(\frac{\mu_0}{\varepsilon_0})^{\frac{1}{2}}}{T^{-\frac{1}{2}}-1} \qquad \text{Equation 1.8}$$

where T is the transmittance, R_{sheet} is the sheet resistance, and μ_0 and ε_0 are the free space permeability ($4\pi \times 10^{-7}$ N A^{-2}) and permittivity (8.854×10^{-12} C^2 N^{-1} m^{-2}), respectively. In order to characterise the properties of TCFs, one can either input T, and R_{sheet} with the σ_{OP} value at 550 nm (150 or 200 S cm^{-1}),[123] to calculate σ_{DC} or substitute T and R_{sheet} to calculate the ratio of σ_{DC}/σ_{OP}, in which both T and R_{sheet} can be measured experimentally to obtain the "figure of merit" (FOM). The calculated values can then be used to compare the TCFs reported in the different studies. Alternatively, σ_{DC} can be directly determined by the film thickness (t) (normally estimated by atomic force microscopy (AFM)) with the R_{sheet} value, as shown in Equation 1.9:

$$\sigma_{DC} = (R_{sheet}t)^{-1} \qquad \text{Equation 1.9}$$

It is worth noting that the σ_{OP} is related to the number of shells of the CNT, and thus one can only use this equation to compare the films made of the same type of CNTs when σ_{DC} is applied to compare the properties of TCFs. Furthermore, this formula is founded on two assumptions: (1) the film is thin enough so that the wavelength of the incident light is much larger than the thickness of the film, and (2) the reflected light is negligible when compared to the absorbed fraction. For most CNT films, since both of the conditions are met (specifically, the film thickness is generally less than 50 nm and the reflection of CNT films is very low on glass or PET substrates)this equation is applicable for comparison.

The ratio of σ_{DC}/σ_{OP} is very popular and useful in comparing the properties of TCFs. Higher values of σ_{DC}/σ_{OP} indicate better optoelectronic properties of TCFs. Therefore, the ratio will be used to compare TCFs properties from different literature in the following sections.

1.2.2.2 Practical requirements of TCFs

Different applications require TCFs with different optoelectronic performance. For instance, a TCF applied in a touch panel requires slight flexibility with high transmittance (above 85%) so that it can deform with touch. The R_{sheet} of a touchscreen can be relatively high (500 Ω sq^{-1}), since the working parameters are inductive in most cases. Specifically, the required σ_{DC}/σ_{OP} is about 4.5 after combining these parameters. In contrast, the ideal TCFs used in photovoltaics need both low R_{sheet} and high T to meet the requirement of being transparent as well as conductive and achieve high energy harvesting efficiency (as high as 25%). Table 1.2 shows the optoelectronic requirements for some potential practical applications.[124-130]

Table 1.2 Minimal requirements of CNT TCFs for the practical applications

Application	T	R_{sheet} (Ω sq^{-1})	σ_{DC}/σ_{OP}
Touch panel	85 %	500	4.5
LCD screen	85 %	100	22.3
OLED display	90 %	50	69.7
Photovoltaic electrode	90 %	10	348

1.2.3. Optical properties of CNT TCFs

Compared to the other regular TCFs, one of the major advantages of CNT based TCFs is the low and featureless optical absorption. Specifically, the detailed UV-vis-NIR spectra of commonly used different conductive materials are shown in Figure 1.2 (a),[83] including CNT, graphene, Ag grids, poly (3, 4-ethylenedioxythiophene)-poly-(styrenesulfonate) (PEDOT:PSS) and ITO. Because of the similar chemical structures, the visible and NIR transmittance spectra of CNT and graphene films are similar with a minor increase in the transmittance above 1000 nm. In contrast, the transmittance of the conducting polymer PEDOT:PSS and ITO drops significantly above 1000 nm. With increasing wavelength, the reflection of Ag grids increases. Thus, the T of the metal grid (Ag grid) starts to decrease in the NIR region.[131] One of the other advantages of CNT TCFs is the potential to be applied as the electrodes in IR photovoltaics since the charge carrier density is relatively low and it enables a high cut-off wavelength to maintain the transparency. While CNT TCFs are considered transparent in NIR region (above 1000 nm), the absolute T of a particular CNT film is determined by the packing density of the

CNTs. The transmittance of CNT TCFs increases (black → red → green → blue) with a decrease in the packing density of the CNTs, as shown in Figure 1.2 (b).[132] Meanwhile, R_{sheet} is dependent on the optical transmittance (practically, T is determined by the CNT packing density on the film, as shown in Figure 1.2 (c)) due to the fact that the density increases with the decrease in both T and R_{sheet}. The decrease in T is due to more light absorption from denser CNT network. The decrease in R_s is caused by the increase in charge percolation through the network as the CNT coverage becomes higher. As a consequence, for the system in Figure 1.2 (c), the R_{sheet} decreases from 600 to 40 Ω sq^{-1} with the decrease in T, while the R_s is as high as ~2000 Ω sq^{-1} for CNT films with low packing density (when the T at 550 nm is above 95%). Noticeably, the T at 550 nm is widely used to characterise the optical properties of TCFs.

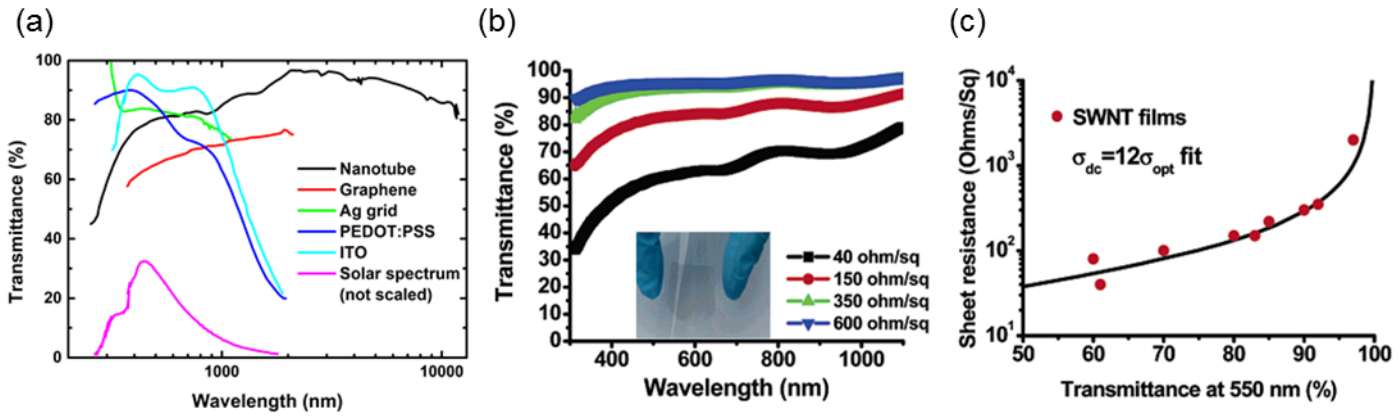

Figure 1.2 (a) UV-vis-NIR spectra comparison of different conducting materials (The y axis of the solar spectrum (purple trace) is irradiance (in W m^{-2} nm^{-1}) not transmittance. Adapted with permission from ref 131. Copyright 2015 Royal Society of Chemistry. Adapted with permission from ref 83. Copyright 2009 AIP Publishing LLC. (b) Transmittance versus wavelength from 300 to 1100 nm with different CNT packing densities (the amount of CNT per unit area) and the inset shows a CNT film coated on a flexible PET substrate.[132] (c) R_{sheet} versus T at 550 nm (SWCNT films) with changing CNT density and its fitting equation.[132] Reprinted with permission from ref 132. Copyright 2006 American Chemical Society.

1.2.4 Transport properties of CNT TCFs

1.2.4.1 Effect of geometry

1.2.4.1.1 Percolation Threshold

Generally speaking, CNTs in a particular TCF contain both semiconducting and metallic SWCNTs species with different chiralities and lengths. The thickness of a CNT film with transmittance above 70% is usually less than 50 nm. In a simplified model, the charge carriers are regarded to be transported along an individual CNT and then hop to the next CNT across the junction. However, the reality is much more complicated than this model. Commonly, people applied percolation system to study the transport behaviour for thin CNT networks.[133-138] The threshold (N_c), in two-dimensional (2D) percolation theory, is defined as Equation 1.10,

$$N_c = f^2/\pi L_S^2 \approx \frac{1}{L} \qquad \text{Equation 1.10}$$

Where *f* is dependent on the length (it is 4.236 for isotropic network), and L_s is the individual length of the CNT while L is the aspect ratio of the CNT.[139] For an individual CNT (1−2 μm long with a diameter of 1−2 nm), the aspect ratio is high, above 500 (though CNT bundles in reality have slightly larger diameters). Therefore, according to 2D percolation theory, the percolation threshold for CNT films is low, and it indicates that the surface coverage (the number of CNTs) required to form a path to transport charge carriers is not high, and hence the corresponding transmittance would be high. The R_{sheet} of CNT networks decreases significantly with the increase in CNT surface coverage above the percolation threshold. Practically, for example, the conductance of CNT networks with thickness (controlled through varying CNT suspension volume in a vacuum filtration to form a TCF) obeys a power law as shown in Figure 1.3.[96]

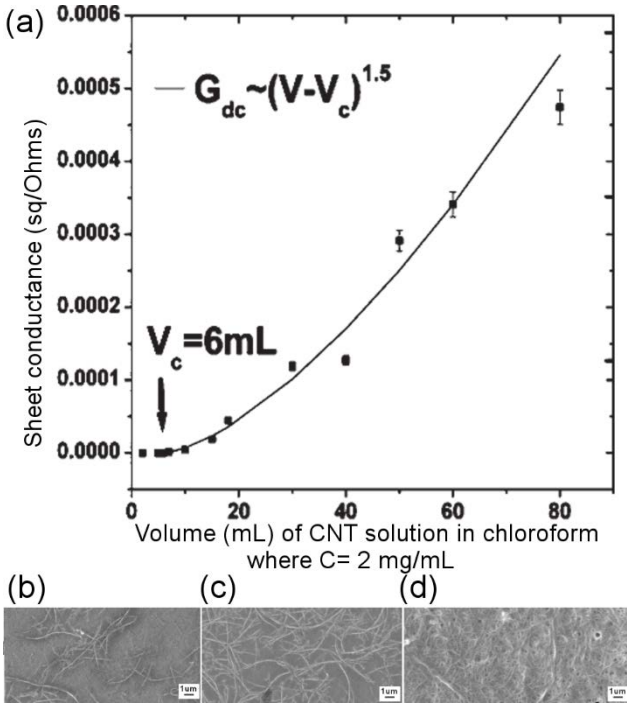

Figure 1.3 (a) Exponential relationship between the conductance of a CNT network and its surface coverage. Scanning electron microscope (SEM) images of the CNT networks with different stock solution volumes added during vacuum filtration process: (b) 7 mL, (c) 10 mL, and (d) 400 mL.[96] Adapted with permission from ref 96. Copyright 2004 American Chemical Society.

1.2.4.1.2 Effect of CNT Alignment

In addition, the alignment of CNTs in a particular network has an impact on the percolation threshold. As shown in Figure 1.4 (a),[140] simulation results by Du et al. have demonstrated that networks made of 50 randomly distributed sticks whose lengths equal 0.255 times the length of the side of the square (with the cut-off angle $\theta_\mu = 90°$, which is used to evaluate the degree of alignment and the cut-off angle is the maximum angle the sticks can reach with respect to y axis) or 100 well-aligned sticks (with the cut-off angle $\theta_\mu = 5°$) do not contain a conducting percolation path because of either low surface coverage or anisotropy. As the number of randomly distributed sticks in the network further increases to 100, a conducting path (the grey area) occurs, as shown in Figure 1.4 (a)-(3). It was also found that slightly anisotropic networks (with cutoff angle θ_μ between 70° and 90°) have a higher percolation probability at low loading of sticks while slightly disordered networks improve the percolation probability dramatically

under high loading condition, as shown in Figure 1.4 (b). Thus, CNT networks with randomly distributed individuals are preferred due to the lower percolation threshold, which provides the potential for high performance TCFs.[141-144] Furthermore, Unalan et al. experimentally determined that the percolation threshold of a metallic CNT network is higher than that of a mixture of metallic and semiconducting CNTs counterpart (5.5×10^{-3} versus 1.8×10^{-3}).[145] In terms of the application of transistors, the surface coverage must between these two thresholds so as to achieve a conduction path with no short circuits. As an example showing the way percolation dominates the conductive properties of TCFs, the width of the CNT film has an impact on the resistance. In detail, as shown in Figure 1.4 (c),[146] the experimentally measured resistivity increased with the decrease in film width to less than 20 μm. Reducing the film width via etching removes some percolation pathways since the percolation paths are not aligned in the current flow direction completely, and as a result, the resistance of the film increases significantly with the reduced film width, especially when close to the length of individual CNT.

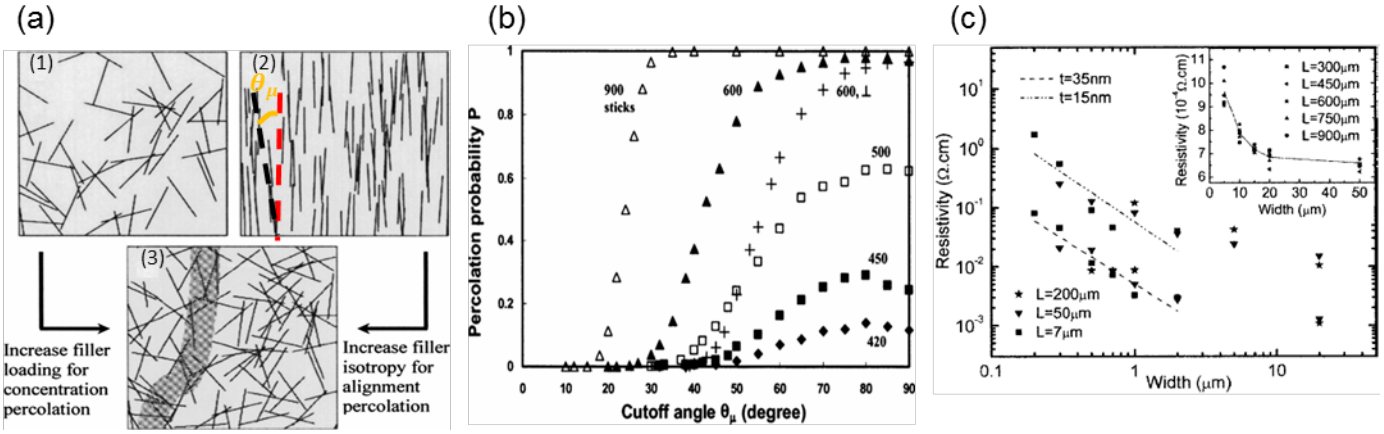

Figure 1.4 (a) Simulation of 2D percolation pathways in (1) 50 randomly distributed sticks with θ_μ = 90°, (2) 100 well-aligned sticks with θ_μ = 5°, and (3) 100 randomly distributed sticks with θ_μ = 90°. (b) The percolation probability versus the cut-off angle with different number of loading sticks (represented by values in (b)). Reprinted with permission from ref 140. Copyright 2005 American Physical Society. (c) The relationship between the resistivity and the channel width of the CNT films with different length (200, 50, and 7 μm) and thicknesses (15 and 35 nm) on a log-log scale. The inset shows the

relationship between the resistivity and width with the film thickness of 55 nm on a linear scale. Reprinted with permission from ref 146. Copyright 2006 AIP Publishing LLC.

1.2.4.1.3 Effect of CNTs bundle length and diameter

Since the junction resistance from the overlapping contacts between CNTs is the main source of the resistance of a CNT network (while the contribution from the tube resistance is small),[147-149] it is believed that films with longer CNTs might result in lower resistance than films containing larger number of shorter CNTs with the same surface coverage. It is experimentally found that there is an exponential relationship between the film conductance and the average bundle length of CNTs, as shown in Figure 1.5 (a).[150] With the benefit of fabricating potentially more conducting films, longer CNTs, however, are more difficult to disperse, particularly in high concentration, which limits many approaches based on solution deposition. Regarding the impact of the CNT bundle diameter on the resistance of the CNT films, it was experimentally found that films formed using smaller bundle sizes have lower R_{sheet}, as shown in Figure 1.5 (b).[151]

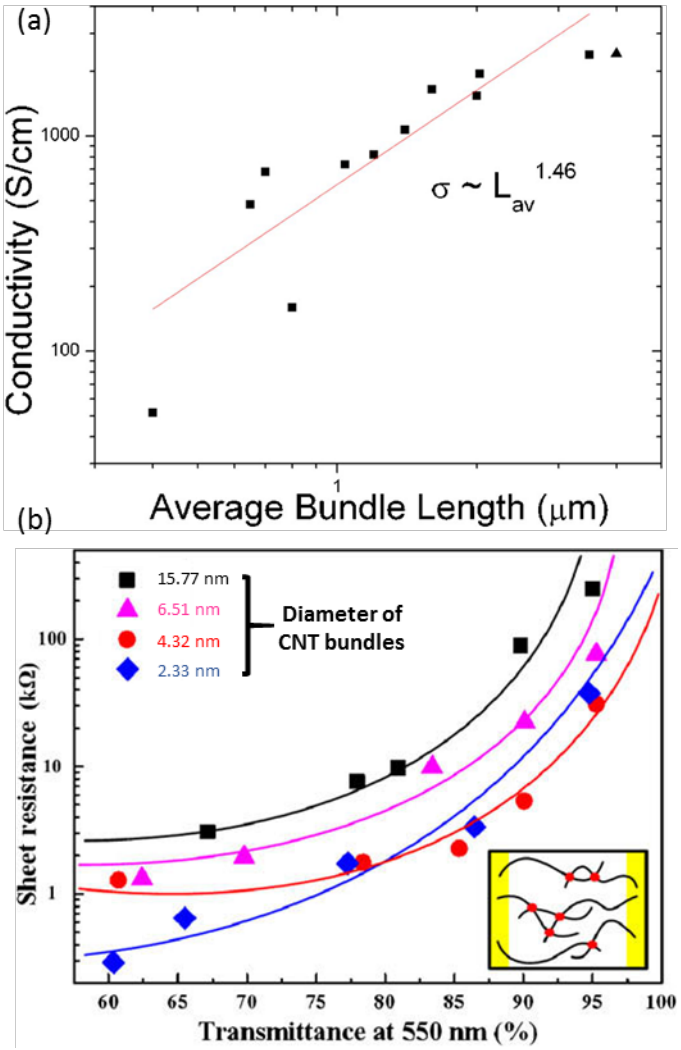

Figure 1.5 (a) The exponential relationship of the CNT film conductivity versus the average bundle length of CNTs. Adapted with permission from ref 150. Copyright 2006 AIP publishing LLC. (b) The relationship between R_{sheet} of CNT films with different CNT bundle diameters and their T at 550 nm. Reprinted with permission from ref 151. Copyright 2009 Elsevier.

1.2.4.1.4. Effect of the geometry of an individual CNT

Since there are more charge carriers for semiconducting SWCNTs with larger diameters due to smaller band gaps at room temperature, a SWCNT film formed with larger diameters has lower R_{sheet}.[152] Additionally, films made of MWCNTs are less conducting than those made of DWCNTs and SWCNTs, as shown in Figure 1.6,[153-154] mostly due to the fact that the diameter

of MWCNTs is much larger than that of DWCNTs and SWCNTs, which absorbs more light but does not increase the conductivity. Furthermore, due to the better dispersity in liquid medium, thin films based on SWCNTs are easier to fabricate practically than the ones made of DWCNTs and MWCNTs.[153,155]

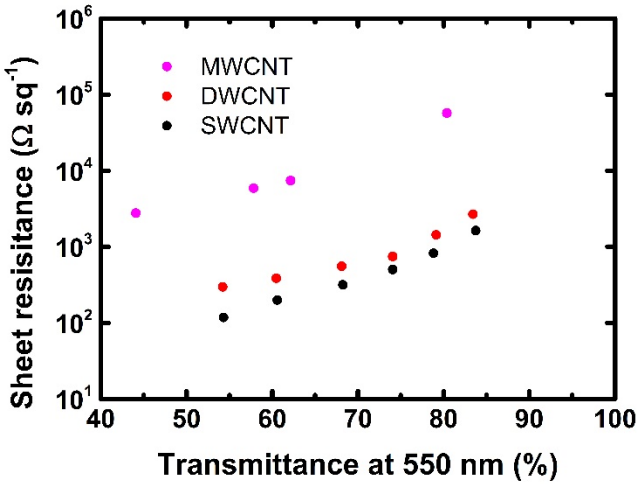

Figure 1.6 Impact of the number of shells of CNTs on the R_{sheet} of CNT films. Data are extracted from refs 156-158.

1.2.4.2. Effect of purity and synthesis methods.

There are a number of other factors, including doping level, purity and so on, that have an influence on the charge-transport properties of CNT TCFs. Among these, the purity of the CNTs can have a great impact on the R_{sheet} of the films since any sp^3 carbon bonds and amorphous carbon in the network are structural defects which leads to charge scattering and therefore increases R_{sheet}. This is clearly demonstrated by the fact that CNT films with a high G to D band intensity ratio (a measure of structural defects degree) in Raman spectrum have lower R_{sheet}.[152] However, this does not mean that functionalisation of CNTs would increase the resistance of the film. For example, acyl chloride groups formed by $SOCl_2$ along the CNT has a doping effect which can effectively improve the optoelectronic properties of the CNT films.[159-160] This synthesis method for CNTs makes a clear difference in the R_{sheet} of the films as well, and arc discharge seems to be better than other synthesis approaches due to the slightly larger diameter of SWCNTs produced via arc discharge, as shown in Figure 1.7.[152]

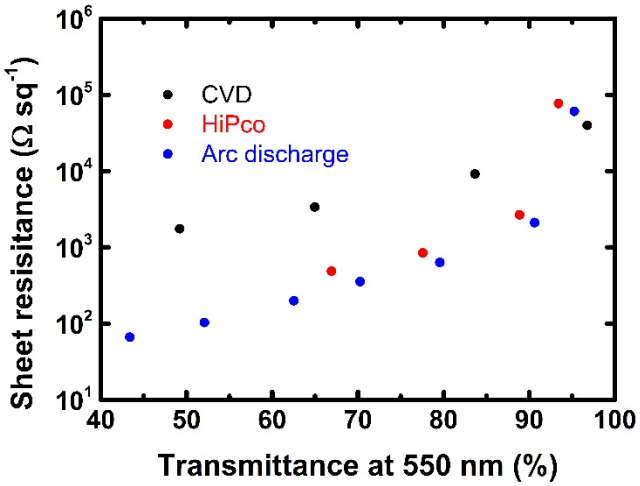

Figure 1.7 Impact of CNT synthesis approach on the optoelectronic properties of CNT TCFs produced via CVD, HiPco, and arc discharge. Data extracted from refs 161-163.

1.2.4.3. Effect of electronic types of CNT

Due to the mixed nature, the electrical conduction behaviour of SWCNT films is related to the transport nature of both junction resistance between SWCNTs and individual SWCNTs under a specific condition. The overall resistance along a conducting path is defined as Equation 1.11:

$$R_{path} = R_{SWCNT-SWCNT} + R_{SWCNT} \qquad \text{Equation 1.11}$$

where $R_{SWCNT-SWCNT}$ and R_{SWCNT} are the overall resistances contributed by the contacts between the overlapping CNTs along the conduction path and the individual SWCNTs.[164] Additionally, when it is measured with metal contact, the resistance of the individual SWCNTs is defined as Equation 1.12,

$$R_{SWCNT} = \frac{h}{4e^2} + R_c + R_t \qquad \text{Equation 1.12}$$

where h is Planck's constant; e is electron charge; R_c and R_t are the resistances contributed from the contact with extra metal (it can normally be neglected if a four-point probe is applied during the measurement) and phonon scattering, respectively.[165]

There are two critical facts here. Firstly, individual semiconducting SWCNTs have much higher resistance (10 Ω cm) at room temperature than their metallic counterparts (10^{-4} -

10^{-3} Ω cm).[166-167] Secondly, the contact resistance between metallic and semiconducting SWCNTs (R_{M-S}, 1 MΩ) is much higher than that between two metallic or two semiconducting CNTs (R_{M-M} and R_{S-S}, 20 kΩ) at ambient temperature.[168-171] The correlation between the conductance of thin SWCNT films and the ratios of metallic and semiconducting SWCNT species (M/S ratios) are simulated in Figure 1.8 (a).[172] Due to the relatively low R_{M-M} and R_{S-S}, pure metallic and semiconducting CNT films have quite high conductance. As shown in Figure 1.8 (a), when there are more than 70% semiconducting species in the film (at point B), Schottky barriers from the junctions between the semiconducting and metallic SWCNTs dominate the conductance, with the conductance path blocked at point C where approximately 80% SWCNTs are semiconducting. However, when the network only contains a small amount of metallic species, the semiconducting path starts to not be blocked via bypassing the Schottky barriers and charge carriers can then transport through semiconducting SWCNT network. A conduction mechanism was proposed by Yanagi et al. for SWCNT networks with various M/S ratios, including variable range hopping models for pure semiconducting network and weak localisation for pure metallic film, respectively.[173] In their report, it was experimentally found that the presence of semiconducting SWCNTs was related to the localisation of the conduction electrons, while the quantum transport was realised in the pure metallic SWCNT films since boundaries between SWCNTs are regarded as weak disorder sources.

It is reported that the as-deposited pure semiconducting SWCNT film has a much higher R_{sheet} than that of pure metallic one.[174] However, comparable conductance was observed between these two films after chemical doping (HNO_3 followed by $SOCl_2$), and this is probably caused by their different electronic density of states (DOS), which results in much fewer charge carriers being added into metallic SWCNTs than into the semiconducting SWCNTs. Specifically, as shown in Figure 1.8 (b) and (c), a metallic SWCNT species, (10, 10), has a first van Hove singularity located at 0.9 eV and the Fermi level is only shifted about 0.8 eV by chemical doping. In comparison, this value is already below the second van Hove singularity of a certain semiconducting species (11, 10) (0.6 eV). As a result, in such an example, metallic SWCNTs have a lower hole occupation probability than that of the semiconducting species. More generally speaking, because the spacing between the first van Hove singularities in the conduction and valence band of semiconducting SWCNTs is much smaller than that of metallic

SWCNTs, the doping plays a less significant role in improving the charge carrier density in metallic SWCNTs than that of semiconducting SWCNTs.[175-178] In addition, the hybridisation of CoO nanoparticles into the metallic SWCNT networks can improve the conductance by 28 times.[179] Taking these facts into consideration, one can imagine that the ratio between the metallic and semiconducting SWCNTs in the network plays a crucial role in the final conductance of the film, and therefore a purification process seems to be essential. An overview of the separation of CNTs will be summarised in section 1.3.

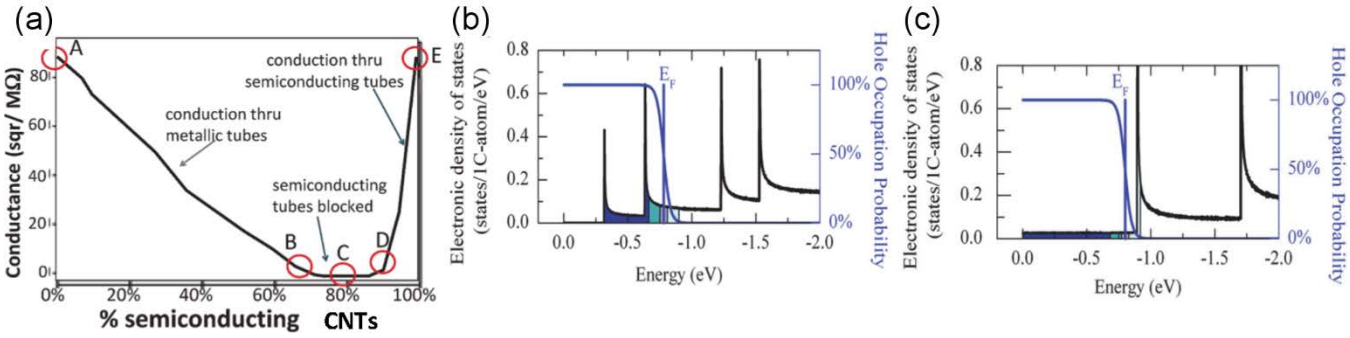

Figure 1.8 (a) The relationship between the conductance of the CNT film and the percentage of semiconducting contents in the network, and this is simulated with CNTs density equal to triple of the percolation threshold while the length of CNTs, positions, and orientations are the same under various ratios.[172] Reprinted with the permission from ref 172. Copyright 2009 American Chemical Society. Density of states of (b) semiconducting CNT (11, 10) and (c) metallic CNT (10, 10) after substantial chemical doping.[164] Reprinted with permission from ref 164. Copyright 2010 American Chemical Society.

In summary, the conductivity of the CNT TCFs is influenced by a variety of parameters which are confirmed by both theoretical and experimental results and these factors include length, diameter, type, synthesis method, the alignment and the purity and the M/S ratio of the CNTs in the network. There definitely is a trade-off between optoelectronic properties of TCF and the cost of fabrication in commercial situations. The common CNT TCF preparation approaches will be compared and investigated in the following section.

1.3 Preparation of transparent CNT films

Nowadays, CNTs can be synthesised via different methods, such as catalytic chemical vapour deposition (CVD), plasma-enhanced CVD, laser-assisted CVD, electric arc discharge, laser ablation, vaporisation induced by a solar beam which is a highly concentrated sunlight from a solar furnace and so on.[180-193] Though some of these approaches contain some energy-consuming steps, industrial-scale synthesis of CNTs with excellent properties is achievable and the output of CNT production reached approximately 5 kiloton in 2011 and the estimated number will be more than 20 kiloton by the end of 2020.[194-195] A number of selective synthesis approaches, which concern control over some critical parameters, including the properties of catalyst particles,[196-199] original carbon source,[200-205] synthesis temperature,[206-208] substrates applied,[209-212] and other related cotreatments,[213] have been designed to achieve CNT soot enriched with either metallic or semiconducting species. Furthermore, the same purpose can also be realised by post-growth purification, such as density-gradient ultracentrifugation,[214-217] gel exclusion chromatography of surfactant-wrapped CNTs,[218] ion-exchange chromatography of DNA-wrapped CNTs,[219] UV irradiation,[220] electrical breakdown,[221-223] selective gas-phase plasma etching,[224] and alternating current dielectrophoresis.[225-226] Recently, a new separation method based on two immiscible aqueous polymer phases was developed to achieve single-chirality SWCNTs species with high purity. In detail, single-stranded deoxyribonucleic acid (ssDNA) was used to wrap and disperse the SWCNTs to form hybrids and the wrapping manner is dependent on the chirality of SWCNTs. Therefore a slight difference between two polymer phases can then differentiate each chirality. More than 20 species were purified out of a commercial mixture starting material in a time-effective manner with a variety of ssDNA sequences, polymer phases, and partition modulators.[227] However, the additional effort to purify single-chirality species may currently not be worth for TCFs, especially for the applications in displays where a colour from the narrow optical absorbance of semiconducting SWCNTs will be a concern.

Commonly speaking, there are two kinds of CNT TCFs fabrication approaches, dry processes and wet processes. Both of these methods have some unique merits. For instance, dry processes-fabricated films usually have excellent conductivity while the wet-processed films

are appropriate for larger-scale fabrication using process such as gravure press and reverse roll painting.[228-232]

Table 1.3 shows the comparison of optoelectronic properties between CNT films fabricated via different dry and wet fabrication methods as well as the commercially prepared TCOs. It also summarises the merits and shortcomings of each.

Table 1.3 Comparison between TCOs and some CNT TCFs with the excellent optoelectronic properties fabricated with various dry and wet processes

Fabrication methods (materials)	T (%)	R_{sheet} (Ω sq^{-1})	σ_{DC}/σ_{OP}	Advantages	Disadvantages	Potential applications
TCOs[124]	85	100-10	22.7-222.7	excellent optoelectronic properties	scarcity, ceramic nature, short lifetime and high production cost	touch panel, LCD screen and OLED display
FCCVD (SWCNTs) [233-234]	90	84	41.5	excellent conductivity; no use of additives	high process temperature	touch panel and LCD screen
roll to roll-dry (MWCNTs) [124,235-236]	83	24	82.7	excellent conductivity; no use of additives; efficient process	aligned CNT forest required	touch panel, LCD screen and OLED display
dip coating (SWCNTs) [237-238]	90	100	34.8	simple; low cost	little control over thickness, uniformity	touch panel and LCD screen
Langmuir-Blodgett (SWCNTs) [239-240]	78	180	7.9	Simple; thickness control	time consuming	touch panel
brush painting (SWCNTs) [241]	79	286	5.1	simplicity	poor uniformity	touch panel
Mayer rod (SWCNTs) [242-243]	82	75	24	great industrial potential	limited to the types of substrates	touch panel and LCD screen
spin coating (SWCNTs) [244-245]	90	128	27.2	fast and simple process	large scale production limited	touch panel and LCD screen

Spray coating (SWCNTs) [246-248]	89	120	26.2	fast and simple process	not very uniform films	touch panel and LCD screen
vacuum filtration (SWCNTs) [249-251]	83	30	64.4	uniform films	time consuming	touch panel and LCD screen
(di)electrophoresis (SWCNTs) [252-253]	81	220	7.7	fast process	additional etching of metal layer	touch panel

1.3.1 Dry methods

Currently, there are two widely used dry approaches to fabricate CNT films. The first one was introduced by Cheng et al. in 1998 and it is based on floating catalyst CVD (FCCVD),[254] and the other one is to draw CNT yarns from an aligned CNT array.[255]

1.3.1.1. Floating catalyst chemical vapour deposition

In a typical process of FCCVD, there is a gas-phase mixture of a carbon source (normally toluene or thiophene) with an iron source (ferrocene). Iron nanoparticles are firstly formed at high temperatures (from 700 to 1200 °C), which then catalyses CNT growth. The CNTs produced by CVD are transferred out of the reaction zone via an inert carrier gas and collected on the low-temperature region of the reaction chamber wall.[254] Ma et al. prepared large-area SWCNT films (5 × 10 cm) with this approach with a R_{sheet} of 50 Ω sq^{-1} and T = 70 % (σ_{DC}/σ_{OP} = 19.3).[256] The way to prepare a CNT TCF with this method is to place a filter membrane at the outlet of the reactor to collect CNTs and then the film is able to be transferred to any kind of substrate, such as PET, as shown in Figure 1.9. A SWCNT film with R_{sheet} of 84 Ω sq^{-1} at T = 90% (σ_{DC}/σ_{OP} = 41.5) was produced by this method.[233] The major reason for such excellent optoelectronic property is that the length of SWCNT bundles is up to about 3 cm prepared by FCCVD, which is beneficial to the transport of charge carriers in the network (refer to section 1.2.4.1.3).

1.3.1.2 Spinning CNT yarns

The other method is using CNTs yarns (that are meters in length) that can be drawn from a super aligned array, following a process firstly introduced by Jiang et al. in 2002.[255,257] Later, CNT films were fabricated via drawing from an aligned MWCNT array.[258] An individual CNT can bridge different bundles by migration from one bundle to another because of the bundled nature. When interconnected CNTs bundles are pulled together, a uniform film of CNT is created with a minimal level of breaks. In 2010, this idea was integrated with a roll-to-roll process with the presence of two protection layers, a substrate layer and a release layer which prevents the attachment of CNTs onto the roller and can be removed afterwards, as shown in Figure 1.9 (b). The produced film had a R_{sheet} of 208 Ω sq^{-1} with T = 90 % (σ_{DC}/σ_{OP} = 16.8) and 24 Ω sq^{-1} with T = 83.4 % (σ_{DC}/σ_{OP} = 82.7) with trimming by laser and the deposition of metal (Ni and Au) (the R_{sheet} was 1000 Ω sq^{-1} at T = 78 % (σ_{DC}/σ_{OP} = 1.42) without these two post treatments).[124] As shown in an SEM image of the CNT film, Figure 1.9 (c), the alignment of CNTs is retained during the roll-to-roll fabrication. Due to the large-diameter CNT bundles, the optoelectronic properties of the as-drawn films are poor, but post treatments (including laser trimming) help to achieve higher transmittance as well as lower R_{sheet} and benefit the charge transport (refer to section 1.2.4.1.3). It is worth noting that though a high percolation threshold for CNT TCF can be caused by alignment (refer to 1.2.4.1.2), a film with highly aligned CNTs has significantly improved packing density than compared to a film with random aligned CNTs when the film is not extremely thin (T is less than 95 %). As a result, the ability for charge-transport along the aligned direction is excellent. More importantly, the aligned films are extremely useful in the fabrication of small-width CNT TCFs. Because of the lack of percolation (refer to 1.2.4.1.2) paths and decreased CNT junction conduction, the transport ability of the narrow films is usually poor. However, in the case of a highly aligned CNT film, the density of junctions along the percolation path with a small-width film can be controlled to a similar standard as that of a wide membrane.

The major benefits of the dry approaches are excellent optoelectronic properties of the resulting TCFs with post treatments (which are similar to that of the commercial TCOs, 10-100 Ω sq^{-1} with T > 85% and σ_{DC}/σ_{OP} = 22.2-222.7), refer to section 1.2.2.2), ideal compatibility with roll-to-roll process, and the resulting high efficiency of production. However, strict control over the reaction conditions is required, which increases the difficulty in automation and therefore may not be appropriate to prepare TCFs on a large scale.

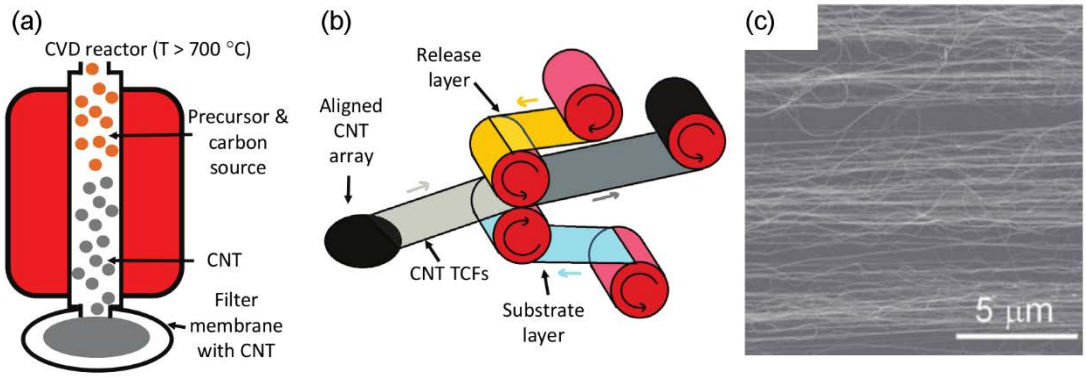

Figure 1.9 Schemes of (a) the FCCVD process to grow CNTs and the direct deposition onto a filter membrane for transfer later, (b) the roll-to-roll process of the CNT TCFs fabrication from an aligned CNT array. (c) SEM image of CNT TCF prepared from the roll-to-roll process. Reprinted with permission from ref 124. Copyright 2010 John Wiley & Sons, Inc.

1.3.2 Wet methods

Generally, a solution-based method is regarded as the collection of CNTs from an aqueous or organic dispersion and then removing the liquid with no or limited aggregation of CNTs.[259-262] In most cases, the removal of undesired components, such as polymers or surfactants, is part of the process. A well-dispersed CNT suspension is required for all wet approaches. There are a large number of publications in this field since the success of filtration transfer[249] and dip coating[263] for TCFs fabrication since 2004.

1.3.2.1 Preparation of CNT dispersion

Because of the attractive van der Waals interactions between each individual CNT, it is difficult to disperse CNTs without bundling.[264] Suspended CNTs tend to flocculate and precipitate from the liquid medium within a short period of time (normally ranging from a few minutes to hours). Among the current studies,[265-272] the main strategies to form a CNT dispersion are divided into 3 classifications,[273] including (1) preparation of a pristine CNT dispersion with neat solvents, (2) the application of dispersing agents, such as surfactants or polymers, and (3) the covalent surface functionalisation on CNT walls.[274-284]

1.3.2.1.1 Neat organic solvents

There are continuous efforts to disperse CNTs with neat organic solvents, and a comprehensive review in this field has been done by Coleman.[285] It is found that the capability of a solvent to disperse CNTs has a close relationship with the Hildebrand solubility parameter where the dispersion component plays a more important role than the polar and hydrogen bonding components.[286] The three most widely used organic solvents are N,N-Dimethyformamide (DMF),[287] N-methyl-2-pyrrolidone (NMP),[288] and dichloroethane (DCE),[289] and sonication is normally necessary in dispersing CNTs in these solvents. From a point view of practical production, one of the advantages of using neat organic solvents is that they do not cause a direct covalent or noncovalent functionalisation of the CNTs, which has the potential to decrease the conductivity of the resultant TCFs.[290] However, it is challenging to prepare CNT dispersions with a relatively high concentration (above 0.1 mg mL^{-1}), not to mention that some of industrial requirements where the amount of solvent is restricted to a small volume (for example, when the level of volatile organic compound needs to be controlled, a high concentration of CNT is required to minimise the volume of solvent used), above 1 mg mL^{-1}, is much higher than this value.[291] In 2010, a CNT suspension was successfully prepared with cyclohexylpyrrolidone and the concentration was approximately 2 mg mL^{-1},[292] but the drawback of this solvent is the high boiling point (280 °C) which prevents the application of CNT films onto most of the plastic substrates during the manufacturing using this solvent. An alternative strategy to improve the concentration of CNT in organic solvents is to use alkali metals to reduce CNT with the formation of polyelectrolyte salts, which then are soluble in polar organic solvents without sonication and additional dispersants. A CNT dispersion with a concentration up to 2.0 mg g^{-1} can be prepared by dissolving CNT salt in dimethyl sulfoxide (DMSO) and a higher concentration (4.2 mg g^{-1}) is realised when sulfolane is used.[163,293]

As an alternative to organic solvents, a superacid, such as chlorosulfonic acid (CSA), also has the ability to disperse CNT with high concentration (4.5 mg mL^{-1}) at room temperature.[294] With the help of this approach, Hecht et al. reported CNT films on PET substrates by filtration transfer (refer to section 1.3.2.2.4) and the R_{sheet} was 60 Ω sq^{-1} at T = 91% (σ_{DC}/σ_{OP} = 65.0).[295] The R_{sheet} of the film prepared by dip coating (refer to section 1.3.2.2.1) was 471 Ω sq^{-1} at T = 86% (σ_{DC}/σ_{OP} = 5.2).[296] The excellent optoelectronic properties of these TCFs are due to the exfoliation effect as well as the doping (refer to section 1.3.4) from the superacid. However, the

major concern of the industrial application of CSA is its extreme toxicity and the corrosive nature.

1.3.2.1.2. Dispersing agents

The other promising method to disperse CNTs in a liquid medium (usually water) involves the use of dispersing agents, such as polymers, porphyrins, polysaccharides, DNA, cellulose derivatives, graphene oxide, and starches.[297-314] In general, the amphiphilic property of these molecules containing a hydrophilic head and hydrophobic tail, enables their interaction with water and CNTs, respectively, and therefore forms a suspension of CNTs. A few comprehensive studies of the function of these surfactants were published in 2006.[315-316] There are a few important factors determining the capability of dispersing CNTs with these surfactants, including the hydrophilic head charge, the hydrophobic tail length, and the existence of certain aromatic groups. In addition, the interaction between surfactants and CNTs is mainly dependent on three forces:[317] (1) Coulombic attraction between the charged heads and the solvent dipole; (2) Van der Waals and the hydrophobic forces between the surfactant tails and CNT walls; and (3) π−π stacking between the aromatic rings on CNT sidewalls and existing aromatic function groups from the surfactants.

The most conventional procedure to prepare the aqueous CNT dispersion is to mix CNTs (~0.1 %, mass ratio) with the dispersing agent (about 1 %, mass ratio), followed by sonicating for a period of time (from 10 to 100 min in most cases). Then, centrifugation is applied to remove the undispersed CNT bundles. By combining this procedure with spray coating (refer to section 1.3.2.2.3), a TCF deposited from a sodium dodecyl sulphate (SDS) dispersed CNT suspension was reported whose R_{sheet} was about 100 Ω sq^{-1} at T = 83 % (σ_{DC}/σ_{OP} = 19.3) after the removal of SDS via acid treatment.[318] There are several advantages with the use of dispersing agents, such as the ease with which a high CNT concentration with excellent stability can be achieved (for instance, 20 mg mL^{-1} with sodium dodecylbenzene sulfonate with no agglomeration),[319] the environmentally friendly aqueous medium (though CNT can also be dispersed in some organic solvents, such as ethanol[320] and chloroform,[321] with the addition of some other dispersants), and no damage to the intrinsic CNT electronic properties. The main shortcoming involves that the remaining surfactants may reduce the conductivity of the as-

prepared CNT TCFs, and some further treatments are required (such as an acid wash or high temperature treatment) to remove these additives.[322]

1.3.2.1.3 Modification of CNTs by covalent functionalisation on the CNT walls

The third solution-processed approach involves the covalent functionalisation of the outer surface of CNTs to improve the interaction with a solvent. A common procedure is described as follows. A mixture of concentrated sulfuric acid (98 wt %) and nitric acid (69 wt %) (with the ratio of 3:1) is firstly used to treat CNT soot so as to introduce the carboxylic groups with negative charges to the CNT surface, and then the CNT aqueous suspension can be formed with no dispersing agents.[323-324] A CNT film on PET substrate by dip coating (refer to 1.3.2.2.1) was reported to have R_{sheet} of 2500 Ω sq^{-1} at T = 86.5 % (σ_{DC}/σ_{OP} = 1.0), the optoelectronic properties of which is quite poor.[325] The main advantage is the simplicity of the processing, such as the use of environmentally friendly medium (water) and no requirement for post treatments to remove the any additives, while the biggest disadvantage is the reduction in the intrinsic conductivity of the CNTs caused by the damage of the conjugated sp^2 carbon network during acid functionalisation as well as the reduced length of CNTs.

1.3.2.2 Coating processes

1.3.2.2.1 Dip coating and Langmuir−Blodgett Approach

Though there are not many dry processes for CNT TCFs, a large number of solution-processed coating methods have been developed in the last 10 years, including filtration, dip coating, and spray coating. Among all of these approaches, dip coating is the simplest method, where a substrate is dipped into a CNT dispersion, withdrawn, and then dried,[326-327] as shown in Figure 1.10 (a). There are a few factors determining the optoelectronic properties of the resulting CNT film, such as the viscosity of the solution, the interaction between the substrate and liquid medium used to disperse CNTs, the duration of the dipping, drying methods and the properties of surfactants.[328] Compared to the charged surfactants, such as SDS, the non-ionic dispersing agents, Triton X-100 can form CNT films on PET with higher uniformity.[263] As far as we know, one of the best CNT films prepared by this method had R_{sheet} of 100 Ω sq^{-1} at T = ~90% (σ_{DC}/σ_{OP} = 34.8), in which a glass slide was dipped into a DWCNTs dispersion stabilised by CSA.[237] The excellent performance is probably due to the high aspect ratio (about 3000) of

the DWCNTs applied in dip-coating, which can dramatically improve the charge transport (refer to section 1.2.4.1.3). In most cases, this method is able to fabricate CNT films with R_{sheet} of 700 Ω sq^{-1} at T = ~90% (σ_{DC}/σ_{OP} = 5). It is an extremely simple, cost-effective, and quick process, but the limited control over the film thickness and the inhomogeneity of the produced film are the major concerns (though precise control over the heating conditions and the choice of the dispersing agents can improve the homogeneity).[329]

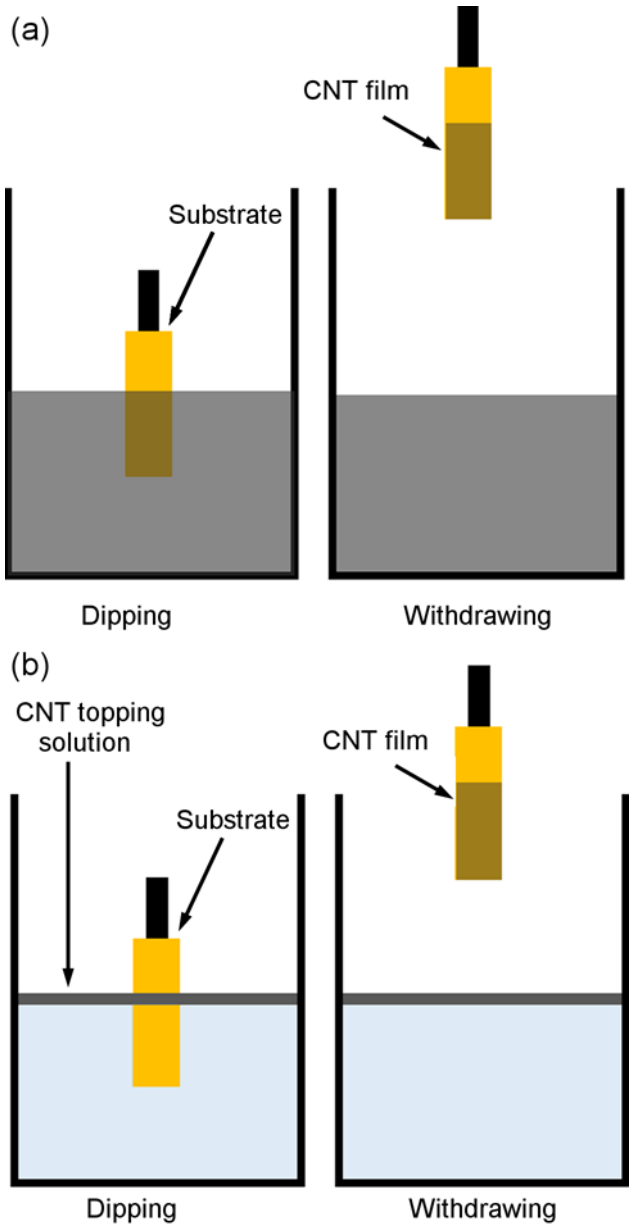

Figure 1.10 (a) Dip Coating and (b) Langmuir−Blodgett approach for the preparation of CNT TCFs.

Better control of the film homogeneity can be realised by a Langmuir−Blodgett (LB) approach, as shown in Figure 1.10 (b), in which the substrate is inserted into the liquid medium and withdrawn with a controlled rate. In detail, H_2O_2/H_2SO_4, thionyl chloride, and octadecylamine were used to treat the CNTs which were dispersed with chloroform (1 mg mL^{-1}); and then CNT were spread on the water surface.[330] The major difference between LB and dip coating is that CNTs only stay at the air-liquid interface. By matching surface chemistry of the target substrate, thickness control of the CNT is realised.[330-333] Multiple layers (more than 100 layers) can be put on substrates (such as quartz or glass) by repeating the process of dipping, withdrawing, and drying. The best reported SWCNT TCF prepared by LB so far had a R_{sheet} of 180 Ω sq^{-1} at T = 78% (σ_{DC}/σ_{OP} = 7.9) with no further chemical doping.[239] Compared to dip coating, the LB approach provides accurate control over the thickness of extremely thin films, even for the preparation of monolayer, with the selectivity to the CNTs orientation to some extent,[330] though the optoelectronic properties of the prepared CNT TCFs are worse. The tedious repetition of the dipping and lifting process during the preparation of multi-layer films is the major disadvantage of this method.

1.3.2.2.2 Brush painting

Brush painting is a variation of dip coating and it is about painting materials on to some certain types of substrates by a conventional brush, as shown in Figure 1.11 (a). An interconnected CNT network is achieved with shear forces, and the concentration of the CNT suspension determines the electrical properties and optical transmittance. There are some commercial CNT inks available in the market. In most cases, substrates are treated with plasma in order to remove contaminants as well as improve the adhesion of CNTs. By painting an SWCNT dispersion onto a PET substrate with the plasma treatment, CNT films with R_{sheet} of 286 Ω sq^{-1} at T = 78.5% (σ_{DC}/σ_{OP} = 5.1) were prepared in 2014 with this method.[241] The optoelectronic properties are not excellent but it is good enough to fulfil the requirement for touch panel applications (σ_{DC}/σ_{OP} = 4.5). The simplicity is the major advantage of this approach, however preparation of a uniform film by this method is challenging.

The Mayer rod coating approach, which is similar to brush coating and has been used in the paint industry for many years, is about passing a Mayer rod (it is normally a heated bar) over an area covered with liquid and drying the resultant film,[334] as shown in Figure 1.11 (b). In

detail, a substrate is first covered with a certain volume of CNT suspension, and then the fluid is spread by passing a rod to form a CNT film with the solvent evaporated at the same time. As shown in Figure 1.11 (b), the thickness of the resultant CNT film is defined by the size of both gauges and wire wrapped on the surface of the Mayer rod (which is a stainless steel wires wrapped metal rod). The surface tension of the suspension and its interaction with the applied substrate determine the properties and quality of the CNT films. In most cases, the CNT ink is an aqueous dispersion with the help of certain types of surfactants, including sodium dodecyl benzenesulfonate. By following the process, the optoelectronic properties of the CNT films have R_{sheet} of 100 and 300 Ω sq^{-1} at T = 70% and 90% (σ_{DC}/σ_{OP} = 9.7 and 11.6), respectively, which was fabricated by painting glass substrates with surfactants (sodium dodecyl benzenesulfonate (1 wt %) and Triton X-100 (3 wt %)) suspended HiPco SWCNTs (0.1 wt %).[335] So far, one of the best films prepared by Mayer rod involved the dispersion of SWCNTs with a polymer derivative of cellulose, sodium carboxymethyl cellulose, and the CNT films then were applied by Mayer rod and dried by a lamp on a glass slide.[242] In order to remove the nonconductive additive, as-prepared films were further treated with HNO_3 overnight, which also can p-dope the CNTs at the same time. Finally, the films had a R_{sheet} of 75 Ω sq^{-1} at T = 82% (σ_{DC}/σ_{OP} = 24), and could be applied as an LCD screen (σ_{DC}/σ_{OP} = 22.5). The potential to be applied in large-scale production combined with slot die and forward/reverse gravure is one of the main advantages of this method, which can be realised by feeding the CNT suspensions as the ink during the process.[336] It is worth pointing out that there are some requirements for the rheological properties of the ink to be applied on a certain type of substrate.

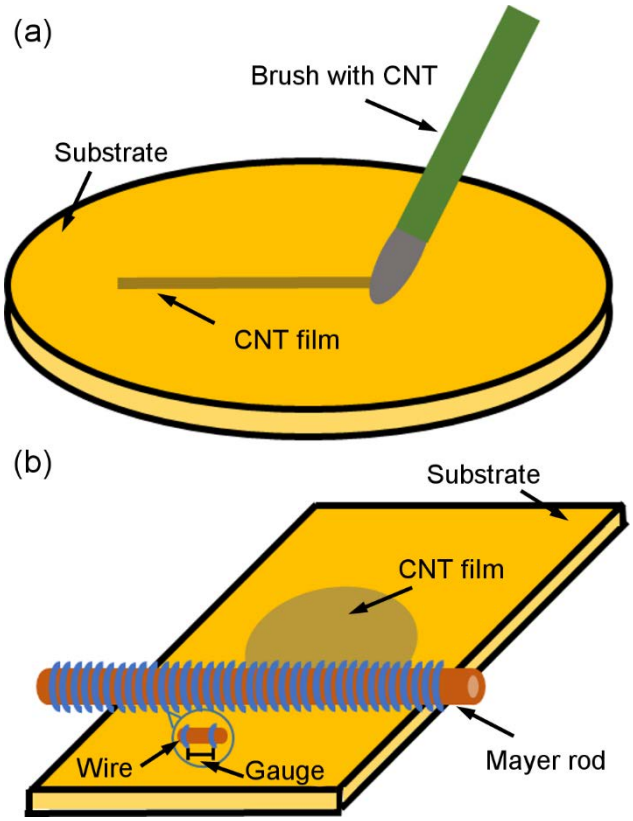

Figure 1.11 (a) Brush painting and (b) Mayer rod coating approach in the preparation of CNT TCFs.

1.3.2.2.3 Spin coating and spray coating

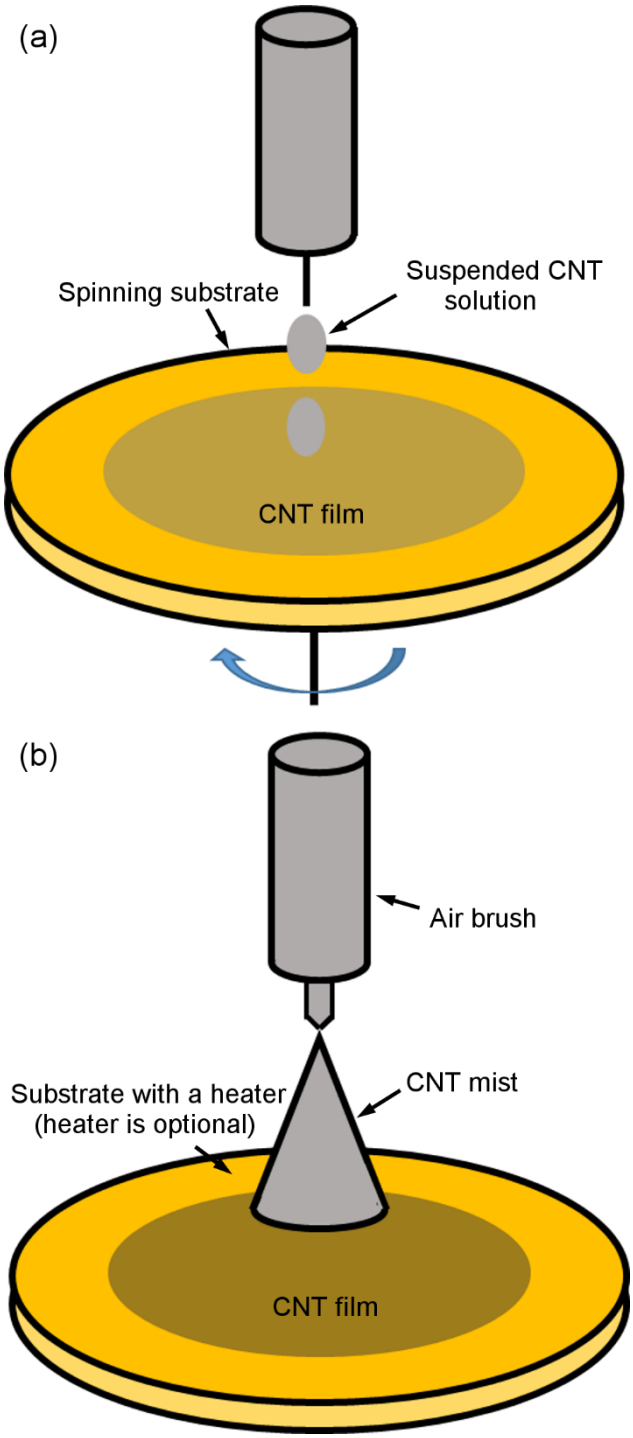

Figure 1.12 (a) Spin and (b) spray coating of CNT TCFs preparation.

A more sophisticated approach than dip coating is spin coating involving the deposition of a small volume of CNT dispersion onto a spinning substrate,[337-338] as shown in Figure 1.12 (a). The spinning substrate provides a way to spread the CNT dispersion with rapid drying at the

same time. In addition, it is good at forming very thin films with high homogeneity. There are some neat organic solvents which dissolve CNT into liquid medium, such as DCE. CNT TCFs with R_{sheet} of 128 Ω sq^{-1} at T = ~90% (σ_{DC}/σ_{OP} = 27.2) have been produced with this method, which is one of the best CNT based TCF reported so far.[244] It is essential to dope the as-prepared CNT films by HNO_3 (see section 1.3.4) to meet the requirement of TCFs for LCD screens. In order to remove the dispersing agents, methanol can be applied to the dropping flow of the liquid during the spin coating process, in which the shear flow forces the liquids to be confined and mixed during the spinning. Interestingly, the resulting films contain CNTs aligned to some degree.[339] Additionally, modification of the spinning surface by either amine (for semiconducting) or phenyl (for metallic) groups can selectively deposit semiconducting or metallic SWCNTs, respectively.[340] Spin coating is a very time-saving process with great simplicity, but it is difficult to apply a film on a large scale and multiple spinning steps are required to form a thick film since the concentration of CNTs suspension is relatively low (normally less than 0.1 mg mL^{-1}).

One of the other preparation approaches is spray coating which involves spraying a diluted CNT dispersion onto a substrate with an air brush,[341] as shown in Figure 1.12 (b). Heating is used in most situations to evaporate the solvent without drying-induced aggregation. This method is generally compatible for CNT suspensions with low toxicity dispersing media such as water and alcoholic solvents. A typical CNT TCF prepared by this method has R_{sheet} of 57 Ω sq^{-1} at T = 65% (σ_{DC}/σ_{OP} = 13.8), in which SDS (0.3 wt %) dispersed CNTs aqueous suspension was applied.[244] A dispersion of unbroken and unbundled SWCNTs by a reductive dissolution process is necessary to prepare CNT TCFs by spray coating with excellent optoelectronic performance.[246] It involves the reduction of CNTs with sodium and liquid ammonia with the resulting nanotubide salt dissolved by DMSO with stirring to form the well-dispersed CNT ink. The film was then oxidised in atmosphere to the neutral species after spray coating. The final film had a R_{sheet} of ~120 Ω sq^{-1} at T = 89% (σ_{DC}/σ_{OP} = 26.2), which is appropriate for LCD screens. The main improvement is contributed by the much longer length (approximately 20 μm) as well as the smaller CNT bundle sizes (the majority were less than 5 nm in diameter) than that of the normal bundles (more than 10 nm in diameter), which offers excellent transport ability of charge carriers (refer to section 1.2.4.1.3). The major advantage of spray coating involves its quick and simple nature of the entire process while the major

disadvantage is that it is not easy to form a very thin and homogeneous film (micrometre-size inhomogeneity), which is related to the droplet size of the CNT dispersion from the nozzle.[342]

1.3.2.2.4. Vacuum filtration

Vacuum filtration is the most widely used solution-based coating approach in preparing in CNT films and it involves vacuum-filtering a diluted CNT dispersion through membrane with certain size of pores. As shown in Figure 1.13, the as-collected CNTs on the membrane can then be transferred from the filter paper to a specific substrate as required.[343] This filtration-transfer method is useful in the fabrication of CNT TCFs on flexible substrates. One of the examples was completed by Zhou et al.[344] which involved a CNT dispersion formed using an SDS (1%) aqueous solution and bath sonication. CNTs were firstly collected onto an alumina filter via filtration, and a large amount of water was used to wash away the residual SDS. Then, the CNT film was transferred from the filter membrane surface onto a polydimethylsiloxane (PDMS) stamp and eventually transferred to the final target substrates (PET, glass, and poly(methyl methacrylate) (PMMA)) with mild heating at 80 °C. By following this approach, CNT films with R_{sheet} of ~120 Ω sq^{-1} at T = ~80% (σ_{DC}/σ_{OP} = 13.3) were produced.[344] So far, the best optoelectronic properties of CNT films prepared by this method had a R_{sheet} of 30 Ω sq^{-1} at T = ~83% (σ_{DC}/σ_{OP} = 64.4). The SWCNTs for these films were purified with acid before filtration, and HNO_3 used during the purification had a p-type doping effect. In that study, Triton X-100 aqueous solution (1%) acted as the dispersing agent to suspend the purified SWCNTs with a final concentration of 2 × 10^{-3} mg mL^{-1}. The dispersion was vacuum filtered onto a mixed cellulose ester membrane (pore size: 0.2 μm) and then the film was transferred to a sapphire substrate with the removal of the membrane dissolved in acetone.[249] HNO_3 probably contributed to the excellent properties by chemical doping during the CNT purification (refer to section 1.3.2.2.4). The optoelectronic properties of the CNT TCFs are already very close to meet the requirement for an OLED anode (σ_{DC}/σ_{OP} = 69.7). One of the most recent reports showed that large monodomains (more than 1 cm^2) with well-aligned SWCNTs in a high packing density were prepared via slow vacuum filtration. The authors pointed out that there were several important parameters in achieving large domain alignment, including the surface hydrophobicity of the filter paper, the concentration of the dispersing agents (must be below critical micelle concentration), the concentration of SWCNT (1−15 μg mL^{-1}), and the flow rate

of the filtration (1−2 mL h^{-1}). Under these optimised situations, the SWCNTs can self-assemble into a closely packed arrangement and the alignment effect occurs with a range of SWCNT types and dispersing agents. Such films are much flatter and homogeneous than the typical ones formed by normal vacuum filtration due to the close packing, which allows for greater control of film thickness.[345]

The main advantages of vacuum filtration include the well-controlled thickness or transmittance of the CNT film by changing either the volume or the concentration of CNT stock suspension, the excellent homogeneity and reproducibility, and the cost-saving nature.[346] However, it is a time-consuming process with the difficulty in the fabrication of a submonolayer film with high quality, and it requires the transfer of the film from the membrane to other substrates.

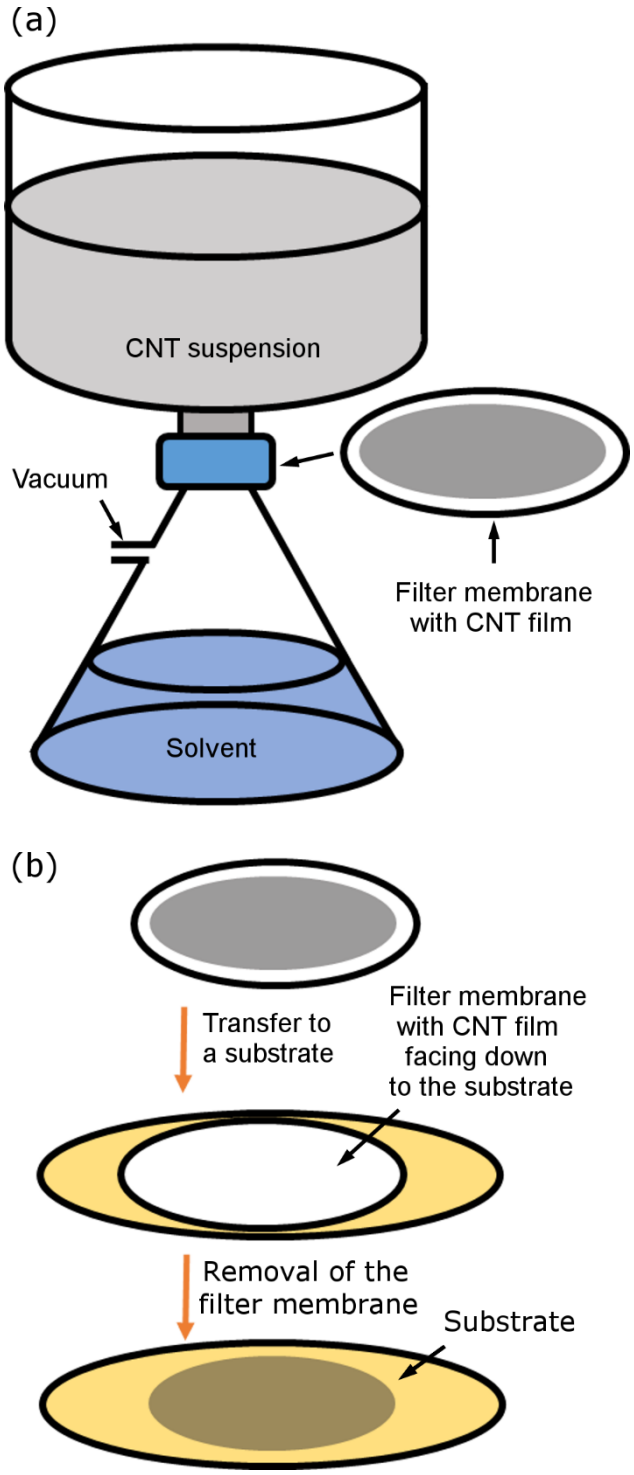

Figure 1.13 (a) Vacuum filtration fabrication of CNT TCFs and (b) transfer of the as-prepared film onto a substrate.

1.3.2.2.5 Electrophoretic deposition

From a practical application point of view, electrophoretic deposition (EPD) is regarded as a potential large-scale deposition method, which applies an electric field between two electrodes dipped in a dispersion of CNTs with covalent functionalisation or coated with ionic surfactants. The CNTs with charge are attracted to the electrode electrostatically,[347] as shown in Figure 1.14. For instance, the carboxylic groups on functionalised CNTs have some negative charges and a CNT film can then be deposited onto the positive electrode during the process. The deposition of CNTs onto an insulating substrate is also achievable, and SWCNT films with R_{sheet} of 900 Ω sq^{-1} at T = 70% (σ_{DC}/σ_{OP} = 1.1) have been fabricated. Specifically, the SWCNTs were first attracted and deposited on a conductive metal thin layer (such as titanium and aluminium) on top of a glass substrate and during EPD process, the metal layer was oxidised and became transparent.[348] The CNT film with one of the best optoelectronic properties by following this approach has a R_{sheet} of 220 Ω sq^{-1} at T = 81% (σ_{DC}/σ_{OP} = 7.7).[252] The SDS aqueous solution (7×10^{-3} mol L^{-1}) was used to disperse SWCNTs first, followed by centrifugation to remove the aggregates, and the diluted supernatant was applied as the bath solution in EPD. The SWCNTs were then deposited onto a stainless steel electrode with the PET film hot-pressed on the film later at 0.5 MPa and 200 °C (below the melting point of the polymer) for 1 min so as to transfer SWCNT film onto PET. Finally, the film was immersed in a HNO_3 aqueous solution (2 mol L^{-1}) which has an effect of p-doping on the CNTs as well as removal of SDS (refer to section 1.3.4). The optoelectronic properties of the films are worse than that prepared by most of the other techniques, and one of the reasons is the application of short CNTs (the length is less than 1 μm), but the films still meet the requirement for touch panel application. Another similar electrochemical process is dielectrophoresis (DEP), in which an alternating current electric field is used to selectively deposit of well-aligned metallic CNTs film because of the much larger polarisability.[349-352]

The short processing periods, the capability of designing patterned films by control over the conductive area shape, and the high accuracy intrinsic to the electrochemical processes are several advantages of these two electrochemical approaches. However, further treatment of etching the metal layer is required to prepare films on nonconductive substrates.

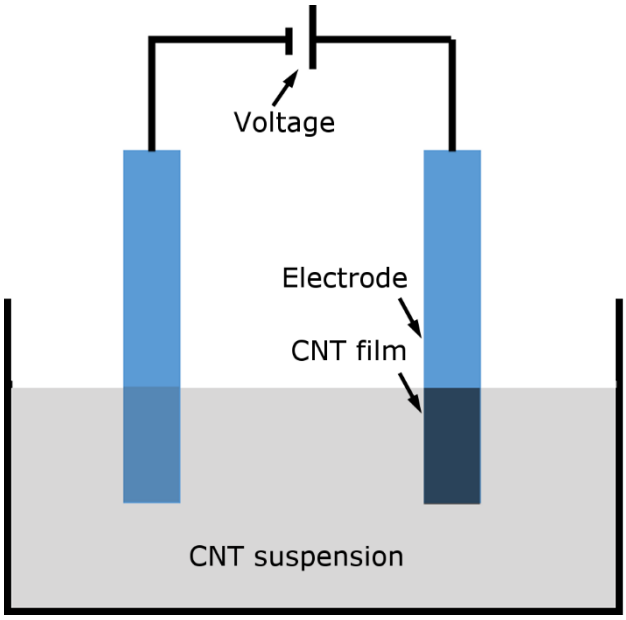

Figure 1.14 Electrophoretic deposition process for the preparation of CNT TCFs.

So far, both dry and wet methods are able to fabricate CNT TCFs on a lab scale. Every method has some advantages and disadvantages. The optoelectronic properties of all of these prepared CNT TCFs are still not as good as that of TCOs, but they are able to satisfy the requirements for some industrial applications, such as touch panels, LCD screens, and OLED displays, as shown in Table 1.2 and Table 1.3. However, none of these films meets the requirement for a thin-film electrode for photovoltaics. From our understanding, dry methods seem to produce high quality CNT TCFs while wet methods are more compatible to different substrates because of their low temperature processes. Among all of these dry and wet methods, the roll-to-roll approach might be the most promising one in the fabrication of CNT TCFs because it is not only highly efficient for large scale manufacturing but also able to produce films with excellent properties.

1.3.3. Methods of patterning CNT films

Patterning of CNT films to the final products, such as touch panels and displays, is critical in improving the compatibility in industrial manufacturing. The excellent chemical stability of CNTs is a benefit for final products with long lifetime, but it makes the traditional TCF etching approaches which are entirely based on corrosive chemicals not effective any more, and

therefore it is essential to develop some new methods in order to achieve CNT TCFs with certain types of patterns.

1.3.3.1. Patterning with surface modification

First of all, a well-developed approach to patterning films from liquid solution is inkjet printing, in which the wettability of a CNT ink or dispersion is essential in precise deposition of CNTs on a particular substrate.[353-354] However, there are several factors affecting the resolution, including the surface properties of the substrate, the liquid medium of the dispersion, and the nozzle size. The control factor during the process is the interaction between the liquid medium and the target substrate, and this determines the homogeneity of the final films. In order to prepare a film with high uniformity, plasma treatment and a low boiling point liquid with excellent volatility are beneficial.[355-356] There are many different types of substrates used for this purpose, such as glass, paper, and some plastics. In order to form a high-quality dispersion, CNTs are normally functionalised with the aid of nitric acid and a solution of potassium permanganate, which can improve the adhesion to substrate surfaces at the same time. The CNT films prepared by multiple prints have R_{sheet} of 40 kΩ sq^{-1} at T = 85% (σ_{DC}/σ_{OP} = 0.1).[353] However, the optoelectronic properties of this resulting film are poor, which may partially be due to the short length of the CNTs (less than 5 μm) in the film. If a common printer was used, the width of the CNT lines is normally more than 200 μm,[353-354] while a CNT strip whose width is about 90 μm has been achieved with proper surface modification, which was first reported in 2011.[357] Specifically, a thick silicon dioxide layer on top of a silicon wafer was first treated with 1,1,1,3,3,3-hexamethyldisilazane to form a hydrophobic self-assembled monolayer on the dioxide surface. Irradiation of the UV light through a metal mask was used to define a hydrophilic strip region. The inkjet printing was then performed covering the strip area, and DMF-dispersed CNTs only attached to the hydrophilic area with surface modification because of the polar hydrophilic nature of the solvent, as shown in Figure 1.15 (a). The width of the CNT strips can be further reduced to about 70 μm with a smaller nozzle in a single printing process,[353-354] but the resolution with a similar level cannot be achieved by multiple prints due to the lack of accuracy in feeding the substrate through the printer.[353] Oppositely**,** surface modification produces high-resolution CNT strips in an easy way during multiple prints, which has the potential to tune the optoelectronic properties. The on/off ratio of a transparent

transistor based on this type of thin CNT TCF is from 1.2 to 320, though this value is not great.[357] Nevertheless, this is an economical process with a high throughput and it is able to produce films on flexible substrates. However, the printer nozzle sometimes may be clogged with large CNT aggregates and thus, a high-quality suspension is necessary.[358-360]

The depletion force (the attractive interaction between CNT colloids) was used to prepare patterned CNT TCFs recently, which is also based on surface modification.[361] In detail, e-beam lithography was applied to define narrow channels in PMMA coated silicon wafer with a layer of silicon dioxide on top. With the use of 3-aminopropyltriethoxysilane (APTES), the exposed oxide layer was functionalised with NH_2 groups. Sorted semiconducting SWCNTs dispersed in 1% sodium cholate (SC) aqueous solution were then self-assembled onto the surface with the control over the concentration of the dispersing agent as well as SWCNTs to tune the depletion forces and attraction to the substrate. Immersion of the substrate in acetone then lifts off the polymer layer, and finally, a raftlike patterned SWCNT thin film with excellent homogeneity over a large region was achieved, as shown in Figure 1.15 (b). The resulting CNT TCFs is one of the candidate materials for transparent transistors with high on/off ratio (higher than 3×10^5 at 1 V bias).[361]

The surface modification can also be achieved by depositing a catalyst on the substrate with a certain type of pattern. In detail, the combination of depositing patterned nanoparticle catalysts (Co) on a n-doped silicon wafer with inkjet printing technique has successfully created patterned MWCNT arrays by the thermal CVD process.[362] The size of the patterned MWCNT dots was from 5 to 30 μm, as shown in Figure 1.15 (c). Although dots may not be appropriate for many purposes, such as acting as a transparent electrode of a solar cell, it is a potential pattern to be applied as a display due to the high current density for the MWCNT dot (83 mA cm^{-2} under the applied field of 1.9 V μm^{-1}). In this method, stabilising the nanoparticle catalysts at high concentration with no aggregation played a critical role in realising highly homogeneous and well-aligned CNT patterns.

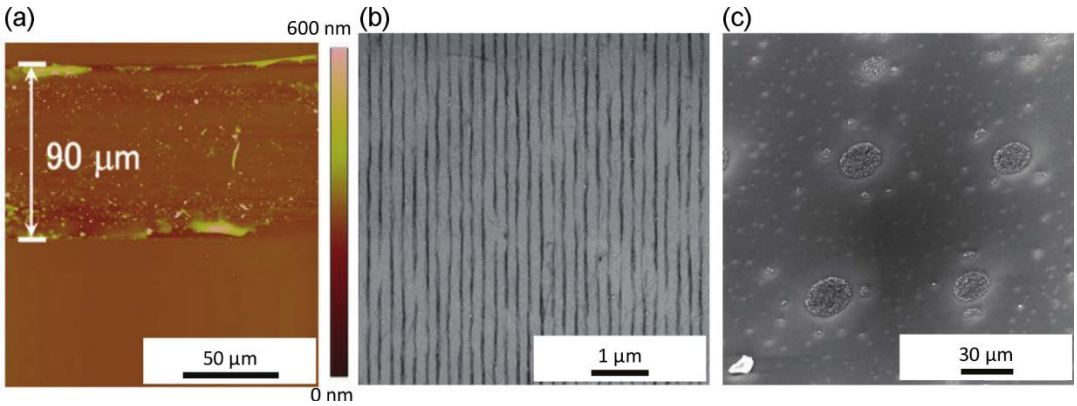

Figure 1.15 (a) AFM and (b, c) SEM images of patterned CNT films prepared by (a) inkjet printing combined with surface modification. Adapted with permission from ref 357. Copyright 2011 AIP Publishing LLC. (b) Surface modification combined with the control of the depletion forces. Adapted with permission from ref 361. Copyright 2014 John Wiley & Sons, Inc. (c) Inkjet printing of the deposition of Co nanoparticle catalysts. Adapted with permission from ref 362. Copyright 2003 AIP Publishing LLC.

1.3.3.2 Patterning with the help of polymers

The copolymer poly(styrene-block-acrylic acid) (PS-b-PAA) can also be used to pattern nanoparticle catalysts by microcontact printing.[363] Specifically, a PDMS stamp was first immersed into a toluene solution of iron-loaded PS-b-PAA micelles, followed by the transfer of the micelles to a silicon wafer coated with aluminium oxide layer by compressing. The PS-b-PAA then self-assembled into spherical micelles in toluene with PAA domains embedded in the PS after the deposition, and this micelle film later acted as the template to form nanoclusters of iron oxide. The copolymer was removed by O_2 plasma, which left the iron oxide nanoparticle catalysts in a certain pattern on the wafer. The patterned CNT films were formed from the patterned catalyst particles through traditional CVD growth. One example of CNT TCFs by microcontact printing is shown in Figure 1.16 (a). The major problem in this approach is that the lateral conductance across the vertical-grown CNT array is poor.

One other polymer-related method for CNT TCFs patterning involves the application of polymer beads with well-defined shape, size, and surface chemistry as the building blocks for template structures (on the nanometer scale) used to deposit CNTs. In this case, a purified SWCNT source dispersed in 1% SDS aqueous solution was firstly mixed with a suspension of

monodispersed PS beads in the mass ratio of 1 to 6. In the mixture, SWCNTs were absorbed on the surface of polymer beads due to the π−π interaction from the aromatic rings. Then, "vertical deposition" was used to deposit a thin PS−SWCNT layer on silicon substrate.[364] Due to the capillary forces at the air/solid/liquid interface, the PS beads self-assembled into a pattern of closely packed stripes along the pulling direction. Precise control over the temperature was essential (at about 60 °C) so that highly ordered PS assemblies were formed. The network of a hemispherical CNT bundles was created over a large region with the removal of the PS beads as well as surfactants by the organic solvents and water, as shown in Figure 1.16 (b).[365] The conductivity of the as-prepared film is similar to that of the bulk materials in SWCNT mats (~100 S cm^{-1}) with dramatically improved transmittance. Noticeably, the T of the resulting TCFs can be adjusted by tuning the size of the monodispersed PS beads.

The third variation for fabrication of patterned films is selective vacuum filtration.[366] The first step of this method is to pattern anodic aluminium oxide filter membranes (whose average pore size equals to 20 nm) by photolithography with a photoresist and developer. CNTs only filled the exposed region during vacuum filtration, as shown in Figure 1.16 (c). PDMS (uncured) was then placed onto the membrane and cured. The patterned CNT films were transferred to PDMS from the filter membranes via peeling off the elastomer. Additionally, this type of design is one of the candidates to be used as a flexible and transparent thin-film transistor. In another piece of work, a similar process was performed with the exception that the patterned filter paper was applied to collect CNTs during the CVD process instead of preparing a CNT dispersion. As a result, high-performance, transparent, conducting CNT films with a microgrid pattern were produced on a plastic substrate.[367] In detail, CNTs grown by FCCVD (in which CO acts as the feed gas and ferrocene nanoparticles are used as the metal catalysts) were collected on the polyvinylidenedifluoride filter (pore size 0.45 μm) with well-defined microgrid by photolithography, and then were transferred onto the target polyethylenenaphthalate film. The resulting CNT films have R_{sheet} of 53 Ω sq^{-1} at T = 80% (σ_{DC}/σ_{OP} = 30.1), which is comparable to some of the commercial TCOs.

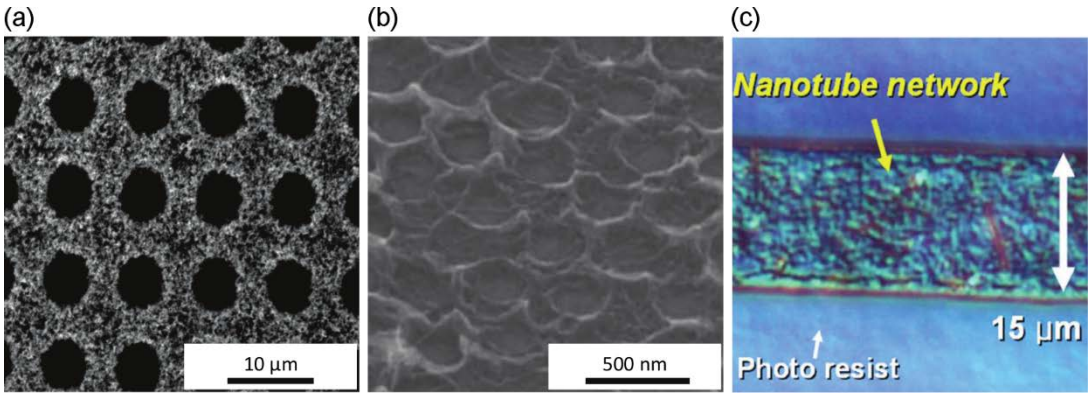

Figure 1.16 (a, b) SEM and (c) optical images of patterned CNT TCFs prepared by (a) microcontact printing with the help of block copolymers.[363] Adapted with permission from ref 363. Copyright 2006 American Chemical Society. (b) Aqueous solution of the beads carriers of PS. Adapted with permission from ref 365. Copyright 2007 Royal Society of Chemistry. (c) Selective vacuum filtration. Reprinted with permission from ref 366. Copyright 2007 AIP Publishing LLC.

1.3.3.3 Patterning with post-treatments

There are also some post-processing approaches which use etching to prepare the CNT TCFs with some certain types of patterns. For instance, O_2 plasma produced by a capacitively coupled plasma system (due to the low ion energies) has been applied to pattern SWCNT films on some plastic substrates,[368] such as PET. In detail, the SWCNT film was first deposited on an anodic aluminium oxide filter via a vacuum filtration process and it was then transferred onto a flexible PET film after the dissolution of the membrane by 3 M NaOH solution. Photolithography was used to define the pattern, in which positive photoresist (AZ4620) was spin-coated and patterned on top of SWCNT films by UV light through a photo mask and development with AZ400K, respectively. The coated surface was then exposed to the O_2 plasma to perform the etching process. The covered SWCNT region was protected by the photoresist while the exposed SWCNTs were damaged from the defects to the entire CNTs, and eventually the amorphous carbon was formed with the by-products of some volatile gases, such as CO_2 and CO.[369] The photoresist residue was dissolved and removed by ethanol, leaving the patterned SWCNTs on PET films. Figure 1.17 (a) shows an example of a patterned CNT film formed by O_2 plasma by following this approach. CNT TCFs with various T and R_{sheet}

were prepared by controlling the power of the plasma and the etching period (generally, lower power and shorter period produces less transparent films with lower R_s). The CNT TCFs normally have R_{sheet} of ~500 Ω sq^{-1} at T = 80% (σ_{DC}/σ_{OP} = 3.0), which can almost satisfy the requirement for a touch panel. It is worth noting that this procedure involves photoresist and a photo mask, which may produce whatever pattern is preferred but has high cost for industrial applications.

In contrast, direct laser interference patterning can also be applied to produce MWCNT films with well-defined patterns, in which there is no photolithography step and it can have the spatial intensity variation with the interference of more than one light beam and the variations can be transferred to a light-sensitive material,[370] as shown in Figure 1.17 (b). In detail, a MWCNT film was first spin-coated on a borosilicate glass and sintered at 300 °C under atmosphere for about 20 min. By tunning the intensity of the laser, MWCNTs were removed at the positions of the interference maximum to achieve patterns in various sizes. MWCNT TCFs with either line- or dot like periodic features were formed on borosilicate glass substrates by using two or three light beams at the same time. This method is very appropriate in the preparation of some regular patterns requiring very high resolution.

The previous two methods require preparation of CNT dispersions before patterning, which may increase the period of processing, but laser-based patterning procedure can also be combined with some dry methods in the preparation of CNT films, such as CVD. With the aid of a laser beam, vertically aligned carbon nanotube arrays (a mixed material of SWCNT and DWCNT) can be transferred and patterned onto polycarbonate (PC) substrate at the same time.[371] Specifically, the vertically aligned CNTs with high uniformity were first grown at 750 °C on a silicon substrate with the iron nanoparticles deposited by e-beam as the catalyst. The requirement of controlling the growth conditions was necessary to obtain the vertically aligned CNTs. The PC film with a piece of glass was then placed above the forest and the pressure was applied. The laser beam was turned on to irradiate the interface, and the heat absorbed enhanced the adhesion between the CNTs to the polymer surface. Positive and negative patterns of CNTs were defined on PC and silicon surface with the control over the movement of the laser before separating the Si−CNT−PC, as shown in Figure 1.17 (c). This method achieves patterning and transferring at the same time without the preparation of any CNT

dispersions, which is highly efficient. The main disadvantages include the difficulty in controlling the CVD reaction conditions and the limited lateral conductivity for the aligned film (0.4−0.6 Ω^{-1} cm^{-1}), though it is possible to increase the conductivity of the film by collapsing them into different orientations.

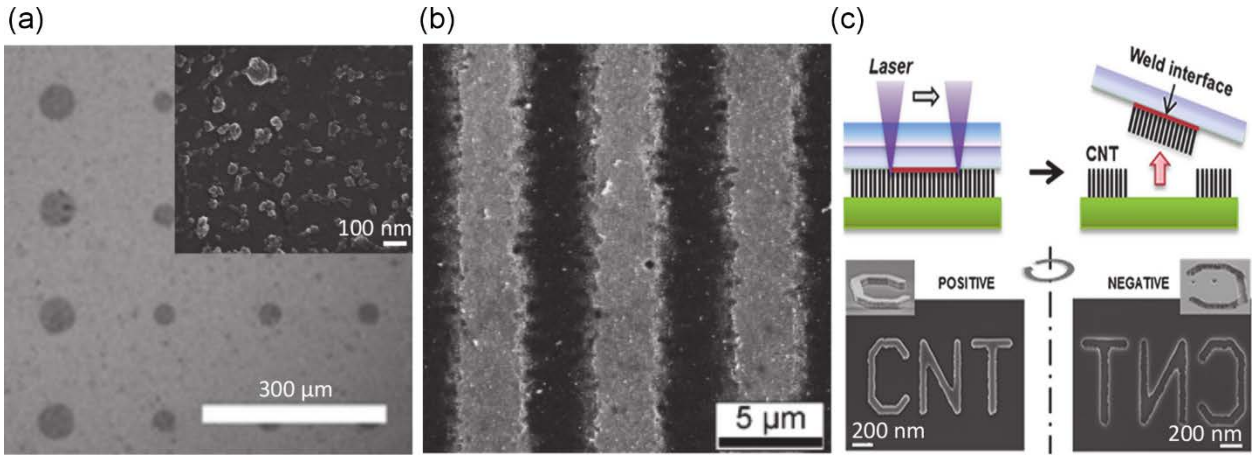

Figure 1.17 SEM images of patterned CNT films produced with (a) O_2 plasma (the inset is the region after the exposure to the O_2 plasma).[368] Adapted with permission from ref 368. Copyright 2010 American Chemical Society. (b) Direct laser interference. Adapted with permission from ref 370. Copyright 2008 Elsevier. (c) Laser-assisted process.[371] Reprinted with permission from ref 371. Copyright 2012 American Chemical Society.

Among all of these methods, CNT patterns are realised on both flexible and rigid substrates. High-resolution patterns (with micron meter resolution) were achieved using some simple and rapid methods with excellent reproducibility. The ability to pattern CNT TCFs is really important for commercial applications, such as touch panels. A matrix of rows and columns of conducting material are required in most of these industrial products. Specifically, either etching CNT TCFs into a microgrid pattern or combining two CNT TCFs with parallel strips in a perpendicular way can solve the problem. Normally, T of the CNT TCFs increases with an increase in R_{sheet} because of the formation of a CNT network with lower packing density. For example, with the increase of the power and the period of the O_2 plasma, the density of the CNT will be below the percolation threshold at some point, and therefore there are no conductive channels. To achieve a higher FOM, both parameters need to be considered. The other important factor to take into account is the width of the strips, as the transport properties

of the film is dependent on the width of the CNT TCFs, especially in the cases of randomly aligned CNT films (refer to section 1.2.4.1.2). However, the patterning processes of CNTs are appropriate on lab-scale generally. Some other issues, including the application of energy-consuming processes and strict control over reaction conditions remain to be resolved.

1.3.4 Doping to improve the properties of CNT TCFs

To satisfy the industrial requirements for CNT TCFs, including the anode of OLED displays (above 50 Ω sq^{-1} at T = 90% (σ_{DC}/σ_{OP} = 69.7)[125]) and LCD screens (above 100 Ω sq^{-1} at T = 85% (σ_{DC}/σ_{OP} = 22.3)),[125] chemical doping is one effective approach to improve the optoelectronic properties of pristine CNT films. The resistance of a CNT network is related to the resistance of each individual CNT and the contact resistance between individuals (refer to 1.2.4). Chemical doping can improve the conductivity of both individual CNT and the contacts by shifting the Fermi level to increase the density of states of charge carriers (holes or electrons determined by the type of the dopants, either p-type or n-type), as shown in Figure 1.18. In addition, it has been shown that the shift of the Fermi level can reduce the Schottky barrier height between metallic and semiconducting SWCNTs.[372] Therefore, doping reduces the R_{sheet} of CNT TCFs by improving the conductance of each individual CNT and enhancing charge percolation within the network.

Theoretically, the Fermi Level of semiconducting species is normally located at an equipotential position (Figure 1.18 (a)) between the valence and conduction band, and therefore both p-type and n-type doping with electron-withdrawing and -donating effects can be achieved by different dopants, as shown in Figure 1.18 (b) and (c). Practically, p-type doping is more widely studied since the oxygen in the air has a slight p-doping effect on CNTs under ambient conditions.[373] Whether a dopant introduces p- or n-type doping is dependent on either the electronegativity (when they are atomic dopants) or the electrochemical potential (when they are molecules and inorganic materials).[372] There are many different types of dopants for p-doping, such as NO_2 ,[374] H_2SO_4 ,[375-376] H_2SO_4 ,[375] HNO_3,[318,377-385] $SOCl_2$,[375,377,379,386-387] the combination of HNO_3 and $SOCl_2$,[159] $SOBr_2$,[388] HCl,[389] Br_2,[390] Nafion,[378] tetrafluorotetracyano-p-quinodimethane (F4TCNQ),[391] MoO_x,[392] oleum,[335] iodine,[375] bromine,[393] triethyloxonium hexachloroantimonate (OA),[394] and bis-(trifluromethanesulfonyl)imide (TFSI).[395]

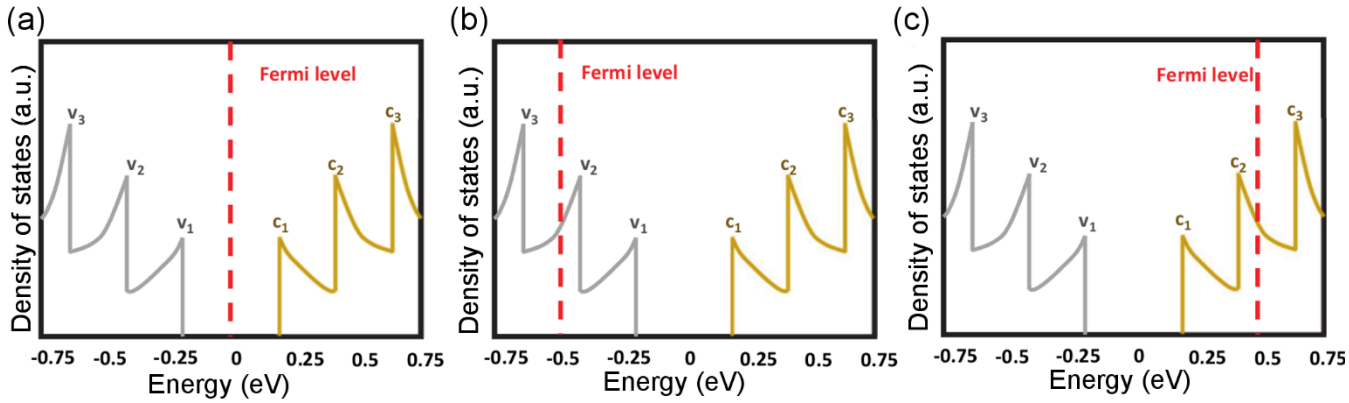

Figure 1.18 Density of states versus energy of semiconducting SWCNTs: (a) Without doping, (b) p-type doping, and (c) n-type doping. v_1, v_2, v_3, c_1, c_2, and c_3 are the i^{th} levels of the valence and conduction band. The red dashed lines show the Fermi level under each condition.

The doping process normally is performed by immersing the CNT TCF into a concentrated solution of dopant for a period of time (ranging from 10 seconds to a few hours) or exposing the films to an atmosphere when gaseous dopants are applied. Table 1.4 shows the optoelectronic properties of CNT films before and after chemical doping (p-type). Among these dopants, H_2SO_4 doping seems to have the highest enhancement of FOM in percentage (5800%), but this value is probably over exaggerated since the starting value of σ_{DC}/σ_{OP} is very low (about 0.1). Although most of the chemically doped TCFs are still below some certain types of industrial requirements, such as the anode for OLED displays, the optoelectronic properties in all the cases are improved. TFSI is particularly promising.

Table 1.4 Influence of the chemical dopants (p-type) on the optoelectronic properties of the CNT films before and after doping; the values in brackets show the increase of σ_{DC}/σ_{OP} in percentage after chemical doping

	Without doping			With doping		
Dopants	T	R_{sheet} (Ω sq^{-1})	σ_{DC}/σ_{OP}	T	R_{sheet} (Ω sq^{-1})	σ_{DC}/σ_{OP}
H_2SO_4 [375, 376]	93.1 %	50500	0.1	93.3 %	1010	5.3 (5200 %)
HNO_3 [383]	83 %	600	3.2	83 %	48.5	39.8 (650 %)
HCl [389]	79.6 %	2800	0.6	79.6 %	330	4.7 (683 %)
$SOCl_2$ [386]	87 %	380	5.3	87%	160	16.3 (138 %)
HNO_3 + $SOCl_2$ [379]	80 %	300	5.3	80 %	105	15.2 (186 %)
$SOBr_2$ [388]	77.6 %	184	7.6	77.6 %	56	24.9 (228 %)
MoO_x [392]	85 %	1000	2.2	85 %	100	22.3 (914 %)
Oleum [335]	90 %	800	4.4	90 %	300	11.6 (164 %)
OA [394]	80 %	200	8.0	80 %	90	17.7 (121 %)
TFSI [395]	85 %	600	3.7	85 %	38.4	58.0 (1468 %)

Recently, a comprehensive study about doping mechanisms was published by Puchades et al.[396] In their study, more than 40 types of dopants were used to dope the SWCNT films and the change in conductivity was used to characterise the doping effect. They noticed that the amount of enhanced electrical conductivity due to doping is dependent on the relative potential difference between the redox potential of the chemical dopant and the SWCNT electronic transitions (in detail, the lower the redox potential, the worse the dopant). Based on this idea, one may deduce that the effect of the dopants might be different with different chiral species of the SWCNTs. Then, it is possible to finely control the conductivity by intentionally choosing a chemical dopant with the required redox potential in a SWCNT film of mixed chiralities. Other mechanisms of the most prevalent chemical dopants of CNTs are listed in Table 1.5 with simple explanations.

Table 1.5 Mechanisms of some prevalent dopants for p-doping CNT

Chemical dopants	Mechanism and effect
H_2SO_4	Intercalated SO_3/SO_4^{2-} attracts the electrons from CNT and lowers the Fermi level (by 0.5 eV) with the creation of more holes in valence band.[397] It helps to remove some amphipathic/polymeric dispersant and thus reconstruct the network to reduce the contact junction between CNTs with tighter contacts.
HNO_3	Physisorbed HNO_3/NO_2 molecules on the surface and bundles of SWCNTs enable the transfer of electrons from CNT to NO_3^- groups, which shifts the Fermi level by 0.2 eV.[397] An enhanced contact between individual CNTs is achieved by removal of impurities, including carbon black, metal catalysts, organic solvents (NMP etc.) and others adsorbed on the walls of CNTs.
HCl	HCl doping is similar to that of H_2SO_4 and HNO_3 via intercalation; It can shift the Fermi level by 0.1 eV.[397] The desorption of HCl is faster than that of H_2SO_4 and HNO_3. [397]
$SOCl_2$	The hole doping effect is due to the electron withdrawing nature of the decomposition of $SOCl_2$ ($2SOCl_2 + 4e^- \rightarrow S + SO_2 + 4Cl^-$). The conduction mechanism changes from thermionic emission to tunnelling through the barriers.
$SOBr_2$	$SOBr_2$ is larger than $SOCl_2$. Br^- anions are chemically bonded to the side walls of CNTs and interact with metallic SWCNT more easily than the semiconducting species. The oxidation of Br^- anion occurs during the process, which is the driving force of the electron transfer. It may cause the formation of -C-S-C- bond with the possibility of crosslinking SWCNTs.[398] The formation of new transport paths via S atoms between CNT is possible.
MoO_x	Electron transfer from CNT to MoO_3 via the following interaction: $MoO_3 + CNT \rightarrow CNT^{\delta+} + MoO_y^{\delta-}$.[392] The stability of this doping effect can be enhanced by thermal activation.
Triethyloxonium	OA is an one electron oxidant.

hexachloroantimonate (OA)	P-type doping is achieved via the following scheme with the formation of a charge-transfer complex: SWCNT + OA → SWCNT $^{+}[Sb(Cl)_6]^{-}$ + C_2H_5Cl + $SbCl_3$ + $(C_cH_5)_2O$[394]
Bis(trifluromethanesulfonyl)imide (TFSI)	Different acidic derivatives of TFSI dopants can adsorb onto defects or the sidewalls of CNTs depending on their chemical structure. They can accept electrons from CNTs and shift the Fermi level down. Among all 3 types of derivatives (bis(trifluoromethanesulfonyl) amine, silver bis(trifluoromethanesulfonyl)imide and N-phenyl-bis(trifluoromethanesulfonyl)imide), bis(trifluoromethanesulfonyl) amine is the most effective dopant.[395]

In most cases, the transmittance of the CNT films does not change significantly after doping, as shown in Figure 1.19 (a).[159] Through the visible light wavelength range, T is maintained at the same level after doping while there is a slight increase around 1.5 eV (at about 830 nm) with certain types of dopants, such as HNO_3 and $SOCl_2$.

In most cases, the R_{sheet} of films decreases by a factor of from 3 to 8 after doping. Typically, in p-doping process, there is a downshift of the Fermi level into the valence band by electron-withdrawing from the CNT to the dopants (corresponding to the increase of the work function of the CNT from 4.5−4.8 eV to more than 5 eV) (as shown in Figure 1.18 (b)).[348] Since there are more charge carriers available, the charge percolation is reinforced with a resulting lower R_{sheet}. In contrast, n-type dopants raise the Fermi level (as shown in Figure 1.18 (c)) by ~1.21 eV in the DOS, such as nitrogen, while the nitrogen states are just above the Fermi level.[399] Some studies show that the contact resistance from one individual CNT to another is decreased during acid treatments and the conductivity of the CNT based network is improved because of the removal of the insulating dispersing agents, including SDS during the preparation of the suspension.[318,381] Furthermore, some intercalated dopants can act as bridges which electrically connect individual CNTs. In detail, the trigonal channels are filled with closely packed ionic chains by alkali metals which act as the dopants in most cases (such as potassium).[400] Therefore, charge carriers moves along outside the tube wall with the overlapping of the K 4s related hybridised bands with the Fermi level.[401]

However, one of the largest concerns is that the chemical doping effect by most of these dopants are not long-lasting since these dopant molecules are only weakly adsorbed on the shells of CNT and they have the potential to desorb. As shown in Figure 1.19 (b),[379] the undoped film has much better stability than that of the doped counterpart, though their R_{sheet} is higher than that of the doped sample. This poor stability will be a practical issue for commercial purposes. It has been shown that a PEDOT:PSS capping layer is able to suppress the degradation of the film properties effectively, as shown in Figure 1.19 (c).[379] Doping ClO_4^- ions on the wall of SWCNTs by an electrochemical method in $LiClO_4$/acetonitrile solution can achieve a similar protection purpose, and as a result, the R_{sheet} of the doped film was stabilised for more than 20 days under atmosphere conditions,[402] as shown in Figure 1.19 (d). The incorporation of MoO_x with CNTs to form a composite (refer to section 1.3.5) is also capable of improving the stability of R_{sheet}. In detail, the activation of the charge transfer from CNT to MoO_x is realised by annealing at high temperature (at 450 °C), and the prepared CNT films show great stability under various conditions, as shown in Figure 1.19 (e).[392] The incorporation of MoO_x produces a film with much better stability in terms of R_{sheet} when compared to conventional chemical doping approaches, such as (2,3,5,6-tetrafluoro-7,7,8,8-tetracyanoquinodimethane) (F4-TCNQ), especially when heated in ambient conditions at high temperature (300 °C). In air, the upper limit of the stability under heating condition of R_{sheet} for MoO_x incorporated CNT films is at ~390 °C, which is due to the oxidisation of CNTs. The non-volatility below 390 °C contributes to the excellent thermal stability. In short, it will be essential to solve the stability concern of the doped CNT TCFs before commercial applications in industry.

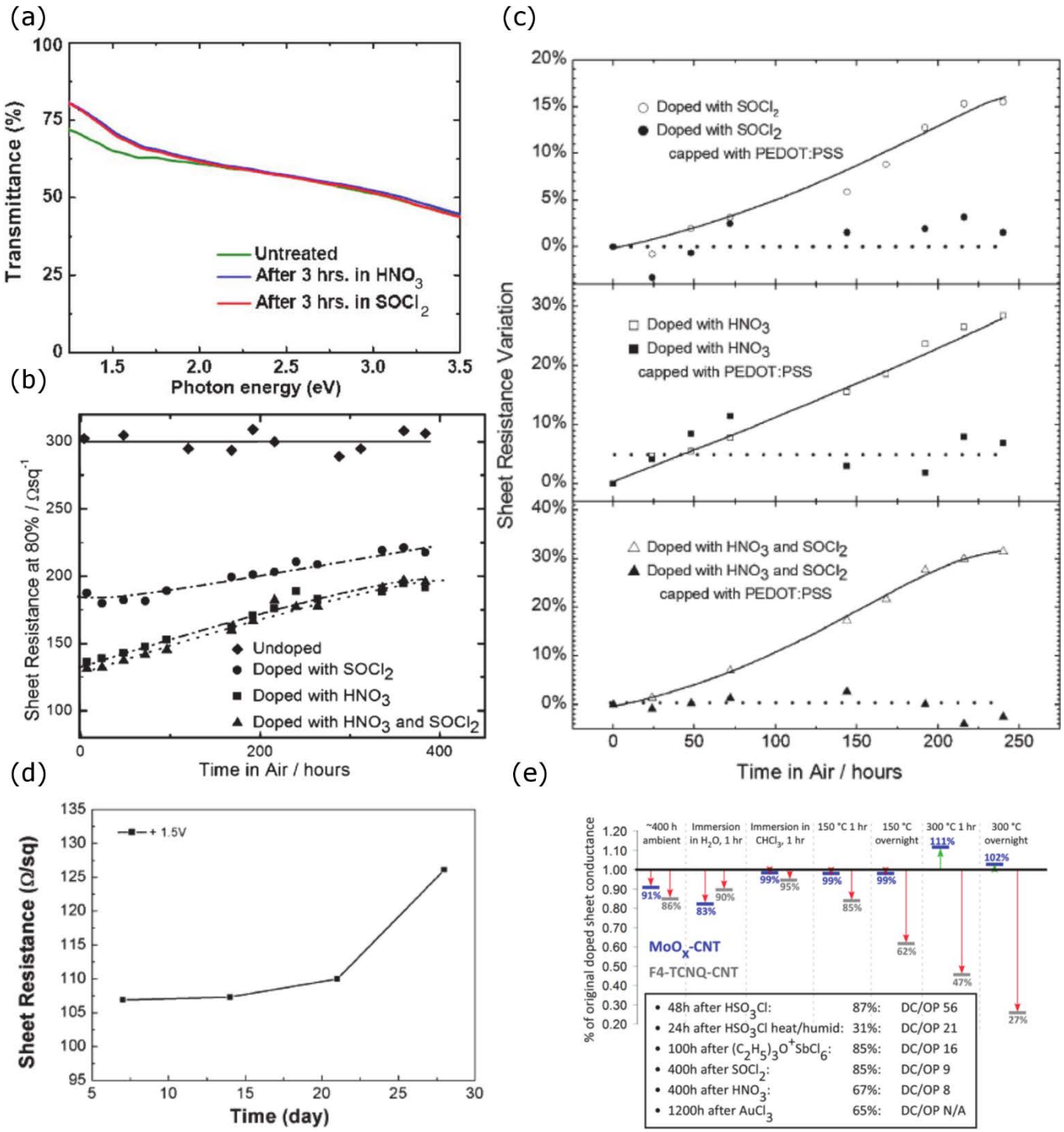

Figure 1.19 (a) Transmittance comparison between the pristine and HNO_3 and $SOCl_2$ doped CNT films. Reprinted with permission from ref 159. Copyright 2007 AIP Publishing LLC. (b) Performance degradation of the doped and undoped films exposed to air. (c) Protection on the R_{sheet} with the addition of a PEDOT:PSS capping layer.

Reprinted with permission from ref 379. Copyright 2008 John Wiley & Sons, Inc. (d) Improvement in the stability of the R_{sheet} by doping of ClO_4^-. Reprinted with permission from ref 402. Copyright 2015 Royal Society of Chemistry. (e) Stability tests of the MoO_x and F4-TCNQ doped CNT films to different conditions. The inset shows the comparison with other material-doped CNT TCFs.[392] Reprinted with permission from ref 392. Copyright 2012 American Chemical Society.

1.3.5 CNT-based hybrid films

Other than chemical doping, hybridisation of CNTs with other materials is another frequently used approach to improve the optoelectronic properties of the films via the combination of the merits of all the components applied. There are common types of materials, such as metal nanoparticles and nanowires, conductive polymers, and graphene based materials. The optoelectronic properties of some selected CNT-based hybrids are listed in Table 1.6.

Table 1.6 Optoelectronic properties of the typical hybrid films based on CNTs

Components	Preparation	T	R_{sheet} (Ω sq^{-1})	σ_{DC}/σ_{OP}
DWCNTs/ AgNPs[403]	Mayer bar coating on PET	90.4 %	45.8	79.5
SWCNTs/ AgNWs[404]	Filtration transfer of the mixture suspension of SWCNT and AgNWs	84 %	20.9	99.0
SWCNTs/ PEDOT:PSS [405]	Vacuum filtration of the mixture suspension of SECNT and PEDOT:PSS	75 %	80	15.2
SWCNTs/ Graphene[406]	CVD growth of graphene films on top of CNT film spin-coated on Cu foil	96.4 %	300	34.0

1.3.5.1 Hybrids with metallic nanomaterials

CNT networks are hybridised with many different types of metal nanoparticles, such as Pt, Ag, and Au via both *in situ* synthesis and *ex situ* filling approaches.[407] For example, silver colloids are modified with $H_2N(CH_2)_2SH$ and terminated with amino groups, which is then followed by the surface condensation with DWCNTs containing −COOH groups functionalised by concentrated nitric acid and sulfuric acid. As shown in the transmission electron microscope

(TEM) image in Figure 1.20 (a), AgNPs are spread all over the DWCNTs in the hybrid. The as prepared soot of Ag−DWCNT was filtered, rinsed with water, collected, and redispersed into aqueous solution with the addition of SDS. The hybrid film was prepared by Mayer bar approach (refer to section 1.3.2.2.2) on a PET substrate and the immersion of the film in HNO_3 was performed to remove the surfactants, SDS (as described in section 1.3.4). The resulting film was then annealed at 150 °C for 30 min to melt Ag so as to increase its contact region with the DWCNTs and the R_{sheet} of the TCF was 45.8 Ω sq^{-1} at T = 90.4% (σ_{DC}/σ_{OP} = 79.5), which meets most of the requirements for TCFs in commercial applications. This improvement was mainly caused by the grafting of AgNPs onto the DWCNT surface, which provided increased contact areas between DWCNTs and therefore reduced the junction resistance. [403] Silver nanowires (AgNWs) were also incorporated with CNTs to form hybrid networks by drop casting[404] as well as filtration transfer.[408] Both methods started with the preparation of hybrid dispersion in ethanol. Figure 1.20 (b) shows the SEM images of the film of the hybrids, in which CNTs and AgNWs are interconnected with each other and create a 3D network. The R_{sheet} of the hybrid films was 29.2 Ω sq^{-1} at T = 80% (σ_{DC}/σ_{OP} = 54.7) and 20.9 Ω sq^{-1} at T = 84% (σ_{DC}/σ_{OP} = 99.0) from drop-coating and filtration transfer approaches, respectively. The optoelectronic properties of the hybridised TCFs are significantly improved compared to those of the pure CNT TCFs. In the control experiment, the R_{sheet} of the pure AgNWs films is ~100 Ω sq^{-1} at T = 80% (σ_{DC}/σ_{OP} = 16.0) and 500 Ω sq^{-1} at T = 84% (σ_{DC}/σ_{OP} = 4.1). The improvement is mainly caused by the high conductivity of the AgNWs, while CNTs function as the additional charge-transport channels as well as the mechanical support matrix. The major issues with metallic NPs and NWs is their relatively expensive precursors and the potential of creating a hazy TCF.[1]

1.3.5.2 Hybrids with conductive polymers

The potential alternatives to inorganic hybrid TCFs is the application of organic components due to the low cost, less toxicity and excellent flexibility.[409] One of the first organic used in this area is polyaniline which was applied to form transparent hybridised CNT films in 1999.[410] More recently, PEDOT:PSS was also applied to create hybridised films with CNT networks. [405] The hybrid solution was first prepared through mixing the stock dispersion of HiPco SWCNT (or arc discharged CNTs) and PEDOT:PSS suspension, which was then collected on a filter

membrane via vacuum filtration and transferred to a flexible PET substrate with the help of heat and pressure. As shown in Figure 1.20 (c), CNTs of both types (HiPco and arc discharge) are merged with PEDOT:PSS in an uniform way in the hybrid films. The R_{sheet} of the hybrid film made with the arc discharge CNTs and PEDOT:PSS was 80 Ω sq^{-1} at T = 75% (σ_{DC}/σ_{OP} = 15.2), which is worse than that of the hybridised TCFs CNT made with AgNPs and AgNWs. The R_{sheet} of both types of hybrid films (CNT/PEDOT:PSS) were very stable under tension (the change of R_{sheet} was less than 10%), but the HiPco CNT/PEDOT:PSS films were less stable under compression. In contrast, the performance of ITO films on PET substrate degraded much faster, with the overall R_{sheet} increased about 2 orders of magnitude, than both types of hybrid films under bendingwhich was mainly caused by the excellent flexibility of both the CNTs and the conducting polymers. Additionally, both films had better R_{sheet} stability than that of ITO on PET, as shown in Figure 1.20 (d).

1.3.5.3 Hybrids with graphene

To take advantage of the merits from both graphene and CNT, hybrid transparent films based on all-carbon materials were prepared, where CNTs bridges the individual graphene sheets.[411-413] CVD is the most common way to synthesise a monolayer of graphene over large area with high transmittance (97.7%) and reasonably low R_{sheet} (~1 kΩ sq^{-1}).[414] Based on this approach, a simple procedure was developed recently,[406] which involved the deposition of SWCNT onto Cu foil via spin coating firstly, followed by the *in situ* synthesis of graphene on the SWCNT/Cu foil surface by thermal CVD. $FeCl_3$ solution etching was used for the removal of Cu foil. As shown in Figure 1.20 (e), SWCNTs were spread uniformly and interconnected with graphene sheets in the hybrid films after the CVD synthesis. The polycrystalline nature of graphene synthesised via CVD results in the decrease in R_{sheet} because the resistance is dependent on charge percolation. At the same time, CNTs bridge each individual graphene crystals and lower R_{sheet}. The R_{sheet} of films prepared by different approaches have been compared at T = ~96.5 %, and the composite film of CNT/graphene has the best quality (300 Ω sq^{-1} at T = 96.4% with σ_{DC}/σ_{OP} = 34.0), as shown in Figure 1.20 (e). Though the optoelectronic property is worse than that of DWCNTs/AgNPs and SWCNTs/AgNWs, it has already met the requirement for LCD screens.

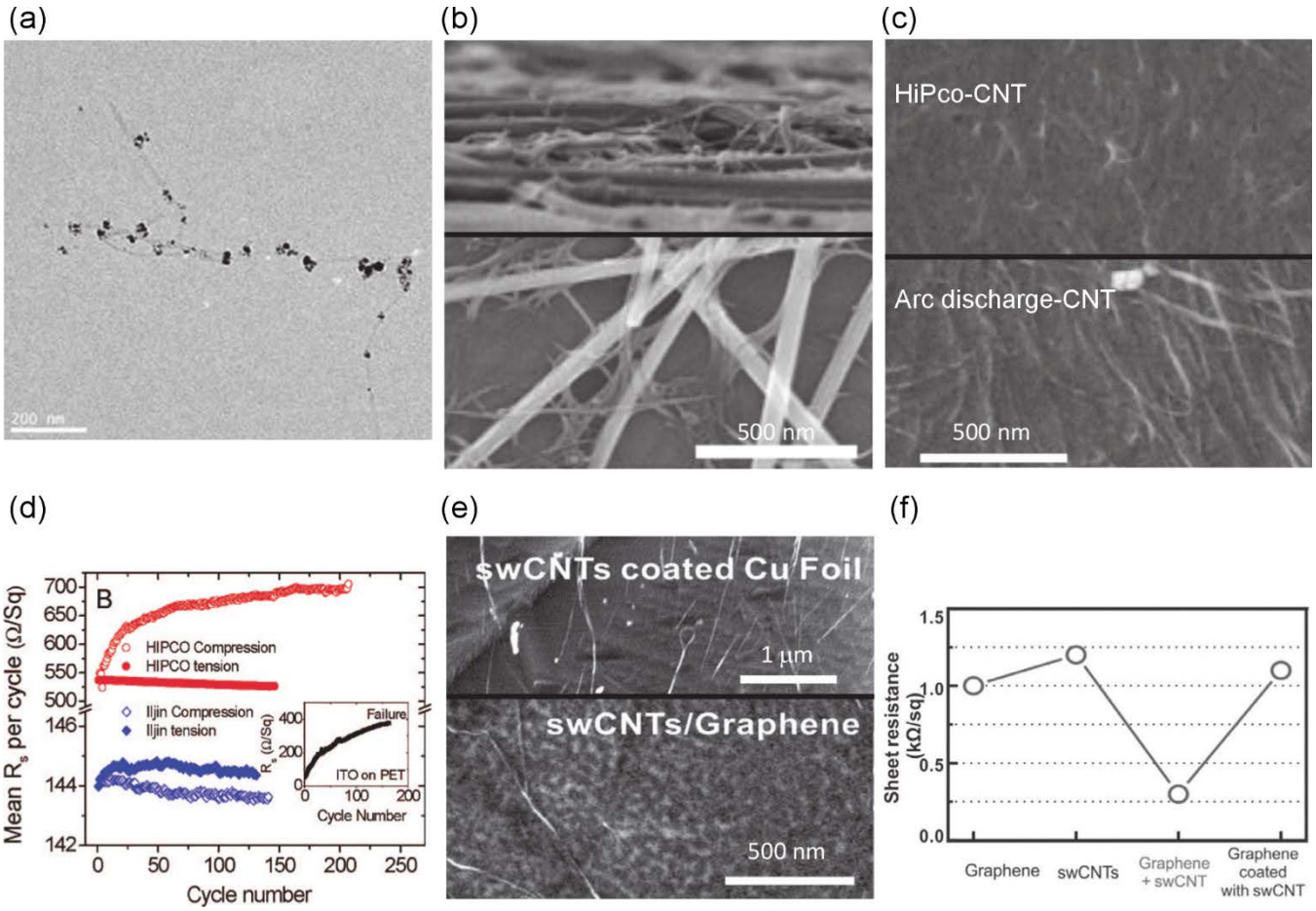

Figure 1.20 (a) TEM image of CNT hybridised with AgNPs (the dark dots are the AgNPs). Adapted with permission from ref 403. Copyright 2011 Elsevier. (b) SEM images of SWCNT/AgNW composite films with both off-angle and top view. Adapted with permission from ref 404. Copyright 2012 Springer. (c) SEM images of CNT/PEDOT:PSS hybrids films and (d) R_{sheet} stability of CNT/PEDOT:PSS hybrid films to compression and tension.[405] Adapted with permission from ref 405. Copyright 2009 American Chemical Society. (e) SEM images of SWCNT/Cu foil before and after the graphene synthesis. (f) R_{sheet} comparison among different kind of transparent films based on CNTs and/or graphene. Adapted with permission from ref 406. Copyright 2014 John Wiley & Sons, Inc.

Since the hybrids provide a potential method to combine the merits of all materials in the films and the current technology has already met many industry requirements, hybrids seem to be a promising approach to replace conventional TCO TCFs. These advantages, including the

improved optoelectronic properties as well as the stability achieved by the incorporation of other material with CNT in the formation of TCFs, are useful in industrial applications, particularly when some specific goals are required. However, the relatively high expense of some starting precursor materials in hybrids (e.g., Ag) and their long term atmospheric instability are the major concerns. Therefore, more research effort to find some cheaper materials for hybrid film fabrication is required before its commercial application.

1.4 Application of CNT TCFs

Transparent conducting films/electrodes play key roles in a variety of electronic devices. With the relatively high expense of doped metal oxide films continuing to increase, and customers and businesses looking for products with high flexibility and strong mechanical properties, we decided to focus on transparent conducting electrodes. It has been shown that the optoelectronic properties of CNT TCFs are rapidly approaching that of traditional TCOs, and at the same time the strength and flexibility of CNTs is much superior to that of inorganic TCFs. It is likely that carbon nanomaterial based films are going to be one alternative for the next generation of TCFs in the near future. Though graphene has shown some promising proof-of-concept devices, the production limitation of high quality graphene remains a concern for this technology. As discussed previously, there are a wide range of fabrication approaches which have the potential to be applied in commercially scalable production of CNT TCFs. The required properties of TCFs in different applications are listed in Table 1.2. In this section, the progress made in photovoltaics, touch panels, LCDs, and OLEDs are summarised with both strengths and challenges in these applications.

1.4.1 Photovoltaics

TCFs based on CNTs and CNT-hybrids have been widely applied in organic photovoltaics (OPVs),[244,415-417] dye sensitised solar cells (DSSCs),[418-421] silicon-based solar cells,[422-424] and perovskite devices.[425-426] Schemes of all these types of cell are shown in Figure 1.21. There are two major important properties from the industry point of view for a solar device: the power conversion efficiency (PCE) and the long term stability.

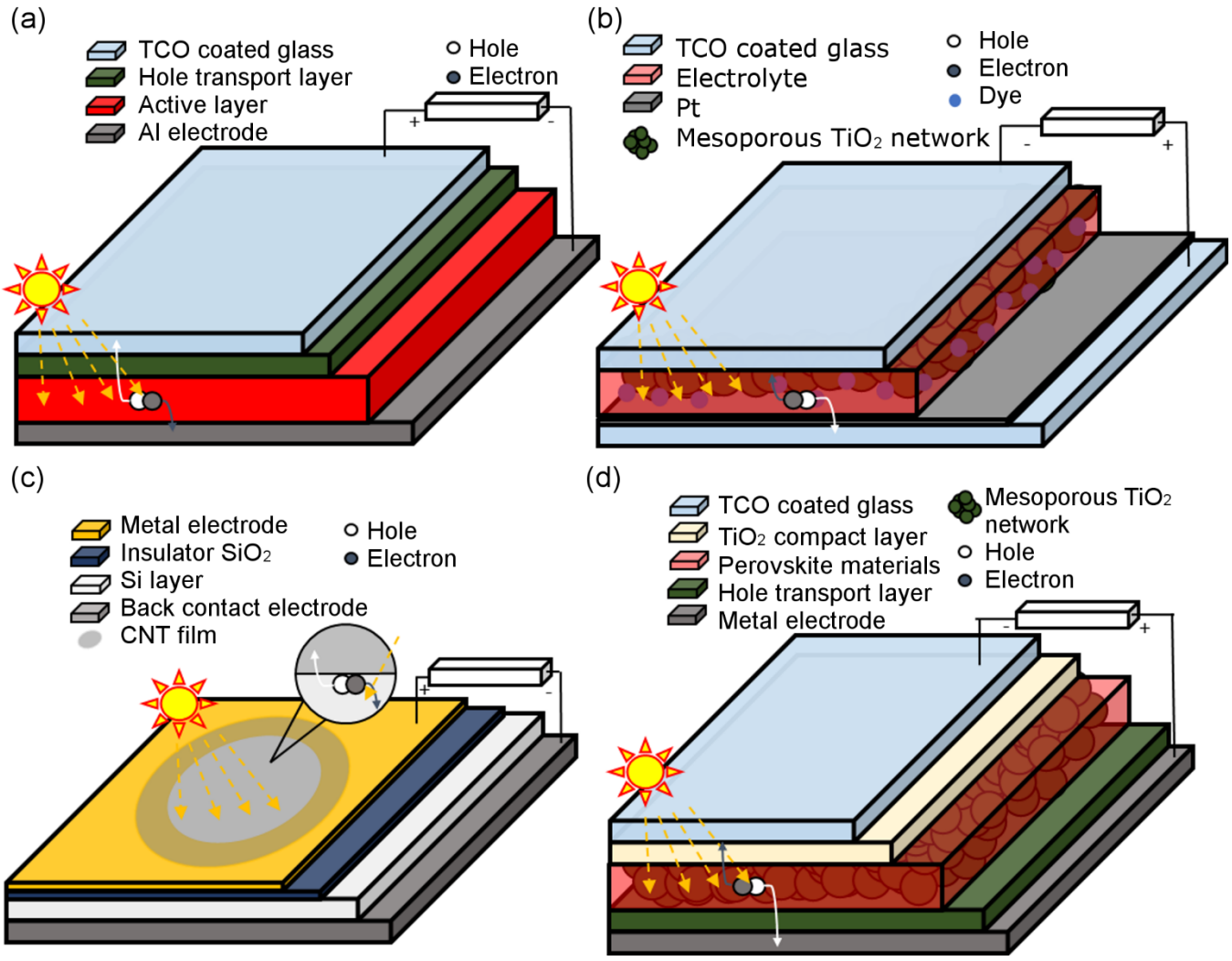

Figure 1.21 Structures of (a) OPVs, (b) DSSCs, (c) CNT/silicon heterojunction devices, and (d) Perovskite solar cells.

1.4.1.1 CNT TCFs in OPVs

As shown in Figure 1.21 (a), the common structure of OPVs has a sandwich-like geometry, including a transparent conducting electrode (generally a TCO-coated glass, such as ITO and FTO); a hole transporting layer (such as PEDOT:PSS) to enhance the hole extraction as well as injection; an photoactive layer (which is a bilayer or bulk heterojunction structure); and an electrode with lower work function compared to the other materials (such as Al). The working mechanisms can be described as following: excitons are firstly formed with the absorption of incident photons in the photo active layer, which then diffuse to the heterojunction interface

where charge separation takes place; the split charge carriers are transported and collected at the respective electrodes as shown in Figure 1.21 (a). In an OPV system, CNT films have the ability to serve as the transparent anode,[427] the cathode to create an inverted structure,[428-429] an interlayer in tandem devices where MWCNT TCF is able to act as an interlayer between two parallel connected devices,[430] and as a substitute to the oxidative metal electrode (such as Al and Ag, as shown in Figure 1.21 (a), which tends to be involved in the tarnish process when there are sulfide species, nitrogen dioxide, and ozone in the ambient atmosphere. For instance, a free-standing film of MWCNT was used on top of an inverted n−i−p structure to create semitransparent organic photovoltaics, as shown in Figure 1.22 (a). [429] Specifically, small-molecule layers (including n-type C_{60} (electron transporting layer), C_{60} (additional absorber layer and electron transporting layer), ZnPc (zinc phthalocyanine):C_{60} (photoactive layer), and p-BF-DPB (2,2′ -(perfluoronaphthalene-2,6-diylidene)dimalononitrile-doped N,N′ ((diphenyl-N,N-bis)9,9-dimethylfluoren-2-yl)benzidine) (hole transporting layer)) of the solar cells were first prepared by thermal evaporation under high-vacuum situation (10−8 mbar). A free-standing film of MWCNT was then drawn from a CVD-prepared CNT array (refer to section 1.3.1.2), and it was deposited on top of the device manually. The immersion of the solar cell in the orthogonal liquid hydrofluoroether (which is damage-free for organic layers) was performed for several seconds so as to achieve the densification of CNTs, which improves T and reduces the R_{sheet} with the formation of denser interconnects (~250 Ω sq^{-1} at T = 38% at 550 nm, σ_{DC}/σ_{OP} = 1.2). The resulting solar cell is able to produce photocurrent under illumination from both sides. Additionally, the lifespan of the device was extended because of the improved stability from MWCNT compared to the traditional oxidative metal electrode. The PCE of the device was up to 1.5% (which is about 80 % of the value of its Ag counterpart (PCE_{Ag} = 1.9 %)) and there was a slightly better stability in efficiency (especially the stability in fill factor) as compared to the counterpart devices with oxidative electrode (though 700 h is still short for commercial purposes), as shown in Figure 1.22 (b). [429] Noticeably, the limited efficiency is caused by the poor optoelectronic properties of the MWCNT TCFs, and thus the PCE can probably be further improved by the application of CNT TCFs with better properties as the electrode.

Instead of substituting the metal electrode, hybridised films of CNTs with polyaniline (PANI) are able to replace the brittle TCOs and work as the transparent top electrodes in OPVs, as shown

in Figure 1.22 (c).[431] Specifically, a composite film of CNT/PANI was fabricated by interfacial polymerisation with toluene as the top phase and ammonium persulphate (APS) acid solution as the bottom phase, where CNTs were self-assembled as a film at the interface with the polymerisation of PANI. As a result, the collection of the nanocomposite film at the interface was realised by lifting a glass substrate from the bottom to the top phase similar to dip coating (refer to section 1.3.2.2.1), as shown in Figure 1.22 (d).[431] The doping with camphorsulfonic acid as well as the exposure to meta-cresol solvent are required to enhance the optoelectronic properties by reducing the R_{sheet} from 85 000 Ω sq^{-1} to 295 Ω sq^{-1} with T = 90% at 550 nm (σ_{DC}/σ_{OP} improving from 0.04 to 11.8) by the polymer expansion from a compact coiled form into chains. As shown in Figure 1.22 (e),[431] the electrode of the composite film on a PET substrate has the best performance (PCE = 2.27 %) among combinations of various substrates and transparent top electrodes. Furthermore, the composite film may be applied in the flexible OPVs as the stability of the conductivity was excellent after 100 cycles of bending and stretching.

The two major advantages for CNT TCFs applied in OPVs are: (A) there are numerous preparation methods of CNT TCF compatible with both solution-based and dry processes, which can meet the requirement for different industrial fabrication procedures and (B) the excellent flexibility and mechanical properties broaden its commercial application area where rigid TCOs are not compatible. However, there are still some disadvantages, such as the relatively poor FOM (11.8) which is still much lower than that of TCOs (22.7−222.7, refer to section 1.3), though the PCE of the composite-based device is slightly higher than that of TCO-based counterparts because of a higher exciton generation active area in the ITO-free devices with rough but regular surface which matches the surface of the active layer and hole transporting layer (PEDOT:PSS), while this is not the case for TCO-coated electrodes.

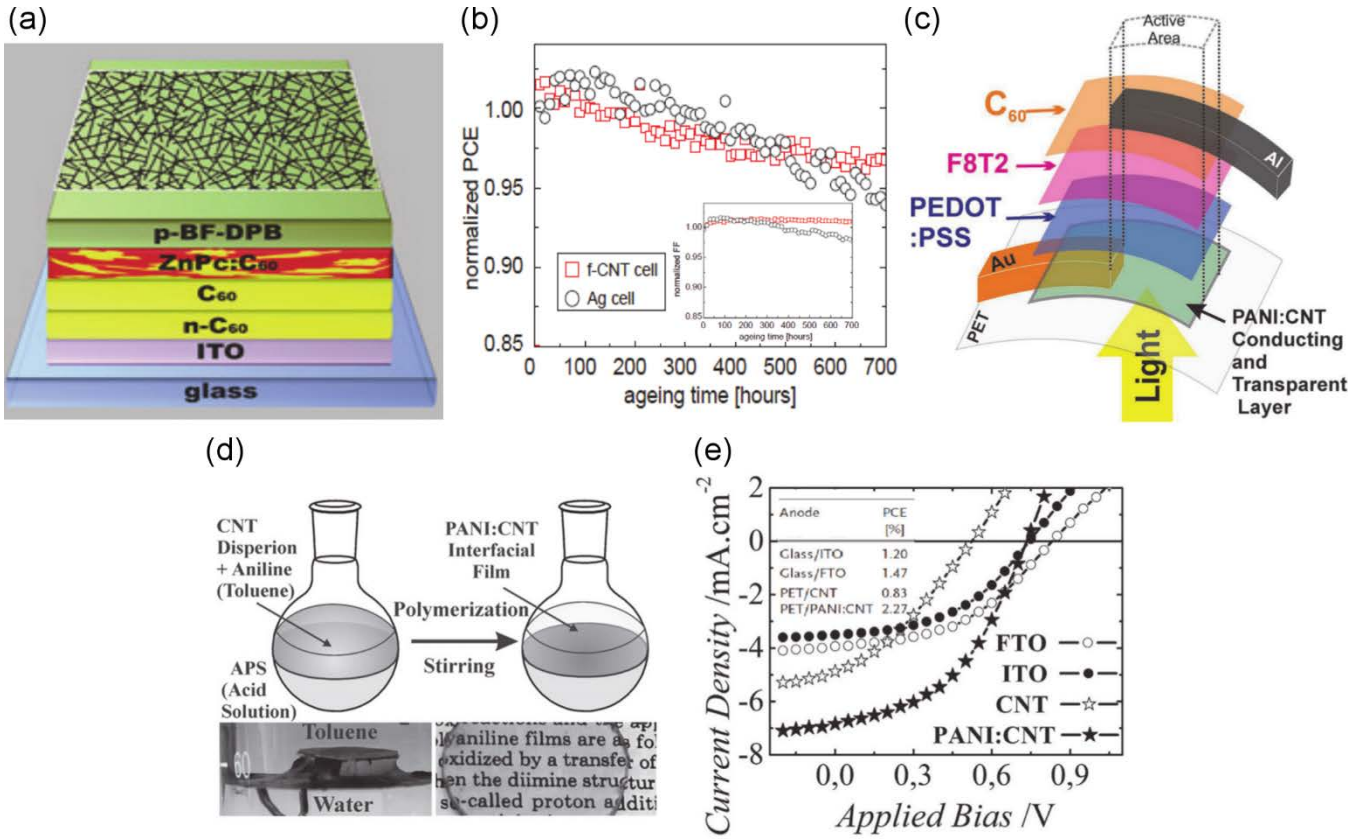

Figure 1.22 (a) Scheme of an OPV with a free-stranding CNT film which replaces an oxidative metal electrode. (b) The comparison of the performance degradation between devices with MWCNT and Ag electrode. Reprinted with permission from ref 429. Copyright 2012 Elsevier. (c) Structure of the TCO-free OPV device with CNT/PANI electrode. (d) Interfacial polymerisation of PANI with CNT present, where the films can be collected by lifting a piece of glass slide from the bottom phase to the top phase (the resulting CNT/PANI film on top of a piece of paper). (e) The comparison of OPVs' performance with different substrates and window electrodes. Reprinted with permission from ref 431. Copyright 2012 John Wiley & Sons, Inc.

1.4.1.2. CNT TCFs in DSSCs

A DSSC, as shown in Figure 1.21 (b), is made of a TCO-based transparent anode that has a thin layer of porous TiO_2 with the adsorbed dye molecules and the catalytic counter electrode (usually Pt-coated TCO) separated by a redox-active electrolyte. In this case, electrons excited from dye molecules are transported to the layer of mesoporous TiO_2 and collected at the

anode, while the oxidised dyes are reduced to the original state by redox transfer with the presence of electrolyte, which occurs at the Pt counter electrode.

Most studies in this area focus on the replacement of the CNT TCF to the TCO-coated glass as the photoanode in DSSCs. As an example in 2008, Wei et al. prepared a solid-state DCCS device with high flexibility where the CNT film was stamped on a PET substrate acting as the transparent conducting electrode, as shown in Figure 1.23 (a).[432] In detail, the SWCNT film was fabricated by filtration/transfer approach where SDS was the dispersing agent to form the suspension. SWCNTs were collected on a filter membrane, and transferred onto a PET substrate to create the electrode with the filter dissolved by acetone and isopropanol. The R_{sheet} of the resulting film was 250 Ω sq^{-1} at T = 65% (σ_{DC}/σ_{OP} = 3.1). The electrode was then acting as a scaffold for the deposition of ZnO nanoparticles by the immersion of the CNT/PET substrate in the ZnO nanoparticles solution, which usually benefits the loading of black dye molecules. As shown in Figure 1.23 (b), the energy diagram of the device shows that the charge flow is facilitated. Electrons produced from the black dye transport to the lowest unoccupied molecular orbital (LUMO) of ZnO and then to SWCNTs, which act as the transporting channels in this case. The PCE of the device was less than 0.5 %, and it was lower than that of a typical DSSC counterpart with electrode coated with TCO and organic solvents instead of ionic liquid gel. With these two changes in the devices, the optoelectronic properties of the electrode (FOM = 3.1) were much worse and the physical diffusion ability of triiodide and iodine ion was worse because of the highly viscous nature of the gel. The PCE of the DSSC further improved to 2.5% with a commercial SWCNT-coated PET as the photoanode prepared by high-speed printing technology from Unidym (R_{sheet} of 470 Ω sq^{-1} at T = 86%, with σ_{DC}/σ_{OP} = 5.1) as well as ZnO deposited electrochemically.[432] In contrast, the PEC of the ITO/PET-based (R_{sheet} of 15 − 70 Ω sq^{-1} at T = 85%, σ_{DC}/σ_{OP} = 148.5−31.8) device was 3.7%. The PCE (2.5%) was quite promising considering that the SWCNT-coated PET substrate had poor optoelectronic properties. There was an issue related to the catalytic properties of the CNTs TCFs as the window electrode, where the recombination of the separated photoelectrons with triiodide occurs ($I_3^- + 2e^- \rightarrow 3I^-$). Kyaw et al. proposed the application of TiO_x sol−gel by spin-coating onto CNT films doped with the sulfuric acid (R_{sheet} of 425 Ω sq^{-1} at T = 76.5%, σ_{DC}/σ_{OP} = 3.1), aiming to retard the recombination, as shown in

Figure 1.23 (c).[433] The PCE of the resulting device was 1.8 % for CNT electrode with TiO_x, and it was higher than that of a control device with CNT electrode without TiO_x (0.004 %).

The major benefit of the application of CNT TCFs is to form flexible DSSCs devices. Although the current performances of these devices are still not as good as that of conventional devices based on TCO electrodes, there is a promising future in DSSCs with CNT TCFs of excellent optoelectronic properties.

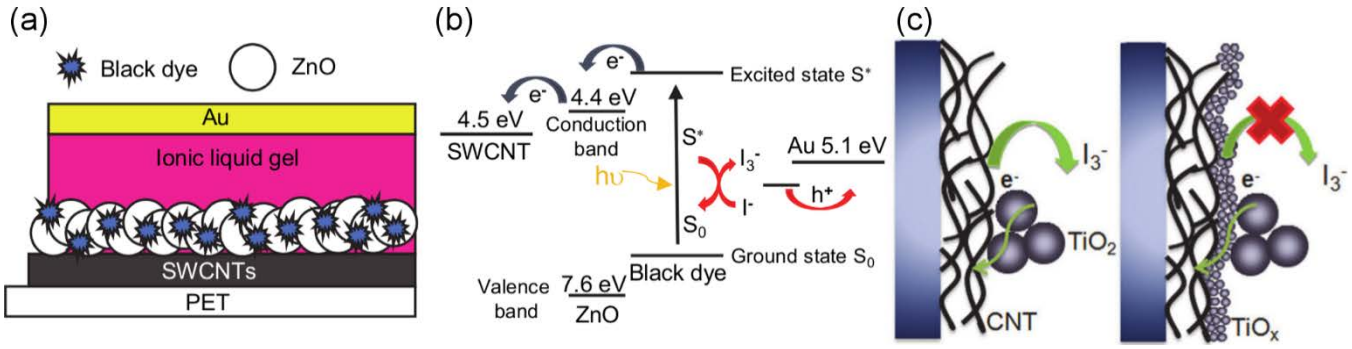

Figure 1.23 (a) Scheme and (b) energy diagram of a flexible solid-state DSSC device with CNT TCF as the transparent electrode. (c) Schematic comparison between the CNT TCF with and without TiO_x to demonstrate the retardation of the recombination caused by TiO_x. Reprinted with permission from ref 433. Copyright 2011 AIP Publishing LLC.

1.4.1.3 CNT TCFs in CNT/silicon heterojunction solar cells

The scheme of a typical CNT/silicon heterojunction device is shown in Figure 1.21 (c), where the most critical part of the device is the interface between silicon (in most cases n-type) and CNT TCFs (normally p-type), and an insulator, SiO_2, separates metallic electrode and silicon in order to avoid any short-circuits. The CNT TCFs can be prepared with the approaches described previously in sections 1.3.1 and 1.3.2. The application of CNT films in this type of device was first reported in 2007.[434] In detail, an n-doped crystalline silicon substrate was covered with a DWCNT film (as shown in the inset in Figure 1.24 (a)). Compared to the previously reported OPVs, the CNT network was used in a different way (transporting the generated charge carriers). Specifically, the silicon layer first absorbs the incident light, and the created electron−hole pairs then diffuse to the depletion region at the interface where the separation takes place under the built-in potential created by the equilibration of Fermi level at

the heterojunction, described as a p−n junction (as shown in Figure 1.24 (b)), or a Schottky junction. The PCE of the resulting device was 1.31 %, (Figure 1.24 (a)).[435] Chemical doping is required to fabricate high performance devices through the improvement in the optoelectronic properties of the CNT TCFs, as discussed in section 1.3.4. One of the simplest p-doping approaches of a CNT film is to add diluted HNO_3 through the CNT network, which decreases the R_{sheet} of the CNT film as well as creates photoelectrochemical cells at the interface of electrolyte and silicon.[422] However, the volatility of the acid groups on the CNTs leads to poor stability of this device. It has been reported that the Au NPs also have p-doping effect on the CNT TCFs and additionally it can improve light absorption by optical scattering.[423] As a result, both the photocurrent and the open-circuit voltage are normally improved. However the excessive Au NPs (more than 10 mM in solution) can introduce some short circuits because of their intimate contact with the silicon surface.[436] In addition, optical designs, such as antireflection layers, have been applied to collect more incident light at the heterojunction region with the presence of polymers[437-438] as well as metal oxides.[424,439] Recently, the PCE of this type of devices has been improved to above 15 % by Matsuda and co-workers.[439] In their study, a layer of molybdenum oxide (MoO_x) was deposited between SWCNT film and the front Au contact, as shown in the inset in Figure 1.24 (c). This layer has two functions, capturing more energy from the incident light by an antireflection effect as well as enhancing the hole extraction/injection efficiency by decreasing the interfacial Schottky barrier between Au and SWCNTs. The PCE of the resulting device improved to 17 % with the presence of the MoO_x layer, as shown in Figure 1.24 (c). Although most studies placed the emphasis on the combination of p-type CNTs and n-type silicon, the heterojunction can also be created with n-type CNTs and p-type silicon. By this design, the collection of holes and electrons now occurs at the silicon layer and CNT films, respectively. Matsuda and coworkers applied ZnO to improve the performance of devices (n-SWCNT/p-Si heterojunction) to 4 % in a similar way.[439]

The major advantage with the application CNT films in CNT/silicon devices is the potentially lower production and material cost than that of conventional silicon-based solar cells while the main problems include the poorer PCEs as well as the poorer stabilities.[435]

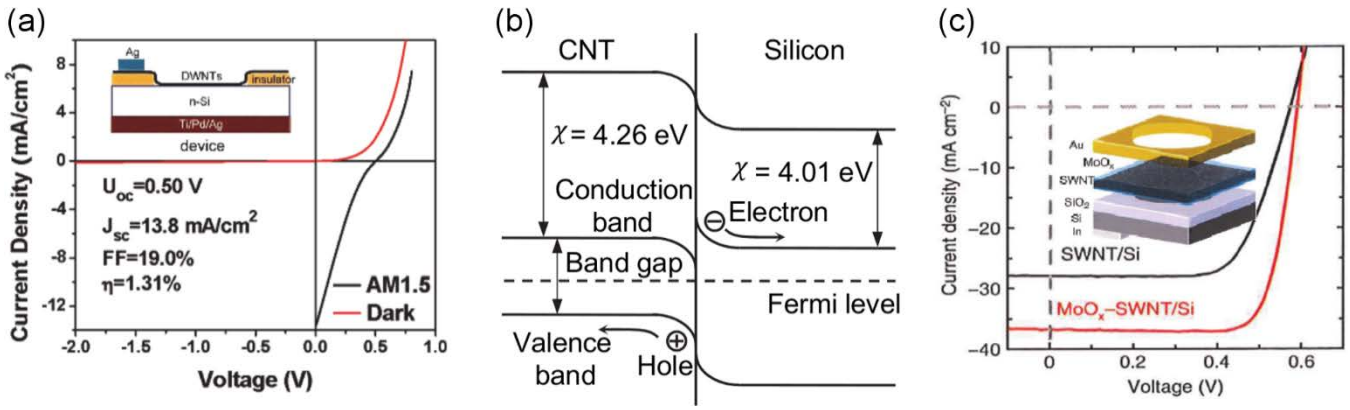

Figure 1.24 (a) Dark and light (AM 1.5 conditions) J−V curves CNT/Silicon heterojunction device (with the structure of the device shown in the inset).[434] Adapted with permission from ref 434. Copyright 2007 American Chemical Society. (b) Energy diagrams of the heterojunction across p-type CNT and n-type silicon. Reprinted with permission from ref 435. Copyright 2012 John Wiley & Sons, Inc. (c) J−V curves of the SWCNT/silicon devices with and without the layer of MoO_x (the inset shows the structure of devices with MoO_x layer). Adapted with permission from ref 439. Copyright 2015 Nature Publishing Group.

1.4.1.4 CNT TCFs in perovskite devices

Perovskite solar cells were first developed in 2009,[440] and Figure 1.21 (d) shows the typical schematic structure of such device. The detail of the working mechanisms is described as follows: the light absorption in perovskite material creates excitons which are then separated into electrons and holes being collected at the TCO-coated glass substrates and the metal electrode, respectively. There are two proposed suggestions for the separation of the created excitons: (A) the thermal energy in the perovskite material and (B) occurs at the interface between the perovskite material and TiO_2 or hole transport material. The relatively expensive metal electrodes (such as Au) used during the fabrication of perovskite devices were replaced by CNT films.[441] After replacing the metal electrode with CNT TCFS, the PCE improved from 5.14 % to 6.87 %. The authors attributed the improvement to the stronger driving force of CNT films for the hole injection referring to the band alignment. The device could be illuminated from both sides due to the sparsity of the CNT network, as shown in Figure 1.25, which makes it possible to be used as a solar cell installed on windows. With the addition of spiro-OMeTAD

(an effective hole transporting material), the PCE of the devices further increased to 9.9 %. Though the performance of devices in this study was not as good as those from some other literature, it still indicated the possibility of fabricating a transparent and flexible perovskite device without the Au deposition process which is energy-consuming. In addition, with P3HT, PMMA-functionalised SWCNTs were reported to enhance the thermal stability dramatically with the presence of P3HT together acting as the hole transporting layer due to their better stability than that of the organic hole transport layer P3HT itself.[442] The major advantages of the application of CNTs in perovskite solar cells are the possible realisation of flexible devices, the economic fabrication process and material, and the potential of devices suitable for two-side illumination.

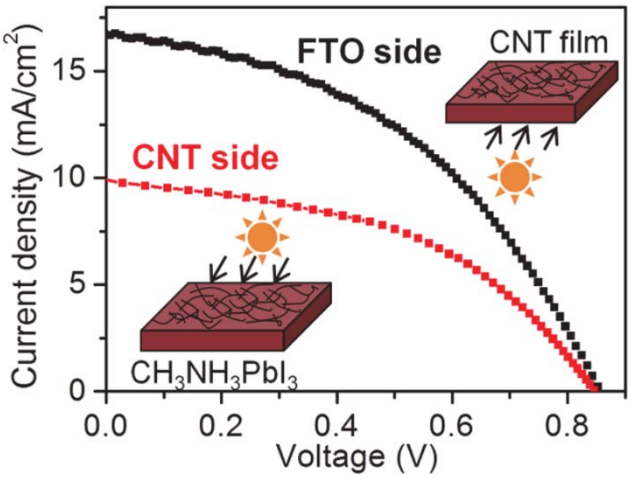

Figure 1.25 The light J-V curves of a perovskite device from two different sides after substituting the Au electrode by CNT TCF.[441] Adapted with permission from ref 441. Copyright 2014 American Chemical Society.

1.4.2 Touch panels

There has been a rapid development of touch panels due to the overwhelming consumption of modern electronic devices, such as the smart phones, tablet computers, and digital cameras. Technically, a touch panel is an interface used to control a digital display device with single and/or multiple touches by fingers or styluses. Though there are many formats of touch panels, such as those based on infrared grids[443] and acoustic pulse recognition[444], the most popular ones are built with either resistive or capacitive technologies.

The following is the description of the working mechanism of a touch panel: when pressure is applied on the electrode from the touch side by a finger or stylus, two electrodes are connected together and the measurement of the resulting current flow between the two electrodes is performed. Meantime, the touch position, x, y, and sometimes z, is identified by a signal-processing controller. Finally, the electronic devices, such as the computer, process the events after recognising the feedback.

Unidym attempted to apply CNT TCFs into a four-wire resistive touch panel whose structure is shown in Figure 1.26 (a).[445] CNT TCFs on PET films (CNTs/PET) were applied to substitute the traditional commercial ITO-coated glass-based touch electrode (ITO/glass), with spacer dots separating the touch-side electrode (CNTs/PET) from the device-side electrode (ITO/glass). At Unidym, purified CVD-grown CNTs were the normal starting materials in the preparation of an aqueous ink which was then used to create TCFs onto the certain types of polymer substrates (such as PET and PC) via different coating procedures (including spray coating, slot coating, inkjet printing, and gravure). The R_{sheet} of a typical CNT film on PET substrate as a touch panel is about 500 Ω sq^{-1} at T = 88 % (σ_{DC}/σ_{OP} = 5.71) through the visible range.[445]

CNT TCFs can also be applied as the electrodes in a capacitive-based touch panel,[446-447] as shown in Figure 1.26 (b). It consists of two CNT TCFs, in which CNTs are physically buried just below the surface of PDMS, as shown in Figure 1.26 (c) and separated with a silicone elastomer (also acting as the pressure monitor) with the CNT lines perpendicular to each other. When it is pressed by a finger or stylus, the distance between the two electrodes is reduced as the deformation of the elastomer by external force. Since there is an inversely proportional relationship between the capacitance and distance between the two electrode plates (shown in Equation 1.13), the resulting capacitance increases.

$$C = \frac{\varepsilon_1 \varepsilon_2 A}{d} \qquad \text{Equation 1.13}$$

in which C is capacitance; ε_1 and ε_2 are the electric constant and the dielectric constant of the separator, respectively; and A and d are the size of the overlapping region and the distance between two electrode plates. The R_{sheet} of the typical CNT TCF was 564 Ω sq^{-1} at T = 65% (at 550 nm) (σ_{DC}/σ_{OP} = 1.39).[446] Although the optoelectronic properties are lower than the

minimal requirement for commercial application, its unique design of CNT buried in PDMS with high flexibility endows the panel with excellent mechanical strength. The stability of the elastic electrodes under repeated stretches with strains of up to 300% was excellent and the electrodes were still functioning (the R_s is about 10 $k\Omega\ sq^{-1}$ and the T increased slightly) after 5 tests with adhesive tape.

In addition, a hybrid-type transparent electrode for touch panels based on the combination of SWCNTs with a silver grid was also created.[448] In terms of the optoelectronic properties, metal grids are the best alternative material to ITO, however, because of the fast oxidation rate when exposed to atmosphere, their instability limits the commercial applications, such as touch panels grids.[449-450] Oppositely, the chemical as well as thermal stability of CNTs are two key advantages over the metal grids. The possible application of a silver grid coated with SWCNTs via EPD (see section 1.3.2.2.5) as touch panels has been reported.[448] The hybridised electrode has excellent optoelectronic properties with R_{sheet} of 15.5 $\Omega\ sq^{-1}$ at T = 80% (σ_{DC}/σ_{OP} = 97.2, and this is much higher than the minimal requirement for many applications, including touch panels).[448] Furthermore, the hybrid also has enhanced stability of the properties with the exposure to warm (85 °C) and humid (85 % humidity) conditions for 5 days, as shown in Figure 1.26 (d).[448] This result was a vivid example of combining the excellent optoelectronic properties from metallic grids with the intrinsic stability of CNT together in a real application of touch panels.

Compared to TCO-based touch panels, there are two major benefits from CNT TCFs. Firstly, CNT has a similar refractive index to that of many other polymers while the refractive index of ITO is much higher ($n_{CNT} \approx 1.5-1.6$, $n_{ITO} \approx 2$, and $n_{PET} \approx 1.5$) so that the reflection at the interface is suppressed when CNT TCFs are applied onto polymeric substrates, such as PET, and thus the readability is better, as shown in Figure 1.26 (e).[445,451] Secondly, the lifetime of CNT TCFs is better due to their chemical and thermal stability. For instance, as shown in Figure 1.26 (f), CNT/ITO devices (where CNT is the top electrode with ITO as the bottom electrode) can function more than 1 million actuations, while ITO/ITO (where ITO-coated glasses are used as both top and bottom electrodes) devices failed after about 50,000 touches by a pen (the tip radius of which is 0.8 mm).[445] Some other advantages of CNT TCFs over metal TCO-based TCFs are their better chemical stability under acidic environment and more

"neutral" colour than ITO (the latter has a tinge of yellow).[452] The lower haze factor is the major superiority of CNT TCFs over metal nanowires since large-diameter metallic nanowires always suffer from optical haze issues.[453]

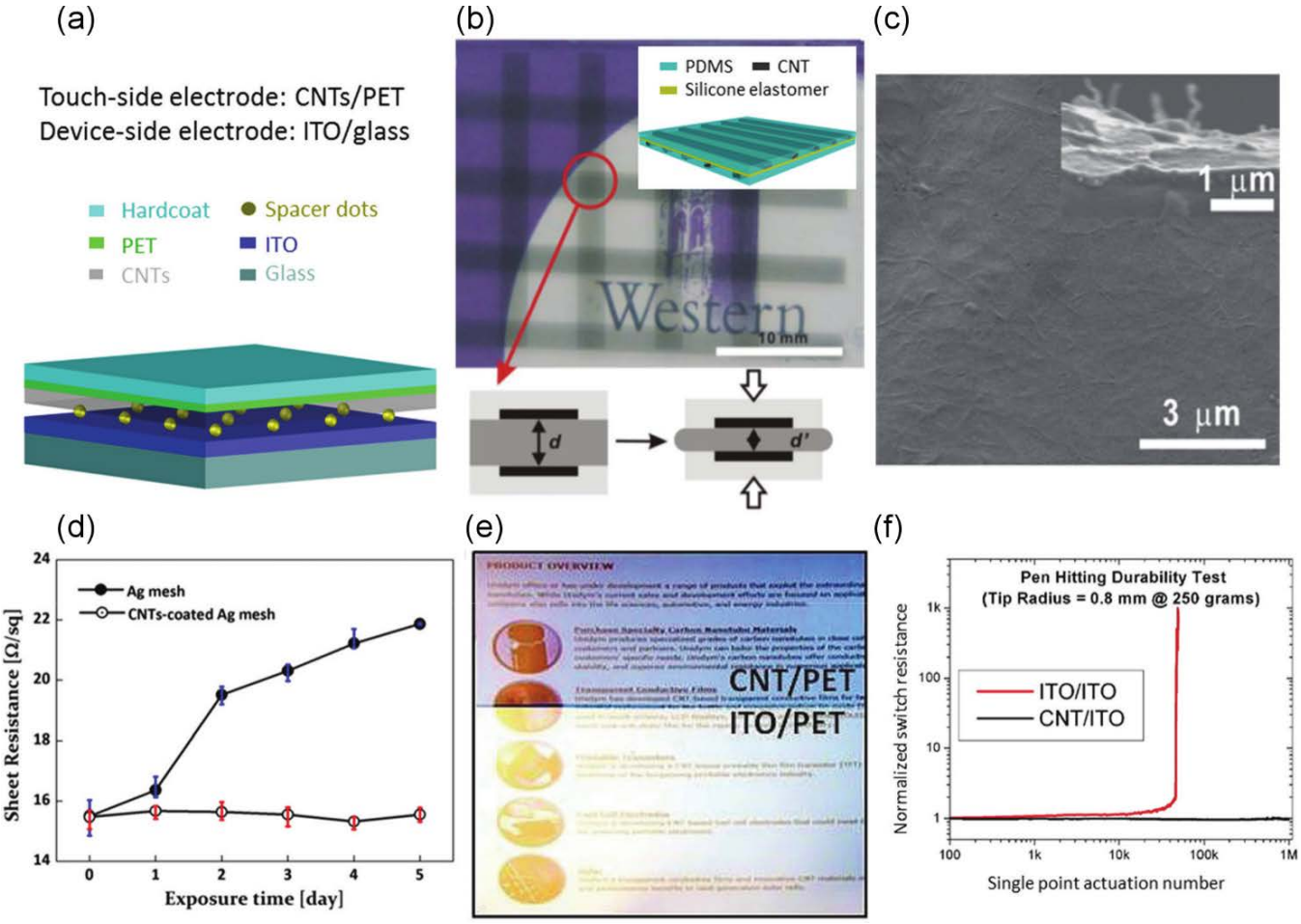

Figure 1.26 (a) Schematic structure of four-wire touch panel.[445] (b) Optical image of a capacitive-based touch panel consisting of two patterned CNT TCFs (the inset shows the 3D structure) and the illustration of the capacitor area with and without the addition of external pressure. Adapted with permission from ref 446. Copyright 2013 Royal Society of Chemistry. (c) SEM image of the SWCNT film buried underneath the surface of PDMS (the inset is the view of the cross section morphology). Adapted with permission from ref 446. Copyright 2013 Royal Society of Chemistry. (d) Stability tests showing the change of the sheet resistance versus time of the TCFs. Reprinted with permission from ref 448. Copyright 2015 Elsevier. (e) Comparison of the optical images viewed through between a CNT/PET and ITO/PET screen under daylight. Reprinted with

the permission from ref 445. Copyright 2009 John Wiley & Sons, Inc. (f) Plot of normalised switch resistance as a function of single point actuation number. Reprinted with permission from ref 445. Copyright 2009 John Wiley & Sons, Inc.

1.4.3 Liquid crystal displays

In the past a few decades, LCDs have become one of the most commonly used display devices in electronic industry. The simplified schematic structure of the key parts of a single pixel of LCD is illustrated in Figure 1.27 (a). It consists of two ITO-coated glasses facing each other, and there is a polymer layer with some groove-like patterns on top of each, which are normally prepared by mechanically rubbing, and their function is to orient the molecules of liquid crystal in a specific direction. There are several problems for the current rubbing polymeric films (usually polyimide), such as the charging of surface electrostatics, damage of the films, and broken debris, all of which lead to a poor performance. Polarizers (not illustrated in the schematic structure) are placed in the same direction as the grooves of the polymers with each electrode (and so they are normally crossed). Usually, when there is no applied voltage (the pixel is in the off state), the liquid crystal molecules are in a twisted configuration, as shown in Figure 1.27 (a). As a result, the light is able to pass through the whole unit with a bright pixel. When there is an external voltage applied to the unit (the pixel is now in the on state), the liquid crystal molecules in the cell are oriented into one direction and all the light can pass through the first electrode but is blocked by the second one; thus, the cell is dark. The colour of the pixel is controlled by placing filters with different colours in front of the whole device.

There are three reasons for the TCFs based on aligned CNTs replacing the polymeric materials and at the same time the expensive ITO: excellent T, high conductivity, and the necessary groove-like structures from aligned CNTs used to orient the liquid crystal molecules.[454-456] The function of CNT TCF replacing the ITO only was studied by Park et al.[457] CNTs were coated on a glass surface via spray coating (refer to 1.3.2.2.3), and the layer of polyimide was then applied. The CNT/glass electrodes were mechanically rubbed in the same manner as a traditional ITO-coated glass/polyimide electrode, and the latter served as a control device. Here, since the groove-like features were realised with polyimide surface, it is not necessary to use the aligned CNT films. The R_{sheet} of the randomly aligned CNT film, as

shown in the inset in Figure 1.27 (b), was 198.4 Ω sq^{-1} at T = 81.8% (σ_{DC}/σ_{OP} = 9), which was much lower than the minimal requirement for LCD (22.3). The transmittance versus voltage curves were collected to explore the alignment features of the liquid crystal molecules in the cell, as shown in Figure 1.27 (b).[457] When there was no applied voltage, both cells had a transmittance of about 100%, and the cells were bright under the backlight. Liquid crystal molecules started orienting along the direction perpendicular to the electrodes with the increase in the applied voltage, and as a result the light beam was blocked. The voltage difference at the transmittance between 90 % and 10 % is defined as the effective switching amplitude. Devices made of ITO-coated glass/polyimide electrodes had a higher effective switching amplitude (1.61 V) than that of the devices fabricated with glass/CNT/polyimide electrodes (1.19 V). This fact was caused by the electric-field effect--a strong localised electric field is induced by CNTs with high aspect ratio.[458] This enabled the production of a concentrated electric field by the CNT electrode under the applied voltage and thus the liquid crystal molecules were polarised at a lower voltage.

Scientists achieved some success in this area earlier in 2010.[455] An aligned MWCNT film was produced by drawing MWCNT from an aligned MWCNT forest onto a substrate (refer to 1.3.1.2). The MWCNTs used in that study had 6 to 12 shells, with a diameter and length of 10 to 15 nm and 250 µm, respectively. As shown in the SEM image of the resulting film on glass (Figure 1.27 (c)), the width of the film (perpendicular to the direction of drawing) was up to 10 cm, and MWCNTs were well-aligned along the drawing direction due to van der Waals interaction. The R_{sheet} of the prepared film was 1200 Ω sq^{-1} at T = 85% (σ_{DC}/σ_{OP} = 1.86, much lower than the minimal commercial requirement for LCD, 22.3). Here, the CNT/glass was used to replace the ITO/glass and the polymeric materials at the same time. With the control over of the applied voltage on the two electrodes, the colour of the cell unit was switched between bright (voltage off) and dark (voltage on), as shown in the inset in Figure 1.27 (c). This successful control was caused by the deep groove-like structures from the surface of the well-aligned MWCNT. In addition, when the voltage was off, it produced the long-range elastic strain energy enabling the liquid crystal molecules to be oriented parallel to the grooves of the MWCNT on glass.

Later, Lee et al. rubbed the well-aligned CNT film on top of glass drawn from an aligned MWCNT array (the diameter and the length of MWCNTs are 10 nm and 400 μm) in the same way as the traditional rubbing process for the polymeric materials.[454] The orientation of the CNT film became more uniform to the direction of rubbing, though the majority of the CNTs were well-aligned to the drawing direction without rubbing process. Unfortunately, the optoelectronic properties of the films were not mentioned in their study. The direct current (DC) residue is defined as Equation 1.14.

$$DC\ residue = \frac{\Delta V_1 + \Delta V_2}{2} \qquad \text{Equation 1.14}$$

in which ΔV_1 and ΔV_2 are the voltage differences at the half maximum of the capacitance as the applied voltage increases and decreases, respectively, as shown in Figure 1.27 (d). The DC residue was compared between the devices based on the glass/rubbed CNT electrode and the conventional ITO-coated glass/polyimide counterpart. The DC residue has a close relationship with the persistence of the image (high value corresponds to severe image retention). It was reported that the DC residue of the glass/rubbed CNT-based device was lower than that of the traditional counterpart. Additionally, glass/rubbed CNT-based device did not contain an insulating polymeric material layer between the TCF and the liquid crystal molecules, which indicates less hysteresis.

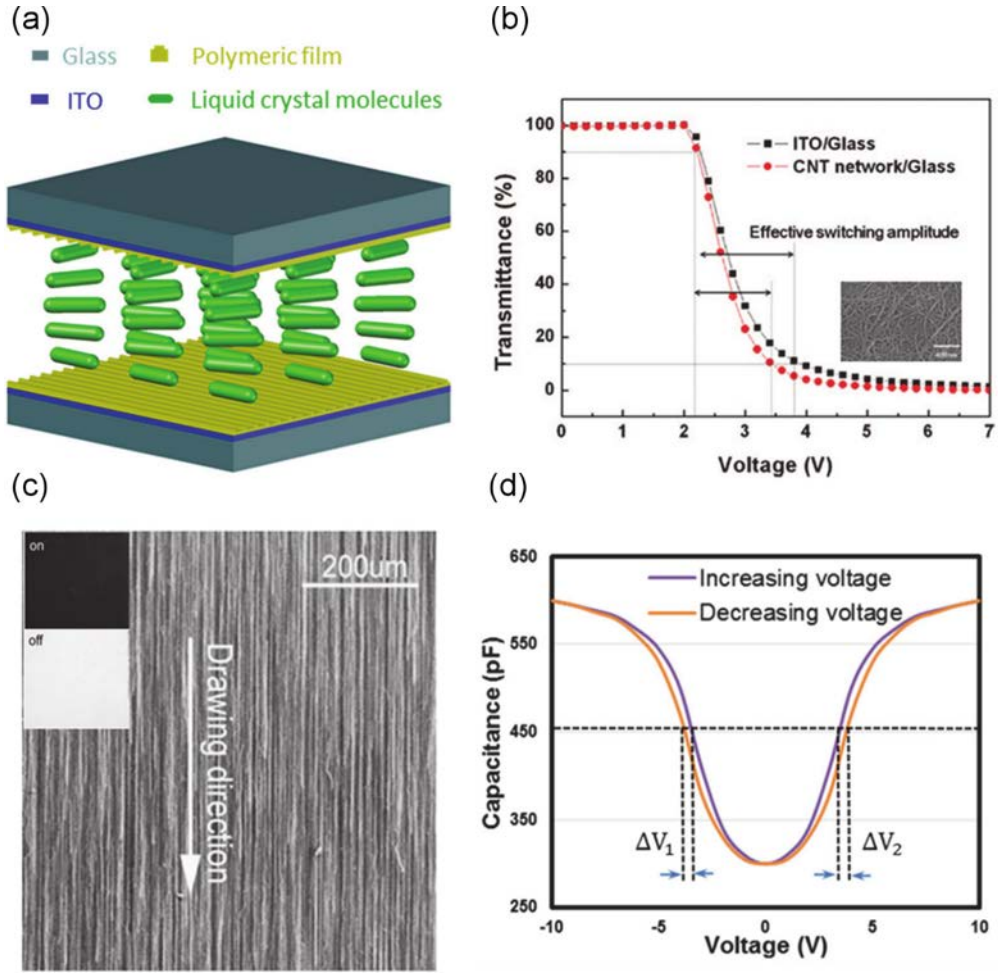

Figure 1.27 (a) Schematic structure of the major parts of a twisted nematic single crystal LCD pixel. (b) Relationship between T and voltage for devices built with two different electrodes, ITO-coated and CNT TCF-coated glass (inset shows the SEM image of the CNT film). Adapted with permission from ref 457. Copyright 2012 Electrochemical Society. (c) SEM image of an LCD electrode (the inset is the on and off state of the LCD cell). Adapted with permission from ref 455. Copyright 2010 Elsevier. (d) Scheme of the capacitance as a function of voltage test to estimate the DC residue from the measurement of the capacitance by increasing and decreasing voltage applied.[454]

1.4.4 Organic light-emitting diodes

There are two electrodes (anode and cathode) in a typical OLED, and between these two electrodes is the emitting layer which contains electroluminescent material (in most cases with electron-transporting and hole-transporting layers at the same time) producing light in

response to the voltage-induced current. When there is a voltage applied between the anode and cathode and the injection of the electrons into the LUMO level of the cathode side occurs, these electrons are then withdrawn to the HOMO level at the anode side due to the relatively positive voltage all the way through the electron transporting, emitting, and hole-transporting layers. The recombination of the electrons and holes and the process of the relaxation at the emitting layer contribute to the production of photons, as illustrated in the energy diagram (Figure 1.28 (a)). There are many excellent properties of OLEDs, which are the basis of one of the best solid-state electronic displays, including the lightweight nature, low power consumption but with high light intensity with short response time, and a broad view angle. Response to the market demand due to these properties, in turn, encourages the technology development. Since CNTs have a similar work function (about 4.5–5.2 eV) as that of ITO, the CNT TCFs with excellent optoelectronic properties then seem to be potential alternative to ITO as the anode in the fabrication of OLEDs, with the extra benefit of high flexiblility.[459-468] The important properties of some CNT TCF-based anodes are listed in Table 1.7. Basically, an ideal OLED would need the roughness to be low (so as to have limited leakage current) and a low turn-on voltage along with a high current efficiency and maximum light output.

Table 1.7 Important parameters of CNT TCF-based anodes in OLEDs

Anode composition	Surface roughness[a] (nm)	Turn-on voltage (V)	Maximum light output (cd m^{-2})	Maximum current efficiency (cd A^{-1})	T	R_{sheet} (Ω sq^{-1})	σ_{DC}/σ_{OP}
SWCNTs/glass[460]	4.2	4.2	4224	3.12	64.8 %	30	25.9
SWCNTs/PET[461]	3	7	2587	5.44	81 %	70.6	24.0
P3HT wrapped SWCNTs with gold grids/glass[462]	2	4.7	8260	3.1	94 %	25	240
PEDOT-SWCNTs composite/PEN[b463]	3.35	12	3400	4.6	86 %	160	15.0
Graphene-SWCNTs composite/PET[464]	1	3.1	29490	14.7	89 %	76	42

[a] Surface roughness: the value is root mean square (RMS) average of the profile height deviations after optimisation.

[b] PEN: polyethylene naphthalate

Liu et al. reported a pure carbon material-based anode electrode with PET substrate for OLEDs in 2014.[464] It consisted of two few-layer graphene sheets (FLGs) on top of a pre-grown array of SWCNTs. The SWCNT array was first grown on a quartz substrate by CVD and was then transferred to a PET substrate with the help of PMMA as a mediator. Before the transfer with the supporting layer of PMMA, FLG sheets were treated with 1-pyrenebutyric acid N-hydroxysuccinimide ester (PBASE) in DMF in order to increase the work function of the FLG surface since high work function benefits the hole injection at the anode.[469] As shown in Figure 1.28 (b), the current density of the devices increases with an increase in the external voltage and, as a result, luminance of devices occurs with the conversion of electricity into light. Compared to ITO-based device, the pure carbon anode-based devices have a lower turn-on voltage (3.1 V), and can also easily reach 1000 cd m^{-2} with relatively low applied voltage (7 V). The highest luminance value for this SWCNT−FLG-based device was much higher than that of pure graphene anode-based device (above 29 000 versus less than 1000 cd m^{-2}).[470] High flexibility of the device is another very attractive benefit for the entire carbon material anode-based OLEDs, as shown in Figure 1.28 (c). It was shown from the results of the bending tests that the device was still able to emit after hundreds circles of bending with an angle up to 90 degrees.

One important parameter for an OLED diode is the roughness which determines the homogeneity of the luminance. The length of SWCNTs, 1−2 μm, is normally larger than the active layer thickness. It is very easy to short the device with SWCNTs penetrating through the active layer and bridging between cathode and anode due to the high current-carrying capacity of SWCNTs. As shown in Figure 1.28 (d) (RMS = 8 nm), there are several large pore areas and protrusion points of a pure SWCNT network, and these are the original sources of possible shorts as well as the light scattering. Thus, most of the studies in the field of CNT TCF anode-based OLED included surface morphology optimisation. The *in situ* polymerisation of PEDOT was used to address this problem.[463] This approach was able to fabricate a very smooth anode with no pores and the RMS was reduced to 3.35 nm. As a result, the failure rate in the device fabrication decreased dramatically with the improvement in the luminance uniformity.

Rather than the *in situ* polymerisation, spray coating and spin coating can also be used to apply conductive polymers with the extra benefit of higher contrast ratio. A SWCNT anode

covered with PEDOT:PSS is able to absorb light and then reduce the amount of the injected ambient light penetrating into the device. As a result, a better contrast ratio is achieved by the reduction of the reflection from the injected ambient hitting at the metal cathode surface. As shown in Figure 1.28 (e), the contrast ratio of PEDOT:PSS-coated SWCNT TCF-based OLEDs was more than three times higher than that of the conventional counterparts based on ITO.[460]

Metal grids are another alternative for the OLED anode, and their optoelectronic properties sometimes are better than those of SWCNT networks. However, there are many large spare areas between the grids to retain the high transmittance. If the gap between grid lines is much larger than the diffusion length of holes, the injected holes in the centre area are difficult to collect. The recombination of the charge carriers (holes and electrons) can only occur at the region next to the grid lines, and then, the luminance would only happen in the area close to the lines with the external applied voltage, as shown in Figure 1.28 (f).[462] By applying P3HT-wrapped SWCNTs via spin coating, the spaces between the grid lines were covered with the SWCNT networks so that the holes were able to transport through the CNT films with the recombination process taking place uniformly, and thus homogeneous luminance was achieved, as shown in the inset in Figure 1.28 (f).[462]

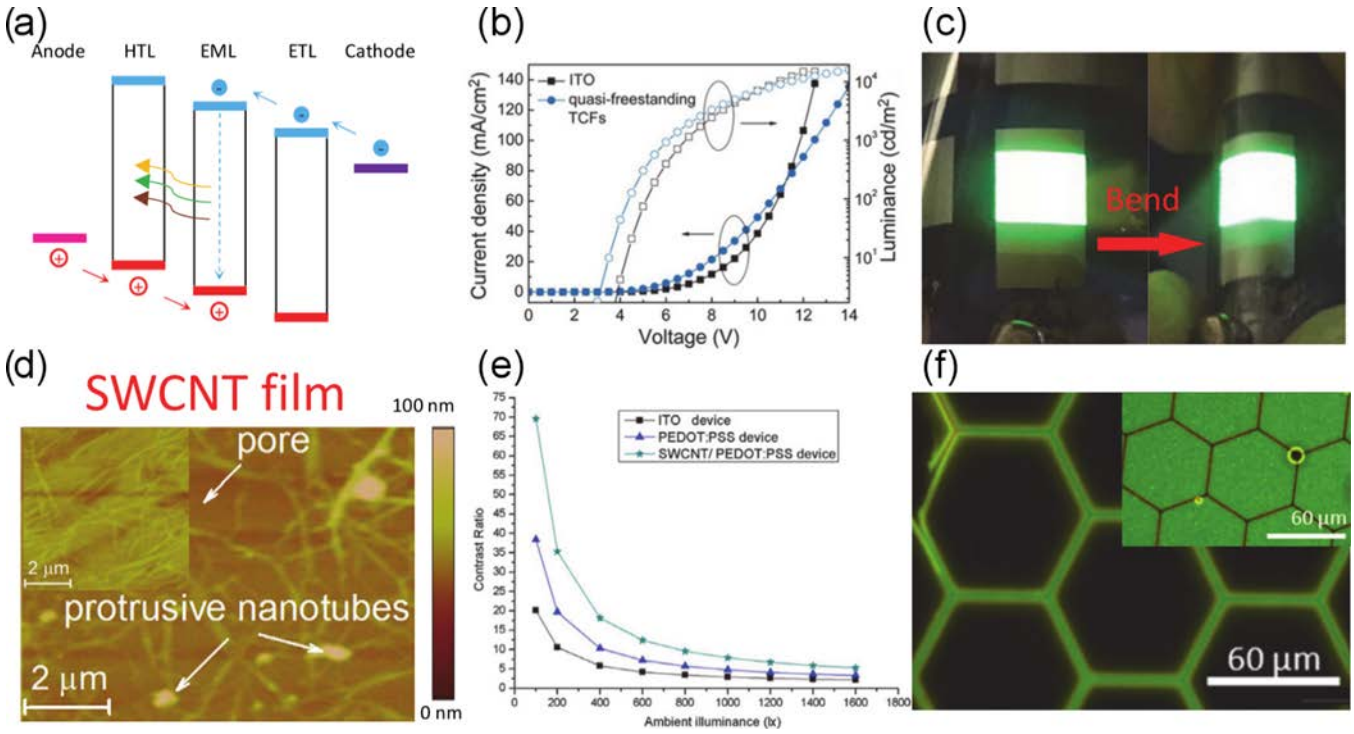

Figure 1.28 (a) Energy diagram of a typical OLED device consisting of an anode, hole-transporting layer (HTL), emitting layer (EML), electron-transporting layer (ETL), and cathode. (b) Current density and luminance versus applied voltage of devices with ITO or pure carbon TCFs. Reprinted with permission from ref 464. Copyright 2014 John Wiley & Sons, Inc. (c) Tests of flexibility of OLED device with pure carbon-based anode. Adapted with permission from ref 464. Copyright 2014 John Wiley & Sons, Inc. (d) AFM image of pure SWCNT films indicating that there are some pores and protrusive nanotubes (inset shows the SWCNT network with PEDOT prepared by in situ polymerisation). Adapted with permission from ref 463. Copyright 2014 Elsevier. (e) Contrast ratio versus ambient luminance. Reprinted with permission from ref 460. Copyright 2012 Elsevier. (f) Optical images of the OLED with Au grid as the anode (state: on) and the inset shows the device with P3HT-wrapped SWCNTs combined with gold grids as the anode (state: on). Adapted with permission from ref 462. Copyright 2014 IOP Publishing.

Thus, CNT-based TCFs have already been successfully applied in a wide range of fields on a lab scale. They have been used in the preparation of many different types of solar cells, touch panels, LCDs, and OLEDs. However, there are still a few issues to be addressed for each of

these applications. First of all, CNT films are usually doped, but the dopants are tend to react with atmosphere or many other materials which they are in contact with, and as a result, R_{sheet} increases with the reducing performance.[471] Secondly, the optoelectronic properties of CNT TCFs are continually being improved, but more advances are required for the application in solar cells in order to match and exceed that of traditional TCOs (the FOM are more than 200 for TCOs but normally less than 50 for CNT TCFs, even after chemical doping). The optoelectronic properties of most CNT-based TCFs are still below the minimum commercial requirements. Thirdly, CNTs are widely used with some other components to form a composite electrode in many cases, especially acting as the anode of the OLEDs. CNTs themselves have fantastic stability even under some extreme conditions, but the rest of the components in the composite, such as some conducting polymers (PEDOT:PSS), suffer from low thermal and chemical stability atmosphere. Thus, further encapsulation processes are required for long-term purposes.

1.5 Summary and motivation

During the last 20 years, the TCF industry has been developed because of the widespread use of final products in daily life, including touch panel-based smartphones and LCD screen-based televisions. TCOs are the most popular current materials in TCFs fabrication, and it is a mature technology but with some issues, such as brittleness and expensive processing. People have expended considerable effort on conductive polymers, but they are still not an appropriate alternative to replace TCOs in commercial TCFs fabrication because of the poor environmental stability. CNTs, with excellent electrical conductivity, mechanical flexibility, and optically neutral colour, have been extensively investigated in TCFs and show great possibility for industrial applications. An important parameter, figure of merit value, FOM (σ_{DC}/σ_{OP}), has been developed to describe the optoelectronic properties of the CNT TCFs and widely used to compare the TCFs prepared by different groups. A great number of both dry and wet processing approaches have been designed to fabricate and pattern CNT TCFs. Furthermore, different types of dopants have been used to modify the work function of the CNTs and hybridisation of CNT TCFs with other materials has been developed to improve the properties of the CNT TCFs and fulfil the requirements for the applications. The optoelectronic properties

of some CNT TCFs, such as the composite TCFs based on CNTs with AgNWs, have already met the requirements for the OLED anode. However, there are still some challenges before the actual industrial manufacturing of CNTs TCFs. First of all, the current synthesis approaches are energy-consuming and produce CNTs with various forms, length, and diameters with a rapid growth rate, and the CNT product is technically a mixture even after purification steps. Additionally, sorted CNTs with specific electronic properties are required for some certain applications. Secondly, patterning of CNT TCFs can be realised with a large number of approaches, but because of different drawbacks few of these have been commercialised. The most important engineering issue is to fabricate CNT TCFs with low cost and over a large area. Thirdly, extensive dopants have been proven to effectively enhance the properties of CNT TCFs, but the effects of doping do not last long enough for industrial application, and for instance, the moisture and other substances in the atmosphere can damage solar cells based on CNT TCFs. Tuning the work function of CNT TCFs has the same issue of instability. Furthermore, the roughness of CNT TCFs surface is another interface issue to be addressed. Thus, reducing the cost of fabrication processes, improvement of the device stability devices involving CNT TCFs, and industrial-scale manufacturing solutions are the three main targets in the future. Despite these challenges, CNT TCFs still have a bright future, because of both the unique properties of CNTs and the promising research results from the continuous efforts in this area.

This Thesis mainly focuses on the application and improvement measures on the solar devices based on CNTs TCFs. Chapter 2 lists the experimental details of the following chapters. The next few chapters are about CNT/silicon solar cells. In detail, Chapter 3 is about the application of composite material based on SWCNTs and PANI in CNT/silicon devices. Chapter 4 looks into the influence of grids on the performance of CNT/silicon cells. Chapter 5 describes the impact of the additional interlayer between CNT and silicon on the performance. Chapter 6 explores the approaches in improving the optoelectronic properties of the CNT based solar cells while Chapter 7 shows importance of the surface structure of Si in the photovoltaics. In addition, Chapter 8 is about the purification of SWCNTs into individual species. Finally, Chapter 9 is the concluding chapter where possible future directions will also be discussed.

REFERENCES:

(1) Hecht, D. S.; Hu, L.; Irvin, G., Emerging transparent electrodes based on thin films of carbon nanotubes, graphene, and metallic nanostructures. *Adv Mater* **2011**, *23*, 1482-1513.

(2) Chang, D. S.; Lai, S. T., Implementation of Cross-Generation Automation Transportation System in the TFT-LCD Industry. *Int. J. Adv. Des. Manuf. Technol.* **2015**, *78*, 753-763.

(3) Du, J. H.; Pei, S. F.; Ma, L. P.; Cheng, H. M., 25th Anniversary Article: Carbon Nanotube- and Graphene-Based Transparent Conductive Films for Optoelectronic Devices. *Adv. Mater.* **2014**, *26*, 1958-1991.

(4) Feldman, D.; Brockway, A. M.; Ulrich, E.; Margolis, R. "Shared Solar: Current Landscape, Market Potential, and the Impact of Federal Securities Regulation," National Renewable Energy Laboratory (NREL) 2015.

(5) Song, J. Z.; Kulinich, S. A.; Li, J. H.; Liu, Y. L.; Zeng, H. B., A General One-Pot Strategy for the Synthesis of High-Performance Transparent-Conducting-Oxide Nanocrystal Inks for All-Solution-Processed Devices. *Angew. Chem.-Int. Edit.* **2015**, *54*, 462-466.

(6) Li, H.; Schirra, L. K.; Shim, J.; Cheun, H.; Kippelen, B.; Monti, O. L. A.; Bredas, J. L., Zinc Oxide as a Model Transparent Conducting Oxide: A Theoretical and Experimental Study of the Impact of Hydroxylation, Vacancies, Interstitials, and Extrinsic Doping on the Electronic Properties of the Polar ZnO (0002) Surface. *Chem. Mat.* **2012**, *24*, 3044-3055.

(7) Klein, A., Transparent Conducting Oxides: Electronic Structure-Property Relationship from Photoelectron Spectroscopy with in situ Sample Preparation *J. Am. Ceram. Soc.* **2013**, *96*, 331-345.

(8) Barnes, T. M.; Reese, M. O.; Bergeson, J. D.; Larsen, B. A.; Blackburn, J. L.; Beard, M. C.; Bult, J.; van de Lagemaat, J., Comparing the Fundamental Physics and Device Performance of Transparent, Conductive Nanostructured Networks with Conventional Transparent Conducting Oxides. *Adv. Energy Mater.* **2012**, *2*, 353-360.

(9) Stadler, A., Transparent Conducting Oxides-An Up-To-Date Overview. *Materials* **2012**, *5*, 661-683.

(10) Hautier, G.; Miglio, A.; Ceder, G.; Rignanese, G. M.; Gonze, X., Identification and Design Principles of Low Hole Effective Mass p-Type Transparent Conducting Oxides. *Nat. Commun.* **2013**, *4*, 2292-2292.

(11) Liu, A.; Liu, G. X.; Zhu, H. H.; Song, H. J.; Shin, B.; Fortunato, E.; Martins, R.; Shan, F. K., Water-Induced Scandium Oxide Dielectric for Low-Operating Voltage n- and p-Type Metal-Oxide Thin-Film Transistors. *Adv. Funct. Mater.* **2015**, *25*, 7180-7188.

(12) Chen, C. Y.; Lee, W. K.; Chen, Y. J.; Lu, C. Y.; Lin, H. Y.; Wu, C. C., Enhancing Optical Out-Coupling of Organic Light-Emitting Devices with Nanostructured Composite Electrodes Consisting of Indium Tin Oxide Nanomesh and Conducting Polymer. *Adv. Mater.* **2015**, *27*, 4883-4888.

(13) Duta, M.; Anastasescu, M.; Calderon-Moreno, J. M.; Predoana, L.; Preda, S.; Nicolescu, M.; Stroescu, H.; Bratan, V.; Dascalu, I.; Aperathitis, E.; Modreanu, M.; Zaharescu, M.; Gartner, M., Sol-Gel versus Sputtering Indium Tin Oxide Films as Transparent Conducting Oxide Materials. *J. Mater. Sci.: Mater. Electron.* **2016**, *27*, 4913-4922.

(14) Chen, Z. X.; Li, W. C.; Li, R.; Zhang, Y. F.; Xu, G. Q.; Cheng, H. S., Fabrication of Highly Transparent and Conductive Indium-Tin Oxide Thin Films with a High Figure of Merit via Solution Processing. *Langmuir* **2013**, *29*, 13836-13842.

(15) Mora, A.; Khan, K. A.; El Sayed, T., Crack Density and Electrical Resistance in Indium-Tin-Oxide/Polymer Thin Films Under Cyclic Loading. *Electron. Mater. Lett.* **2014**, *10*, 1033-1037.

(16) Jeong, J. A.; Kim, H. K.; Koo, H. W.; Kim, T. W., Transmission Electron Microscopy Study of Degradation in Transparent Indium Tin Oxide/Ag/Indium Tin Oxide Multilayer Films. *Appl. Phys. Lett.* **2013**, *103*, 011902.

(17) Ahn, M. H.; Cho, E. S.; Kwon, S. J., Characteristics of ITO-Resistive Touch Film Deposited on a PET Substrate by In-Line DC Magnetron Sputtering *Vacuum* **2014**, *101*, 221-227.

(18) Kim, J. I.; Lee, W.; Hwang, T.; Kim, J.; Lee, S. Y.; Kang, S.; Choi, H.; Hong, S.; Park, H. H.; Moon, T.; Park, B., Quantitative Analyses of Damp-Heat-Induced Degradation in Transparent Conducting Oxides *Sol. Energy Mater. Sol. Cells* **2014**, *122*, 282-286.

(19) Mirletz, H. M.; Peterson, K. A.; Martin, I. T.; French, R. H., Degradation of Transparent Conductive Oxides: Interfacial Engineering and Mechanistic Insights *Sol. Energy Mater. Sol. Cells* **2015**, *143*, 529-538.

(20) Galagan, Y.; Mescheloff, A.; Veenstra, S. C.; Andriessen, R.; Katz, E. A., Reversible Degradation in ITO-Containing Organic Photovoltaics under Concentrated Sunlight *Phys. Chem. Chem. Phys.* **2015**, *17*, 3891-3897.

(21) Madhi, I.; Meddeb, W.; Bouzid, B.; Saadoun, M.; Bessais, B., Effect of Temperature and NO2 Surface Adsorption on Electrical Properties of Screen Printed ITO Thin Film. *Appl. Surf. Sci.* **2015**, *355*, 242-249.

(22) Shen, Y. D.; Turner, S.; Yang, P.; Van Tendeloo, G.; Lebedev, O. I.; Wu, T., Epitaxy-Enabled Vapor-Liquid-Solid Growth of Tin-Doped Indium Oxide Nanowires with Controlled Orientations. *Nano Lett.* **2014**, *14*, 4342-4351.

(23) Kim, M. J.; Song, P. K., High Crystallization of Ultra-Thin Indium Tin Oxide Films Prepared by Direct Current Magnetron Sputtering with Post-Annealing. *Sci. Adv. Mater.* **2016**, *8*, 622-626.

(24) Korosi, L.; Scarpellini, A.; Petrik, P.; Papp, S.; Dekany, I., Sol-Gel Synthesis of Nano Structured Indium Tin Oxide with Controlled Morphology and Porosity. *Appl. Surf. Sci.* **2014**, *320*, 725-731.

(25) Eisa, W. H.; Khafagi, M. G.; Shabaka, A. A.; Talaat, H.; Abd El-Karim, A. M., Femtosecond Pulsed Laser Induced Growth of Highly Transparent Indium-Tin-Oxide Thin Films: Effect of Deposition Temperature and Oxygen Partial Pressure. *Optik* **2015**, *126*, 3789-3794.

(26) Cheon, J.; Lee, J.; Jeong, C., Improvement in Properties of Indium Tin Oxide Thin Films by Electron Beam Irradiation. *Sci. Adv. Mater.* **2016**, *8*, 596-600.

(27) Su, Y.; Zhitomirsky, I., Influence of Dopants on Performance of Polypyrrole Coated Carbon Nanotube Electrodes and Devices. *J. Electrochem. Soc.* **2015**, *162*, A5013-A5019.

(28) Zhu, Y. L.; Zhitomirsky, I., Influence of Dopant Structure and Charge on Supercapacitive Behavior of Polypyrrole Electrodes with High Mass Loading. *Synth. Met.* **2013**, *185*, 126-132.

(29) Muhsin, B.; Roesch, R.; Gobsch, G.; Hoppe, H., Flexible ITO-Free Polymer Solar Cells Based on Highly Conductive PEDOT:PSS and a Printed Silver Grid. *Sol. Energy Mater. Sol. Cells* **2014**, *130*, 551-554.

(30) Hu, X. T.; Chen, L.; Zhang, Y.; Hu, Q.; Yang, J. L.; Chen, Y. W., Large-Scale Flexible and Highly Conductive Carbon Transparent Electrodes via Roll-to-Roll Process and Its High Performance Lab-Scale Indium Tin Oxide-Free Polymer Solar Cells. *Chem. Mat.* **2014**, *26*, 6293-6302.

(31) Kumar, P.; Santhakumar, K.; Tatsugi, J.; Shin, P. K.; Ochiai, S., Comparison of Properties of Polymer Organic Solar Cells Prepared Using Highly Conductive Modified PEDOT:PSS Films by Spin- and Spray-Coating Methods *Jpn. J. Appl. Phys.* **2014**, *53*, 01AB08.

(32) Kwon, J.; Ganapathy, V.; Kim, Y. H.; Song, K. D.; Park, H. G.; Jun, Y.; Yoo, P. J.; Park, J. H., Nanopatterned Conductive Polymer Films as a Pt, TCO-Free Counter Electrode for Low-Cost Dye-Sensitized Solar Cells *Nanoscale* **2013**, *5*, 7838-7843.

(33) Trchova, M.; Sedenkova, I.; Moravkova, Z.; Stejskal, J., Conducting Polymer and Ionic Liquid: Improved Thermal Stability of the Material - A Spectroscopic Study. *Polym. Degrad. Stabil.* **2014**, *109*, 27-32.

(34) Lu, B. Y.; Zhen, S. J.; Zhang, S. M.; Xu, J. K.; Zhao, G. Q., Highly Stable Hybrid Selenophene-3,4-Ethylenedioxythiophene as Electrically Conducting and Electrochromic Polymers. *Polym. Chem.* **2014**, *5*, 4896-4908.

(35) Xia, C.; Chen, W.; Wang, X. B.; Hedhili, M. N.; Wei, N. N.; Alshareef, H. N., Highly Stable Supercapacitors with Conducting Polymer Core-Shell Electrodes for Energy Storage Applications. *Adv. Energy Mater.* **2015**, *5*, 1401805.

(36) Lee, J.; Kang, H.; Kee, S.; Lee, S. H.; Jeong, S. Y.; Kim, G.; Kim, J.; Hong, S.; Back, H.; Lee, K., Long-Term Stable Recombination Layer for Tandem Polymer Solar Cells Using Self-Doped Conducting Polymers. *ACS Appl. Mater. Interfaces* **2016**, *8*, 6144-6151.

(37) Chiang, C. H.; Chen, S. C.; Wu, C. G., Preparation of Highly Concentrated and Stable Conducting Polymer Solutions and Their Application in High-Efficiency Dye-Sensitized Solar Cell *Org. Electron.* **2013**, *14*, 2369-2378.
(38) Ramesh, S.; Lu, S. C., A Simple P(Vdf-HFP)-Litf System Yielding Highly Ionic Conducting and Thermally Stable Solid Polymer Electrolytes *J. Mol. Liq.* **2013**, *177*, 73-77.
(39) Chandrasekhar, P.; Zay, B. J.; Cai, C. M.; Chai, Y. J.; Lawrence, D., Matched-Dual-Polymer Electrochromic Lenses, Using New Cathodically Coloring Conducting Polymers, with Exceptional Performance and Incorporated into Automated Sunglasses. *J. Appl. Polym. Sci.* **2014**, *131*, 41043.
(40) Menamparambath, M. M.; Ajmal, C. M.; Kim, K. H.; Yang, D.; Roh, J.; Park, H. C.; Kwak, C.; Choi, J. Y.; Baik, S., Silver Nanowires Decorated with Silver Nanoparticles for Low-Haze Flexible Transparent Conductive Films *Sci Rep* **2015**, *5*, 16371.
(41) Sugawara, K.; Hayashi, Y.; Fukushima, J.; Takizawa, H., Facile Synthesis of Silver-Nanobeadwire Transparent Conductive Film by Organic-Precursor Paint Reduction *Cryst. Res. Technol.* **2015**, *50*, 319-330.
(42) Andres, L. J.; Menendez, M. F.; Gomez, D.; Martinez, A. L.; Bristow, N.; Kettle, J. P.; Menendez, A.; Ruiz, B., Rapid Synthesis of Ultra-Long Silver Nanowires for Tailor-Made Transparent Conductive Electrodes: Proof of Concept in Organic Solar Cells *Nanotechnology* **2015**, *26*, 265201.
(43) Jiang, Y. W.; Lan, C. Y., Low Temperature Synthesis of Multiwall Carbon Nanotubes from Carbonaceous Solid Prepared By Sol-Gel Autocombustion. *Mater. Lett.* **2015**, *157*, 269-272.
(44) Li, Z. L.; Xie, H.; Jun, D.; Wang, Y. H.; Wang, X. Y.; Li, J. Z., A Comprehensive Study of Transparent Conductive Silver Nanowires Films with Mixed Cellulose Ester as Matrix *J. Mater. Sci.: Mater. Electron.* **2015**, *26*, 6532-6538.
(45) Jing, M. X.; Pi, Z. C.; Chen, C. Y.; Shen, X. Q., Scalable Fabrication of Silver Nanowires-Polyethylene Terephthalate Transparent Conductive Films by Rolling-Pressing Transfer Technique at Room Temperature. *Sci. Adv. Mater.* **2015**, *7*, 1599-1604.
(46) Ahn, K.; Kim, D.; Kim, O.; Nam, J., Analysis of Transparent Conductive Silver Nanowire Films from Dip Coating Flow *J. Coating. Tech. Res.* **2015**, *12*, 855-862.
(47) Oh, M.; Jin, W. Y.; Jeong, H. J.; Jeong, M. S.; Kang, J. W.; Kim, H., Silver Nanowire Transparent Conductive Electrodes for High-Efficiency III-Nitride Light-Emitting Diodes *Sci Rep* **2015**, *5*, 13483.
(48) Cho, E. H.; Hwang, J.; Kim, J.; Lee, J.; Kwak, C.; Lee, C. S., Low-Visibility Patterning of Transparent Conductive Silver-Nanowire Films *Opt. Express* **2015**, *23*, 26095-26103.
(49) Chen, Y. X.; Lan, W.; Wang, J. Y.; Zhu, R. R.; Yang, Z. W.; Ding, D. L.; Tang, G. M.; Wang, K. R.; Su, Q.; Xie, E. Q., Highly Flexible, Transparent, Conductive and Antibacterial Films Made of Spin-Coated Silver Nanowires and a Protective ZnO Layer *Physica E Low Dimens. Syst. Nanostruct.* **2016**, *76*, 88-94.
(50) Mo, L. X.; Ran, J.; Yang, L.; Fang, Y.; Zhai, Q. B.; Li, L. H., Flexible Transparent Conductive Films Combining Flexographic Printed Silver Grids with CNT Coating. *Nanotechnology* **2016**, *27*, 065202.
(51) Xu, W.; Xu, Q. S.; Huang, Q. J.; Tan, R. Q.; Shen, W. F.; Song, W. J., Fabrication of Flexible Transparent Conductive Films with Silver Nanowire by Vacuum Filtration and PET Mold Transfer. *J. Mater. Sci. Technol.* **2016**, *32*, 158-161.
(52) Yu, P. C.; Hong, C. C.; Liou, T. M., Bendable Transparent Conductive Meshes Based on Multi-Layer Inkjet-Printed Silver Patterns. *J. Micromech. Microeng.* **2016**, *26*, 035012.
(53) Jia, Y. G.; Chen, C.; Jia, D.; Li, S. X.; Ji, S. L.; Ye, C. H., Silver Nanowire Transparent Conductive Films with High Uniformity Fabricated via a Dynamic Heating Method. *ACS Appl. Mater. Interfaces* **2016**, *8*, 9865-9871.
(54) Tian, J. L.; Zhang, H. Y.; Wang, H. J., Preparation and Properties of Silver Nanowire-Based Transparent Conductive Composite Films. *J. Electron. Mater.* **2016**, *45*, 3040-3045.
(55) Betard, A.; Fischer, R. A., Metal-Organic Framework Thin Films: From Fundamentals to Applications. *Chem. Rev.* **2012**, *112*, 1055-1083.

(56) Ding, L.; Tselev, A.; Wang, J.; Yuan, D.; Chu, H.; McNicholas, T. P.; Li, Y.; Liu, J., Selective Growth of Well-Aligned Semiconducting Single-Walled Carbon Nanotubes. *Nano Lett.* **2009**, *9*, 800-805.
(57) Carlson, A.; Bowen, A. M.; Huang, Y. G.; Nuzzo, R. G.; Rogers, J. A., Transfer Printing Techniques for Materials Assembly and Micro/Nanodevice Fabrication. *Adv. Mater.* **2012**, *24*, 5284-5318.
(58) Hunger, C.; Rao, K. D. M.; Gupta, R.; Singh, C. R.; Kulkarni, G. U.; Thelakkat, M., Transparent Metal Network with Low Haze and High Figure of Merit applied to Front and Back Electrodes in Semitransparent ITO-free Polymer Solar Cells. *Energy Technol.* **2015**, *3*, 638-645.
(59) Marzbanrad, E.; Rivers, G.; Peng, P.; Zhao, B. X.; Zhou, N. Y., How Morphology and Surface Crystal Texture Affect Thermal Stability of a Metallic Nanoparticle: The Case of Silver Nanobelts and Pentagonal Silver Nanowires. *Phys. Chem. Chem. Phys.* **2015**, *17*, 315-324.
(60) Macocinschi, D.; Filip, D.; Zaltariov, M. F.; Varganici, C. D., Thermal and Hydrolytic Stability of Silver Nanoparticle Polyurethane Biocomposites for Medical Applications. *Polym. Degrad. Stabil.* **2015**, *121*, 238-246.
(61) Song, T.-B.; Chen, Y.; Chung, C.-H.; Yang, Y.; Bob, B.; Duan, H.-S.; Li, G.; Tu, K.-N.; Huang, Y.; Yang, Y., Nanoscale Joule Heating and Electromigration Enhanced Ripening of Silver Nanowire Contacts. *ACS Nano* **2014**, *8*, 2804-2811.
(62) Park, S.; Vosguerichian, M.; Bao, Z. A., A Review of Fabrication and Applications of Carbon Nanotube Film-Based Flexible Electronics. *Nanoscale* **2013**, *5*, 1727-1752.
(63) Iijima, S., Helical Microtubules of Graphitic Carbon. *Nature* **1991**, *354*, 56-58.
(64) Maiti, U. N.; Lee, W. J.; Lee, J. M.; Oh, Y.; Kim, J. Y.; Kim, J. E.; Shim, J.; Han, T. H.; Kim, S. O., 25th Anniversary Article: Chemically Modified/Doped Carbon Nanotubes & Graphene for Optimized Nanostructures & Nanodevices. *Adv. Mater.* **2014**, *26*, 40-67.
(65) Yang, F.; Wang, X.; Zhang, D. Q.; Yang, J.; Luo, D.; Xu, Z. W.; Wei, J. K.; Wang, J. Q.; Xu, Z.; Peng, F.; Li, X. M.; Li, R. M.; Li, Y. L.; Li, M. H.; Bai, X. D.; Ding, F.; Li, Y., Chirality-Specific Growth of Single-Walled Carbon Nanotubes on Solid Alloy Catalysts. *Nature* **2014**, *510*, 522-524.
(66) Popov, V. N., Carbon Nanotubes: Properties and Application. *Mater. Sci. Eng., R* **2004**, *43*, 61-102.
(67) Dresselhaus, M. S.; Dresselhaus, G.; Saito, R.; Jorio, A., Raman Spectroscopy of Carbon Nanotubes. *Phys. Rep.* **2005**, *409*, 47-99.
(68) Anantram, M. P.; Leonard, F., Physics of Carbon Nanotube Electronic Devices. *Rep. Prog. Phys.* **2006**, *69*, 507-561.
(69) Weisman, R. B.; Bachilo, S. M., Dependence of Optical Transition Energies on Structure for Single-Walled Carbon Nanotubes in Aqueous Suspension: An Empirical Kataura Plot. *Nano Lett.* **2003**, *3*, 1235-1238.
(70) Moore, K. E.; Tune, D. D.; Flavel, B. S., Double-Walled Carbon Nanotube Processing. *Adv. Mater.* **2015**, *27*, 3105-3137.
(71) Hasegawa, T.; Arenas, D. J.; Kohno, H., Optimizing Growth Conditions for Coaxial Multi-Walled Carbon Nanotubes. *Fuller Nanotube Car. N.* **2015**, *23*, 687-690.
(72) Baibarac, M.; Matea, A.; Ilie, M.; Baltog, I.; Magrez, A., Anti-Stokes Raman Spectroscopy as a Method to Identify Metallic and Mixed Metallic/Semiconducting Configurations of Multi-Walled Carbon Nanotubes. *Anal. Methods* **2015**, *7*, 6225-6230.
(73) Hayashi, H.; Takahashi, K.; Ikuta, T.; Nishiyama, T.; Takata, Y.; Zhang, X., Direct Evaluation of Ballistic Phonon Transport in a Multi-Walled Carbon Nanotube. *Appl. Phys. Lett.* **2014**, *104*, 113112.
(74) Lee, J.; Stein, I. Y.; Devoe, M. E.; Lewis, D. J.; Lachman, N.; Kessler, S. S.; Buschhorn, S. T.; Wardle, B. L., Impact of Carbon Nanotube Length on Electron Transport in Aligned Carbon Nanotube Networks. *Appl. Phys. Lett.* **2015**, *106*, 053110.
(75) Li, Y. S.; Ge, J.; Cai, J. H.; Zhang, J.; Lu, W.; Liu, J.; Chen, L. W., Contactless Probing of the Intrinsic Carrier Transport in Single-Walled Carbon Nanotubes. *Nano Res.* **2014**, *7*, 1623-1630.

(76) Shimotani, H.; Tsuda, S.; Yuan, H. T.; Yomogida, Y.; Moriya, R.; Takenobu, T.; Yanagi, K.; Iwasa, Y., Continuous Band-Filling Control and One-Dimensional Transport in Metallic and Semiconducting Carbon Nanotube Tangled Films. *Adv. Funct. Mater.* 2014, *24*, 3305-3311.
(77) Goh, P. S.; Ismail, A. F.; Ng, B. C., Directional Alignment of Carbon Nanotubes in Polymer Matrices: Contemporary Approaches and Future Advances *Compos. Part A Appl. Sci. Manuf.* 2014, *56*, 103-126.
(78) Durkop, T.; Getty, S. A.; Cobas, E.; Fuhrer, M. S., Extraordinary Mobility in Semiconducting Carbon Nanotubes. *Nano Lett.* 2004, *4*, 35-39.
(79) Zhou, X. J.; Park, J. Y.; Huang, S. M.; Liu, J.; McEuen, P. L., Band Structure, Phonon Scattering, and the Performance Limit of Single-Walled Carbon Nanotube Transistors. *Phys. Rev. Lett.* 2005, *95*, 146805.
(80) Arora, N. D.; Hauser, J. R.; Roulston, D. J., Electron and Hole Mobilities in Silicon as a Function of Concentration and Temperature. *IEEE Trans. Electron Devices* 1982, *29*, 292-295.
(81) Li, D. A.; Shao, Z. G.; Hao, Q.; Zhao, H. B., Intrinsic Carrier Mobility of a Single-Layer Graphene Covalently Bonded With Single-Walled Carbon Nanotubes. *J. Appl. Phys.* 2014, *115*, 233701.
(82) Bahk, Y. K.; He, X.; Gitsis, E.; Kuo, Y. Y.; Kim, N.; Wang, J., Enhanced Dispersion Stability and Mobility of Carboxyl-Functionalized Carbon Nanotubes in Aqueous Solutions through Strong Hydrogen Bonds. *J. Nanopart. Res.* 2015, *17*, 396.
(83) Hu, L. B.; Hecht, D. S.; Gruner, G., Infrared Transparent Carbon Nanotube Thin Films. *Appl. Phys. Lett.* 2009, *94*, 081103.
(84) Ferguson, A. J.; Dowgiallo, A. M.; Bindl, D. J.; Mistry, K. S.; Reid, O. G.; Kopidakis, N.; Arnold, M. S.; Blackburn, J. L., Trap-Limited Carrier Recombination in Single-Walled Carbon Nanotube Heterojunctions with Fullerene Acceptor Layers. *Phys. Rev. B* 2015, *91*, 245311
(85) Morozov, S. V.; Novoselov, K. S.; Katsnelson, M. I.; Schedin, F.; Elias, D. C.; Jaszczak, J. A.; Geim, A. K., Giant Intrinsic Carrier Mobilities in Graphene and Its Bilayer. *Phys. Rev. Lett.* 2008, *100*, 016602.
(86) Ding, Y. C.; Singh, V.; Goodman, S. M.; Nagpal, P., Low Exciton-Phonon Coupling, High Charge Carrier Mobilities, and Multiexciton Properties in Two-Dimensional Lead, Silver, Cadmium, and Copper Chalcogenide Nanostructures. *J. Phys. Chem. Lett.* 2014, *5*, 4291-4297.
(87) Yao, Z.; Kane, C. L.; Dekker, C., High-Field Electrical Transport in Single-Wall Carbon Nanotubes. *Phys. Rev. Lett.* 2000, *84*, 2941-2944.
(88) Subramaniam, C.; Yamada, T.; Kobashi, K.; Sekiguchi, A.; Futaba, D. N.; Yumura, M.; Hata, K., One Hundred Fold Increase in Current Carrying Capacity in a Carbon Nanotube-Copper Composite. *Nat. Commun.* 2013, *4*, 2202-2206.
(89) Fischer, J. E.; Dai, H.; Thess, A.; Lee, R.; Hanjani, N. M.; Dehaas, D. L.; Smalley, R. E., Metallic Resistivity in Crystalline Ropes of Single-Wall Carbon Nanotubes. *Phys. Rev. B* 1997, *55*, R4921-R4924.
(90) Panhuis, M. I. H., Carbon Nanotubes: Enhancing the Polymer Building Blocks for Intelligent Materials. *J. Mater. Chem.* 2006, *16*, 3598-3605.
(91) Mann, D.; Javey, A.; Kong, J.; Wang, Q.; Dai, H. J., Ballistic Transport in Metallic Nanotubes with Reliable Pd Ohmic Contacts. *Nano Lett.* 2003, *3*, 1541-1544.
(92) Chen, G. H.; Futaba, D. N.; Sakurai, S.; Yumura, M.; Hata, K., Interplay of Wall Number and Diameter on the Electrical Conductivity of Carbon Nanotube Thin Films. *Carbon* 2014, *67*, 318-325.
(93) Giancoli, D. C. *Physics: Principles with Applications*; Prentice Hall: London, 1995.
(94) Yong, Y. Q.; Yonezawa, T.; Matsubara, M.; Tsukamoto, H., The Mechanism of Alkylamine-Stabilized Copper Fine Particles Towards Improving the Electrical Conductivity of Copper Films at Low Sintering Temperature. *J. Mater. Chem. C* 2015, *3*, 5890-5895.
(95) Javey, A.; Kim, H.; Brink, M.; Wang, Q.; Ural, A.; Guo, J.; McIntyre, P.; McEuen, P.; Lundstrom, M.; Dai, H. J., High-Kappa Dielectrics for Advanced Carbon-Nanotube Transistors and Logic Gates. *Nat. Mater.* 2002, *1*, 241-246.
(96) Hu, L.; Hecht, D. S.; Gruner, G., Percolation in Transparent and Conducting Carbon Nanotube Networks. *Nano Lett.* 2004, *4*, 2513-2517.

(97) Qiu, C. G.; Zhang, Z. Y.; Zhong, D. L.; Si, J.; Yang, Y. J.; Peng, L. M., Carbon Nanotube Feedback-Gate Field-Effect Transistor: Suppressing Current Leakage and Increasing On/Off Ratio. *ACS Nano* 2015, *9*, 969-977.
(98) Xia, F. N.; Farmer, D. B.; Lin, Y. M.; Avouris, P., Graphene Field-Effect Transistors with High On/Off Current Ratio and Large Transport Band Gap at Room Temperature. *Nano Lett.* 2010, *10*, 715-718.
(99) Pop, E.; Mann, D.; Wang, Q.; Goodson, K. E.; Dai, H. J., Thermal Conductance of an Individual Single-Wall Carbon Nanotube above Room Temperature. *Nano Lett.* 2006, *6*, 96-100.
(100) Kim, P.; Shi, L.; Majumdar, A.; McEuen, P. L., Thermal Transport Measurements of Individual Multiwalled Nanotubes. *Phys. Rev. Lett.* 2001, *87*, 215502.
(101) Salaway, R. N.; Zhigilei, L. V., Molecular Dynamics Simulations of Thermal Conductivity of Carbon Nanotubes: Resolving the Effects of Computational Parameters. *Int. J. Heat Mass Tran.* 2014, *70*, 954-964.
(102) Wei, L. H.; Kuo, P. K.; Thomas, R. L.; Anthony, T. R.; Banholzer, W. F., Thermal-Conductivity of Isotopically Modified Single-Crystal Diamond. *Phys. Rev. Lett.* 1993, *70*, 3764-3767.
(103) Katcho, N. A.; Carrete, J.; Li, W.; Mingo, N., Effect of Nitrogen and Vacancy Defects on the Thermal Conductivity of Diamond: An Ab Initio Green's Function Approach. *Phys. Rev. B* 2014, *90*, 094117.
(104) Yu, M. F.; Lourie, O.; Dyer, M. J.; Moloni, K.; Kelly, T. F.; Ruoff, R. S., Strength and Breaking Mechanism of Multiwalled Carbon Nanotubes under Tensile Load. *Science* 2000, *287*, 637-640.
(105) Pan, Z. W.; Xie, S. S.; Lu, L.; Chang, B. H.; Sun, L. F.; Zhou, W. Y.; Wang, G.; Zhang, D. L., Tensile Tests of Ropes of Very Long Aligned Multiwall Carbon Nanotubes. *Appl. Phys. Lett.* 1999, *74*, 3152-3154.
(106) Poncharal, P.; Wang, Z. L.; Ugarte, D.; de Heer, W. A., Electrostatic Deflections and Electromechanical Resonances of Carbon Nanotubes. *Science* 1999, *283*, 1513-1516.
(107) Salvetat, J. P.; Briggs, G. A. D.; Bonard, J. M.; Bacsa, R. R.; Kulik, A. J.; Stockli, T.; Burnham, N. A.; Forro, L., Elastic and Shear Moduli of Single-Walled Carbon Nanotube Ropes. *Phys. Rev. Lett.* 1999, *82*, 944-947.
(108) Treacy, M. M. J.; Ebbesen, T. W.; Gibson, J. M., Exceptionally High Young's Modulus Observed for Individual Carbon Nanotubes. *Nature* 1996, *381*, 678-680.
(109) Khang, D. Y.; Xiao, J. L.; Kocabas, C.; MacLaren, S.; Banks, T.; Jiang, H. Q.; Huang, Y. Y. G.; Rogers, J. A., Molecular Scale Buckling Mechanics on Individual Aligned Single-Wall Carbon Nanotubes on Elastomeric Substrates. *Nano Lett.* 2008, *8*, 124-130.
(110) Zhou, P.; Yang, X.; He, L.; Hao, Z. M.; Luo, W.; Xiong, B.; Xu, X.; Niu, C. J.; Yan, M. Y.; Mai, L. Q., The Young's Modulus of High-Aspect-Ratio Carbon/Carbon Nanotube Composite Microcantilevers by Experimental and Modeling Validation. *Appl. Phys. Lett.* 2015, *106*, 111908
(111) Szuecs, F.; Werner, M.; Sussmann, R. S.; Pickles, C. S. J.; Fecht, H. J., Temperature Dependence of Young's Modulus and Degradation of Chemical Vapor Deposited Diamond. *J. Appl. Phys.* 1999, *86*, 6010-6017.
(112) Yu, M. F.; Files, B. S.; Arepalli, S.; Ruoff, R. S., Tensile Loading of Ropes of Single Wall Carbon Nanotubes and Their Mechanical Properties. *Phys. Rev. Lett.* 2000, *84*, 5552-5555.
(113) Walters, D. A.; Ericson, L. M.; Casavant, M. J.; Liu, J.; Colbert, D. T.; Smith, K. A.; Smalley, R. E., Elastic Strain of Freely Suspended Single-Wall Carbon Nanotube Ropes. *Appl. Phys. Lett.* 1999, *74*, 3803-3805.
(114) Viet, N. V.; Kuo, W. S., Stress Distribution in Carbon Nanotubes with Bending Fracture. *Eng. Fract. Mech.* 2015, *136*, 158-171.
(115) Wong, E. W.; Sheehan, P. E.; Lieber, C. M., Nanobeam Mechanics: Elasticity, Strength, and Toughness of Nanorods and Nanotubes. *Science* 1997, *277*, 1971-1975.
(116) Chakraborti, P. C.; Kundu, A.; Dutta, B. K., Weibull Analysis of Low Temperature Fracture Stress Data of 20mnmoni55 and SA333 (Grade 6) Steels. *Mat. Sci. Eng. A-Struct.* 2014, *594*, 89-97.
(117) Cinke, M.; Li, J.; Chen, B.; Cassell, A.; Delzeit, L.; Han, J.; Meyyappan, M., Pore Structure of Raw and Purified HiPco Single-Walled Carbon Nanotubes. *Chem. Phys. Lett.* 2002, *365*, 69-74.
(118) Kim, K. H.; Oh, Y.; Islam, M. F., Mechanical and Thermal Management Characteristics of Ultrahigh Surface Area Single-Walled Carbon Nanotube Aerogels. *Adv. Funct. Mater.* 2013, *23*, 377-383.
(119) Barbieri, O.; Hahn, M.; Herzog, A.; Kotz, R., Capacitance Limits of High Surface Area Activated Carbons for Double Layer Capacitors. *Carbon* 2005, *43*, 1303-1310.

(120) Li, D. W.; Tian, Y. Y.; Qiao, Y. Y.; Wen, L., Conversion of Powdered Active Carbon into Monoliths without Reducing Specific Surface Area Using H3PO4-Impregnated Waste Sawdust. *Mater. Lett.* 2014, *125*, 175-178.
(121) Ellmer, K., Past Achievements and Future Challenges in the Development of Optically Transparent Electrodes. *Nat. Photonics* 2012, *6*, 809-817.
(122) De, S.; King, P. J.; Lyons, P. E.; Khan, U.; Coleman, J. N., Size Effects and the Problem with Percolation in Nanostructured Transparent Conductors. *ACS Nano* 2010, *4*, 7064-7072.
(123) Ruzicka, B.; Degiorgi, L.; Gaal, R.; Thien-Nga, L.; Bacsa, R.; Salvetat, J. P.; Forro, L., Optical and DC Conductivity Study of Potassium-Doped Single-Walled Carbon Nanotube Films. *Phys. Rev. B* 2000, *61*, R2468-R2471.
(124) Feng, C.; Liu, K.; Wu, J. S.; Liu, L.; Cheng, J. S.; Zhang, Y. Y.; Sun, Y. H.; Li, Q. Q.; Fan, S. S.; Jiang, K. L., Flexible, Stretchable, Transparent Conducting Films Made from Superaligned Carbon Nanotubes. *Adv. Funct. Mater.* 2010, *20*, 885-891.
(125) Bae, S.; Kim, S. J.; Shin, D.; Ahn, J. H.; Hong, B. H., Towards Industrial Applications of Graphene Electrodes. *Phys. Scr.* 2012, *T146*, 014024.
(126) Rowell, M. W.; McGehee, M. D., Transparent Electrode Requirements for Thin Film Solar Cell Modules. *Energy Environ. Sci.* 2011, *4*, 131-134.
(127) Lee, J.; Cole, M. T.; Lai, J. C. S.; Nathan, A., An Analysis of Electrode Patterns in Capacitive Touch Screen Panels. *J. Display Technol.* 2014, *10*, 362-366.
(128) Silveira, A. V. M.; Fuchs, M. S.; Pinheiro, D. K.; Tanabe, E. H.; Bertuol, D. A., Recovery of Indium from LCD Screens of Discarded Cell Phones. *Waste Manage.* 2015, *45*, 334-342.
(129) Thejokalyani, N.; Dhoble, S. J., Novel Approaches for Energy Efficient Solid State Lighting by RGB Organic Light Emitting Diodes - A Review. *Renew. Sust. Energ. Rev.* 2014, *32*, 448-467.
(130) Jariwala, D.; Sangwan, V. K.; Lauhon, L. J.; Marks, T. J.; Hersam, M. C., Carbon Nanomaterials for Electronics, Optoelectronics, Photovoltaics, and Sensing. *Chem. Soc. Rev.* 2013, *42*, 2824-2860.
(131) Han, J.; Yuan, S.; Liu, L.; Qiu, X.; Gong, H.; Yang, X.; Li, C.; Hao, Y.; Cao, B., Fully Indium-Free Flexible Ag Nanowires/ZnO:F Composite Transparent Conductive Electrodes with High Haze. *J. Mater. Chem. A* 2015, *3*, 5375-5384.
(132) Li, J.; Hu, L.; Wang, L.; Zhou, Y.; Gruner, G.; Marks, T. J., Organic Light-Emitting Diodes Having Carbon Nanotube Anodes. *Nano Lett.* 2006, *6*, 2472-2477.
(133) Huang, J. R.; Mao, C.; Zhu, Y. T.; Jiang, W.; Yang, X. D., Control of Carbon Nanotubes at the Interface of a Co-Continuous Immiscible Polymer Blend to Fabricate Conductive Composites with Ultralow Percolation Thresholds. *Carbon* 2014, *73*, 267-274.
(134) Ameli, A.; Nofar, M.; Park, C. B.; Potschke, P.; Rizvi, G., Polypropylene/Carbon Nanotube Nano/Microcellular Structures with High Dielectric Permittivity, Low Dielectric Loss, and Low Percolation Threshold. *Carbon* 2014, *71*, 206-217.
(135) Harris, J. M.; Huh, J. Y.; Semler, M. R.; Ihle, T.; Stafford, C. M.; Hudson, S. D.; Fagan, J. A.; Hobbie, E. K., Elasticity and Rigidity Percolation in Flexible Carbon Nanotube Films on PDMS Substrates. *Soft Matter* 2013, *9*, 11568-11575.
(136) Saravanan, M.; Sennu, P.; Ganesan, M.; Ambalavanan, S., Multi-Walled Carbon Nanotubes Percolation Network Enhanced the Performance of Negative Electrode for Lead-Acid Battery. *J. Electrochem. Soc.* 2013, *160*, A70-A76.
(137) Tian, X. J.; Moser, M. L.; Pekker, A.; Sarkar, S.; Ramirez, J.; Bekyarova, E.; Itkis, M. E.; Haddon, R. C., Effect of Atomic Interconnects on Percolation in Single-Walled Carbon Nanotube Thin Film Networks. *Nano Lett.* 2014, *14*, 3930-3937.
(138) Wang, Y.; Weng, G. J.; Meguid, S. A.; Hamouda, A. M., A Continuum Model with a Percolation Threshold and Tunneling-Assisted Interfacial Conductivity for Carbon Nanotube-Based Nanocomposites. *J. Appl. Phys.* 2014, *115*, 193706.

(139) Simien, D.; Fagan, J. A.; Luo, W.; Douglas, J. F.; Migler, K.; Obrzut, J., Influence of Nanotube Length on the Optical and Conductivity Properties of Thin Single-Wall Carbon Nanotube Networks. *ACS Nano* **2008**, *2*, 1879-1884.
(140) Du, F. M.; Fischer, J. E.; Winey, K. I., Effect of Nanotube Alignment on Percolation Conductivity in Carbon Nanotube/Polymer Composites. *Phys. Rev. B* **2005**, *72*, 121404.
(141) Balberg, I.; Binenbaum, N., Computer Study of the Percolation-Threshold in a Two-Dimensional Anisotropic System of Conducting Sticks. *Phys. Rev. B* **1983**, *28*, 3799-3812.
(142) Kim, D. H.; Jin, J. E.; Piao, M.; Choi, J. H.; Kim, G. T., Electrical Percolation Characteristics of Metallic Single-Walled Carbon Nanotube Networks by Vacancy Evolution. *Phys. Chem. Chem. Phys.* **2014**, *16*, 18370-18374.
(143) Prikhod'ko, A. V.; Kon'kov, O. I., Modification of the Structure and Percolation of Current in an Array of Single-Walled Carbon Nanotubes. *Phys. Solid State* **2014**, *56*, 1463-1466.
(144) Jang, H. K.; Jin, J. E.; Choi, J. H.; Kang, P. S.; Kim, D. H.; Kim, G. T., Electrical Percolation Thresholds of Semiconducting Single-Walled Carbon Nanotube Networks in Field-Effect Transistors. *Phys. Chem. Chem. Phys.* **2015**, *17*, 6874-6880.
(145) Unalan, H. E.; Fanchini, G.; Kanwal, A.; Du Pasquier, A.; Chhowalla, M., Design Criteria for Transparent Single-Wall Carbon Nanotube Thin-Film Transistors. *Nano Lett.* **2006**, *6*, 677-682.
(146) Behnam, A.; Noriega, L.; Choi, Y.; Wu, Z. C.; Rinzler, A. G.; Ural, A., Resistivity Scaling in Single-Walled Carbon Nanotube Films Patterned to Submicron Dimensions. *Appl. Phys. Lett.* **2006**, *89*, 093107.
(147) Kiran, M.; Ramamurty, U.; Misra, A., Mechanical and Electrical Contact Resistance Characteristics of a Cellular Assembly of Carbon Nanotubes. *Nanotechnology* **2013**, *24*, 015707.
(148) Mitchell, R. R.; Yamamoto, N.; Cebeci, H.; Wardle, B. L.; Thompson, C. V., A Technique for Spatially-Resolved Contact Resistance-Free Electrical Conductivity Measurements of Aligned-Carbon Nanotube/Polymer Nanocomposites. *Compos. Sci. Technol.* **2013**, *74*, 205-210.
(149) Franklin, A. D.; Farmer, D. B.; Haensch, W., Defining and Overcoming the Contact Resistance Challenge in Scaled Carbon Nanotube Transistors. *ACS Nano* **2014**, *8*, 7333-7339.
(150) Hecht, D.; Hu, L. B.; Gruner, G., Conductivity Scaling with Bundle Length and Diameter in Single Walled Carbon Nanotube Networks. *Appl. Phys. Lett.* **2006**, *89*, 133112.
(151) Shin, D. H.; Shim, H. C.; Song, J. W.; Kim, S.; Hana, C. S., Conductivity of Films Made from Single-Walled Carbon Nanotubes in Terms of Bundle Diameter. *Scr. Mater.* **2009**, *60*, 607-610.
(152) Geng, H. Z.; Kim, K. K.; Lee, K.; Kim, G. Y.; Choi, H. K.; Lee, D. S.; An, K. H.; Lee, Y. H.; Chang, Y.; Lee, Y. S.; Kim, B.; Lee, Y. J., Dependence of Material Quality on Performance of Flexible Transparent Conducting Films with Single-Walled Carbon Nanotubes. *Nano* **2007**, *2*, 157-167.
(153) Kaempgen, M.; Duesberg, G. S.; Roth, S., Transparent Carbon Nanotube Coatings. *Appl. Surf. Sci.* **2005**, *252*, 425-429.
(154) Geng, H. Z.; Lee, D. S.; Kim, K. K.; Kim, S. J.; Bae, J. J.; Lee, Y. H., Effect of Carbon Nanotube Types in Fabricating Flexible Transparent Conducting Films. *J. Korean Phys. Soc.* **2008**, *53*, 979-985.
(155) Grace, T.; Yu, L.; Gibson, C.; Tune, D.; Alturaif, H.; Al Othman, Z.; Shapter, J., Investigating the Effect of Carbon Nanotube Diameter and Wall Number in Carbon Nanotube/Silicon Heterojunction Solar Cells. *Nanomaterials* **2016**, *6*, 52.
(156) Hou, P. X.; Yu, B.; Su, Y.; Shi, C.; Zhang, L. L.; Liu, C.; Li, S. S.; Du, J. H.; Cheng, H. M., Double-wall Carbon Nanotube Transparent Conductive Films with Excellent Performance. *J. Mater. Chem. A* **2014**, *2*, 1159-1164.
(157) Xu, G. H.; Huang, J. Q.; Zhang, Q.; Zhao, M. Q.; Wei, F., Fabrication of Double- and Multi-walled Carbon Nanotube Transparent Conductive Films by Filtration-transfer Process and Their Property Improvement by Acid Treatment. *Appl. Phys. A: Mater. Sci. Process.* **2011**, *103*, 403-411.

(158) De Nicola, F.; Salvato, M.; Cirillo, C.; Crivellari, M.; Boscardin, M.; Scarselli, M.; Nanni, F.; Cacciotti, I.; De Crescenzi, M.; Castrucci, P., Record Efficiency of Air-stable Multi-walled Carbon Nanotube/Silicon Solar Cells. *Carbon* 2016, *101*, 226-234.
(159) Parekh, B. B.; Fanchini, G.; Eda, G.; Chhowalla, M., Improved Conductivity of Transparent Single-Wall Carbon Nanotube Thin Films via Stable Postdeposition Functionalization. *Appl. Phys. Lett.* 2007, *90*, 121913.
(160) Sarkar, S. K.; Jha, A.; Chattopadhyay, K. K., Thionyl Chloride Assisted Functionalization of Amorphous Carbon Nanotubes: A Better Field Emitter and Stable Nanofluid with Better Thermal Conductivity. *Mater. Res. Bull.* 2015, *66*, 1-8.
(161) Kaskela, A.; Nasibulin, A. G.; Timmermans, M. Y.; Aitchison, B.; Papadimitratos, A.; Tian, Y.; Zhu, Z.; Jiang, H.; Brown, D. P.; Zakhidov, A.; Kauppinen, E. I., Aerosol-Synthesized SWCNT Networks with Tunable Conductivity and Transparency by a Dry Transfer Technique. *Nano Lett.* 2010, *10*, 4349-4355.
(162) Tune, D. D.; Blanch, A. J.; Shearer, C. J.; Moore, K. E.; Pfohl, M.; Shapter, J. G.; Flavel, B. S., Aligned Carbon Nanotube Thin Films from Liquid Crystal Polyelectrolyte Inks. *ACS Appl. Mater. Interfaces* 2015, *7*, 25857-25864.
(163) Tune, D. D.; Shapter, J. G., Effect of Nanotube Film Thickness on the Performance of Nanotube-Silicon Hybrid Solar Cells. *Nanomaterials* 2013, *3*, 655-673.
(164) Jackson, R. K.; Munro, A.; Nebesny, K.; Armstrong, N.; Graham, S., Evaluation of Transparent Carbon Nanotube Networks of Homogeneous Electronic Type. *ACS Nano* 2010, *4*, 1377-1384.
(165) McEuen, P. L.; Park, J. Y., Electron Transport in Single-Walled Carbon Nanotubes. *MRS Bull.* 2004, *29*, 272-275.
(166) Yang, S. B.; Kong, B. S.; Jung, D. H.; Baek, Y. K.; Han, C. S.; Oh, S. K.; Jung, H. T., Recent Advances in Hybrids of Carbon Nanotube Network Films and Nanomaterials for Their Potential Applications as Transparent Conducting Films. *Nanoscale* 2011, *3*, 1361-1373.
(167) Dehghani, S.; Moravvej-Farshi, M. K.; Sheikhi, M. H., Compact Formulas for the Electrical Resistance of Semiconducting and Metallic Single Wall Carbon Nanotubes. *Fuller Nanotube Car. N.* 2015, *23*, 899-905.
(168) Yao, Z.; Postma, H. W. C.; Balents, L.; Dekker, C., Carbon Nanotube Intramolecular Junctions. *Nature* 1999, *402*, 273-276.
(169) Farajian, A. A.; Esfarjani, K.; Kawazoe, Y., Nonlinear Coherent Transport through Doped Nanotube Junctions. *Phys. Rev. Lett.* 1999, *82*, 5084-5087.
(170) Barboza, A. P. M.; Carara, S. S.; Batista, R. J. C.; Chacham, H.; Neves, B. R. A., Controlling the Electrical Behavior of Semiconducting Carbon Nanotubes via Tube Contact. *Small* 2012, *8*, 220-224.
(171) Xu, F. B.; Sadrzadeh, A.; Xu, Z. P.; Yakobson, B. I., Can Carbon Nanotube Fibers Achieve the Ultimate Conductivity?-Coupled-Mode Analysis for Electron Transport through the Carbon Nanotube Contact. *J. Appl. Phys.* 2013, *114*, 063714.
(172) Topinka, M. A.; Rowell, M. W.; Goldhaber-Gordon, D.; McGehee, M. D.; Hecht, D. S.; Gruner, G., Charge Transport in Interpenetrating Networks of Semiconducting and Metallic Carbon Nanotubes. *Nano Lett.* 2009, *9*, 1866-1871.
(173) Yanagi, K.; Udoguchi, H.; Sagitani, S.; Oshima, Y.; Takenobu, T.; Kataura, H.; Ishida, T.; Matsuda, K.; Maniwa, Y., Transport Mechanisms in Metallic and Semiconducting Single-Wall Carbon Nanotube Networks. *ACS Nano* 2010, *4*, 4027-4032.
(174) Sarker, B. K.; Kang, N.; Khondaker, S. I., High Performance Semiconducting Enriched Carbon Nanotube Thin Film Transistors Using Metallic Carbon Nanotubes as Electrodes. *Nanoscale* 2014, *6*, 4896-4902.
(175) Kim, P.; Odom, T. W.; Huang, J. L.; Lieber, C. M., Electronic Density of States of Atomically Resolved Single-Walled Carbon Nanotubes: van Hove Singularities and End States. *Phys. Rev. Lett.* 1999, *82*, 1225-1228.
(176) Zhang, L. X.; Chen, A. Q.; Shao, Q. Y., Effects of Boron/Phosphorus Co-Doping in Metallic Single-Walled Carbon Nanotubes. *Phys. Scr.* 2012, *85*, 045701.

(177) Park, Y. R.; Ko, M. J.; Song, Y. H.; Lee, C. J., Surface Electronic Structure of Nitrogen-Doped Semiconducting Single-Walled Carbon Nanotube Networks. *J. Appl. Phys.* 2013, *114*, 153516.
(178) Prudkovskiy, V.; Berd, M.; Pavlenko, E.; Katin, K.; Maslov, M.; Puech, P.; Monthioux, M.; Escoffier, W.; Goiran, M.; Raquet, B., Electronic Coupling in Fullerene-Doped Semiconducting Carbon Nanotubes Probed by Raman Spectroscopy and Electronic Transport. *Carbon* 2013, *57*, 498-506.
(179) Kim, D. H.; Lee, S. Y.; Jin, J. E.; Kim, G. T.; Lee, D. J., Electrical Conductivity Enhancement of Metallic Single-Walled Carbon Nanotube Networks by CoO Decoration. *Phys. Chem. Chem. Phys.* 2014, *16*, 6980-6985.
(180) Journet, C.; Picher, M.; Jourdain, V., Carbon Nanotube Synthesis: From Large-Scale Production to Atom-By-Atom Growth. *Nanotechnology* 2012, *23*, 142001.
(181) Segawa, Y.; Yagi, A.; Matsui, K.; Itami, K., Design and Synthesis of Carbon Nanotube Segments. *Angew. Chem.-Int. Edit.* 2016, *55*, 5136-5158.
(182) Fujisawa, K.; Kim, H. J.; Go, S. H.; Muramatsu, H.; Hayashi, T.; Endo, M.; Hirschmann, T. C.; Dresselhaus, M. S.; Kim, Y. A.; Araujo, P. T., A Review of Double-Walled and Triple-Walled Carbon Nanotube Synthesis and Applications. *Appl. Sci.* 2016, *6*, UNSP 109.
(183) Yang, F.; Wang, X.; Li, M. H.; Liu, X. Y.; Zhao, X. L.; Zhang, D. Q.; Zhang, Y.; Yang, J.; Li, Y., Templated Synthesis of Single-Walled Carbon Nanotubes with Specific Structure. *Accounts Chem. Res.* 2016, *49*, 606-615.
(184) Shah, K. A.; Tali, B. A., Synthesis of Carbon Nanotubes by Catalytic Chemical Vapour Deposition: A Review on Carbon Sources, Catalysts and Substrates. *Mater. Sci. Semicond. Process.* 2016, *41*, 67-82.
(185) Mittal, G.; Dhand, V.; Rhee, K. Y.; Kim, H. J.; Jung, D. H., Carbon Nanotubes Synthesis Using Diffusion and Premixed Flame Methods: A Review. *Carbon Lett.* 2015, *16*, 1-10.
(186) Yan, Y. B.; Miao, J. W.; Yang, Z. H.; Xiao, F. X.; Yang, H. B.; Liu, B.; Yang, Y. H., Carbon Nanotube Catalysts: Recent Advances in Synthesis, Characterization and Applications. *Chem. Soc. Rev.* 2015, *44*, 3295-3346.
(187) Arora, N.; Sharma, N. N., Arc Discharge Synthesis of Carbon Nanotubes: Comprehensive Review. *Diamond Relat. Mater.* 2014, *50*, 135-150.
(188) Danilov, P. A.; Ionin, A. A.; Kudryashov, S. I.; Makarov, S. V.; Mel'nik, N. N.; Rudenko, A. A.; Yurovskikh, V. I.; Zayarny, D. V.; Lednev, V. N.; Obraztsova, E. D.; Pershin, S. M.; Bunkin, A. F., Femtosecond Laser Ablation of Single-Wall Carbon Nanotube-Based Material. *Laser Phys. Lett.* 2014, *11*, 106101.
(189) Arutyunyan, N. R.; Komlenok, M. S.; Kononenko, V. V.; Pashinin, V. P.; Pozharov, A. S.; Konov, V. I.; Obraztsova, E. D., Resonant Ablation of Single-Wall Carbon Nanotubes by Femtosecond Laser Pulses. *Laser Phys.* 2015, *25*, 015902.
(190) Yousefi, A. T.; Bagheri, S.; Kadri, N. A.; Mahmood, M. R.; Ikeda, S., Controlling Vaporization Time as Effective Parameter on Purified Vertically Aligned Carbon Nanotubes Based on CVD Method. *Fuller Nanotube Car. N.* 2015, *23*, 1103-1107.
(191) Jourdain, V.; Bichara, C., Current Understanding of the Growth of Carbon Nanotubes in Catalytic Chemical Vapour Deposition. *Carbon* 2013, *58*, 2-39.
(192) Fu, X.; Cui, X. Z.; Wei, X. H.; Ma, J. N., Investigation of Low and Mild Temperature for Synthesis of High Quality Carbon Nanotubes by Chemical Vapor Deposition. *Appl. Surf. Sci.* 2014, *292*, 645-649.
(193) Sun, Y.; Kitaura, R.; Zhang, J. Y.; Miyata, Y.; Shinohara, H., Metal Catalyst-Free Mist Flow Chemical Vapor Deposition Growth of Single-Wall Carbon Nanotubes Using C-60 Colloidal Solutions. *Carbon* 2014, *68*, 80-86.
(194) De Volder, M. F. L.; Tawfick, S. H.; Baughman, R. H.; Hart, A. J., Carbon Nanotubes: Present and Future Commercial Applications. *Science* 2013, *339*, 535-539.
(195) "Carbon Nanotubes (CNT) Market Analysis by Product (Single Walled Carbon Nanotubes (SWCNT), Multi Walled Carbon Nanotubes (MWCNT)), by Application (Polymers, Energy, Electrical & Electronics) and Segment Forecasts to 2022," 2015.

(196) Kang, L. X.; Hu, Y.; Liu, L. L.; Wu, J. X.; Zhang, S. C.; Zhao, Q. C.; Ding, F.; Li, Q. W.; Zhang, J., Growth of Close-Packed Semiconducting Single-Walled Carbon Nanotube Arrays Using Oxygen-Deficient TiO2 Nanoparticles as Catalysts. *Nano Lett.* 2015, *15*, 403-409.
(197) Fouquet, M.; Bayer, B. C.; Esconjauregui, S.; Thomsen, C.; Hofmann, S.; Robertson, J., Effect of Catalyst Pretreatment on Chirality-Selective Growth of Single-Walled Carbon Nanotubes. *J. Phys. Chem. C* 2014, *118*, 5773-5781.
(198) Zhong, G. F.; Xie, R. S.; Yang, J. W.; Robertson, J., Single-Step CVD Growth of High-Density Carbon Nanotube Forests on Metallic Ti Coatings through Catalyst Engineering. *Carbon* 2014, *67*, 680-687.
(199) Cartwright, R.; Esconjauregui, S.; Hardeman, D.; Bhardwaj, S.; Weatherup, R.; Guo, Y.; D'Arsie, L.; Bayer, B.; Kidambi, P.; Hofmann, S.; Wright, E.; Clarke, J.; Oakes, D.; Cepek, C.; Robertson, J., Low Temperature Growth of Carbon Nanotubes on Tetrahedral Amorphous Carbon Using Fe-Cu Catalyst. *Carbon* 2015, *81*, 639-649.
(200) Anoshkin, I. V.; Nasibulin, A. G.; Tian, Y.; Liu, B.; Jiang, H.; Kauppinen, E. I., Hybrid Carbon Source for Single-Walled Carbon Nanotube Synthesis by Aerosol CVD Method. *Carbon* 2014, *78*, 130-136.
(201) Kozawa, A.; Kiribayashi, H.; Ogawa, S.; Saida, T.; Naritsuka, S.; Maruyama, T., Single-Walled Carbon Nanotube Growth on SiO2/Si Using Rh Catalysts by Alcohol Gas Source Chemical Vapor Deposition. *Diamond Relat. Mater.* 2016, *63*, 159-164.
(202) Kozawa, A.; Saida, T.; Naritsuka, S.; Maruyama, T., Synthesis of Single-Walled Carbon Nanotubes from Pd Catalysts by Gas Source Method Using Ethanol in High Vacuum. *Jpn. J. Appl. Phys.* 2016, *55*, 01AE02.
(203) Zhang, Z.; Mu, S. C.; Zhang, B. W.; Tao, L.; Huang, S. F.; Huang, Y. Z.; Gao, F. M.; Zhao, Y. F., A Novel Synthesis of Carbon Nanotubes Directly From an Indecomposable Solid Carbon Source for Electrochemical Applications. *J. Mater. Chem. A* 2016, *4*, 2137-2146.
(204) Liu, Y. C.; Che, J. T.; Ren, J. H. In *Advances in Textile Engineering and Materials Iv*; Liu, H., Kuroda, S. I., Zheng, L., Eds., 2014; Vol. 1048.
(205) Zhang, S.; Qin, L.; Song, H. H.; Chen, X. H.; Zhou, J. S.; Ma, Z. K., From Solid Carbon Sources to Carbon Nanotubes: A General Water-Assisted Approach. *RSC Adv.* 2014, *4*, 54244-54248.
(206) Lopez, D.; Abe, I. Y.; Pereyra, I., Temperature Effect on the Synthesis of Carbon Nanotubes and Core-Shell Ni Nanoparticle by Thermal CVD. *Diamond Relat. Mater.* 2015, *52*, 59-65.
(207) Woo, D. J.; Hooper, J. P.; Osswald, S.; Bottolfson, B. A.; Brewer, L. N., Low Temperature Synthesis of Carbon Nanotube-Reinforced Aluminum Metal Composite Powders Using Cryogenic Milling. *J. Mater. Res.* 2014, *29*, 2644-2656.
(208) Jiang, Y. Q.; Xi, J.; Wu, Z. X.; Dong, H.; Zhao, Z. X.; Jiao, B.; Hou, X., Highly Transparent, Conductive, Flexible Resin Films Embedded with Silver Nanowires. *Langmuir* 2015, *31*, 4950-4957.
(209) Sridhar, V.; Lee, I.; Chun, H. H.; Park, H., Microwave Synthesis of Nitrogen-Doped Carbon Nanotubes Anchored on Graphene Substrates. *Carbon* 2015, *87*, 186-192.
(210) Cui, R. X.; Pan, L. J.; Li, D. W.; Ma, H.; Peng, W., Controlled Synthesis of Carbon Nanocoils and Carbon Nanotubes on Common Paper Substrates. *Carbon* 2014, *76*, 455-458.
(211) Zhao, W.; Basnet, B.; Kim, S.; Kim, I. J., Synthesis of Vertically Aligned Carbon Nanotubes on Silicalite-1 Monolayer-Supported Substrate. *J. Nanomater.* 2014, 327398.
(212) Yamagiwa, K.; Ayato, Y.; Kuwano, J., Liquid-Phase Synthesis of Highly Aligned Carbon Nanotubes on Preheated Stainless Steel Substrates. *Carbon* 2016, *98*, 225-231.
(213) Shanbedi, M.; Hens, S. Z.; Amiri, A.; Hosseinipour, E.; Eshghi, H.; Kazi, S. N., Synthesis of Aspartic Acid-Treated Multi-Walled Carbon Nanotubes Based Water Coolant and Experimental Investigation of Thermal and Hydrodynamic Properties in Circular Tube. *Energ. Convers. Manage.* 2015, *105*, 1366-1376.
(214) Homenick, C. M.; Rousina-Webb, A.; Cheng, F.; Jakubinek, M. B.; Malenfant, P. R. L.; Simard, B., High-Yield, Single-Step Separation of Metallic and Semiconducting SWCNTs Using Block Copolymers at Low Temperatures. *J. Phys. Chem. C* 2014, *118*, 16156-16164.

(215) Rohringer, P.; Shi, L.; Liu, X. J.; Yanagi, K.; Pichler, T., Purification, Separation and Extraction of Inner Tubes from Double-Walled Carbon Nanotubes by Tailoring Density Gradient Ultracentrifugation Using Optical Probes. *Carbon* **2014**, *74*, 282-290.
(216) Cambre, S.; Muyshondt, P.; Federicci, R.; Wenseleers, W., Chirality-Dependent Densities of Carbon Nanotubes by in situ 2D Fluorescence-Excitation and Raman Characterisation in a Density Gradient after Ultracentrifugation. *Nanoscale* **2015**, *7*, 20015-20024.
(217) Scharfenberg, L.; Mertig, M., Semiconducting Enrichment of Arc Discharge Single-Walled Carbon Nanotubes by Density Gradient Ultracentrifugation. *Phys. Status Solidi A-Appl. Mat.* **2015**, *212*, 1395-1398.
(218) Moore, K. E.; Pfohl, M.; Hennrich, F.; Chakradhanula, V. S. K.; Kuebel, C.; Kappes, M. M.; Shapter, J. G.; Krupke, R.; Flavel, B. S., Separation of Double-Walled Carbon Nanotubes by Size Exclusion Column Chromatography. *ACS Nano* **2014**, *8*, 6756-6764.
(219) Zheng, M.; Jagota, A.; Semke, E. D.; Diner, B. A.; McLean, R. S.; Lustig, S. R.; Richardson, R. E.; Tassi, N. G., DNA-assisted dispersion and separation of carbon nanotubes. *Nat. Mater.* **2003**, *2*, 338-342.
(220) Chen, Y.; Zhang, J., Chemical Vapor Deposition Growth of Single-Walled Carbon Nanotubes with Controlled Structures for Nanodevice Applications. *Accounts Chem. Res.* **2014**, *47*, 2273-2281.
(221) Takase, M.; Ajiki, H.; Mizumoto, Y.; Komeda, K.; Nara, M.; Nabika, H.; Yasuda, S.; Ishihara, H.; Murakoshi, K., Selection-Rule Breakdown in Plasmon-Induced Electronic Excitation of an Isolated Single-Walled Carbon Nanotube. *Nat. Photonics* **2013**, *7*, 550-554.
(222) Otsuka, K.; Inoue, T.; Chiashi, S.; Maruyama, S., Selective Removal of Metallic Single-Walled Carbon Nanotubes in Full Length by Organic Film-Assisted Electrical Breakdown. *Nanoscale* **2014**, *6*, 8831-8835.
(223) Li, S. S.; Sakurai, S.; Futaba, D. N.; Hata, K., Breakdown of Metallic Single-Wall Carbon Nanotube Paths by NiO Nanoparticle Point Etching for High Performance Thin Film Transistors. *Nanoscale* **2015**, *7*, 1280-1284.
(224) Zhang, G.; Qi, P.; Wang, X.; Lu, Y.; Li, X.; Tu, R.; Bangsaruntip, S.; Mann, D.; Zhang, L.; Dai, H., Selective Etching of Metallic Carbon Nanotubes by Gas-Phase Reaction. *Science* **2006**, *314*, 974-977.
(225) Naieni, A. K.; Nojeh, A., Effect of Solution Conductivity and Electrode Shape on the Deposition of Carbon Nanotubes from Solution Using Dielectrophoresis. *Nanotechnology* **2012**, *23*, 495606
(226) Li, W. S.; Pyatkov, F.; Dehm, S.; Flavel, B. S.; Krupke, R., Deposition of Semiconducting Single-Walled Carbon Nanotubes Using Light-Assisted Dielectrophoresis. *Phys. Status Solidi B* **2014**, *251*, 2475-2479.
(227) Ao, G. Y.; Khripin, C. Y.; Zheng, M., DNA-Controlled Partition of Carbon Nanotubes in Polymer Aqueous Two-Phase Systems. *J. Am. Chem. Soc.* **2014**, *136*, 10383-10392.
(228) Cao, Z. Y.; Wei, B. Q., A Perspective: Carbon Nanotube Macro-Films for Energy Storage. *Energy Environ. Sci.* **2013**, *6*, 3183-3201.
(229) Ko, W. Y.; Lin, K. J., Highly Conductive, Transparent Flexible Films Based on Metal Nanoparticle-Carbon Nanotube Composites. *J. Nanomater.* **2013**, 505292.
(230) Wu, Y. C.; Lin, X. N.; Zhang, M., Carbon Nanotubes for Thin Film Transistor: Fabrication, Properties, and Applications. *J. Nanomater.* **2013**, 627215.
(231) Kanoun, O.; Muller, C.; Benchirouf, A.; Sanli, A.; Dinh, T. N.; Al-Hamry, A.; Bu, L.; Gerlach, C.; Bouhamed, A., Flexible Carbon Nanotube Films for High Performance Strain Sensors. *Sensors* **2014**, *14*, 10042-10071.
(232) Chen, H. Y.; Zeng, S.; Chen, M. H.; Zhang, Y. Y.; Li, Q. W., Fabrication and Functionalization of Carbon Nanotube Films for High-Performance Flexible Supercapacitors. *Carbon* **2015**, *92*, 271-296.
(233) Nasibulin, A. G.; Kaskela, A.; Mustonen, K.; Anisimov, A. S.; Ruiz, V.; Kivisto, S.; Rackauskas, S.; Timmermans, M. Y.; Pudas, M.; Aitchison, B.; Kauppinen, M.; Brown, D. P.; Okhotnikov, O. G.; Kauppinen, E. I., Multifunctional Free-Standing Single-Walled Carbon Nanotube Films. *ACS Nano* **2011**, *5*, 3214-3221.
(234) Arod, P.; Shivashankar, S. A., Single-Step Synthesis of Carbon Nanotubes/Iron/Iron Oxide Composite Films through Inert-Ambient CVD Using Ferric Acetylacetonate as a Precursor. *RSC Adv.* **2015**, *5*, 59463-59471.

(235) Kiriya, D.; Chen, K.; Ota, H.; Lin, Y. J.; Zhao, P. D.; Yu, Z. B.; Ha, T. J.; Javey, A., Design of Surfactant-Substrate Interactions for Roll-to-Roll Assembly of Carbon Nanotubes for Thin-Film Transistors. *J. Am. Chem. Soc.* 2014, *136*, 11188-11194.
(236) Koo, H.; Lee, W.; Choi, Y.; Sun, J.; Bak, J.; Noh, J.; Subramanian, V.; Azuma, Y.; Majima, Y.; Cho, G., Scalability of Carbon-Nanotube-Based Thin Film Transistors for Flexible Electronic Devices Manufactured Using an All Roll-To-Roll Gravure Printing System. *Sci Rep* 2015, *5*, 14459.
(237) Mirri, F.; Ma, A. W. K.; Hsu, T. T.; Behabtu, N.; Eichmann, S. L.; Young, C. C.; Tsentalovich, D. E.; Pasquali, M., High-Performance Carbon Nanotube Transparent Conductive Films by Scalable Dip Coating. *ACS Nano* 2012, *6*, 9737-9744.
(238) Piloto, C.; Mirri, F.; Bengio, E. A.; Notarianni, M.; Gupta, B.; Shafiei, M.; Pasquali, M.; Motta, N., Room Temperature Gas Sensing Properties of Ultrathin Carbon Nanotube Films by Surfactant-Free Dip Coating. *Sens. Actuators, B* 2016, *227*, 128-134.
(239) Zheng, Q. B.; Zhang, B.; Lin, X. Y.; Shen, X.; Yousefi, N.; Huang, Z. D.; Li, Z. G.; Kim, J. K., Highly Transparent and Conducting Ultralarge Graphene Oxide/Single-Walled Carbon Nanotube Hybrid Films Produced by Langmuir-Blodgett Assembly. *J. Mater. Chem.* 2012, *22*, 25072-25082.
(240) Lee, J. H.; Kang, W. S.; Najeeb, C. K.; Choi, B. S.; Choi, S. W.; Lee, H. J.; Lee, S. S.; Kim, J. H., A Hydrogen Gas Sensor Using Single-Walled Carbon Nanotube Langmuir-Blodgett Films Decorated With Palladium Nanoparticles. *Sens. Actuators, B* 2013, *188*, 169-175.
(241) Cho, D. Y.; Eun, K.; Choa, S. H.; Kim, H. K., Highly Flexible and Stretchable Carbon Nanotube Network Electrodes Prepared by Simple Brush Painting for Cost-Effective Flexible Organic Solar Cells. *Carbon* 2014, *66*, 530-538.
(242) Li, X.; Gittleson, F.; Carmo, M.; Sekol, R. C.; Taylor, A. D., Scalable Fabrication of Multifunctional Freestanding Carbon Nanotube/Polymer Composite Thin Films for Energy Conversion *ACS Nano* 2012, *6*, 1347-1356.
(243) Meng, Y.; Xu, X. B.; Li, H.; Wang, Y.; Ding, E. X.; Zhang, Z. C.; Geng, H. Z., Optimisation of Carbon Nanotube Ink for Large-Area Transparent Conducting Films Fabricated Bb Controllable Rod-Coating Method. *Carbon* 2014, *70*, 103-110.
(244) Kim, S.; Yim, J.; Wang, X.; Bradley, D. D. C.; Lee, S.; Demello, J. C., Spin- and Spray-Deposited Single-Walled Carbon-Nanotube Electrodes for Organic Solar Cells. *Adv. Funct. Mater.* 2010, *20*, 2310-2316.
(245) Kymakis, E.; Stylianakis, M. M.; Spyropoulos, G. D.; Stratakis, E.; Koudoumas, E.; Fotakis, C., Spin Coated Carbon Nanotubes as the Hole Transport Layer in Organic Photovoltaics. *Sol. Energy Mater. Sol. Cells* 2012, *96*, 298-301.
(246) Ostfeld, A. E.; Catheline, A.; Ligsay, K.; Kim, K. C.; Chen, Z. H.; Facchetti, A.; Fogden, S.; Arias, A. C., Single-Walled Carbon Nanotube Transparent Conductive Films Fabricated by Reductive Dissolution and Spray Coating for Organic Photovoltaics. *Appl. Phys. Lett.* 2014, *105*, 253301.
(247) Jeong, M.; Lee, K.; Choi, E.; Kim, A.; Lee, S. B., Spray-Coated Carbon Nanotube Thin-Film Transistors with Striped Transport Channels. *Nanotechnology* 2012, *23*, 505203.
(248) Kim, S. Y.; Kim, Y.; Lee, K. M.; Yoon, W. S.; Lee, H. S.; Lee, J. T.; Kim, S. J.; Ahn, Y. H.; Park, J. Y.; Lee, T. K.; Lee, S., Fully Solution-Processed Transparent Conducting Oxide-Free Counter Electrodes for Dye-Sensitized Solar Cells: Spray-Coated Single-Wall Carbon Nanotube Thin Films Loaded with Chemically-Reduced Platinum Nanoparticles. *ACS Appl. Mater. Interfaces* 2014, *6*, 13430-13437.
(249) Wu, Z. C.; Chen, Z. H.; Du, X.; Logan, J. M.; Sippel, J.; Nikolou, M.; Kamaras, K.; Reynolds, J. R.; Tanner, D. B.; Hebard, A. F.; Rinzler, A. G., Transparent, Conductive Carbon Nanotube Films. *Science* 2004, *305*, 1273-1276.
(250) Xu, J. Z.; Feng, T.; Chen, Y. W.; Sun, Z., Field Emission Properties of the Graphene Double-Walled Carbon Nanotube Hybrid Films Prepared by Vacuum Filtration and Screen Printing. *J. Nanomater.* 2013, 536302
(251) Li, J. Y.; Zhu, Y.; Wang, X.; Wang, N.; Zhang, J., Light-Induced Vibration Characteristics of Free-Standing Carbon Nanotube Films Fabricated by Vacuum Filtration. *J. Appl. Phys.* 2014, *116*, 023101.

(252) Pei, S. F.; Du, J. H.; Zeng, Y.; Liu, C.; Cheng, H. M., The Fabrication of a Carbon Nanotube Transparent Conductive Film by Electrophoretic Deposition and Hot-Pressing Transfer. *Nanotechnology* **2009**, *20*, 235707.
(253) Hakamada, M.; Moriguchi, A.; Matsumura, S.; Mabuchi, M., Synthesis of Carbon Nanotube/Ni Nanocomposite Film by Electrophoresis and Electroless Deposition Without Pd Pretreatment. *Thin Solid Films* **2013**, *531*, 99-102.
(254) Cheng, H. M.; Li, F.; Sun, X.; Brown, S. D. M.; Pimenta, M. A.; Marucci, A.; Dresselhaus, G.; Dresselhaus, M. S., Bulk Morphology and Diameter Distribution of Single-Walled Carbon Nanotubes Synthesized by Catalytic Decomposition of Hydrocarbons. *Chem. Phys. Lett.* **1998**, *289*, 602-610.
(255) Jiang, K. L.; Li, Q. Q.; Fan, S. S., Nanotechnology: Spinning Continuous Carbon Nanotube Yarns - Carbon Nanotubes Weave Their Way into a Range of Imaginative Macroscopic Applications. *Nature* **2002**, *419*, 801-801.
(256) Ma, W. J.; Song, L.; Yang, R.; Zhang, T. H.; Zhao, Y. C.; Sun, L. F.; Ren, Y.; Liu, D. F.; Liu, L. F.; Shen, J.; Zhang, Z. X.; Xiang, Y. J.; Zhou, W. Y.; Xie, S. S., Directly Synthesized Strong, Highly Conducting, Transparent Single-Walled Carbon Nanotube Films. *Nano Lett.* **2007**, *7*, 2307-2311.
(257) Behabtu, N.; Young, C. C.; Tsentalovich, D. E.; Kleinerman, O.; Wang, X.; Ma, A. W. K.; Bengio, E. A.; ter Waarbeek, R. F.; de Jong, J. J.; Hoogerwerf, R. E.; Fairchild, S. B.; Ferguson, J. B.; Maruyama, B.; Kono, J.; Talmon, Y.; Cohen, Y.; Otto, M. J.; Pasquali, M., Strong, Light, Multifunctional Fibers of Carbon Nanotubes with Ultrahigh Conductivity. *Science* **2013**, *339*, 182-186.
(258) Zhang, M.; Fang, S. L.; Zakhidov, A. A.; Lee, S. B.; Aliev, A. E.; Williams, C. D.; Atkinson, K. R.; Baughman, R. H., Strong, Transparent, Multifunctional, Carbon Nanotube Sheets. *Science* **2005**, *309*, 1215-1219.
(259) Lu, Y. Y.; Yang, K.; Lin, D. H., Transport of Surfactant-Facilitated Multiwalled Carbon Nanotube Suspensions in Columns Packed with Sized Soil Particles. *Environ. Pollut.* **2014**, *192*, 36-43.
(260) Shanbedi, M.; Heris, S. Z.; Maskooki, A., Experimental Investigation of Stability and Thermophysical Properties of Carbon Nanotubes Suspension in the Presence of Different Surfactants. *J. Therm. Anal. Calorim.* **2015**, *120*, 1193-1201.
(261) Natale, G.; Heuzey, M. C.; Carreau, P. J.; Ausias, G.; Ferec, J., Rheological Modeling of Carbon Nanotube Suspensions with Rod-Rod Interactions. *AlChE J.* **2014**, *60*, 1476-1487.
(262) Cogan, N. M. B.; Bowerman, C. J.; Nogaj, L. J.; Nilsson, B. L.; Krauss, T. D., Selective Suspension of Single-Walled Carbon Nanotubes Using beta-Sheet Polypeptides. *J. Phys. Chem. C* **2014**, *118*, 5935-5944.
(263) Saran, N.; Parikh, K.; Suh, D. S.; Munoz, E.; Kolla, H.; Manohar, S. K., Fabrication and Characterization of Thin Films of Single-Walled Carbon Nanotube Bundles on Flexible Plastic Substrates. *J. Am. Chem. Soc.* **2004**, *126*, 4462-4463.
(264) Ruoff, R. S.; Tersoff, J.; Lorents, D. C.; Subramoney, S.; Chan, B., Radial Deformation of Carbon Nanotubes by Van - Der - Waals Forces. *Nature* **1993**, *364*, 514-516.
(265) Munkhbayar, B.; Nine, M. J.; Jeoun, J.; Bat-Erdene, M.; Chung, H.; Jeong, H., Influence of Dry and Wet Ball Milling on Dispersion Characteristics of the Multi-Walled Carbon Nanotubes in Aqueous Solution with and without Surfactant. *Powder Technol.* **2013**, *234*, 132-140.
(266) Kharissova, O. V.; Kharisov, B. I.; Ortiz, E. G. D., Dispersion of Carbon Nanotubes in Water and Non-Aqueous Solvents. *RSC Adv.* **2013**, *3*, 24812-24852.
(267) Yao, S. H.; Bethani, A.; Ziane, N.; Brochon, C.; Fleury, G.; Hadziioannou, G.; Poulin, P.; Salmon, J. B.; Cloutet, E., Synthesis of a Conductive Copolymer and Phase Diagram of Its Suspension with Single-Walled Carbon Nanotubes by Microfluidic Technology. *Macromolecules* **2015**, *48*, 7473-7480.
(268) Dalcanale, F.; Grossenbacher, J.; Blugan, G.; Gullo, M. R.; Brugger, J.; Tevaearai, H.; Graule, T.; Kuebler, J., Rapid Carbon Nanotubes Suspension in Organic Solvents Using Organosilicon Polymers. *J. Colloid Interface Sci.* **2016**, *470*, 123-131.
(269) Badard, M.; Combessis, A.; Allais, A.; Flandin, L., Electric Field as a Tuning Key to Process Carbon Nanotube Suspensions with Controlled Conductivity. *Polymer* **2016**, *82*, 198-205.

(270) Manilo, M. V.; Lebovka, N. I.; Barany, S., Stability of Multi-Walled Carbon Nanotube Plus Laponite Hybrid Particles in Aqueous Suspensions. *Colloids Surf., A* **2015**, *481*, 199-206.
(271) Natale, G.; Reddy, N. K.; Ausias, G.; Ferec, J.; Heuzey, M. C.; Carreau, P. J., Rheo-Optical Response of Carbon Nanotube Suspensions. *J. Rheol.* **2015**, *59*, 499-524.
(272) Njuguna, J.; Vanli, O. A.; Liang, R., A Review of Spectral Methods for Dispersion Characterization of Carbon Nanotubes in Aqueous Suspensions. *J. Spectrosc.* **2015**, 463156.
(273) Batmunkh, M.; Biggs, M. J.; Shapter, J. G., Carbon Nanotubes for Dye-Sensitized Solar Cells. *Small* **2015**, *11*, 2963-2989.
(274) DeBorde, T.; Aspitarte, L.; Sharf, T.; Kevek, J. W.; Minot, E. D., Photothermoelectric Effect in Suspended Semiconducting Carbon Nanotubes. *ACS Nano* **2014**, *8*, 216-221.
(275) Zhang, X.; Yang, F.; Zhao, D.; Cai, L.; Luan, P. S.; Zhang, Q.; Zhou, W. B.; Zhang, N.; Fan, Q. X.; Wang, Y. C.; Liu, H. P.; Zhou, W. Y.; Xie, S. S., Temperature Dependent Raman Spectra of Isolated Suspended Single-Walled Carbon Nanotubes. *Nanoscale* **2014**, *6*, 3949-3953.
(276) Willey, A. D.; Holt, J. M.; Larsen, B. A.; Blackburn, J. L.; Liddiard, S.; Abbott, J.; Coffin, M.; Vanfleet, R. R.; Davis, R. C., Thin Films of Carbon Nanotubes via Ultrasonic Spraying of Suspensions in N-Methyl-2-Pyrrolidone and N-Cyclohexyl-2-Pyrrolidone. *J. Vac. Sci. Technol., B* **2014**, *32*, 011218.
(277) Venediktova, A. V.; Bocharov, V. N.; Vlasov, A. Y.; Kislyakov, I. M.; Kiselev, V. M.; Kats, E. A.; Obraztsova, E. D.; Pozharov, A. S.; Povarov, S. A., Aqueous Suspensions of Single-Wall Carbon Nanotubes: Degree of Aggregation into Bundles and Optical Properties. *Opt. Spectrosc.* **2014**, *116*, 418-423.
(278) Samanta, S. K.; Fritsch, M.; Scherf, U.; Gomulya, W.; Bisri, S. Z.; Loi, M. A., Conjugated Polymer-Assisted Dispersion of Single-Wall Carbon Nanotubes: The Power of Polymer Wrapping. *Accounts Chem. Res.* **2014**, *47*, 2446-2456.
(279) Ling, X. L.; Wei, Y. Z.; Zou, L. M.; Xu, S., Functionalization and Dispersion of Multiwalled Carbon Nanotubes Modified With Poly-L-Lysine. *Colloids Surf., A* **2014**, *443*, 19-26.
(280) Berton, N.; Lemasson, F.; Poschlad, A.; Meded, V.; Tristram, F.; Wenzel, W.; Hennrich, F.; Kappes, M. M.; Mayor, M., Selective Dispersion of Large-Diameter Semiconducting Single-Walled Carbon Nanotubes with Pyridine-Containing Copolymers. *Small* **2014**, *10*, 360-367.
(281) Pochorovski, I.; Wang, H. L.; Feldblyum, J. I.; Zhang, X. D.; Antaris, A. L.; Bao, Z. N., H-Bonded Supramolecular Polymer for the Selective Dispersion and Subsequent Release of Large-Diameter Semiconducting Single-Walled Carbon Nanotubes. *J. Am. Chem. Soc.* **2015**, *137*, 4328-4331.
(282) Mohamed, A.; Anas, A. K.; Abu Bakar, S.; Ardyani, T.; Zin, W. M. W.; Ibrahim, S.; Sagisaka, M.; Brown, P.; Eastoe, J., Enhanced Dispersion of Multiwall Carbon Nanotubes in Natural Rubber Latex Nanocomposites by Surfactants Bearing Phenyl Groups. *J. Colloid Interface Sci.* **2015**, *455*, 179-187.
(283) Gubitosi, M.; Trilo, J. V.; Vargas, A. A.; Pavel, N. V.; Gazzoli, D.; Sennato, S.; Jover, A.; Meijide, F.; Galantini, L., Characterization of Carbon Nanotube Dispersions in Solutions of Bile Salts and Derivatives Containing Aromatic Substituents. *J. Phys. Chem. B* **2014**, *118*, 1012-1021.
(284) Dassios, K. G.; Alafogianni, P.; Antiohos, S. K.; Leptokaridis, C.; Barkoula, N. M.; Matikas, T. E., Optimization of Sonication Parameters for Homogeneous Surfactant-Assisted Dispersion of Multiwalled Carbon Nanotubes in Aqueous Solutions. *J. Phys. Chem. C* **2015**, *119*, 7506-7516.
(285) Coleman, J. N., Liquid-Phase Exfoliation of Nanotubes and Graphene. *Adv. Funct. Mater.* **2009**, *19*, 3680-3695.
(286) Ham, H. T.; Choi, Y. S.; Chung, I. J., An Explanation of Dispersion States of Single-Walled Carbon Nanotubes in Solvents and Aqueous Surfactant Solutions Using Solubility Parameters. *J. Colloid Interface Sci.* **2005**, *286*, 216-223.
(287) Li, Z. R.; Kandel, H. R.; Dervishi, E.; Saini, V.; Biris, A. S.; Biris, A. R.; Lupu, D., Does the Wall Number of Carbon Nanotubes Matter as Conductive Transparent Material? *Appl. Phys. Lett.* **2007**, *91*, 053115.
(288) Bahr, J. L.; Mickelson, E. T.; Bronikowski, M. J.; Smalley, R. E.; Tour, J. M., Dissolution of Small Diameter Single-Wall Carbon Nanotubes in Organic Solvents? *Chem. Commun.* **2001**, 193-194.

(289) Song, Y. I.; Yang, C. M.; Kim, D. Y.; Kanoh, H.; Kaneko, K., Flexible Transparent Conducting Single-Wall Carbon Nanotube Film with Network Bridging Method. *J. Colloid Interface Sci.* 2008, *318*, 365-371.
(290) Wang, J. P.; Sun, J.; Gao, L.; Wang, Y.; Zhang, J.; Kajiura, H.; Li, Y. M.; Noda, K., Removal of the Residual Surfactants in Transparent and Conductive Single-Walled Carbon Nanotube Films. *J. Phys. Chem. C* 2009, *113*, 17685-17690.
(291) Hu, L. B.; Hecht, D. S.; Gruner, G., Carbon Nanotube Thin Films: Fabrication, Properties, and Applications. *Chem. Rev.* 2010, *110*, 5790-5844.
(292) Bergin, S. D.; Sun, Z. Y.; Streich, P.; Hamilton, J.; Coleman, J. N., New Solvents for Nanotubes: Approaching the Dispersibility of Surfactants. *J. Phys. Chem. C* 2010, *114*, 231-237.
(293) Penicaud, A.; Poulin, P.; Derre, A.; Anglaret, E.; Petit, P., Spontaneous Dissolution of a Single-Wall Carbon Nanotube Salt. *J. Am. Chem. Soc.* 2005, *127*, 8-9.
(294) Ramesh, S.; Ericson, L. M.; Davis, V. A.; Saini, R. K.; Kittrell, C.; Pasquali, M.; Billups, W. E.; Adams, W. W.; Hauge, R. H.; Smalley, R. E., Dissolution of Pristine Single Walled Carbon Nanotubes in Superacids by Direct Protonation. *J. Phys. Chem. B* 2004, *108*, 8794-8798.
(295) Hecht, D. S.; Heintz, A. M.; Lee, R.; Hu, L. B.; Moore, B.; Cucksey, C.; Risser, S., High Conductivity Transparent Carbon Nanotube Films Deposited from Superacid. *Nanotechnology* 2011, *22*, 169501.
(296) Saha, A.; Ghosh, S.; Weisman, R. B.; Marti, A. A., Films of Bare Single-Walled Carbon Nanotubes from Superacids with Tailored Electronic and Photoluminescence Properties. *ACS Nano* 2012, *6*, 5727-5734.
(297) Park, C.; Ounaies, Z.; Watson, K. A.; Crooks, R. E.; Smith, J.; Lowther, S. E.; Connell, J. W.; Siochi, E. J.; Harrison, J. S.; Clair, T. L. S., Dispersion of Single Wall Carbon Nanotubes by in situ Polymerization under Sonication. *Chem. Phys. Lett.* 2002, *364*, 303-308.
(298) Hecht, D. S.; Ramirez, R. J. A.; Briman, M.; Artukovic, E.; Chichak, K. S.; Stoddart, J. F.; Gruner, G., Bioinspired Detection of Light Using a Porphyrin-Sensitized Single-Wall Nanotube Field Effect Transistor. *Nano Lett.* 2006, *6*, 2031-2036.
(299) Wang, H.; Li, S.; Si, Y. M.; Sun, Z. Z.; Li, S. Y.; Lin, Y. H., Recyclable Enzyme Mimic of Cubic Fe3O4 Nanoparticles Loaded on Graphene Oxide-Dispersed Carbon Nanotubes wth Enhanced Peroxidase-Like Catalysis and Electrocatalysis. *J. Mater. Chem. B* 2014, *2*, 4442-4448.
(300) Wang, H.; Li, S.; Si, Y. M.; Zhang, N.; Sun, Z. Z.; Wu, H.; Lin, Y. H., Platinum Nanocatalysts Loaded on Graphene Oxide-Dispersed Carbon Nanotubes with Greatly Enhanced Peroxidase-Like Catalysis and Electrocatalysis Activities. *Nanoscale* 2014, *6*, 8107-8116.
(301) Zhu, X. B.; Cui, Y. M.; Chang, X. J.; Wang, H., Selective Solid-Phase Extraction and Analysis of Trace-Level Cr(III), Fe(III), Pb(II), and Mn(II) Ions in Wastewater Using Diethylenetriamine-Functionalized Carbon Nanotubes Dispersed in Graphene Oxide Colloids. *Talanta* 2016, *146*, 358-363.
(302) Prusty, G.; Swain, S. K., Dispersion of Multiwalled Carbon Nanotubes in Polyacrylonitrile-Co-Starch Copolymer Matrix for Enhancement of Electrical, Thermal, and Gas Barrier Properties. *Polym. Composite* 2013, *34*, 330-334.
(303) Grosse, W.; Champavert, J.; Gambhir, S.; Wallace, G. G.; Moulton, S. E., Aqueous Dispersions of Reduced Graphene Oxide and Multi Wall Carbon Nanotubes for Enhanced Glucose Oxidase Bioelectrode Performance. *Carbon* 2013, *61*, 467-475.
(304) Shieh, Y. T.; Jiang, H. F., Graphene Oxide-Assisted Dispersion of Carbon Nanotubes in Sulfonated Chitosan-Modified Electrode for Selective Detections of Dopamine, Uric Acid, and Ascorbic Acid. *J. Electroanal. Chem.* 2015, *736*, 132-138.
(305) Avendano, C.; Brun, N.; Fontaine, O.; In, M.; Mehdi, A.; Stocco, A.; Vioux, A., Multiwalled Carbon Nanotube/Cellulose Composite: From Aqueous Dispersions to Pickering Emulsions. *Langmuir* 2016, *32*, 3907-3916.
(306) Venkatesan, J.; Pallela, R.; Kim, S. K., Dispersion of Single Walled Carbon Nanotubes in Marine Polysaccharides for Bone Tissue Engineering. *J. Biomater. Tissue. Eng.* 2014, *4*, 501-505.

(307) Mallakpour, S.; Zadehnazari, A., One-Pot Synthesis of Glucose Functionalized Multi-Walled Carbon Nanotubes: Dispersion in Hydroxylated Poly(Amide-Imide) Composites and Their Thermo-Mechanical Properties. *Polymer* **2013**, *54*, 6329-6338.
(308) Mistry, K. S.; Larsen, B. A.; Blackburn, J. L., High-Yield Dispersions of Large-Diameter Semiconducting Single-Walled Carbon Nanotubes with Tunable Narrow Chirality Distributions. *ACS Nano* **2013**, *7*, 2231-2239.
(309) Polo-Luque, M. L.; Simonet, B. M.; Valcarcel, M., Functionalization and Dispersion of Carbon Nanotubes in Ionic Liquids. *tical Chemistry* **2013**, *47*, 99-110.
(310) Wang, H. L.; Mei, J. G.; Liu, P.; Schmidt, K.; Jimenez-Oses, G.; Osuna, S.; Fang, L.; Tassone, C. J.; Zoombelt, A. P.; Sokolov, A. N.; Houk, K. N.; Toney, M. F.; Bao, Z. A., Scalable and Selective Dispersion of Semiconducting Arc-Discharged Carbon Nanotubes by Dithiafulvalene/Thiophene Copolymers for Thin Film Transistors. *ACS Nano* **2013**, *7*, 2659-2668.
(311) Hamedi, M. M.; Hajian, A.; Fall, A. B.; Hakansson, K.; Salajkova, M.; Lundell, F.; Wagberg, L.; Berglund, L. A., Highly Conducting, Strong Nanocomposites Based on Nanocellulose-Assisted Aqueous Dispersions of Single-Wall Carbon Nanotubes. *ACS Nano* **2014**, *8*, 2467-2476.
(312) Yang, J.; Yu, G. C.; Xia, D. Y.; Huang, F. H., A Pillar 6 Arene-Based UV-Responsive Supra-Amphiphile: Synthesis, Self-Assembly, and Application in Dispersion of Multiwalled Carbon Nanotubes in Water. *Chem. Commun.* **2014**, *50*, 3993-3995.
(313) Primo, E. N.; Canete-Rosales, P.; Bollo, S.; Rubianes, M. D.; Rivas, G. A., Dispersion of Bamboo Type Multi-Wall Carbon Nanotubes in Calf-Thymus Double Stranded DNA. *Colloids Surf. B. Biointerfaces* **2013**, *108*, 329-336.
(314) Tardani, F.; Sennato, S., Phase Behavior of DNA-Stabilized Carbon Nanotubes Dispersions: Association with Oppositely-Charged Additives. *J. Phys. Chem. C* **2014**, *118*, 9268-9274.
(315) Vaisman, L.; Marom, G.; Wagner, H. D., Dispersions of Surface-Modified Carbon Nanotubes in Water-Soluble and Water-Insoluble Polymers. *Adv. Funct. Mater.* **2006**, *16*, 357-363.
(316) Shastry, T. A.; Morris-Cohen, A. J.; Weiss, E. A.; Hersam, M. C., Probing Carbon Nanotube-Surfactant Interactions with Two-Dimensional DOSY NMR. *J. Am. Chem. Soc.* **2013**, *135*, 6750-6753.
(317) Matarredona, O.; Rhoads, H.; Li, Z. R.; Harwell, J. H.; Balzano, L.; Resasco, D. E., Dispersion of Single-Walled Carbon Nanotubes in Aqueous Solutions of the Anionic Surfactant Naddbs. *J. Phys. Chem. B* **2003**, *107*, 13357-13367.
(318) Geng, H. Z.; Kim, K. K.; So, K. P.; Lee, Y. S.; Chang, Y.; Lee, Y. H., Effect of Acid Treatment on Carbon Nanotube-Based Flexible Transparent Conducting Films. *J. Am. Chem. Soc.* **2007**, *129*, 7758-7759.
(319) Islam, M. F.; Rojas, E.; Bergey, D. M.; Johnson, A. T.; Yodh, A. G., High Weight Fraction Surfactant Solubilization of Single-Wall Carbon Nanotubes in Water. *Nano Lett.* **2003**, *3*, 269-273.
(320) Jo, J. W.; Jung, J. W.; Lee, J. U.; Jo, W. H., Fabrication of Highly Conductive and Transparent Thin Films from Single-Walled Carbon Nanotubes Using a New Non-Ionic Surfactant via Spin Coating. *ACS Nano* **2010**, *4*, 5382-5388.
(321) Hellstrom, S. L.; Lee, H. W.; Bao, Z. N., Polymer-Assisted Direct Deposition of Uniform Carbon Nanotube Bundle Networks for High Performance Transparent Electrodes. *ACS Nano* **2009**, *3*, 1423-1430.
(322) Khripin, C. Y.; Tu, X. M.; Heddleston, J. M.; Silvera-Batista, C.; Walker, A. R. H.; Fagan, J.; Zheng, M., High-Resolution Length Fractionation of Surfactant-Dispersed Carbon Nanotubes. *Anal. Chem.* **2013**, *85*, 1382-1388.
(323) Andrade, N. F.; Martinez, D. S. T.; Paula, A. J.; Silveira, J. V.; Alves, O. L.; Souza, A. G., Temperature Effects on the Nitric Acid Oxidation of Industrial Grade Multiwalled Carbon Nanotubes. *J. Nanopart. Res.* **2013**, *15*, UNSP 1761.
(324) He, R.; Pei, X. B.; Pan, L. L.; Tian, L. Y.; Luo, F.; Sui, L.; Wan, Q. B.; Wang, J., Effects of Ultrasonic Radiation Intensity on the Oxidation of Single-Walled Carbon Nanotubes in a Mixture of Sulfuric and Nitric Acids. *Nano* **2013**, *8*, 1350040.

(325) Yu, X.; Rajamani, R.; Stelson, K. A.; Cui, T., Fabrication of Carbon Nanotube Based Transparent Conductive Thin Films Using Layer-By-Layer Technology. *Surf. Coat. Technol.* 2008, *202*, 2002-2007.
(326) Li, X.; Li, Q. F.; Chen, G. X., Alkali Metal Surfactant-Facilitated Formation of Thick Boron Nitride Layers on Carbon Nanotubes by Dip-Coating. *Mater. Lett.* 2014, *134*, 38-41.
(327) Jamnani, B. D.; Hosseini, S.; Rahmanian, S.; Rashid, S. A.; Mustapha, S. B.; Balavandy, S. K., Grafting Carbon Nanotubes on Glass Fiber by Dip Coating Technique to Enhance Tensile and Interfacial Shear Strength. *J. Nanomater.* 2015, 149736.
(328) Abrishamchian, A.; Hooshmand, T.; Mohammadi, M.; Najafi, F., Preparation and Characterization of Multi-Walled Carbon Nanotube/Hydroxyapatite Nanocomposite Film Dip Coated on Ti-6Al-4V By Sol-Gel Method for Biomedical Applications: An in vitro Study. *Mater. Sci. Eng., C* 2013, *33*, 2002-2010.
(329) Champougny, L.; Scheid, B.; Restagno, F.; Vermant, J.; Rio, E., Surfactant-Induced Rigidity of Interfaces: A Unified Approach to Free and Dip-Coated Films. *Soft Matter* 2015, *11*, 2758-2770.
(330) Kim, Y.; Minami, N.; Zhu, W. H.; Kazaoui, S.; Azumi, R.; Matsumoto, M., Langmuir-Blodgett Films of Single-Wall Carbon Nanotubes: Layer-By-Layer Deposition and In-Plane Orientation of Tubes. *Jpn. J. Appl. Phys., Part 1* 2003, *42*, 7629-7634.
(331) Ohba, T., Anomalously Enhanced Hydration of Aqueous Electrolyte Solution in Hydrophobic Carbon Nanotubes to Maintain Stability. *Chemphyschem* 2014, *15*, 415-419.
(332) Sun, H. X.; La, P. Q.; Zhu, Z. Q.; Liang, W. D.; Yang, B. P.; Zhao, X. H.; Pei, C. J.; Li, A., Hydrophobic Carbon Nanotubes for Removal of Oils and Organics from Water. *J. Mater. Sci.* 2014, *49*, 6855-6861.
(333) De Nicola, F.; Castrucci, P.; Scarselli, M.; Nanni, F.; Cacciotti, I.; De Crescenzi, M., Multi-Fractal Hierarchy of Single-Walled Carbon Nanotube Hydrophobic Coatings. *Sci Rep* 2015, *5*, 8583.
(334) Wang, J.; Liang, M. H.; Fang, Y.; Qiu, T. F.; Zhang, J.; Zhi, L. J., Rod-Coating: Towards Large-Area Fabrication of Uniform Reduced Graphene Oxide Films for Flexible Touch Screens. *Adv. Mater.* 2012, *24*, 2874-2878.
(335) Dan, B.; Irvin, G. C.; Pasquali, M., Continuous and Scalable Fabrication of Transparent Conducting Carbon Nanotube Films. *ACS Nano* 2009, *3*, 835-843.
(336) Duan, S. S.; Zhang, L.; Wang, Z. H.; Li, C. Z., One-Step Rod Coating of High-Performance Silver Nanowire-PEDOT:PSS Flexible Electrodes with Enhanced Adhesion after Sulfuric Acid Post-Treatment. *RSC Adv.* 2015, *5*, 95280-95286.
(337) Pichumani, M.; Bagheri, P.; Poduska, K. M.; Gonzalez-Vinas, W.; Yethiraj, A., Dynamics, Crystallization and Structures in Colloid Spin CoatingDynamics, crystallization and structures in colloid spin coating. *Soft Matter* 2013, *9*, 3220-3229.
(338) Toolan, D. T. W.; Hodgkinson, R.; Howse, J. R., Stroboscopic Microscopy-Direct Imaging of Structure Development and Phase Separation During Spin-Coating. *J. Polym. Sci. Part B Polym. Phys.* 2014, *52*, 17-25.
(339) Meitl, M. A.; Zhou, Y. X.; Gaur, A.; Jeon, S.; Usrey, M. L.; Strano, M. S.; Rogers, J. A., Solution Casting and Transfer Printing Single-Walled Carbon Nanotube Films. *Nano Lett.* 2004, *4*, 1643-1647.
(340) LeMieux, M. C.; Roberts, M.; Barman, S.; Jin, Y. W.; Kim, J. M.; Bao, Z. N., Self-Sorted, Aligned Nanotube Networks for Thin-Film Transistors. *Science* 2008, *321*, 101-104.
(341) Tuukkanen, S.; Valimaki, M.; Lehtimaki, S.; Vuorinen, T.; Lupo, D., Behaviour of One-Step Spray-Coated Carbon Nanotube Supercapacitor in Ambient Light Harvester Circuit with Printed Organic Solar Cell and Electrochromic Display. *Sci Rep* 2016, *6*, 22967.
(342) Moridi, A.; Hassani-Gangaraj, S. M.; Guagliano, M.; Dao, M., Cold Spray Coating: Review of Material Systems and Future Perspectives. *Surf. Eng.* 2014, *30*, 369-U329.
(343) Benjamin, K.; Balaji, P., Vacuum Filtration Based Formation of Liquid Crystal Films of Semiconducting Carbon Nanotubes and High Performance Transistor Devices. *Nanotechnology* 2014, *25*, 175201.
(344) Zhou, Y. X.; Hu, L. B.; Gruner, G., A Method of Printing Carbon Nanotube Thin Films. *Appl. Phys. Lett.* 2006, *88*, 123109.

(345) He, X.; Gao, W.; Xie, L.; Li, B.; Zhang, Q.; Lei, S.; Robinson, J. M.; Hároz, E. H.; Doorn, S. K.; Wang, W.; Vajtai, R.; Ajayan, P. M.; Adams, W. W.; Hauge, R. H.; Kono, J., Wafer-Scale Monodomain Films of Spontaneously Aligned Single-Walled Carbon Nanotubes. *Nat. Nanotechnol.* **2016**, *11*, 633-638.
(346) Zhang, J. W.; Jiang, D. Z.; Peng, H. X., A Pressurized Filtration Technique for Fabricating Carbon Nanotube Buckypaper: Structure, Mechanical and Conductive Properties. *Micropor. Mesopor. Mat.* **2014**, *184*, 127-133.
(347) An, Q.; Rider, A. N.; Thostenson, E. T., Hierarchical Composite Structures Prepared by Electrophoretic Deposition of Carbon Nanotubes onto Glass Fibers. *ACS Appl. Mater. Interfaces* **2013**, *5*, 2022-2032.
(348) Lima, M. D.; de Andrade, M. J.; Bergmann, C. P.; Roth, S., Thin, Conductive, Carbon Nanotube Networks over Transparent Substrates by Electrophoretic Deposition. *J. Mater. Chem.* **2008**, *18*, 776-779.
(349) Yang, B.; Yang, Z. H.; Zhao, Z. Y.; Hu, Y. W.; Li, J. P., The Assembly of Carbon Nanotubes by Dielectrophoresis: Insights into the Dielectrophoretic Nanotube-Nanotube Interactions. *Physica E Low Dimens. Syst. Nanostruct.* **2014**, *56*, 117-122.
(350) Naieni, A. K.; Nojeh, A., The Mutual Interactions of Carbon Nanotubes During Dielectrophoresis. *IEEE Trans. Nanotechnol.* **2013**, *12*, 1068-1074.
(351) Islam, M. R.; Khondaker, S. I., Recent Progress in Parallel Fabrication of Individual Single Walled Carbon Nanotube Devices Using Dielectrophoresis. *Mater. Express* **2014**, *4*, 263-278.
(352) Hashim, U.; Low, F. W.; Liu, W. W., Precise Alignment of Individual Single-Walled Carbon Nanotube Using Dielectrophoresis Method for Development and Fabrication of pH Sensor. *J. Nanomater.* **2013**, 825285.
(353) Kordas, K.; Mustonen, T.; Toth, G.; Jantunen, H.; Lajunen, M.; Soldano, C.; Talapatra, S.; Kar, S.; Vajtai, R.; Ajayan, P. M., Inkjet Printing of Electrically Conductive Patterns of Carbon Nanotubes. *Small* **2006**, *2*, 1021-1025.
(354) Okimoto, H.; Takenobu, T.; Yanagi, K.; Miyata, Y.; Shimotani, H.; Kataura, H.; Iwasa, Y., Tunable Carbon Nanotube Thin-Film Transistors Produced Exclusively via Inkjet Printing. *Adv. Mater.* **2010**, *22*, 3981-3986.
(355) Tortorich, R. P.; Song, E.; Choi, J. W., Inkjet-Printed Carbon Nanotube Electrodes with Low Sheet Resistance for Electrochemical Sensor Applications. *J. Electrochem. Soc.* **2014**, *161*, B3044-B3048.
(356) Tortorich, R. P.; Choi, J. W., Inkjet Printing of Carbon Nanotubes. *Nanomaterials* **2013**, *3*, 453-468.
(357) Nobusa, Y.; Yomogida, Y.; Matsuzaki, S.; Yanagi, K.; Kataura, H.; Takenobu, T., Inkjet Printing of Single-Walled Carbon Nanotube Thin-Film Transistors Patterned by Surface Modification. *Appl. Phys. Lett.* **2011**, *99*, 183106.
(358) Shimoni, A.; Azoubel, S.; Magdassi, S., Inkjet Printing of Flexible High-Performance Carbon Nanotube Transparent Conductive Films by "Coffee Ring Effect". *Nanoscale* **2014**, *6*, 11084-11089.
(359) Lee, Y. I.; Kim, S.; Lee, K. J.; Myung, N. V.; Choa, Y. H., Inkjet Printed Transparent Conductive Films Using Water-Dispersible Single-Walled Carbon Nanotubes Treated by UV/Ozone Irradiation. *Thin Solid Films* **2013**, *536*, 160-165.
(360) Kwon, O. S.; Kim, H.; Ko, H.; Lee, J.; Lee, B.; Jung, C. H.; Choi, J. H.; Shin, K., Fabrication and Characterization of Inkjet-Printed Carbon Nanotube Electrode Patterns on Paper. *Carbon* **2013**, *58*, 116-127.
(361) Wu, J.; Antaris, A.; Gong, M.; Dai, H., Top-Down Patterning and Self-Assembly for Regular Arrays of Semiconducting Single-Walled Carbon Nanotubes. *Adv. Mater.* **2014**, *26*, 6151-6156.
(362) Ago, H.; Murata, K.; Yumura, M.; Yotani, J.; Uemura, S., Ink-Jet Printing of Nanoparticle Catalyst for Site-Selective Carbon Nanotube Growth. *Appl. Phys. Lett.* **2003**, *82*, 811-813.
(363) Bennett, R. D.; Hart, A. J.; Miller, A. C.; Hammond, P. T.; Irvine, D. J.; Cohen, R. E., Creating Patterned Carbon Nanotube Catalysts through the Microcontact Printing of Block Copolymer Micellar Thin Films. *Langmuir* **2006**, *22*, 8273-8276.
(364) Nagayama, K., Two-Dimensional Self-Assembly of Colloids in Thin Liquid Films. *Colloids Surf., A* **1996**, *109*, 363-374.

(365) Dionigi, C.; Stoliar, P.; Ruani, G.; Quiroga, S. D.; Facchini, M.; Biscarini, F., Carbon Nanotube Networks Patterned from Aqueous Solutions of Latex Bead Carriers. *J. Mater. Chem.* 2007, *17*, 3681-3686.
(366) Lim, C. H.; Min, D. H.; Lee, S. B., Direct Patterning of Carbon Nanotube Network Devices by Selective Vacuum Filtration. *Appl. Phys. Lett.* 2007, *91*, 243117.
(367) Fukaya, N.; Kim, D. Y.; Kishimoto, S.; Noda, S.; Ohno, Y., One-Step Sub-10 μm Patterning Of Carbon-Nanotube Thin Films for Transparent Conductor Applications. *ACS Nano* 2014, *8*, 3285-3293.
(368) Han, K. N.; Li, C. A.; Bui, M. P. N.; Seong, G. H., Patterning of Single-Walled Carbon Nanotube Films on Flexible, Transparent Plastic Substrates. *Langmuir* 2010, *26*, 598-602.
(369) Lu, S. X.; Panchapakesan, B., Nanotube Micro-Optomechanical Actuators. *Appl. Phys. Lett.* 2006, *88*, 253107.
(370) Castro, M. R. S.; Lasagni, A. F.; Schmidt, H. K.; Muecklich, F., Direct Laser Interference Patterning of Multi-Walled Carbon Nanotube-Based Transparent Conductive Coatings. *Appl. Surf. Sci.* 2008, *254*, 5874-5878.
(371) In, J. B.; Lee, D.; Fornasiero, F.; Noy, A.; Grigoropoulos, C. P., Laser-Assisted Simultaneous Transfer and Patterning of Vertically Aligned Carbon Nanotube Arrays on Polymer Substrates for Flexible Devices. *ACS Nano* 2012, *6*, 7858-7866.
(372) Kim, K. K.; Kim, S. M.; Lee, Y. H., Chemically Conjugated Carbon Nanotubes and Graphene for Carrier Modulation. *Accounts Chem. Res.* 2016, *49*, 390-399.
(373) Ma, X. D.; Adamska, L.; Yamaguchi, H.; Yalcin, S. E.; Tretiak, S.; Doorn, S. K.; Htoon, H., Electronic Structure and Chemical Nature of Oxygen Dopant States in Carbon Nanotubes. *ACS Nano* 2014, *8*, 10782-10789.
(374) Kong, J.; Franklin, N. R.; Zhou, C. W.; Chapline, M. G.; Peng, S.; Cho, K. J.; Dai, H. J., Nanotube Molecular Wires as Chemical Sensors. *Science* 2000, *287*, 622-625.
(375) Skakalova, V.; Kaiser, A. B.; Dettlaff-Weglikowska, U.; Hrncarikova, K.; Roth, S., Effect of Chemical Treatment on Electrical Conductivity, Infrared Absorption, and Raman Spectra of Single-Walled Carbon Nanotubes. *J. Phys. Chem. B* 2005, *109*, 7174-7181.
(376) Shim, B. S.; Zhu, J. A.; Jan, E.; Critchley, K.; Kotov, N. A., Transparent Conductors from Layer-By-Layer Assembled SWNT Films: Importance of Mechanical Properties and a New Figure of Merit. *ACS Nano* 2010, *4*, 3725-3734.
(377) Blackburn, J. L.; Barnes, T. M.; Beard, M. C.; Kim, Y. H.; Tenent, R. C.; McDonald, T. J.; To, B.; Coutts, T. J.; Heben, M. J., Transparent Conductive Single-Walled Carbon Nanotube Networks with Precisely Tunable Ratios of Semiconducting and Metallic Nanotubes. *ACS Nano* 2008, *2*, 1266-1274.
(378) Geng, H. Z.; Kim, K. K.; Song, C.; Xuyen, N. T.; Kim, S. M.; Park, K. A.; Lee, D. S.; An, K. H.; Lee, Y. S.; Chang, Y.; Lee, Y. J.; Choi, J. Y.; Benayad, A.; Lee, Y. H., Doping and De-Doping of Carbon Nanotube Transparent Conducting Films by Dispersant and Chemical Treatment. *J. Mater. Chem.* 2008, *18*, 1261-1266.
(379) Jackson, R.; Domercq, B.; Jain, R.; Kippelen, B.; Graham, S., Stability of Doped Transparent Carbon Nanotube Electrodes. *Adv. Funct. Mater.* 2008, *18*, 2548-2554.
(380) Mistry, K. S.; Larsen, B. A.; Bergeson, J. D.; Barnes, T. M.; Teeter, G.; Engtrakul, C.; Blackburn, J. L., n-Type Transparent Conducting Films of Small Molecule and Polymer Amine Doped Single-Walled Carbon Nanotubes. *ACS Nano* 2011, *5*, 3714-3723.
(381) Nirmalraj, P. N.; Lyons, P. E.; De, S.; Coleman, J. N.; Boland, J. J., Electrical Connectivity in Single-Walled Carbon Nanotube Networks. *Nano Lett.* 2009, *9*, 3890-3895.
(382) Manivannan, S.; Ryu, J. H.; Lim, H. E.; Nakamoto, M.; Jang, J.; Park, K. C., Properties of Surface Treated Transparent Conducting Single Walled Carbon Nanotube Films. *J. Mater. Sci.: Mater. Electron.* 2010, *21*, 72-77.
(383) Shin, D. W.; Lee, J. H.; Kim, Y. H.; Yu, S. M.; Park, S. Y.; Yoo, J. B., A Role of HNO3 on Transparent Conducting Film with Single-Walled Carbon Nanotubes. *Nanotechnology* 2009, *20*, 475703.
(384) Zhao, Y. L.; Li, W. Z., Effect of Annealing and HNO3-Treatment on the Electrical Properties of Transparent Conducting Carbon Nanotube Films. *Microelectron. Eng.* 2010, *87*, 576-579.

(385) Yim, J. H.; Kim, Y. S.; Koh, K. H.; Lee, S., Fabrication of Transparent Single Wall Carbon Nanotube Films with Low Sheet Resistance. *J. Vac. Sci. Technol., B* 2008, *26*, 851-855.
(386) Zhang, D. H.; Ryu, K.; Liu, X. L.; Polikarpov, E.; Ly, J.; Tompson, M. E.; Zhou, C. W., Transparent, Conductive, and Flexible Carbon Nanotube Films and Their Application in Organic Light-Emitting Diodes. *Nano Lett.* 2006, *6*, 1880-1886.
(387) Wang, Y.; Di, C. A.; Liu, Y. Q.; Kajiura, H.; Ye, S. H.; Cao, L. C.; Wei, D. C.; Zhang, H. L.; Li, Y. M.; Noda, K., Optimizing Single-Walled Carbon Nanotube Films for Applications in Electroluminescent Devices. *Adv. Mater.* 2008, *20*, 4442-4449.
(388) Wang, Y.; Di, C.-a.; Liu, Y.; Kajiura, H.; Ye, S.; Cao, L.; Wei, D.; Zhang, H.; Li, Y.; Noda, K., Optimizing Single-Walled Carbon Nanotube Films for Applications in Electroluminescent Devices. *Adv. Mater.* 2008, *20*, 4442-4449.
(389) Maeda, Y.; Hashimoto, M.; Kaneko, S.; Kanda, M.; Hasegawa, T.; Tsuchiya, T.; Akasaka, T.; Naitoh, Y.; Shimizu, T.; Tokumoto, H.; Lu, J.; Nagase, S., Preparation of Transparent and Conductive Thin Films of Metallic Single-Walled Carbon Nanotubes. *J. Mater. Chem.* 2008, *18*, 4189-4192.
(390) Lee, R. S.; Kim, H. J.; Fischer, J. E.; Thess, A.; Smalley, R. E., Conductivity Enhancement in Single-Walled Carbon Nanotube Bundles Doped with K and Br. *Nature* 1997, *388*, 255-257.
(391) Takenobu, T.; Kanbara, T.; Akima, N.; Takahashi, T.; Shiraishi, M.; Tsukagoshi, K.; Kataura, H.; Aoyagi, Y.; Iwasa, Y., Control of Carrier Density by a Solution Method in Carbon-Nanotube Devices. *Adv. Mater.* 2005, *17*, 2430-2434.
(392) Hellstrom, S. L.; Vosgueritchian, M.; Stoltenberg, R. M.; Irfan, I.; Hammock, M.; Wang, Y. B.; Jia, C.; Guo, X.; Gao, Y.; Bao, Z., Strong and Stable Doping of Carbon Nanotubes and Graphene by MoOx for Transparent Electrodes. *Nano Lett.* 2012, *12*, 3574-3580.
(393) Fanchini, G.; Unalan, H. E.; Chhowalla, M., Modification of Transparent and Conducting Single Wall Carbon Nanotube Thin Films via Bromine Functionalization. *Appl. Phys. Lett.* 2007, *90*, 092114.
(394) Chandra, B.; Afzali, A.; Khare, N.; El-Ashry, M. M.; Tulevski, G. S., Stable Charge-Transfer Doping of Transparent Single-Walled Carbon Nanotube Films. *Chem. Mat.* 2010, *22*, 5179-5183.
(395) Kim, S. M.; Jo, Y. W.; Kim, K. K.; Duong, D. L.; Shin, H. J.; Han, J. H.; Choi, J. Y.; Kong, J.; Lee, Y. H., Transparent Organic p-Dopant In Carbon Nanotubes: Bis(Trifluoromethanesulfonyl)imide. *ACS Nano* 2010, *4*, 6998-7004.
(396) Puchades, I.; Lawlor, C. C.; Schauerman, C. M.; Bucossi, A. R.; Rossi, J. E.; Cox, N. D.; Landi, B. J., Mechanism of Chemical Doping in Electronic-Type-Separated Single Wall Carbon Nanotubes towards High Electrical Conductivity. *J. Mater. Chem. C* 2015, *3*, 10256-10266.
(397) Graupner, R.; Abraham, J.; Vencelova, A.; Seyller, T.; Hennrich, F.; Kappes, M. M.; Hirsch, A.; Ley, L., Doping of Single-Walled Carbon Nanotube Bundles by Bronsted acids. *Phys. Chem. Chem. Phys.* 2003, *5*, 5472-5476.
(398) Wu, Y. P.; Fang, S. B.; Jiang, Y. Y.; Holze, R., Effects of Doped Sulfur on Electrochemical Performance of Carbon Anode. *J. Power Sources* 2002, *108*, 245-249.
(399) Czerw, R.; Terrones, M.; Charlier, J. C.; Blase, X.; Foley, B.; Kamalakaran, R.; Grobert, N.; Terrones, H.; Tekleab, D.; Ajayan, P. M.; Blau, W.; Ruhle, M.; Carroll, D. L., Identification of Electron Donor States in n-Doped Carbon Nanotubes. *Nano Lett.* 2001, *1*, 457-460.
(400) Fischer, J. E., Chemical Doping of Single-Wall Carbon Nanotubes. *Accounts Chem. Res.* 2002, *35*, 1079-1086.
(401) Lu, J.; Nagase, S.; Zhang, S.; Peng, L. M., Energetic, Geometric, and Electronic Evolutions of K-Doped Single-Wall Carbon Nanotube Ropes with K Intercalation Concentration. *Phys. Rev. B* 2004, *69*, 205304.
(402) Park, C. S.; Lee, C. J.; Kim, E. K., Stable p-Type Properties of Single Walled Carbon Nanotubes by Electrochemical Doping. *Phys. Chem. Chem. Phys.* 2015, *17*, 16243-16245.
(403) Lee, S. H.; Teng, C. C.; Ma, C. C. M.; Wang, I., Highly Transparent and Conductive Thin Films Fabricated with Nano-Silver/Double-Walled Carbon Nanotube Composites. *J. Colloid Interface Sci.* 2011, *364*, 1-9.

(404) Tokuno, T.; Nogi, M.; Jiu, J.; Suganuma, K., Hybrid Transparent Electrodes of Silver Nanowires and Carbon Nanotubes: A Low-Temperature Solution Process. *Nanoscale Res. Lett.* **2012**, *7*, 1-7.
(405) De, S.; Lyons, P. E.; Sorel, S.; Doherty, E. M.; King, P. J.; Blau, W. J.; Nirmalraj, P. N.; Boland, J. J.; Scardaci, V.; Joimel, J.; Coleman, J. N., Transparent, Flexible, and Highly Conductive Thin Films Based on Polymer - Nanotube Composites. *ACS Nano* **2009**, *3*, 714-720.
(406) Kim, S. H.; Song, W.; Jung, M. W.; Kang, M. A.; Kim, K.; Chang, S. J.; Lee, S. S.; Lim, J.; Hwang, J.; Myung, S.; An, K. S., Carbon Nanotube and Graphene Hybrid Thin Film for Transparent Electrodes and Field Effect Transistors. *Adv. Mater.* **2014**, *26*, 4247-4252.
(407) Soldano, C., Hybrid Metal-Based Carbon Nanotubes: Novel Platform for Multifunctional Applications. *Prog. Mater. Sci.* **2015**, *69*, 183-212.
(408) Jing, M. X.; Han, C.; Li, M.; Shen, X. Q., High Performance of Carbon Nanotubes/Silver Nanowires-PET Hybrid Flexible Transparent Conductive Films via Facile Pressing-Transfer Technique. *Nanoscale Res. Lett.* **2014**, *9*, 588.
(409) Fan, J. H.; Wan, M. X.; Zhu, D. B.; Chang, B. H.; Pan, Z. W.; Xie, S. S., Synthesis and Properties of Carbon Nanotube-Polypyrrole Composites. *Synth. Met.* **1999**, *102*, 1266-1267.
(410) Downs, C.; Nugent, J.; Ajayan, P. M.; Duquette, D. J.; Santhanam, S. V., Efficient Polymerization of Aniline at Carbon Nanotube Electrodes. *Adv. Mater.* **1999**, *11*, 1028-1031.
(411) Tung, V. C.; Chen, L. M.; Allen, M. J.; Wassei, J. K.; Nelson, K.; Kaner, R. B.; Yang, Y., Low-Temperature Solution Processing of Graphene-Carbon Nanotube Hybrid Materials for High-Performance Transparent Conductors. *Nano Lett.* **2009**, *9*, 1949-1955.
(412) Wang, R. R.; Sun, J.; Gao, L. A.; Xu, C. H.; Zhang, J.; Liu, Y. Q., Effective Post Treatment for Preparing Highly Conductive Carbon Nanotube/Reduced Graphite Oxide Hybrid Films. *Nanoscale* **2011**, *3*, 904-906.
(413) Peng, L. W.; Feng, Y. Y.; Lv, P.; Lei, D.; Shen, Y. T.; Li, Y.; Feng, W., Transparent, Conductive, and Flexible Multiwalled Carbon Nanotube/Graphene Hybrid Electrodes with Two Three-Dimensional Microstructures. *J. Phys. Chem. C* **2012**, *116*, 4970-4978.
(414) Nair, R. R.; Blake, P.; Grigorenko, A. N.; Novoselov, K. S.; Booth, T. J.; Stauber, T.; Peres, N. M. R.; Geim, A. K., Fine Structure Constant Defines Visual Transparency of Graphene. *Science* **2008**, *320*, 1308-1308.
(415) Barnes, T. M.; Bergeson, J. D.; Tenent, R. C.; Larsen, B. A.; Teeter, G.; Jones, K. M.; Blackburn, J. L.; van de Lagemaat, J., Carbon Nanotube Network Electrodes Enabling Efficient Organic Solar Cells without a Hole Transport Layer. *Appl. Phys. Lett.* **2010**, *96*, 243309.
(416) Lee, J. M.; Park, J. S.; Lee, S. H.; Kim, H.; Yoo, S.; Kim, S. O., Selective Electron- or Hole-Transport Enhancement in Bulk-Heterojunction Organic Solar Cells with N- or B-Doped Carbon Nanotubes. *Adv. Mater.* **2011**, *23*, 629-633.
(417) Yang, Z. B.; Chen, T.; He, R. X.; Guan, G. Z.; Li, H. P.; Qiu, L. B.; Peng, H. S., Aligned Carbon Nanotube Sheets for the Electrodes of Organic Solar Cells. *Adv. Mater.* **2011**, *23*, 5436-5439.
(418) Han, J.; Kim, H.; Kim, D. Y.; Jo, S. M.; Jang, S. Y., Water-Soluble Polyelectrolyte-Grafted Multiwalled Carbon Nanotube Thin Films for Efficient Counter Electrode of Dye-Sensitized Solar Cells. *ACS Nano* **2010**, *4*, 3503-3509.
(419) Li, G. R.; Wang, F.; Jiang, Q. W.; Gao, X. P.; Shen, P. W., Carbon Nanotubes with Titanium Nitride as a Low-Cost Counter-Electrode Material for Dye-Sensitized Solar Cells. *Angew. Chem.-Int. Edit.* **2010**, *49*, 3653-3656.
(420) Nam, J. G.; Park, Y. J.; Kim, B. S.; Lee, J. S., Enhancement of the Efficiency of Dye-Sensitized Solar Cell by Utilizing Carbon Nanotube Counter Electrode. *Scr. Mater.* **2010**, *62*, 148-150.
(421) Yu, J. G.; Fan, J. J.; Cheng, B., Dye-Sensitized Solar Cells Based on Anatase TiO2 Hollow Spheres/Carbon Nanotube Composite Films. *J. Power Sources* **2011**, *196*, 7891-7898.
(422) Jia, Y.; Cao, A. Y.; Bai, X.; Li, Z.; Zhang, L. H.; Guo, N.; Wei, J. Q.; Wang, K. L.; Zhu, H. W.; Wu, D. H.; Ajayan, P. M., Achieving High Efficiency Silicon-Carbon Nanotube Heterojunction Solar Cells by Acid Doping. *Nano Lett.* **2011**, *11*, 1901-1905.

(423) Jung, Y.; Li, X. K.; Rajan, N. K.; Tayor, A. D.; Reed, M. A., Record High Efficiency Single-Walled Carbon Nanotube/Silicon p-n Junction Solar Cells. *Nano Lett.* 2013, *13*, 95-99.
(424) Shi, E. Z.; Zhang, L. H.; Li, Z.; Li, P. X.; Shang, Y. Y.; Jia, Y.; Wei, J. Q.; Wang, K. L.; Zhu, H. W.; Wu, D. H.; Zhang, S.; Cao, A. Y., TiO2-Coated Carbon Nanotube-Silicon Solar Cells with Efficiency of 15%. *Sci Rep* 2012, *2*, 884.
(425) Cai, M. L.; Tiong, V. T.; Hreid, T.; Bell, J.; Wang, H. X., An Efficient Hole Transport Material Composite Based on Poly(3-Hexylthiophene) and Bamboo-Structured Carbon Nanotubes for High Performance Perovskite Solar Cells. *J. Mater. Chem. A* 2015, *3*, 2784-2793.
(426) Habisreutinger, S. N.; Leijtens, T.; Eperon, G. E.; Stranks, S. D.; Nicholas, R. J.; Snaith, H. J., Enhanced Hole Extraction in Perovskite Solar Cells through Carbon Nanotubes. *J. Phys. Chem. Lett.* 2014, *5*, 4207-4212.
(427) Rowell, M. W.; Topinka, M. A.; McGehee, M. D.; Prall, H. J.; Dennler, G.; Sariciftci, N. S.; Hu, L. B.; Gruner, G., Organic Solar Cells with Carbon Nanotube Network Electrodes. *Appl. Phys. Lett.* 2006, *88*, 233506.
(428) Unalan, H. E.; Hiralal, P.; Kuo, D.; Parekh, B.; Amaratunga, G.; Chhowalla, M., Flexible Organic Photovoltaics from Zinc Oxide Nanowires Grown On Transparent and Conducting Single Walled Carbon Nanotube Thin Films. *J. Mater. Chem.* 2008, *18*, 5909-5912.
(429) Kim, Y. H.; Muller-Meskamp, L.; Zakhidov, A. A.; Sachse, C.; Meiss, J.; Bikova, J.; Cook, A.; Zakhidov, A. A.; Leo, K., Semi-Transparent Small Molecule Organic Solar Cells with Laminated Free-Standing Carbon Nanotube Top Electrodes. *Sol. Energy Mater. Sol. Cells* 2012, *96*, 244-250.
(430) Tanaka, S.; Mielczarek, K.; Ovalle-Robles, R.; Wang, B.; Hsu, D.; Zakhidov, A. A., Monolithic Parallel Tandem Organic Photovoltaic Cell with Transparent Carbon Nanotube Interlayer. *Appl. Phys. Lett.* 2009, *94*, 113506.
(431) Salvatierra, R. V.; Cava, C. E.; Roman, L. S.; Zarbin, A. J. G., ITO-Free and Flexible Organic Photovoltaic Device Based on High Transparent and Conductive Polyaniline/Carbon Nanotube Thin Films. *Adv. Funct. Mater.* 2013, *23*, 1490-1499.
(432) Wei, D.; Unalan, H. E.; Han, D. X.; Zhang, Q. X.; Niu, L.; Amaratunga, G.; Ryhanen, T., A Solid-State Dye-Sensitized Solar Cell Based on a Novel Ionic Liquid Gel and ZnO Nanoparticles on a Flexible Polymer Substrate. *Nanotechnology* 2008, *19*, 424006.
(433) Kyaw, A. K. K.; Tantang, H.; Wu, T.; Ke, L.; Peh, C.; Huang, Z. H.; Zeng, X. T.; Demir, H. V.; Zhang, Q.; Sun, X. W., Dye-Sensitized Solar Cell with a Titanium-Oxide-Modified Carbon Nanotube Transparent Electrode. *Appl. Phys. Lett.* 2011, *99*, 021107.
(434) Wei, J. Q.; Jia, Y.; Shu, Q. K.; Gu, Z. Y.; Wang, K. L.; Zhuang, D. M.; Zhang, G.; Wang, Z. C.; Luo, J. B.; Cao, A. Y.; Wu, D. H., Double-walled carbon nanotube solar cells. *Nano Lett.* 2007, *7*, 2317-2321.
(435) Tune, D. D.; Flavel, B. S.; Krupke, R.; Shapter, J. G., Carbon Nanotube-Silicon Solar Cells. *Adv. Energy Mater.* 2012, *2*, 1043-1055.
(436) Li, X. K.; Jung, Y.; Sakimoto, K.; Goh, T. H.; Reed, M. A.; Taylor, A. D., Improved efficiency of smooth and aligned single walled carbon nanotube/silicon hybrid solar cells. *Energy Environ. Sci.* 2013, *6*, 879-887.
(437) Jia, Y.; Li, P. X.; Gui, X. C.; Wei, J. Q.; Wang, K. L.; Zhu, H. W.; Wu, D. H.; Zhang, L. H.; Cao, A. Y.; Xu, Y., Encapsulated carbon nanotube-oxide-silicon solar cells with stable 10% efficiency. *Appl. Phys. Lett.* 2011, *98*, 133115.
(438) Li, R.; Di, J. T.; Yong, Z. Z.; Sun, B. Q.; Li, Q. W., Polymethylmethacrylate coating on aligned carbon nanotube-silicon solar cells for performance improvement. *J. Mater. Chem. A* 2014, *2*, 4140-4143.
(439) Wang, F. J.; Kozawa, D.; Miyauchi, Y.; Hiraoka, K.; Mouri, S.; Ohno, Y.; Matsuda, K., Considerably Improved Photovoltaic Performance of Carbon Nanotube-Based Solar Cells Using Metal Oxide Layers. *Nat. Commun.* 2015, *6*, 6305.
(440) Kojima, A.; Teshima, K.; Shirai, Y.; Miyasaka, T., Organometal Halide Perovskites as Visible-Light Sensitizers for Photovoltaic Cells. *J. Am. Chem. Soc.* 2009, *131*, 6050-6051.

(441) Li, Z.; Kulkarni, S. A.; Boix, P. P.; Shi, E. Z.; Cao, A. Y.; Fu, K. W.; Batabyal, S. K.; Zhang, J.; Xiong, Q. H.; Wong, L. H.; Mathews, N.; Mhaisalkar, S. G., Laminated Carbon Nanotube Networks for Metal Electrode-Free Efficient Perovskite Solar Cells. *ACS Nano* **2014**, *8*, 6797-6804.

(442) Habisreutinger, S. N.; Leijtens, T.; Eperon, G. E.; Stranks, S. D.; Nicholas, R. J.; Snaith, H. J., Carbon Nanotube/Polymer Composites as a Highly Stable Hole Collection Layer in Perovskite Solar Cells. *Nano Lett.* **2014**, *14*, 5561-5568.

(443) Lim, S.-C.; Shin, J.; Kim, S.-C.; Park, J., Expansion of Smartwatch Touch Interface from Touchscreen to Around Device Interface Using Infrared Line Image Sensors. *Sensors* **2015**, *15*, 16642-16648.

(444) Marks, P., Acoustic Trick Gives 'Dumbphones' Touchscreen Feel. *New Sci.* **2010**, *207*, 21-21.

(445) Hecht, D. S.; Thomas, D.; Hu, L.; Ladous, C.; Lam, T.; Park, Y.; Irvin, G.; Drzaic, P., Carbon-Nanotube Film on Plastic as Transparent Electrode for Resistive Touch Screens. *J. Soc. Inf. Disp.* **2009**, *17*, 941-946.

(446) Wang, X.; Li, T.; Adams, J.; Yang, J., Transparent, Stretchable, Carbon-Nanotube-Inlaid Conductors Enabled by Standard Replication Technology for Capacitive Pressure, Strain and Touch Sensors. *J. Mater. Chem. A* **2013**, *1*, 3580-3586.

(447) Kim, W.; Oh, H.; Kwak, Y.; Park, K.; Ju, B.-K.; Kim, K., Development of a Carbon Nanotube-Based Touchscreen Capable of Multi-Touch and Multi-Force Sensing. *Sensors* **2015**, *15*, 28732-28741.

(448) Kim, B.-J.; Park, J.-S.; Hwang, Y.-J.; Park, J.-S., Characteristics of Silver Meshes Coated With Carbon Nanotubes via Spray-Coating and Electrophoretic Deposition for Touch Screen Panels. *Thin Solid Films* **2015**, *596*, 68-71.

(449) Im, H.-G.; Jin, J.; Ko, J.-H.; Lee, J.; Lee, J.-Y.; Bae, B.-S., Flexible Transparent Conducting Composite Films Using a Monolithically Embedded AgNW Electrode with Robust Performance Stability. *Nanoscale* **2014**, *6*, 711-715.

(450) Lee, D.; Lee, H.; Ahn, Y.; Jeong, Y.; Lee, D.-Y.; Lee, Y., Highly Stable and Flexible Silver Nanowire-Graphene Hybrid Transparent Conducting Electrodes for Emerging Optoelectronic Devices. *Nanoscale* **2013**, *5*, 7750-7755.

(451) Gaynor, W.; Hofmann, S.; Christoforo, M. G.; Sachse, C.; Mehra, S.; Salleo, A.; McGehee, M. D.; Gather, M. C.; Lüssem, B.; Müller-Meskamp, L.; Peumans, P.; Leo, K., Color in the Corners: ITO-Free White OLEDs with Angular Color Stability. *Adv. Mater.* **2013**, *25*, 4006-4013.

(452) Yu, S.; Yang, W.; Li, L.; Zhang, W., Improved Chemical Stability of ITO Transparent Anodes with A SnO2 Buffer Layer for Organic Solar Cells. *Sol. Energy Mater. Sol. Cells* **2016**, *144*, 652-656.

(453) Preston, C.; Xu, Y.; Han, X.; Munday, J. N.; Hu, L., Optical Haze of Transparent and Conductive Silver Nanowire Films. *Nano Res.* **2013**, *6*, 461-468.

(454) Lee, H.; Lee, J.-H.; Huynh, C. P.; Hawkins, S. C.; Musameh, M.; Kim, D. H.; Lee, S. H.; Choi, J., Orientational and Electro-Optical Properties of Liquid Crystal Aligned with a Directly Spinnable Carbon Nanotube Web. *Liq. Cryst.* **2015**, *42*, 322-327.

(455) Fu, W. Q.; Liu, L.; Jiang, K. L.; Li, Q. Q.; Fan, S. S., Super-Aligned Carbon Nanotube Films as Aligning Layers and Transparent Electrodes for Liquid Crystal Displays. *Carbon* **2010**, *48*, 1876-1879.

(456) Roussel, F.; Brun, J.-F.; Allart, A.; Huang, L.; O'Brien, S., Horizontally-Aligned Carbon Nanotubes Arrays and Their Interactions with Liquid Crystal Molecules: Physical Characteristics and Display Applications. *AIP Adv.* **2012**, *2*, 012110.

(457) Park, H.-G.; Lee, M.-J.; Kim, K.; Seo, D.-S., Transparent Conductive Single Wall Carbon Nanotube Network Films for Liquid Crystal Displays. *ECS Solid State Let.* **2012**, *1*, R31-R33.

(458) Fu, W.; Xu, Z.; Bai, X.; Gu, C.; Wang, E., Intrinsic Memory Function of Carbon Nanotube-Based Ferroelectric Field-Effect Transistor. *Nano Lett.* **2009**, *9*, 921-925.

(459) Hu, L. B.; Li, J. F.; Liu, J.; Gruner, G.; Marks, T., Flexible Organic Light-Emitting Diodes with Transparent Carbon Nanotube Electrodes: Problems and Solutions. *Nanotechnology* **2010**, *21*, 155202.

(460) Xu, F.; Zhu, W. Q.; Yan, L.; Xu, H.; Xiong, L. H.; Li, J. H., Single Walled Carbon Nanotube Anodes Based High Performance Organic Light-Emitting Diodes with Enhanced Contrast Ratio. *Org. Electron.* **2012**, *13*, 302-308.

(461) Gao, J.; Mu, X.; Li, X. Y.; Wang, W. Y.; Meng, Y.; Xu, X. B.; Chen, L. T.; Cui, L. J.; Wu, X. M.; Geng, H. Z., Modification of Carbon Nanotube Transparent Conducting Films for Electrodes in Organic Light-Emitting Diodes. *Nanotechnology* **2013**, *24*, 435201.

(462) Sam, F. L. M.; Dabera, G.; Lai, K. T.; Mills, C. A.; Rozanski, L. J.; Silva, S. R. P., Hybrid Metal Grid-Polymer-Carbon Nanotube Electrodes for High Luminance Organic Light Emitting Diodes. *Nanotechnology* **2014**, *25*, 345202.

(463) Kim, M.; Kim, Y. C., Single Wall Carbon Nanotube/Poly(3,4-Ethylenedioxythiophene) Nanocomposite Film as a Transparent Electrode for Flexible Organic Light-Emitting Diodes. *Synth. Met.* **2014**, *198*, 31-35.

(464) Liu, Y. P.; Jung, E.; Wang, Y.; Zheng, Y.; Park, E. J.; Cho, S. M.; Loh, K. P., Quasi- Freestanding" Graphene-on- Single Walled Carbon Nanotube Electrode for Applications in Organic Light- Emitting Diode. *Small* **2014**, *10*, 944-949.

(465) Yu, D. M.; Liu, H. P.; Peng, L. M.; Wang, S., Flexible Light-Emitting Devices Based on Chirality-Sorted Semiconducting Carbon Nanotube Films. *ACS Appl. Mater. Interfaces* **2015**, *7*, 3462-3467.

(466) Shan, L.; Wei, T. B.; Sun, Y. P.; Zhang, Y. H.; Zhen, A. G.; Xiong, Z.; Wei, Y.; Yuan, G. D.; Wang, J. X.; Li, J. M., Super-Aligned Carbon Nanotubes Patterned Sapphire Substrate to Improve Quantum Efficiency of InGaN/GaN Light-Emitting Diodes. *Opt. Express* **2015**, *23*, A957-A965.

(467) Shan, L.; Wei, T. B.; Sun, Y. P.; Zhang, Y. H.; Xiong, Z.; Zhen, A. G.; Wang, J. X.; Wei, Y.; Li, J. M., Effect of Layers of Carbon-Nanotube-Patterned Substrate on GaN-Based Light-Emitting Diodes. *Jpn. J. Appl. Phys.* **2015**, *54*, 065102.

(468) Seo, T. H.; Lee, G. H.; Park, S.; Chandramohan, S.; Park, A. H.; Cho, H.; Park, M.; Kim, M. J.; Suh, E. K., Hybrid Electrode Based on Carbon Nanotube and Graphene for Ultraviolet Light-Emitting Diodes. *Appl. Phys. Express* **2015**, *8*, 102101.

(469) Li, X.; Magnuson, C. W.; Venugopal, A.; Tromp, R. M.; Hannon, J. B.; Vogel, E. M.; Colombo, L.; Ruoff, R. S., Large-Area Graphene Single Crystals Grown by Low-Pressure Chemical Vapor Deposition of Methane on Copper. *J. Am. Chem. Soc.* **2011**, *133*, 2816-2819.

(470) Meng, H.; Dai, Y.; Ye, Y.; Luo, J. X.; Shi, Z. J.; Dai, L.; Qin, G. G., Bilayer Graphene Anode for Small Molecular Organic Electroluminescence. *J. Phys. D Appl. Phys.* **2012**, *45*, 245103.

(471) Ulbricht, H.; Moos, G.; Hertel, T., Physisorption of Molecular Oxygen on Single-Wall Carbon Nanotube Bundles and Graphite. *Phys. Rev. B* **2002**, *66*, 075404.

Chapter 2 Experimental Details

Some parts of this Chapter have been published and are extracted from the following published articles:

Yu, L.; Grace, T.; Batmunkh, M.; Dadkhah, M.; Shearer, C.; Shapter, J. Insights into Chemical Doping to Engineer the Carbon Nanotube/Silicon Photovoltaic Heterojunction Interface. *J. Mater. Chem. A* **2017**. 5, 24247-24256.

Yu, L.; Batmunkh, M.; Grace, T.; Dadkhah, M.; Shearer, C.; Shapter, J. Application of a Hole Transporting Organic Interlayer in Graphene oxide/Single walled Carbon Nanotube-Silicon Heterojunction Solar Cells. *J. Mater. Chem. A* **2017**. 5, 8624-8634.

Yu, L.; Grace, T.; Jazi, M. D.; Shearer, C.; Shapter, J. Optimization of the Metal Front Contact Design for Single-Walled Carbon Nanotube-Silicon Heterojunction Solar Cells. *Solar RRL* **2017**. 1600026.

Yu, L.; Shearer, C.; Shapter, J. Recent Development of Carbon Nanotube Transparent Conductive Films. *Chem. Rev.* **2016**. 116, 13413-13453.

Yu, L.; Tune, D.; Shearer, C.; Grace, T.; Shapter, J. Heterojunction Solar Cells Based on Silicon and Composite Films of Polyaniline and Carbon Nanotubes. *IEEE J. Photovolt* **2016.** 6, 688-695.

2.1 Overview

This Chapter focuses on the methods used through the entire Thesis, including the preparation of stock solutions and suspensions, the fabrication of the CNT-based electrode, the preparation of the solar cells and different types of characterisation techniques.

2.2 Preparation of stock solution or suspension

2.2.1 Organic and aqueous stock solutions

2.2.1.1 PANI

Emeraldine base (Mw: 60 000, Sigma-Aldrich, Australia) was dissolved in ethanoic acid (80% v/v, prepared by diluting glacial acetic acid, ChemSupply, Australia) to prepare PANI stock solution with a starting concentration of 1 mg mL^{-1}. This was then followed by 15 min vigorous stirring and the resulting solution was dark green. In order to remove any large insoluble particles, the solution was filtered through a nylon membrane (0.2 µm, Pall Life Sciences).

2.2.1.2 spiro-OMeTAD

The stock solution of spiro-OMeTAD was prepared by dissolving 144.6 mg spiro-OMeTAD (Merck), 57.6 µL 4-tert-butylpyridine (tBP) (Sigma-Aldrich) and 35 µL of a stock solution of 520 mg mL^{-1} lithium bis(trifluoromethylsulphonyl)imide (Li-TFSI) (Sigma-Aldrich) in acetonitrile, in 1 mL chlorobenzene.[1]

2.2.1.3 GO

40 mL H_3PO_4 (86.5 %, BDH Chemicals) and concentrated 360 mL H_2SO_4 (98.0 %, RCI Labscan) (9:1) was mixed with graphite flakes (Sigma-Aldrich) and $KMnO_4$ (99.0 %, Chem-Supply) (3 g/ 18 g). The reaction solution was heated for 12 h at 50 °C with stirring, after which it was cooled down to room temperature and the liquid was centrifuged at 1800 g for 4 h. The top 70 % of the solid contents at the bottom of the centrifuge tube were collected and washed with deionised water (200 mL), 30 % HCl (200 mL) and ethanol (200 mL two times). After each rinse step, the mixture was centrifuged at 1800 g for 4 h and the supernatant was discarded

while the top 70 % of the solid content was collected for the following wash. After the final wash, the solid was dried in a freeze dryer overnight, and collected as the as prepared GO solids. The solids were then dispersed with deionised water by bath sonication for 20 min with the final concentration to be 1 mg mL^{-1}.[2]

2.2.1.4 AgNWs

Polyvinylpyrrolidone (6 g, PVP, MW = 55000 g mol^{-1}, Sigma-Aldrich) was dissolved in 190 mL of glycerol (99.5 %, Chem-Supply) at 80 °C. The solution was cooled down to room temperature and poured into a round-bottom flask placed in a silicone oil bath. Silver nitrate (1.58 g, AgNO3, 99.0 %, Sigma-Aldrich) was then added with vigorous stirring. 0.5 mL water was used to dissolve 58.5 mg of sodium chloride (NaCl, 99.7 %, Chem-Supply) and the solution was mixed with 10 mL glycerol. The NaCl solution was added into the reactor and the temperature was raised to 205 °C within 25 min. The reaction was carried out in air at 205 ± 1 °C for 60 min. The reactor was cooled down to room temperature before the liquid medium was mixed with deionised water in a volume ratio of 1 : 1. The mixed solution was centrifuged at 4000 g for 5 min at room temperature. The supernatant was discarded but the precipitate was collected and redispersed with deionised water and centrifuged in the identical manner three times to remove the PVP and nanoparticles. After a final rinse step, the AgNWs were dispersed in deionised water with a final concentration of 0.2 mg mL^{-1}.[3]

2.2.1.5 $CuCl_2$

The redox colloidal solution ($CuCl_2$ (99.0 %, Sigma-Aldrich)/$Cu(OH)_2$, (denoted $CuCl_2$ in Chapter 6 since Cu^{2+} in $CuCl_2$ is considered to be the active part for rapid p-type doping of SWCNTs through extraction of electrons leading to reduction to Cu^{1+} while Cu^{2+} hydroxide provides long-term stability of doping)[4] was prepared by the addition of a 1 M NaOH (98.0 %, Chem-Supply) aqueous solution into a 0.1 M $CuCl_2$ ethanol solution. The volume ratio of these two solutions was kept at 1 : 2000.[4]

2.2.1.6 Si etching solution

3.8 g NaOH (98.0 %, Chem-Supply) was first dissolved in 160 mL deionised water, and then the solution was mixed with 40 mL isopropanol (99.5 %, Chem-Supply). The final solution was bath sonicated for 3 min to create a homogeneous liquid medium.

2.2.1.7 Aqueous solutions in ATPE (aqueous two phase extraction)

2.2.1.7.1 ATPE solutions

The stock solutions of 25 wt% polyethylene glycol (PEG, M_w = 6000 Da, Alfa Aesar) and 25 wt% dextran 70 (DX, M_w = 70 000 Da, TCI) were prepared by dissolving the powder in deionised water with the help of vigorous vortex mixing for 5 min at room temperature. The aqueous stock solution of 50 wt% polyacrylamide (PAM, M_w = 10 000 Da, Sigma-Aldrich) was used as received. The composition and the recipe of the initial ATPE system solutions are listed in Table 2.1. For example, the initial ATPE solution of PEG/PAM was prepared by mixing 20.826 mL 25 wt% PEG, 23.922 g 50 wt% PAM and 6 mL deionised water in a 50 mL centrifuge tube. Because of the phase equilibration at room temperature (20 °C), the system tended to separate into a PEG enriched top phase and a PAM enriched bottom phase after several minutes. Thus, it was required to vortex mix the initial ATPE solution each time before use.[5]

In order to prepare the blank top and bottom phase, 7 volume parts of the premixed initial ATPE solution was mixed with 3 volume parts of deionised water by vortex mixing for 3 min at room temperature. The final compositions of the polymers are shown in Table 2.1. The resulting mixture was centrifuged at 5000 g for 10 min at room temperature, after which the top and bottom phase were collected by pipette and stored. Temperature control during centrifugation is critical due to the temperature dependent nature of ATPE systems.[5]

Table 2.1 ATPE system applied for ssDNA-SWCNT separation

ATPE system (Top/Bottom phase)	PEG/PAM	PEG/DX
Initial ATPE solution composition	PEG 11.09 wt% PAM 21.43 wt%	PEG 7.86 wt% DX 10.71 wt%
Preparation of the initial ATPE solution	25 wt% PEG 20.826 mL 50 wt% PAM 20.122 mL* Deionized water 6 mL	25 wt% PEG 14.669 mL 25 wt% DX 19.988 mL Deionized water 12 mL
Final ATPE solution composition	PEG 7.76 wt%	PEG 5.50 wt%

	PAM 15.0 wt%	DX 7.50 wt%

* Practically, the accurate measurement of PAM stock solution volume was difficult due to its high viscosity. Instead, 23.922 g 50 wt% PAM stock solution was used by converting volume into mass with the solution density on the label (1.189 g mL^{-1}).

2.2.1.7.2 Solutions of modulating agents

The as-prepared 25 wt% DX was a commonly used modulator in PEG/PAM system while polyvinylpyrrolidone (PVP, M_w = 10 000 Da, Sigma-Aldrich), NaCl and NaSCN were used in both PEG/PAM and PEG/DX systems. 40 wt% PVP, 5 M NaCl, 1 M HCl and 10 M NaSCN were prepared first and diluted to different levels to meet the requirement of different concentration levels in each individual case of separation since the sensitivity of ssDNA-SWCNT to modulator is often highly sequence dependent, as shown in Table 2.2.[6]

Table 2.2 Modulators in ATPE

Modulator	Level of concentrations			
PVP	40 wt%	10 wt%	1 wt%	0.1 wt%
NaCl	5 M	1 M	0.1 M	
HCl	1 M	0.1 M		
NaSCN	10 M	1 M	0.1 M	

2.2.2 Carbon nanotube suspensions

2.2.2.1 SWCNT suspension with different surfactants

2.2.2.1.1 Triton X-100

CNT stock dispersion (starting concentration: 0.1 mg mL^{-1}) was prepared by the addition of arc-discharge CNT soot (P3-SWNT, Carbon Solutions Inc., USA) to an aqueous solution of Triton X-100 (1% v/v, Sigma-Aldrich, Australia) by the help of bath sonication in an ice bath (S 30H, Elmasonic) for 1 h. The resulting CNT dispersion was centrifuged at 17500 g for 1 h (Allegra X-22 Centrifuge, Beckman Coulter). The supernatants from all centrifuge tubes were collected and combined, followed by a further centrifugation in the identical manner as previously, with the bottom residue being discarded.[7]

2.2.2.1.2 Sodium dodecyl sulphate

HiPco SWCNT dispersion was prepared with the addition of 25 mg as-received soot (Unidym, Houston, TX, USA) into 25 mL 0.5 wt% SDS (Sigma-Aldrich, ≥ 98.5 %) aqueous solution to make the starting concentration 1 mg mL^{-1}, followed by probe ultrasonication (Sonics VCX 750 W) for 45 min. Sonication was conducted at 20 000 Hz with a Ti microtip (6.5 mm) and the amplitude was set at 22 % of the maximum value (giving a final input of power of about 0.4 W mL^{-1}). During sonication, in order to have good control of the reaction temperature, the container was placed in an ice bath. After sonication, ultracentrifugation was performed to remove bundles and other impurities, such as metal catalysts, at 41200 rpm (about 120 000 g) in a 60Ti rotor at 15 °C for 90 min. The upper 80 % supernatant was collected as the starting parent dispersion via a glass pipette for several times.[8-9]

2.2.2.1.3 Sodium cholate

25 mg HiPco as-received soot (Unidym, Houston, TX, USA) was added in 25 mL of 0.5 wt% SC aqueous solution to target the starting concentration of 1 mg mL^{-1}. Probe sonicator (Sonics VCX 750 W) was then used to disperse SWCNTs with a Ti microtip (6.5 mm) and the amplitude was set at 22 % of the maximum value (3 h, in ice bath). In order to remove the large undispersed agglomerates and other impurities, including metal catalyst, the dispersed solution was centrifuged at 41200 rpm (about 120 000 g) in a 60Ti rotor at 15 °C for 90 min. The top 80 % supernatant was collected and used as the starting material in single-chirality separation by gel chromatography process.[10]

2.2.2.2 Graphene oxide

CNT aqueous dispersion can also be prepared with the help of GO. GO solid was obtained by exposing 3 mL of 5 mg mL^{-1} GO in ethanol (Graphene Supermarket, USA) to air in a 20 mL scintillation vial inside a fume hood at 20 °C. The GO solids were then redispersed in deionised water with sonication for 30 min in an ice bath to give a final concentration of 1mg mL^{-1}. CNT (P3-SWNT, Carbon Solutions Inc., USA) were first dispersed in deionised water by bath sonication with the final concentration to be 0.1 mg mL^{-1}. 2 mL GO stock suspension was added to 45 mL CNT stock suspension so as to target the ideal mass ratio of GO : CNT (1 : 2.25), and GOCNT hybrid films with this ratio have the lowest sheet resistance.[11] The mixture dispersion was sonicated for 90 min in an ice bath and centrifuged at 17 500 g for 1 h at 10 °C

to remove any large aggregates. The supernatant was collected and centrifuged in the same manner. The second supernatant was collected and used as the source dispersion for the fabrication of GOCNT TCFs.

2.2.2.3 DNA dispersed SWCNTs

The stock SWCNT (CoMoCAT SG 65 or CoMoCAT SG 65i or EG 150X, Sigma-Aldrich)/water mixture was prepared by adding the as-received CNT soot to deionised water with a final concentration of 4 mg mL^{-1}. 20 min bath sonication was applied to reduce the number of large aggregates and improve the homogeneity of the mixture. 200 µL of DNA stock solution (10 mg mL^{-1}), 250 µL SWCNT/water mixture (4 mg mL^{-1}), 100 µL of 1 M NaCl (or 25 µL of SSC buffer solution 20X), and 450 µL (or 525 µL) of deionised water were mixed (total volume is 1 mL) and tip-sonicated in an ice bath at 1 W mL^{-1} for 1 hour. After sonication, the 1 mL mixture was divided into 100 µL aliquots and centrifuged at 17 000 g for 90 min at 20 °C. The 90 µL supernatant in each centrifuge tube was collected and used as the parent material in ATPE separation.

2.3 Separation of SWCNTs

2.3.1 Gel chromatography

2.3.1.1 Metal/semiconductor separation by gel chromatography

The separation was performed with 0.5 wt% SDS dispersed HiPco SWCNTs (refer to section 2.2.2.1.2) in a glass column with a fritted disc. The column was filled with approximately 30 mL of as-received solution of dextran-based gel beads in ethanol (Sephacryl S-200 HR) and the height of the gel beads is about 20 cm. A gentle nitrogen stream on top of the column was used to flush the liquid medium at a flow rate of 1 mL min^{-1}. The gel bed was first eluted with 30 mL water and 30 mL of 0.5 wt% SDS aqueous solution prior to the addition of 10 mL CNT dispersion. Then, 15 mL 0.5 wt% SDS was added to the column to flush and collect the unbound CNTs until the filtrate was colourless. In order to remove the metallic species completely, a large amount (about 80 mL) of 1 wt% SDS aqueous solution was added to the column until the eluted fraction was colourless. In order to collect a fraction enriched with

semiconducting species, 30 mL of 0.5 wt% sodium deoxycholate (DOC) aqueous solution was added to the column to elute the next fraction of SWCNTs.

2.3.1.2 Single-chirality species separation by gel chromatography

To begin with, the starting SWCNT dispersion (prepared according to the description in section 2.2.2.1.3) was diluted to give a final SC and SDS concentration of 0.5 and 2 wt% respectively. The loading of the CNT suspension was performed with 3 individual columns. A glass column with a fritted disc was used for the equilibration with different concentrations of SDS (2, 1 and 0.5 wt% for the 1st, 2nd and 3rd column respectively) but the same concentration of SC (0.5 wt%). 30 mL of as-received dispersion of dextran-based gel beads was packed in the column. In the first column, after the equilibration of the gel bed with the aqueous solution of 0.5 wt% SC and 2 wt% SDS, about 10 mL of SWCNT dispersion (in 0.5 wt% SC and 2 wt% SDS) was loaded. The elutriate containing the unbound SWCNTs from the first column was diluted to target SC and SDS concentrations of 0.5 and 1 wt%. In the same manner, the diluted elutriate was loaded to the second column after the equilibration of the gel bed with 0.5 wt% SC and 1 wt% SDS solution. The unbound SWCNT elutriate from the second column was collected and diluted to obtain the SC and SDS concentrations of 0.5 and 0.5 wt%, which was then loaded to the third column equilibrated with 0.5 wt% SC and 0.5 wt% SDS solution.[10]

The SWCNTs absorbed in the gel bed were eluted and collected with the addition of aqueous solution with increasing DOC concentration but the same SC and SDS concentration in each column, as shown in Table 2.3. Specifically, for the first column, the concentration of DOC was increased from 0 to 0.4 wt% in 0.04 wt% steps with fixed SC and SDS concentration of 0.5 and 2 wt%. For the second column, the DOC concentration increased from 0 to 0.2 wt% in 0.02 wt% steps with constant concentrations of 0.5 wt% SC and 1 wt% SDS and for the third column with the constant concentrations of 0.5 wt% SC and 1 wt% SDS, the DOC concentration ranged from 0 to 0.1 wt% with steps of 0.01 wt%. For each elution, after the collection of the eluted SWCNTs with relatively high concentrations, large amounts of these aqueous background solutions containing surfactants alone were used to rinse the gel bed until the elution is colourless, and then the procedure moved to next step.[10]

Table 2.3 The concentration of the aqueous solutions used to elute SWCNTs absorbed on the gel in each individual column. The concentration of SC for all of three columns was constant at 0.5 wt% while the SDS concentration decreased from 2 to 1 to 0.5 wt% from the first column to the third one. In each column, a series of aqueous solution with different DOC concentrations with certain steps was used to elute the SWCNTs.

Column	SC concentration (wt%)	SDS concentration (wt%)	DOC concentration range (wt%)	Steps of DOC (wt%)
No. 1	0.5	2	0 - 0.4	0.04
No. 2	0.5	1	0 - 0.2	0.02
No. 3	0.5	0.5	0 - 0.1	0.01

2.3.1.3 Single-chirality species separation by ATPE

For the first step, 7 parts of the initial ATPE solution (refer to section 2.2.1.7) were added with 3 parts of parent suspension (refer to section 2.2.2.3), followed by vortexing for 1 min and centrifuging at 17 000 g for 1 min at room temperature. The total volume of the solution was either 0.5 or 1 mL. After centrifugation, two immiscible phases were formed with the top phase (labelled 1T) and the bottom phase (labelled 1B).

In the second step, 1T (or 1B) containing the target species was collected and the volume of the phase was estimated by the graduation on the centrifuge tubes (not accurately). It was then mixed with an equal volume of opposite blank bottom (or top) phase without SWCNTs from the same ATPE system. In most cases, an appropriate amount of modulating agents (refer to 2.2.1.7.2) was added into the system from the second step. The vortex mixing and the centrifugation were repeated in an identical manner as before at each step during multi-step separation. The labelling system of these fractions is shown in Figure 2.1. Importantly, since the estimated volumes of the factions were not completely accurate, the amount of modulating agents added in the system varies slightly for each repetition of the same separation with the same ssDNA sequence since the effectiveness of the modulators are determined by their final concentration in the separation. Smaller amounts of modulator was used at the very beginning of each step in the multi-step separation and more modulating agents were added (by adding

more volume solution of the same concentration or adding some more concentrated modulator solutions) if it is required.

In order to precipitate the separated SWCNTs from a specific fraction, a final concentration of 2 M NaSCN was added and the mixture was then incubated overnight in the fridge, which was followed by centrifuging at 17 000 g for 10 - 15 min at room temperature to collect the SWCNT pellet at the bottom of the tube. The supernatant was removed and the SWCNTs were redispersed with the addition of deionised water. Furthermore, the long term stability of the SWCNTs dispersion could be improved with addition of a small amount of DNA stock solution to the final concentration of 100 µg mL^{-1} for storage.

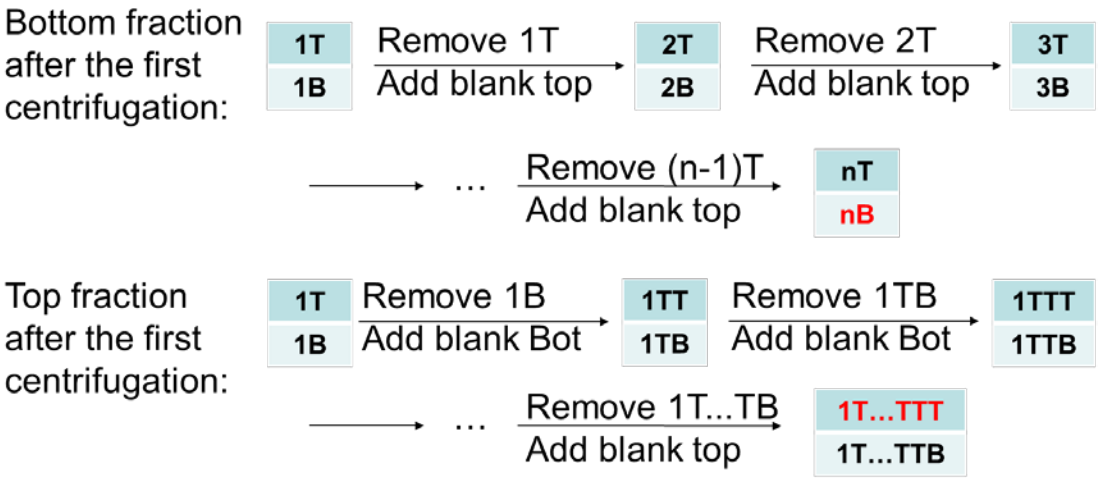

Figure 2.1 Labelling of fractions in ATPE.

2.4 Preparation of CNT-based films as the electrodes

2.4.1 PANI-CNT composite films

In order to study the influence of the ratio of PANI to CNT in the composite film, different volumes of PANI stock solution (refer to 2.2.1.1) were added with a constant volume of CNT dispersion (refer to 2.2.2.1.1). In each individual case, mild sonication (10 min) was performed for both CNT dispersion and PANI solution to ensure homogeneity. 200 µL CNT suspension was diluted by an aqueous Triton X-100 solution (0.01% v/v, 250 mL) with the addition of

different volumes of PANI solution (0, 5.1, 8.8, 17.5, 25, and 35 µL). In order to study the thickness effect on the shape of the incident photon-to-current efficiency (or external quantum efficiency) (IPCE/EQE) curves, 400 µL CNT suspension and 50 µL PANI stock solution were mixed and diluted in the same aqueous medium, which was in the same material ratio as that of 25 µL/200 µL samples (PANI-CNT). The PANI-CNT hybrids were then collected on a filter membrane by vacuum filtration. In detail, with a "stencil" filter membrane (nitrocellulose, 25 nm, VSWP, Millipore, Australia) having 4 × 0.49 cm^2 circular holes, PANI and CNTs were collected onto a membrane filter (mixed cellulose ester, MCE membrane, 0.45 µm, HAWP, Millipore, Australia). It is worth noting that PANI particles can still be collected on the filter because of the their interaction with CNTs even though the pore size of the filter is larger than that of the nylon filters used to filter the PANI solution. The flow rate of the suspension passing the different pore sizes in the "stencil" and membrane filters resulted in a faster flow rate in the patterned circular area, and hence, four identical PANI-CNT membranes were collected on one MCE filter by one filtration, as shown in Figure 2.2. After the filtering the PANI-CNT diluted suspensions, a large amount of deionised water was used to rinse the composite film to remove the residue of Triton X-100. A smaller circular area (0.32 cm^2) was cut out from the MCE filter by a hole punch and used for the fabrication of the solar cells. To investigate the influence of the PANI/CNT composite, 130 µL CNT dispersion and 5.7 µL PANI stock solution were used to fabricate a composite film to target a similar transmittance to that of a pure CNT film made by 200 µL CNT stock dispersion solely. To optimise the thickness of the composite films, the volume ratio (PANI stock solution to CNT suspensions) was kept at a constant level by changing volumes of both materials at the same time (2.7 µL/60 µL, 5.7 µL/130 µL, 6.6 µL/150 µL, 8.8 µL/200 µL and 13.2 µL/300 µL, of PANI to CNT).[7]

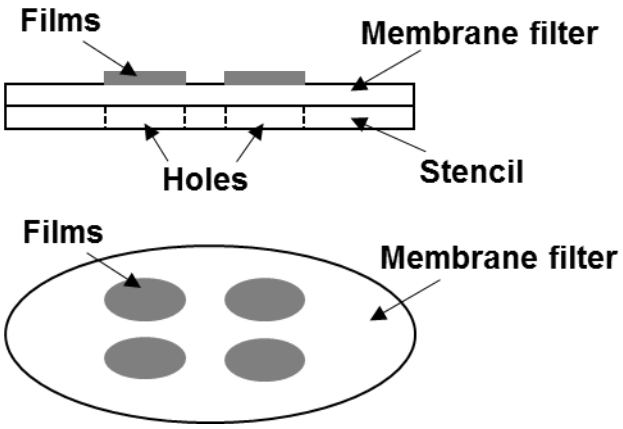

Figure 2.2 Preparation of four identical films with the help of stencil and membrane filters via vacuum filtration.

2.4.2 Pure SWCNT films

In Chapter 4, in order to optimise the grid structure of the front metal electrode, pure SWCNT films were prepared and used to investigate the influence of the different pattern in SWCNT/Si solar cells. Different volumes of SWCNT stock suspension (refer to 2.2.2.1.1) were used to prepare the SWCNT transparent conducting thin films with different optoelectronic properties. The SWCNT stock dispersion was sonicated for 10 min firstly to ensure homogeneity. Then, a particular amount of stock suspension (from 100 to 1300 μL) was diluted with an aqueous Triton X-100 solution (0.01% v/v) to 250 mL. The vacuum filtration process is the same as the description in section 2.4.1.[12]

2.4.3 GOCNT films

Similar to PANI-CNT composite films, the fabrication of GOCNT electrodes started with vacuum filtration.[13] The optoelectronic properties of GOCNT electrodes with different transmittance were studied by vacuum filtration of 250 mL diluted aqueous solution with different volumes of GOCNT stock suspension (200, 300, 400, 500, 600, 700, 800 mL). GOCNT networks were collected on filter membranes made of mixed cellulose ester (MCE, 0.45 μm, HAWP, Millipore, Australia) which were on top of a nitrocellulose membrane (25 nm, VSWP, Millipore, Australia) with four holes (0.49 cm^2 each). A gentle nitrogen flow was used to dry the GOCNT films completely. The individual GOCNT TCF on MCE was then cut with a pair

of scissors and placed into an acetone bath for 3 × 30 min to dissolve the MCE. The now free-floating GOCNT films were then transferred from the acetone bath to a water bath by a homemade Teflon spoon. The GOCNT electrodes were able to float at the interface between air and water, as shown in Figure 2.3. These films were then picked up with a prefabricated Si substrate to prepare solar devices or a microscope glass slide to evaluate the T as well as sheet resistance of the TCFs.

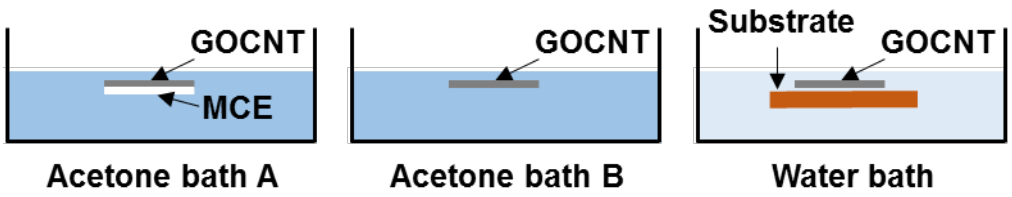

Figure 2.3 Floating transfer of GOCNT films.

2.5 Solar cell fabrication

2.5.1 PANI-CNT/Si

2.5.1.1 As-prepared devices

N-type silicon wafers (phosphorous-doped, 5-10 Ω cm, 525 μm thick with a 100 nm thermal oxide, ABC GmbH, Germany) were used as the starting material for the substrate of the devices. Positive photoresist (AZ1518, microresist technology GmbH, Munich, Germany) was applied onto the wafer by spin coating at 3000 rpm for 30 s, followed by the soft baking (1 min, 100 °C) on a hot plate (AREC heating magnetic stirrer, Rowe Scientific). After cooling the substrate to room temperature, a photo mask was placed on top of the surface of photoresist and ultraviolet light was used to define an active area (0.079 cm^2). The wafer with the defined features was then immersed in a developer bath (AZ 326 MIF, AZ Electronic Materials GmbH, Munich, Germany) for 1 min to develop the photoresist, washed gently with water, and dried under a nitrogen flow. The metal front electrode (Cr/Au (5/145 nm)) was deposited by a dual target sputter coater (Quorumtech, Q300T-D) with a quartz crystal microbalance monitoring the thickness. Then, the substrate was immersed in acetone bath (60 min) to dissolve the rest of the photoresist. One drop of buffered oxide etch (6:1 of 40 % NH_4F and 49 % hydrofluoric

acid (HF), Sigma Aldrich, Australia) was placed on the active area for about 90 s to dissolve the thermal oxide layer (100 nm). The pure CNT/MCE or PANI-CNT/MCE were then placed onto the substrate with a defined active area (CNT or PANI-CNT side down). A water drop was put on the top to wet the membrane and increase the adhesion of the electrode to the Si surface and the excess water absorbed by a tissue. Finally, a piece of Teflon was put on the membrane. The whole device was clamped and baked for 15 min at 80 °C. After cooling the device to room temperature, devices were immersed in 3 ×30 min acetone bath to dissolve the MCE. After scratching of the back oxide layer of the Si, the device was mounted onto a stainless steel plate with gallium indium eutectic (eGaIn) providing the adhesion as well as the carrier transport paths. Such devices were referred to as the "as-prepared" solar cells. For each type of composite film, at least three identical devices were fabricated.[7]

2.5.1.2 Post treatments

There are three post treatments for these composite films. First of all, a droplet of HF (2% in water) was applied in the active area (5 - 10 s), followed by rinsing of the electrode surface with water, ethanol and drying with a nitrogen stream in order to remove the silicon oxide layer created during the film transfer of the device fabrication. Importantly, instead of HF, hydrochloric acid (2 % in water) was used in the identical manner on the glass slides (for the characterisation of the optoelectronic properties of the electrodes) to avoid the reaction between the glass and HF. Secondly, a droplet of $SOCl_2$ was placed onto the PANI-CNT or pure CNT surfaces to chemically dope the electrode by shifting the Fermi level of the CNT below the top of the valence band as well as reduce the junction resistances between individual CNTs.[14] Thirdly, a second 2 % HF treatment was performed in the same manner as the previous one to remove the silicon oxide layer formed by the $SOCl_2$ doping process.[7]

2.5.2 Definition of grid pattern on Si substrate

Photolithography was used to define the Au grid pattern on the Si wafer in a clean room (Class 1000). Positive photoresist (AZ1518, micro resist technology GmbH, Munich, Germany) was spin-coated on the wafer at 3000 rpm for 30 s, followed by soft baking at 100 °C for 50 s on a hot plate (AREC heating magnetic stirrer, Rowe Scientific). After cooling the coated wafer to room temperature, the grid patterns were then defined with a photo mask and a mask aligner

(EVG 610, EVG). Then, the wafer was immersed in a developer bath (AZ 726 MIF, AZ electronic Materials, GmbH, Munich, Germany) for 15-20 s to develop the photoresist on the wafer, rinsed with deionised water and dried under a nitrogen flow. After removal of the photoresist in the area which was not exposed to the UV light, the Si wafer with the defined pattern was subjected to a post baking process at 115 °C for 50 s on a hot plate and then allowed to cool down to the room temperature. The deposition process was the same as the description in section 2.5.1.1.[12]

The grid patterns were applied on both circular and square areas. The radius of the circle was 0.159 cm and thus its area was 0.079 cm^2. The length of the side of the square was 0.3 cm and its area was 0.09 cm^2. Circular and square areas with no metal grid patterns had also been defined and the resulting devices were considered control devices. A smaller square with sides of 0.2 cm and an area of 0.04 cm^2 was defined to investigate the impact of the active area on the solar cell performances. Some “finger” patterns only containing Au lines in one direction were fabricated to further study the influence of the different pattern strategies on the device performance.[12]

2.5.3 spiro-OMeTAD related devices

The preparation of the silicon substrate and the definition of the grid pattern were referred to sections 2.5.1.1 and 2.5.2. In order to prepare GOCNT/Si devices, the free-standing GOCNT on the surface of deionised water was picked up by the Si substrate after removal of the SiO_2 by HF. In terms of the GOCNT-spiro-OMeTAD/Si (and the spiro-OMeTAD/Si control) devices, different volumes of spiro-OMeTAD stock solution (2.5, 10, 20, 30, 40, and 80 µL; 30 µL for the spiro-OMeTAD/Si control device) were spin-coated onto the Si surface for 20 s at 4000 rpm in a nitrogen-filled glovebox after the removal of the SiO_2. Then, these organic material coated Si substrates were heated for 40 min at 80 °C inside the glovebox and then cooled down to the room temperature and used to pick up the GOCNT films from deionised water. For the fabrication of GOCNT/Si and GOCNT/spiro-OMeTAD/Si solar cells, the underside of the silicon was scratched with a diamond pen to remove the oxide layer and create the conduction path from Si to the back electrode after the GOCNT films being dried by a very gentle nitrogen stream. As described in 2.5.1.1, gallium indium eutectic (eGaIn) was used to mount the device onto a stainless steel plate. For the spiro-OMeTAD/Si control device, the substrates were

mounted on the stainless steel plate right after the deposition of spiro-OMeTAD and the removal of the underside of the silicon oxide layer. During the exploration of the role of the organic interlayer in GOCNT/Si devices, 30 µL of stock solution was used to create the interlayer in spin-coating. During the transmittance optimisation of GOCNT in the GOCNT/spiro-OMeTAD/Si devices, 20 µL of stock solution was used to apply the interlayer in spin-coating.

GOCNT TCFs were picked up in the same manner by microscope slide to measure the optical transmittance and the sheet resistance.

2.5.3.2 Post treatments

A post treatment (gold chloride doping) was applied to the GOCNT films. 20 µL of 5 mM $HAuCl_4 \cdot 3H_2O$ (Sigma-Aldrich) aqueous solution was applied on top of GOCNT by spin-coating at 5000 rpm for 20 s.

2.6 Characterisation techniques

2.6.1 PANI-CNT/Si

2.6.1.1 Characterisation of the electrodes

Pure CNT and PANI-CNT on MCE filters were attached to glass slides in a same manner to that described in 2.5.1.1 to evaluate the optical transmittance and the sheet resistance. The transmittance of the films was estimated from the UV-Vis-NIR spectra with the background subtraction of a clean glass slide while the sheet resistance of the films was measured by a four-point probe in linear configuration (Keithlink). The morphology of the surface of the electrodes was characterised by scanning electron microscopy (Inspect F50, FEI). AFM images were recorded in atmosphere by tapping mode and Nanoscope Multimode V controller (Bruker). In order to measure the film thickness, a scalpel was used to make a thin scratch and the edge of the scratch was imaged. Average thickness was evaluated with the depth analysis feature after flattening and plane fitting image with Nanoscope Analysis v1.4.[7]

2.6.1.2 Solar cell performance

The performance of the solar cells (current density versus voltage curves, J–V) was evaluated by a custom Labview virtual instrument connected to a Keithley 2400 source-measure unit. The irradiance of the collimated Xenon-arc light (with an AM 1.5G filter) at the cell surface was calibrated to 100 mW cm^{-2} with a standard cell (PV Measurements, NIST-traceable certification). Both the J-V curves under light and the dark conditions were measured to evaluate the efficiencies and the diode properties of the solar cells. The diode properties were estimated by fitting the linear part of the dark curve to Equation 2.1:

$$J = J_{sat}[e^{\frac{qv}{nkt}} - 1] \qquad \text{Equation 2.1}$$

where J_{sat} is reverse saturation current; q is elemental charge; V is applied voltage; n is ideality; k is Boltzmann constant and T is ambient temperature).[15]

Pseudo internal quantum efficiency (IQE) curves were calculated based on the IPCE curves and the transmittance of the films by (IPCE/T%).[7]

2.6.2 GOCNT/spiro-OMeTAD/Si

The characterisation of the GOCNT or CNT electrodes were covered in section 2.6.1.1 and the performance of the solar cells was tested as described in section 2.6.1.2. In addition, the Schottky barrier height (ϕ_B) can be estimated by Equation 2.2,[16]

$$\phi_B = -kT \ln(\frac{J_{Sat}}{A^* T^2}) \qquad \text{Equation 2.2}$$

where A* is Richardson constant (112 A cm^{-2} K^{-2} for Si).[17]

2.6.3 Separation of SWCNTs

The chirality distribution of SWCNT dispersion and the purity of the purified fraction were determined by UV-Vis-NIR spectrometer (PerkinElmer Lambda 950). The tests were performed by scanning the samples from 250 to 1350 nm with the background subtraction of an aqueous solution of surfactants or polymers at the same concentration without SWCNTs as that of the samples.

REFERENCES:

(1) Batmunkh, M.; Shearer, C. J.; Biggs, M. J.; Shapter, J. G., Solution Processed Graphene Structures for Perovskite Solar Cells. *J. Mater. Chem. A* 2016, *4*, 2605-2616.

(2) Marcano, D. C.; Kosynkin, D. V.; Berlin, J. M.; Sinitskii, A.; Sun, Z.; Slesarev, A.; Alemany, L. B.; Lu, W.; Tour, J. M., Improved Synthesis of Graphene Oxide. *ACS Nano* 2010, *4*, 4806-4814.

(3) Yang, C.; Tang, Y.; Su, Z.; Zhang, Z.; Fang, C., Preparation of Silver Nanowires via a Rapid, Scalable and Green Pathway. *J. Mater. Sci. Technol.* 2015, *31*, 16-22.

(4) Cui, K.; Qian, Y.; Jeon, I.; Anisimov, A.; Matsuo, Y.; Kauppinen, E. I.; Maruyama, S., Scalable and Solid-State Redox Functionalization of Transparent Single-Walled Carbon Nanotube Films for Highly Efficient and Stable Solar Cells. *Adv. Energy Mater.* 2017, *7*, 1700449.

(5) Ao, G. Y.; Khripin, C. Y.; Zheng, M., DNA-Controlled Partition of Carbon Nanotubes in Polymer Aqueous Two-Phase Systems. *J. Am. Chem. Soc.* 2014, *136*, 10383-10392.

(6) Ao, G. Y.; Streit, J. K.; Fagan, J. A.; Zheng, M., Differentiating Left- and Right-Handed Carbon Nanotubes by DNA. *J. Am. Chem. Soc.* 2016, *138*, 16677-16685.

(7) Yu, L. P.; Tune, D.; Shearer, C.; Grace, T.; Shapter, J., Heterojunction Solar Cells Based on Silicon and Composite Films of Polyaniline and Carbon Nanotubes. *IEEE J. Photovolt* 2016, *6*, 688-695.

(8) Blanch, A. J.; Lenehan, C. E.; Quinton, J. S., Parametric analysis of sonication and centrifugation variables for dispersion of single walled carbon nanotubes in aqueous solutions of sodium dodecylbenzene sulfonate. *Carbon* 2011, *49*, 5213-5228.

(9) Blanch, A. J.; Quinton, J. S.; Shapter, J. G., The role of sodium dodecyl sulfate concentration in the separation of carbon nanotubes using gel chromatography. *Carbon* 2013, *60*, 471-480.

(10) Yomogida, Y.; Tanaka, T.; Zhang, M. F.; Yudasaka, M.; Wei, X. J.; Kataura, H., Industrial-scale separation of high-purity single-chirality single-wall carbon nanotubes for biological imaging. *Nat. Commun.* 2016, *7*, 12056.

(11) Yu, L.; Tune, D.; Shearer, C.; Shapter, J., Heterojunction Solar Cells Based on Silicon and Composite Films of Graphene Oxide and Carbon Nanotubes. *ChemSusChem* 2015, *8*, 2940-2947.

(12) Yu, L.; Grace, T.; Dadkhah, M.; Shearer, C.; Shapter, J., Optimization of the Metal Front Contact Design for Single-walled Carbon Nanotube Silicon Heterojunction Solar Cells. *Solar RRL* 2017 1600026.

(13) Wu, F.; Li, X.; Tong, Y.; Zhang, T., Hysteresis Analysis in Dye-Sensitized Solar Cells Based on External Bias Field Effects. *J. Power Sources* 2017, *342*, 704-708.

(14) Jia, Y.; Cao, A. Y.; Bai, X.; Li, Z.; Zhang, L. H.; Guo, N.; Wei, J. Q.; Wang, K. L.; Zhu, H. W.; Wu, D. H.; Ajayan, P. M., Achieving High Efficiency Silicon-Carbon Nanotube Heterojunction Solar Cells by Acid Doping. *Nano Lett.* 2011, *11*, 1901-1905.

(15) Cheung, S. K.; Cheung, N. W., Extraction of Schottky diode parameters from forward current-voltage characteristics. *Appl. Phys. Lett.* 1986, *49*, 85-87.

(16) He, H.; Yu, X.; Wu, Y.; Mu, X.; Zhu, H.; Yuan, S.; Yang, D., 13.7% Efficiency Graphene-Gallium Arsenide Schottky Junction Solar Cells with a P3HT Hole Transport Layer. *Nano Energy* 2015, *16*, 91-98.

(17) Zhang, K.; Wang, L.; Liang, Y.; Yang, S.; Liang, J.; Cheng, F.; Chen, J., A Thermally and Electrochemically Stable Organic Hole-Transporting Material with an Adamantane Central Core and Triarylamine moieties. *Synth. Met.* 2012, *162*, 490-496.

Chapter 3 Heterojunction Solar Cells Based on Silicon and Composite Films of Polyaniline and Carbon Nanotubes

This Chapter has been published as “Heterojunction Solar Cells Based on Silicon and Composite Films of Polyaniline and Carbon Nanotubes” in IEEE Journal of Photovoltaics in 2016.

Yu, L.; Tune, D.; Shearer, C.; Grace, T.; Shapter, J. Heterojunction Solar Cells Based on Silicon and Composite Films of Polyaniline and Carbon Nanotubes. IEEE J. Photovolt 2016. 6, 688-695.

3.1 Overview

Composite films made of single-walled carbon nanotubes and polyaniline are fabricated by a method based on vacuum filtration and transfer from aqueous stock solutions, which have been applied on n-type silicon to create solar cells with PANI-CNT/Si architecture. The influence of the ratios of different constituents in the composite and the thickness of the films on the performance of the solar cells have been studied. It was found that the sheet resistance of the film reduces with the incorporation of the conducting polymer and the amount of light transmitted through to the silicon was determined by the overall thickness of the composite films. With the optimised composition and thickness of the films, devices with a power conversion efficiency of 7.4% are obtained which was a 60% increase over that of devices without the polymer. It was shown by analysing the DC electrical to optical conductivity ratios (refer to 1.2.2.1) of the various films and the dependence of solar cell performance on FOM that the improved output was not only due to better optoelectronic properties but strongly relies on the exact nature of the heterojunction as well, which was related to PANI content in the films.

3.2 Introduction

To realise the needed supply of power using an environmentally friendly approach, research about the replacement of current energy strategies with novel materials [1-2] and methods[3-8] has been a hot topic around the world. Among all of the potential approaches, techniques based on solar energy are extremely attractive due to the relatively simple procedures, the incredible size of the solar resource, and its availability over most of the world. Carbon nanotube/silicon heterojunction solar cells (CNT/Si) are an attractive example because of their fast increases in efficiency,[9-19] and the values from recent reports[20-22] are comparable with those of the commercial solid-state semiconductor-based photovoltaics, which have several issues, such as material scarcity, cost, and toxicity.[23] The architecture of a Si-CNT heterojunction is similar to that of a traditional silicon-based device, with the expensive p-type silicon layer replaced by a transparent conducting electrode (CNT film).[24] When the photons in the incident light beam pass through the CNT film and are absorbed by the silicon layer, excitons (electron–hole pairs)

are created and diffuse into the depletion region near the heterojunction. These excitons are then separated under the influence of the built-in potential across the junction due to the Fermi level equilibration. The holes and the electrons, being the majority charge carriers, are then transported through the CNT network and silicon substrate, respectively.[25]

Polymers, due to the low fabrication cost on large scale,[26-28] have attracted tremendous interest and attention in the past century.[29-31] Recently, there have been a large number of reports about the application of conducting polymers in solar cells,[32-35] and the efficiencies of the devices have been improved to above 10%.[36-45] In previous reports, there are two ways to incorporate polymers into CNT/Si devices, either acting as an antireflection top layer above the CNT film[15,46-47] or an interlayer [48-49] between the CNT network and the Si substrate. Among these intermediate layer materials, polyaniline (PANI) as the emeraldine salt (the most conducting state among all the different forms),[50] is the one of the most effective materials, and the improvements on the device performance are attributed to the creation of a better contact between the CNT network and the silicon surface.[48] A similar effect can be achieved with the application of some other conducting polymers, such as poly(3,4-ethylenedioxythiophene): poly(styrene sulfonate) (PEDOT:PSS) and poly(3-hexylthiophene-2,5-diyl)(P3HT).[49,51] During the past 10 years, studies about the composites based on the conducting polymers and CNTs have revealed some benefits, including enhancement in the flexibility, lower weights, and the excellent conductivity.[52-53] Specifically, CNT networks, providing the transport paths, can considerably improve the charge transport in composite films.[54-55] There is a broad range of applications of these composites, including electrodes for supercapacitors,[56] electrochemical electrodes,[57] and the counter electrodes in dye-sensitized solar cells.[58]

In this Chapter, in order to further investigate the application of the composites based on the conducting polymers and CNTs in CNT/Si solar cells, composite films of PANI and CNTs are prepared via premixing CNTs and PANI in aqueous solutions followed by vacuum filtration. It is expected that by creating more intimate contact over greater areas, the quality of the interface might be improved. The effect of the component ratio in the composite and its thickness on the solar cell performance are also explored. Figure 3.1 shows a schematic architecture of the device studied in this Chapter.

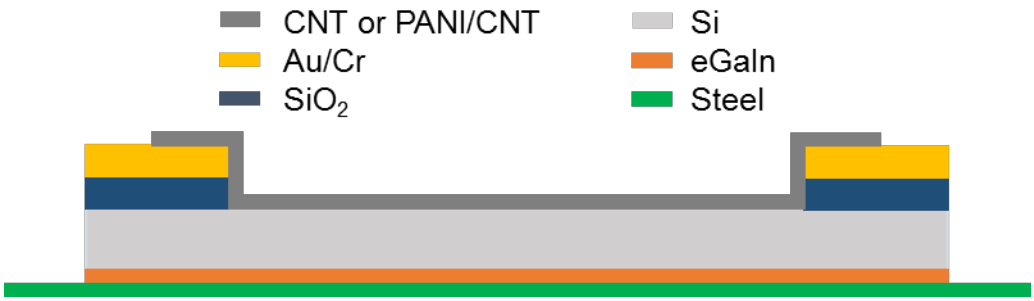

Figure 3.1 Schematic structure of the PANI-CNT/Si solar cells.

3.3 Experimental details

PANI stock solution and CNT stock dispersion were prepared as described in 2.2.1.1 and 2.2.2.1.1. The preparation and characterisation of the electrode are described in sections 2.4.1 and 2.5.1.1. In addition, the method of the device fabrication and the testing of the performance are described in sections 2.6.1 and 2.6.1.2.

3.4 Results and discussion

3.4.1 Ratio of components in the composite film

3.4.1.1 Surface morphologies of the electrodes

PANI-CNT composite films with different component ratios were prepared with a constant amount of CNT suspension and different loadings of PANI stock solution. As shown in Figure 3.2 (from (a) to (f)), the surface roughness increases with PANI loadings in these composite films. The pure CNT film, as shown in Figure 3.2 (a), consists of a random CNT bundling network of poor homogeneity with some dense regions and some vacant areas. With the addition of PANI, the vacant areas are filled with the polymer and fewer isolated CNT bundles are observed, as shown in Figure 3.2 (b) and (c). As the amount of PANI increases, the conducting polymer begins to form a complete covering over the Si surface. In addition, as shown in Figure 3.2 (d), (e) and (f), some large PANI blocks are observed and the individual CNT bundles are less discernible from the PANI-CNT composite surface when compared to the surface of pure CNT film. Therefore, it is confirmed that the conducting polymer has been

successfully collected along with the CNTs during the vacuum filtration-transfer process and dramatically different surface morphologies of PANI-CNT have been created with different PANI content in the composite.

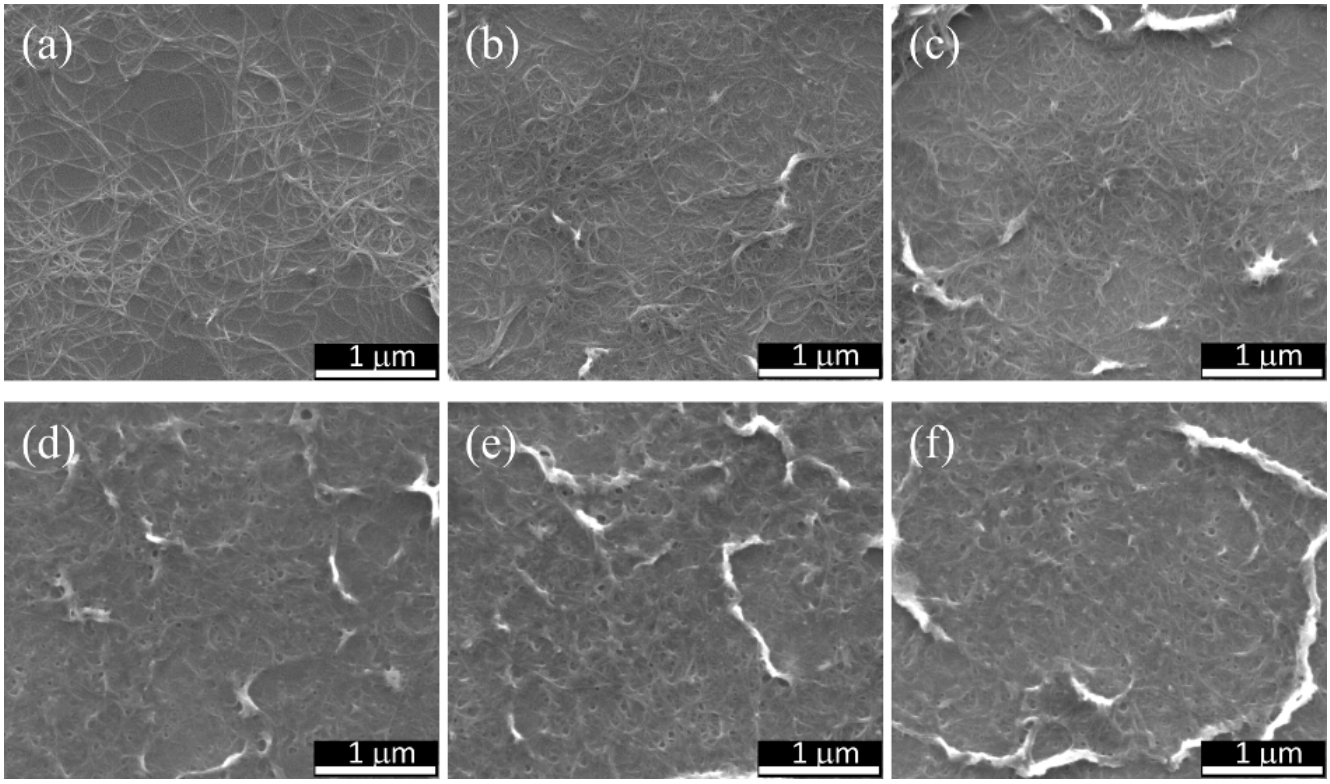

Figure 3.2 SEM images of PANI-CNT composite films prepared with the same amount of CNT dispersions (200 µL) but different loadings of PANI stock solutions. (a) 0 µL, (b) 5.1 µL, (c) 8.8 µL, (d) 17.5 µL, (e) 25 µL and (f) 35 µL.

3.4.1.2 Optoelectronic properties of the transparent conducting electrodes

As shown in Figure 3.3 (a), the transmittance of the film is calculated from the absorbance at 550 nm. The sheet resistance of the pure CNT film and the PANI-CNT composite films are plotted as a function of the transmittance of the films in Figure 3.3 (b). Overall, the films become both less conductive and more transparent with decreasing amounts of PANI in the composite. Meantime, the conducting polymer contributes some absorbance from 400 to 500 nm and in the range of 600–1000 nm (especially at the characteristic peak position, near 825 nm, which is due to the Peierl's gap in the conformation of expanded coil after chemical doping).[59]

The ratio of the DC electrical to optical conductivity (FOM, σ_{DC}/σ_{OP}) was used to compare the optoelectronic properties of these films as well as CNT TCFs from other reports (refer to Equation 1.7 and Equation 1.8) The calculated σ_{DC}/σ_{OP} for these films are shown in Table 3.1. The σ_{DC}/σ_{OP} value decreases with the increase in the amount of PANI added to the composite, which infers that R_{sheet} decreases at a slower rate than T. Since the R_{sheet} of the pure polymer film is extremely high (10^5 Ω sq^{-1}), the FOM is the lowest (less than 0.01). Despite this, adding about 8.8 µL of PANI into the pure CNT network can still evidently decrease R_{sheet} without much loss of T. This reduction is likely due to the formation of a better electrical network with a greater number of percolation pathways from conducting chians of PANI compared to the pure CNT network.[60]

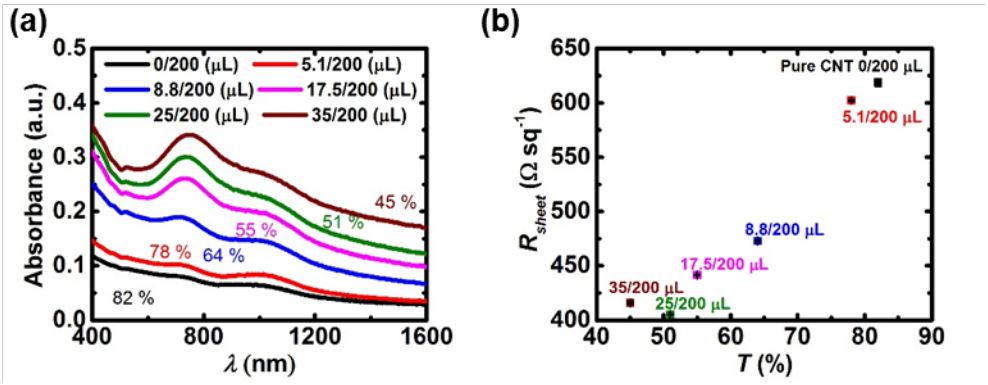

Figure 3.3 (a) The optical absorbance (from 400 to 1600 nm) of pure CNT and PAN-CNT composites. (b) Sheet resistance of pure CNT and PANI-CNT hybrid electrodes as a function of the optical absorbance (after all three chemical treatments). Labels are volume of PANI dispersion/volume of CNT dispersion.

Table 3.1 Calculated FOM of pure CNT, pure PANI and PANI-CNT composite films

	Pure CNT	5.1/200 (µL/µL)	8.8/200 (µL/µL)	17.5/200 (µL/µL)	25/200 (µL/µL)	35/200 (µL/µL)	Pure PANI
σ_{DC}/σ_{OP}	2.7	2.3	1.8	1.5	1.4	1.1	0.0043

3.4.1.3 Performance of solar cells

The performance of the solar cells with the pure CNTs, pure PANI, and PANI-CNT composite films are listed in Table 3.2 and plotted in Figure 3.4. The J–V curves under light conditions of

the devices with the pure CNT film and films with different ratio of PANI to CNT are shown in Figure 3.4 (a). A specific device with the highest observed efficiency of 6.44 % was prepared after forming the heterojunction with a ratio of 0.044 PANI:CNT (volume ratio; 8.8 µL PANI and 200 µL CNT stock solution) in the hybrid film.

Table 3.2 The detailed performance of devices with pure CNT, PANI-CNT with different PANI loadings, and pure PANI. The performance of the best device in each group are shown in brackets.

PANI/CNT (µL/µL)	J_{SC} (mA cm^{-2})	V_{OC} (V)	FF	Average Efficiency (%)	Ideality	J_{sat} (mA cm^{-2})	R_{series} (Ω)
0/200	23.7 ± 0.6 (24.1)	0.53 ± 0.01 (0.53)	0.37 ± 0.02 (0.38)	4.59 ± 0.34 (4.86)	2.1 ± 0.1 (2.0)	3.95×10^{-4} ± 7.45×10^{-5} (3.86×10^{-4})	186 ± 19 (179)
5.1/200	26.2 ± 0.6 (25.8)	0.51 ± 0.03 (0.53)	0.42 ± 0.02 (0.42)	5.55 ± 0.33 (5.77)	2.3 ± 0.1 (2.3)	3.95×10^{-4} ± 1.09×10^{-4} (3.37×10^{-4})	165 ± 24 (152)
8.8/200	23.1 ± 0.6 (23.1)	0.48 ± 0.01 (0.49)	0.56 ± 0.01 (0.57)	6.21 ± 0.22 (6.44)	2.1 ± 0.1 (2.0)	8.90×10^{-5} ± 8.06×10^{-6} (8.87×10^{-5})	75 ± 8 (69)
17.5/200	21.5 ± 0.4 (21.2)	0.56 ± 0.03 (0.57)	0.51 ± 0.03 (0.51)	6.01 ± 0.21 (6.17)	1.8 ± 0.1 (1.7)	6.20×10^{-5} ± 2.50×10^{-5} (5.78×10^{-5})	93 ± 18 (86)
25/200	21.3 ± 0.5 (21.7)	0.48 ± 0.02 (0.49)	0.53 ± 0.02 (0.54)	5.43 ± 0.47 (5.76)	1.7 ± 0.1 (1.6)	5.41×10^{-5} ± 1.34×10^{-5} (4.76×10^{-5})	109 ± 17 (98)
35/200	19.8 ± 0.5 (20.1)	0.40 ± 0.01 (0.40)	0.37 ± 0.02 (0.39)	2.96 ± 0.40 (3.21)	1.6 ± 0.1 (1.5)	2.03×10^{-5} ± 9.98×10^{-6} (2.05×10^{-5})	182 ± 18 (169)
Pure PANI	4.8 ± 0.3 (4.5)	0.38 ± 0.01 (0.38)	0.35 ± 0.01 (0.36)	0.62 ± 0.14 (0.72)	2.6 ± 0.2 (2.5)	4.78×10^{-3} ± 4.71×10^{-4} (4.77×10^{-3})	189 ± 29 (173)

With a small amount of PANI (5.1 µL) used in the composite film, the short-circuit current density (J_{sc}) improved from 23.5 to 26.0 mA cm^{-2}, although further increase in the polymer content showed a decrease in the J_{SC} of the devices, while the PANI/Si devices without CNTs produced much less current (4.7 mA cm^{-2}), as shown in Figure 3.4 (b). However, with higher PANI loading, the T is significantly decreased without further improvement in the optoelectronic properties. This was further evidenced by the overall reduction in the IPCE signal when large

amounts of PANI (17.5, 25, and 35 µL) were applied (Figure 3.4 (c)). As shown in Figure 3.4 (d), when a very thick film containing a large amount of polymer in the hybrid film was used in the fabrication of device, open-circuit voltages (V_{OC}) decreased considerably to ~0.4 V. This could be explained by the fact that the PANI began to dominate the heterojunction properties since the V_{OC} for PANI/Si devices is less than 0.4 V. In terms of the fill factor (FF), as shown in Figure 3.4 (e), lower loadings of polymer (5.1, 8.8, 17.5, and 25 µL) in the composite electrodes effectively enhanced the performance, but an excessive amount of PANI (35 µL) in the composite again had an adverse effect. The power conversion efficiency (PCE, Figure 3.4 (f)) also changed with PANI loading, with the 8.8 µL/200 µL device having the best average performance (PCE of 6.2%). As the content of polymer increased, the PANI again dominated the performance and the efficiency of the devices decreased considerably to below 3 %. Since there were large errors in R_{shunt}, it seemed that there is not a clear trend with the loadings of polymer (not shown here). For low polymer loadings, the series resistance (R_{series}) of the devices decreased compared with that of CNT/Si devices but with higher PANI loadings in the composite, R_{series} increased. The lowest R_{series} was for the hybrid films of T = 64 % (PANI/CNT volumes: 8.8 µL/200 µL), and it showed a reverse trend to that of the efficiency, as shown in Figure 3.4 (g). The R_{series} of PANI/Si was much higher than that of other devices, which was possible a result of the much higher R_{sheet} of the PANI electrode.

In terms of the diode properties, as shown in Figure 3.4 (h), with low loading of polymer (5.1 µL), the ideality of the devices increased to 2.2, but it then reduced to around 1.5 with higher contents of PANI in the films. A similar tendency was observed with the reverse saturation current density (J_{sat}), as shown in Figure 3.4 (i). These two properties together indicated that the heterojunction quality improved with increasing polymer content, which could be due to the reduction of charge traps, and the resulting increased lifetime of the carrier at the heterojunction.

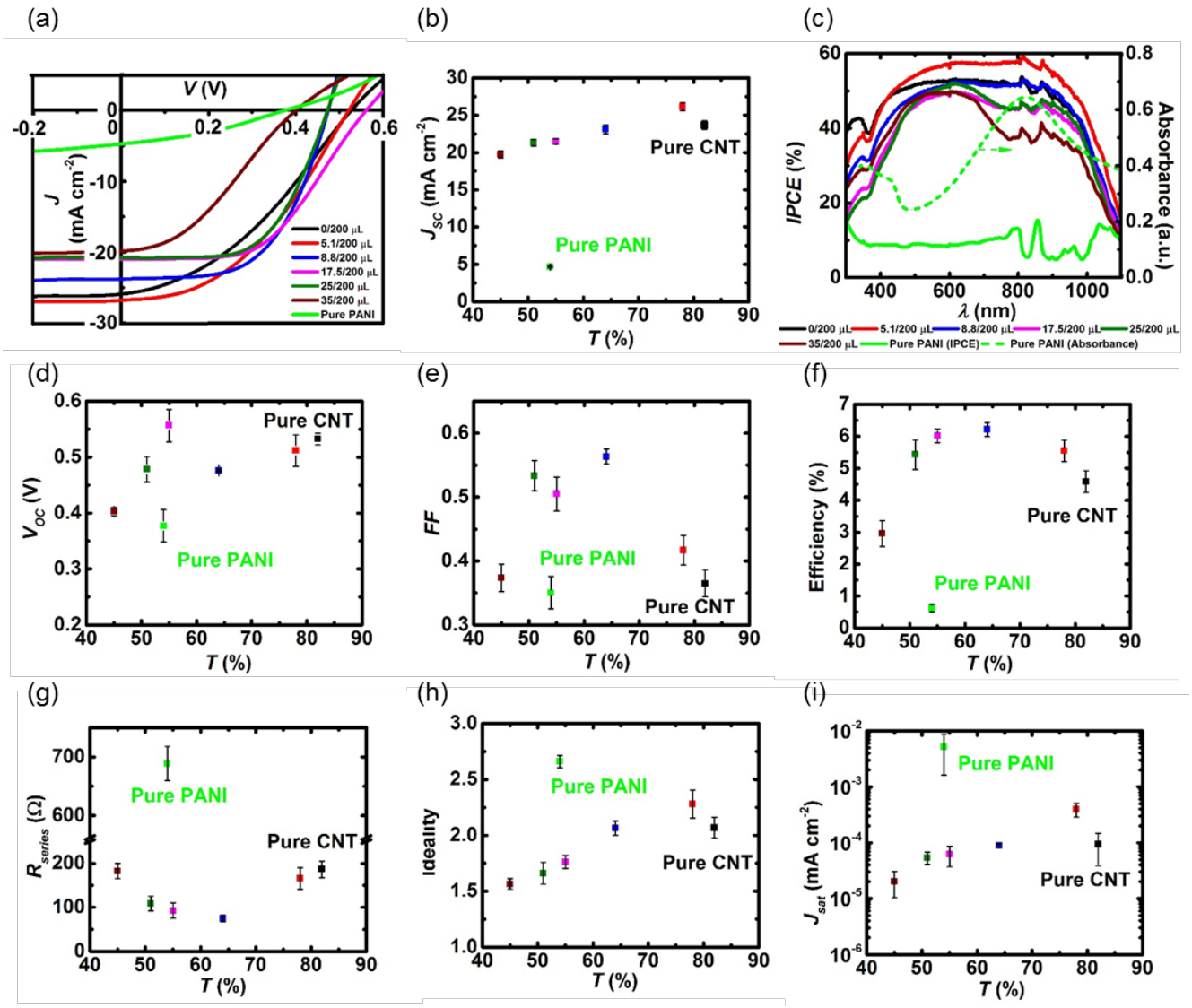

Figure 3.4 The performance of the PANI/Si, CNT/Si and PANI-CNT/Si devices. (a) J-V curves under light conditions, (b) J_{SC}; (c) IPCE, (d) V_{OC}, (e) FF, (f) Efficiency, (g) R_{series}, (h) Ideality and (i) J_{sat}.

3.4.1.4 Further analysis of IPCE

Figure 3.4 (c) compares the IPCE of solar cells with varied proportions of PANI in the composite films. The reduction in IPCE from 600 to 900 nm and in the UV region in these devices with composite films was attributed to the strong polymer absorbance in these regions, especially when high loadings of PANI were applied (17.5, 25, and 35 µL). The IPCE curves of PANI-CNT/Si devices with PANI-CNT films with two different thicknesses (119 and 234 nm,

measured by AFM) but the same material ratio (PANI/CNT: 25 µL/200 µL and 50 µL/400 µL), are plotted in Figure 3.5 (a) (solid). For the device with thicker electrode, the decrease in IPCE caused by polymer absorption is no longer observed. We speculate that this change of curve shape and the shifting of the maximum IPCE wavelength may be caused by the optical interference effects within the film.[61-62] The pseudo IQE of these two films was calculated to further investigate the internal mechanism of the devices,[61] also plotted in Figure 3.5 (a). The pseudo IQE exhibits a more intense peak for devices with the thicker electrode and we hypothesise offsets the absorption of light because of the presence of polymer. However, the increase in IQE could also be introduced by interference effects in the thicker films (thickness is above 200 nm) resulting in the wavelength-dependent interference at the heterojunction.[61-62]

PANI/Si devices had a very low IPCE signal as expected from the poor optoelectronic properties of thin PANI films, and these devices had the worst performance in all aspects. The pseudo IQE curves of devices of PANI-CNT/Si with films in various ratios and CNT/Si are shown in Figure 3.5 (b) (solid). After applying different loadings of PANI, the intensity of IQE seems to increase, which might further support the assumption that a better junction is formed with silicon by PANI-CNT than pure CNT network.

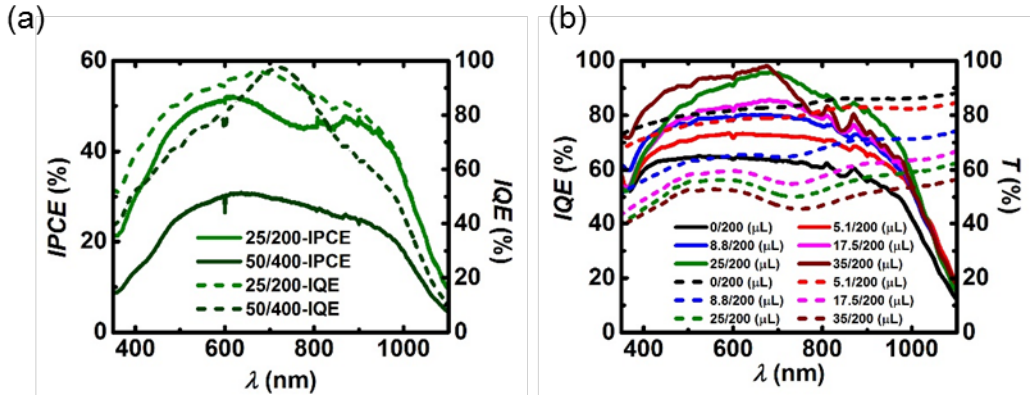

Figure 3.5 (a) IPCE (solid) and IQE (short dash) of the PANI-CNT/Si devices with PANI-CNT composites in different thicknesses but the same ratio. (b) IQE (solid curves) and transmittance (short dash) of CNT/Si and PANI-CNT/Si devices.

3.4.1.5 Relationship between efficiency and FOM

The relationship between FOM and PCE is plotted in Figure 3.6. There is no linear correlation between the efficiency of the solar cells and the FOM values. This is because the solar cell performance depends on the absolute photon flux reaching to the silicon as well. Though devices with thicker films have better optoelectronic properties, sometimes, the devices have lower efficiency due to the absorbance of the light by the electrode. The film with highest FOM values (the pure CNT film) does not achieve the highest efficiency, but in this case, it is also likely caused by inhomogeneity of the surface coverage. Thus, the combination of an appropriate amount of conducting polymer with the CNT network to create a composite film enhances the device performance since the improved performance in those PANI-CNT/Si devices occurs with a better heterojunction, even though fewer incident photons arrive at the silicon surface. The ratio of 0.044 (PANI/CNT) had the best performance among all PANI-CNT/Si devices, and films with this optimised ratio were investigated further.

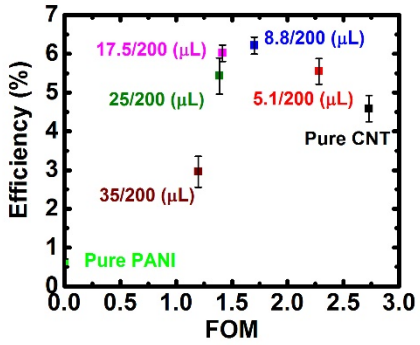

Figure 3.6 PCE versus FOM of PANI-CNT films in different content ratios.

3.4.2 The role of PANI

3.4.2.1 Characterisation of the transparent conducting electrode

In order to investigate the role of PANI in the hybrid films, pure CNT and PANI-CNT films (with the optimised components ratio, PANI/CNT = 0.044) were prepared with similar transmittance over the visible range (T = 82 %), as shown in Figure 3.7 (a). For pure CNT film, the absorbance generally increases with decreasing wavelength while the wide absorbance feature at about 800 nm caused by PANI broadens the peak of CNT at 700 nm slightly, which is the spectroscopic evidence that PANI was incorporated into the composite electrode. Meanwhile, the SEM images in Figure 3.7 (b) illustrate the presence of an amorphous material

on and between the CNT networks. As shown in the inset in Figure 3.7 (a), the pure CNT electrode has a slightly higher R_{sheet} of than that of its composite counterpart at the same transmittance.

The FOM values are 2.7 and 3.1 for pure CNT and PANI-CNT composite, respectively, which were different from what was observed during the optimisation of the component ratio (FOM increased with decreasing PANI content), since now the PANI-CNT electrode has the same T at 550 nm but lower R_{sheet}.

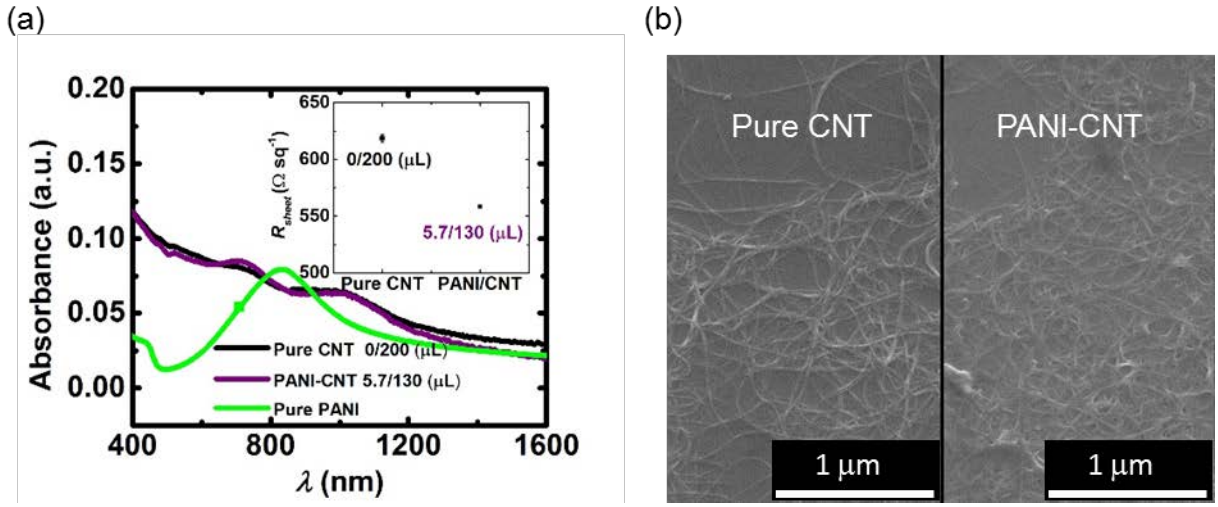

Figure 3.7 (a) Vis-NIR spectra of the pure CNT and the PANI-CNT with the optimised ratio 0.044 (5.7 µL/130 µL) electrode after all post treatments. (b) SEM images of pure CNT (left) and PANI-CNT (right) electrode on silicon.

3.4.2.2 Performance of the solar cells

Typical J-V curves of CNT/Si and PANI-CNT/Si devices under light conditions are shown in Figure 3.8 (a). The efficiency of the device with PANI-CNT electrode is higher than that of the counterpart with a pure CNT electrode (6.67 % versus 5.11%). In more detail, as shown in Figure 3.8 (b), the devices with the hybrid electrodes had higher J_{SC}, V_{OC}, FF, and PCE values than the control devices without polymer in the window electrode. Additionally, the lower ideality factor indicates that the diode properties of polymer related device are better as well.

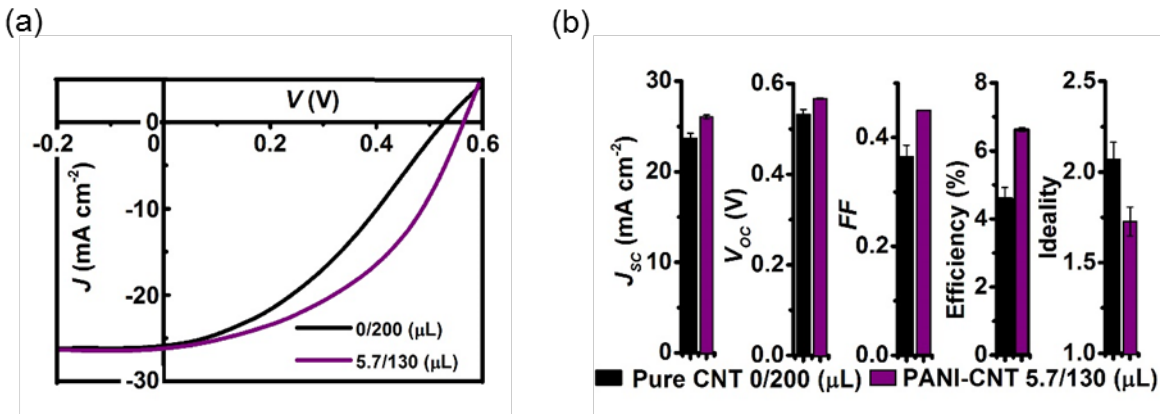

Figure 3.8 (a) Typical J-V curves of CNT/Si and PANI-CNT/Si devices after all three post treatments. (b) Comparison between performance of the CNT/Si and PANI-CNT/Si devices in terms of J_{SC}, V_{OC}, FF, PCE and Ideality.

3.4.3 Thickness of PANI-CNT films

3.4.3.1 Optoelectronic properties of the transparent conducting electrodes

As discussed in Chapter 1, the thickness of the transparent electrode has a significant influence on the performance of solar cells. Here, in order to optimise the ideal thickness at the optimal component ratio, a series of hybrid electrodes were prepared with the same content (in percentage) of individual material (PANI and CNT) but different transmittances.

As shown in Figure 3.9 (a), as the amount of each individual component increases in the preparation of composite films, the overall absorbance increases, and as a result, the transmittance of the film decreases from 91 % to 52 % at 550 nm. The thicknesses of these films are measured by AFM, and they are 13, 26, 38, 48 and 63 nm. In addition, the R_{sheet} decreases (from above 2500 Ω sq^{-1} to below 250 Ω sq^{-1}) with the increasing thickness from 13 to 63 nm as more percolation paths are formed in thicker films/denser CNT networks to transport the charge carriers, as shown in Figure 3.9 (b). For the thinnest film (13 nm, T = 91 %), the R_{sheet} is much higher than the rest, which is possibly due to a limited number of conducting paths in the CNT network.

In terms of the FOM of these films, as shown in Figure 3.9 (c), the thinnest film (13 nm, 91 %) has the lowest value while the decrease in T by approximately 10 % can significantly improve

the optoelectronic properties of the devices (FOM is above 3). However, further increase in the thickness (from 26 to 48) results in decreased values due to the limited improvement in R_{sheet} but decrease in transmittance. The FOM of the 62 nm film is higher than that of 38 and 48 nm counterparts due to the dramatic decrease in the R_{sheet} to below 250 Ω sq^{-1}. Overall, for the application of the thin film photovoltaics, the 26 nm film thickness seems to have the best optoelectronic properties and the effect of film thickness on the solar cell performance is further analysed in the following section.

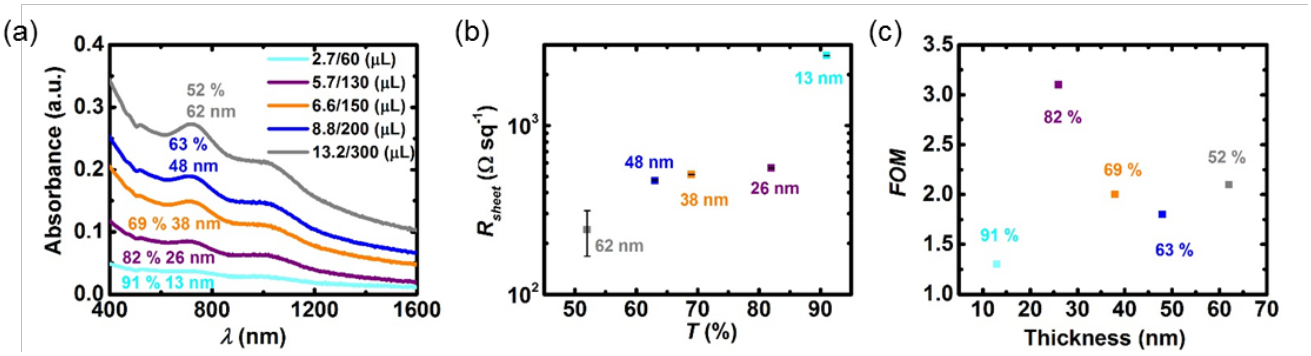

Figure 3.9 (a) Vis-NIR spectra, (b) sheet resistance and (c) FOM of the PANI-CNT hybrid films at the optimal components ratio but different thickness.

3.4.3.2 Performance of the solar cells

The J-V curves of typical devices with the same optimal component ratio but different thicknesses are shown in Figure 3.10 (a), where a device with a 38 nm hybrid electrode (T = 69 %) shows a highest observed efficiency of 7.42 %. In general, devices with 38 nm composite films had the best performance of above 7 %, as shown in Figure 3.10 (b), while the devices with the thinnest films (13 nm, T = 91 %) yielded the worst performance, less than 4 % efficiency. Compared to devices with the same optimal ratio in previous sections, the higher efficiency was caused by the enhanced light absorption by the silicon layer and more excitons were produced. The details of the performance of these devices are shown in Table 3.3 and plotted in Figure 3.10.

The J_{SC} increased gradually as the films became thinner and thinner (from 62 nm to 26 nm) due to the increasing amount of light passing through and reaching the Si surface, and it then decreased for the extremely thin films (13 nm) because of its high sheet resistance, as shown

in Figure 3.10 (c). The V_{OC} peaked at devices with 38 nm PANI-CNT electrode, with a slight decrease for devices coated with thinner films (13 and 26 nm) but a significant decrease (below 0.5 V, which is similar to that of the devices with a regrown silicon dioxide layer after several days from fabrication[49]) for devices applied with thicker films (48 and 62 nm), as shown in Figure 3.10 (d). It is possible that the polymer in these thick films protects the insulating silicon oxide layer from being etched by the HF treatment. There was a decreasing trend in the FF as the thickness of the films decreased from 62 to 13 nm, as shown in Figure 3.10 (e), which was probably due to the lower R_{sheet} of the thicker films with more conducting paths. The error bars in R_{shunt} were large (not shown here) and thus no clear trend was observed. The devices with 38 nm films had the lowest R_{series}, as shown in Figure 3.10 (f), which had a reverse trend as that of the efficiencies. In addition, the R_{series} for 13 nm film coated devices was much higher than others probably due to a worse heterojunction.

Table 3.3 The performance details of PANI-CNT/Si devices with different thicknesses at the same optimal component ratio. The performance of the best device in each group are shown in the brackets.

Average thickness (nm)	J_{SC} (mA cm^{-2})	V_{OC} (V)	FF	Efficiency (%)	Ideality	J_{sat} (mA cm^{-2})	R_{series} (Ω)
13	15.2 ± 0.1 (15.2)	0.55 ± 0.01 (0.58)	0.39 ± 0.01 (0.39)	3.26 ± 0.57 (3.43)	2.3 ± 0.1 (2.2)	8.57×10^{-3} ± 1.43×10^{-3} (7.98×10^{-3})	188 ± 8 (182)
26	26.0 ± 0.2 (25.9)	0.57 ± 0.00 (0.57)	0.45 ± 0.00 (0.45)	6.63 ± 0.06 (6.65)	1.7 ± 0.1 (1.6)	2.22×10^{-6} ± 9.95×10^{-7} (2.32×10^{-6})	95 ± 2 (94)
38	25.0 ± 0.4 (25.4)	0.58 ± 0.00 (0.58)	0.49 ± 0.01 (0.5)	7.22 ± 0.29 (7.42)	1.9 ± 0.1 (1.8)	8.52×10^{-6} ± 7.06×10^{-7} (8.53×10^{-6})	57 ± 4 (55)
48	23.1 ± 0.6 (23.1)	0.48 ± 0.01 (0.49)	0.56 ± 0.01 (0.57)	6.21 ± 0.22 (6.44)	2.1 ± 0.1 (2.0)	8.90×10^{-5} ± 8.06×10^{-6} (8.87×10^{-5})	75 ± 8 (69)
62	20.9 ± 0.9 (20.1)	0.46 ± 0.01 (0.47)	0.58 ± 0.01 (0.58)	5.46 ± 0.16 (5.49)	2.2 ± 0.1 (2.2)	4.54×10^{-4} ± 1.45×10^{-4} (4.50×10^{-4})	104 ± 18 (98)

In terms of the diode properties, a better heterojunction seemed to be created with the decrease in the thickness from 62 nm to 26 nm with the same ratio, where lower ideality and

J_{sat} values were achieved, as shown in Figure 3.10 (g) and (h). The exception existed in the devices with the thinnest films (13 nm). This is again most likely due to the extremely sparse PANI-CNT network which is not able to form a good heterojunction with the beneath Si layer.

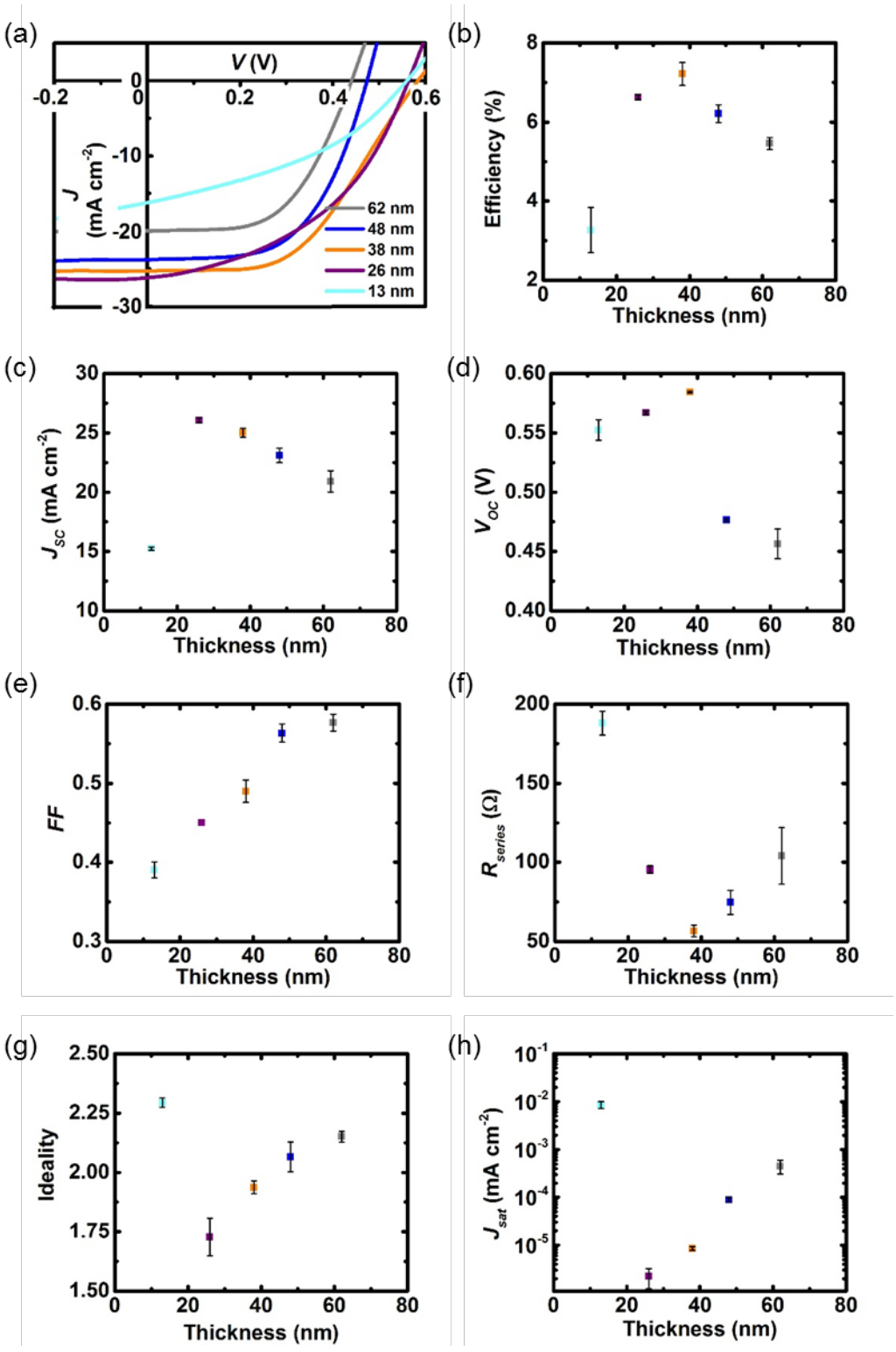

Figure 3.10 Performance of the PANI-CNT/Si devices with hybrid films of different thicknesses but the identical optimal component ratio. (a) J-V curves of typical devices

under light conditions, (b) Efficiency, (c) J_{SC}, (d) V_{OC}, (e) FF, (f) R_{series}, (g) Ideality and (h) J_{sat}.

3.4.3.3 Relationship between efficiency and FOM

The efficiency of the devices as a function of FOM is plotted in Figure 3.11. There seems no clear correlation between these two parameters, in which the films with the best FOM value does not lead to the devices with the best performance. However, the worst performing devices have the lowest FOM value among all of these films. It suggests that the performance of the devices is not entirely dependent on the optoelectronic properties of the TCFs, and the quality of the heterojunction also plays an important role in these devices.

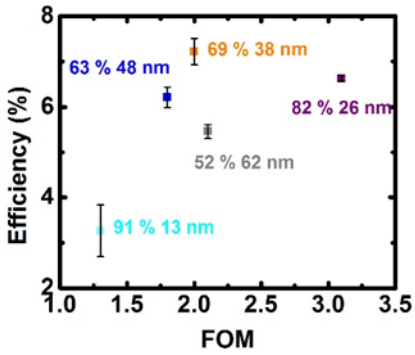

Figure 3.11 Efficiency versus FOM for PANI-CNT/Si devices with films in the same component ratio but different thicknesses.

With the preparation of the PANI-CNT composite films, one of the limitations of CNTs in CNT/Si solar cells is overcome, namely, the incomplete contact between the sparse CNT network and the underneath Si light absorbing layer. This finding is evidenced by the fact that the devices with the highest efficiency were fabricated with hybrid films which did not have the best optoelectronic properties. Future work in this field might be to replace PANI with another conducting polymer having limited absorbance in the same wavelength range as silicon so that large amount of polymer could be applied on the Si surface. These findings are also relevant to other carbon material-based photovoltaics, including graphene–silicon solar cells.[63]

3.5 Conclusions

Single-walled carbon nanotubes were combined with polyaniline to create a homogenous composite electrode by a simple vacuum filtration process, and the resulting films were used as the transparent conducting electrodes (p-type) on silicon (n-type) to form heterojunction solar cells. It is found that the addition of conducting polymer into CNT network can significantly reduce the sheet resistance and therefore enhance the performance of the photovoltaics. By studying the influence of the component ratio on the solar cell performance, the efficiency of the devices was increased dramatically after the optimisation of the film composition. The role of the conducting polymer was further investigated and it was found that the polymer played an important role in the formation of a good heterojunction. In addition, the thickness of the composite film was optimised with the efficiency of the best device above 7.4 %. More importantly, the results in this Chapter indicate that the morphology at the interface, which determines the heterojunction quality, is more important than the optoelectronic properties of the transparent conducting films applied on top of Si in such devices.

REFERENCES:

(1) Amouroux, J.; Siffert, P.; Massue, J. P.; Cavadias, S.; Trujillo, B.; Hashimoto, K.; Rutberg, P.; Dresvin, S.; Wang, X. H., Carbon dioxide: A new material for energy storage. *Prog. Nat. Sci.* 2014, *24*, 295-304.

(2) Wong, K. T.; Bassani, D. M., Energy transfer in supramolecular materials for new applications in photonics and electronics. *NPG Asia Mater.* 2014, *6*, 10.

(3) Cao, L.; Su, D.; Tang, Y. J.; Fang, G. Y.; Tang, F., Properties evaluation and applications of thermal energy storage materials in buildings. *Renew. Sust. Energ. Rev.* 2015, *48*, 500-522.

(4) Carlisle, J. E.; Kane, S. L.; Solan, D.; Bowman, M.; Joe, J. C., Public attitudes regarding large-scale solar energy development in the US. *Renew. Sust. Energ. Rev.* 2015, *48*, 835-847.

(5) Dalton, G.; Allan, G.; Beaumont, N.; Georgakaki, A.; Hacking, N.; Hooper, T.; Kerr, S.; O'Hagan, A. M.; Reilly, K.; Ricci, P.; Sheng, W. N.; Stallard, T., Economic and socio-economic assessment methods for ocean renewable energy: Public and private perspectives. *Renew. Sust. Energ. Rev.* 2015, *45*, 850-878.

(6) Galik, C. S., Exploring the determinants of emerging bioenergy market participation. *Renew. Sust. Energ. Rev.* 2015, *47*, 107-116.

(7) Wang, S. F.; Wang, S. C., Impacts of wind energy on environment: A review. *Renew. Sust. Energ. Rev.* 2015, *49*, 437-443.

(8) Webb, D. J., Tides and tidal energy. *Contemp. Phys.* 1982, *23*, 419-442.

(9) Behnam, A.; Johnson, J. L.; Choi, Y. H.; Ertosun, M. G.; Okyay, A. K.; Kapur, P.; Saraswat, K. C.; Ural, A., Experimental characterization of single-walled carbon nanotube film-Si Schottky contacts using metal-semiconductor-metal structures. *Appl. Phys. Lett.* 2008, *92*, 3.

(10) Tune, D. D.; Flavel, B. S.; Krupke, R.; Shapter, J. G., Carbon Nanotube-Silicon Solar Cells. *Adv. Energy Mater.* 2012, *2*, 1043-1055.

(11) Jia, Y.; Wei, J.; Wang, K.; Cao, A.; Shu, Q.; Gui, X.; Zhu, Y.; Zhuang, D.; Zhang, G.; Ma, B.; Wang, L.; Liu, W.; Wang, Z.; Luo, J.; Wu, D., Nanotube-Silicon Heterojunction Solar Cells. *Adv. Mater.* **2008**, *20*, 4594-4598.

(12) Li, Z. R.; Kunets, V. P.; Saini, V.; Xu, Y.; Dervishi, E.; Salamo, G. J.; Biris, A. R.; Biris, A. S., $SOCl_2$ enhanced photovoltaic conversion of single wall carbon nanotube/n-silicon heterojunctions. *Appl. Phys. Lett.* **2008**, *93*, 3.

(13) Jia, Y.; Li, P. X.; Wei, J. Q.; Cao, A. Y.; Wang, K. L.; Li, C. L.; Zhuang, D. M.; Zhu, H. W.; Wu, D. H., Carbon Nanotube Films by Filtration for Nanotube-Silicon Heterojunction Solar Cells. *Mater. Res. Bull.* **2010**, *45*, 1401-1405.

(14) Wadhwa, P.; Liu, B.; McCarthy, M. A.; Wu, Z. C.; Rinzler, A. G., Electronic Junction Control in a Nanotube-Semiconductor Schottky Junction Solar Cell. *Nano Lett.* **2010**, *10*, 5001-5005.

(15) Jia, Y.; Li, P.; Gui, X.; Wei, J.; Wang, K.; Zhu, H.; Wu, D.; Zhang, L.; Cao, A.; Xu, Y., Encapsulated Carbon Nanotube-Oxide-Silicon Solar Cells with Stable 10% Efficiency. *Appl. Phys. Lett.* **2011**, *98*, 133115.

(16) Jia, Y.; Cao, A. Y.; Kang, F. Y.; Li, P. X.; Gui, X. C.; Zhang, L. H.; Shi, E. Z.; Wei, J. Q.; Wang, K. L.; Zhu, H. W.; Wu, D. H., Strong and Reversible Modulation of Carbon Nanotube-Silicon Heterojunction Solar Cells by an Interfacial Oxide Layer. *Phys. Chem. Chem. Phys.* **2012**, *14*, 8391-8396.

(17) Tune, D. D.; Hennrich, F.; Dehm, S.; Klein, M. F. G.; Glaser, K.; Colsmann, A.; Shapter, J. G.; Lemmer, U.; Kappes, M. M.; Krupke, R.; Flavel, B. S., The Role of Nanotubes in Carbon Nanotube-Silicon Solar Cells. *Adv. Energy Mater.* **2013**, *3*, 1091-1097.

(18) Tune, D. D.; Shapter, J. G., Effect of Nanotube Film Thickness on the Performance of Nanotube-Silicon Hybrid Solar Cells. *Nanomaterials* **2013**, *3*, 655-673.

(19) Tune, D. D.; Blanch, A. J.; Krupke, R.; Flavel, B. S.; Shapter, J. G., Nanotube Film Metallicity and Its Effect on the Performance of Carbon Nanotube-Silicon Solar Cells. *Phys. Status Solidi A-Appl. Mat.* **2014**, *211*, 1479-1487.

(20) Shi, E. Z.; Zhang, L. H.; Li, Z.; Li, P. X.; Shang, Y. Y.; Jia, Y.; Wei, J. Q.; Wang, K. L.; Zhu, H. W.; Wu, D. H.; Zhang, S.; Cao, A. Y., TiO2-Coated Carbon Nanotube-Silicon Solar Cells With Efficiency of 15%. *Sci Rep* **2012**, *2*, 884.

(21) Li, X. K.; Jung, Y.; Sakimoto, K.; Goh, T. H.; Reed, M. A.; Taylor, A. D., Improved Efficiency of Smooth and Aligned Single Walled Carbon Nanotube/Silicon Hybrid Solar Cells. *Energy Environ. Sci.* **2013**, *6*, 879-887.

(22) Jung, Y.; Li, X. K.; Rajan, N. K.; Tayor, A. D.; Reed, M. A., Record High Efficiency Single-Walled Carbon Nanotube/Silicon P-N Junction Solar Cells. *Nano Lett.* **2013**, *13*, 95-99.

(23) Saini, V.; Bourdo, S. E.; Abdulrazzaq, O.; Dervishi, E.; Kannarpady, G. K.; Biris, A. S., Performance Dependence of SWCNT/N-Silicon Hybrid Solar Cells on the Charge Carrier Concentration in Silicon Substrates. *RSC Adv.* **2015**, *5*, 621-627.

(24) Wei, J. Q.; Jia, Y.; Shu, Q. K.; Gu, Z. Y.; Wang, K. L.; Zhuang, D. M.; Zhang, G.; Wang, Z. C.; Luo, J. B.; Cao, A. Y.; Wu, D. H., Double-Walled Carbon Nanotube Solar Cells. *Nano Lett.* **2007**, *7*, 2317-2321.

(25) Jia, Y.; Cao, A. Y.; Bai, X.; Li, Z.; Zhang, L. H.; Guo, N.; Wei, J. Q.; Wang, K. L.; Zhu, H. W.; Wu, D. H.; Ajayan, P. M., Achieving High Efficiency Silicon-Carbon Nanotube Heterojunction Solar Cells by Acid Doping. *Nano Lett.* **2011**, *11*, 1901-1905.

(26) Drury, C. J.; Mutsaers, C. M. J.; Hart, C. M.; Matters, M.; de Leeuw, D. M., Low-cost all-polymer integrated circuits. *Appl. Phys. Lett.* **1998**, *73*, 108-110.

(27) Ting, C. J.; Huang, M. C.; Tsai, H. Y.; Chou, C. P.; Fu, C. C., Low cost fabrication of the large-area anti-reflection films from polymer by nanoimprint/hot-embossing technology. *Nanotechnology* **2008**, *19*, 5.

(28) Po, R.; Carbonera, C.; Bernardi, A.; Tinti, F.; Camaioni, N., Polymer- and carbon-based electrodes for polymer solar cells: Toward low-cost, continuous fabrication over large area. *Sol. Energy Mater. Sol. Cells* **2012**, *100*, 97-114.

(29) Stuart, M. A. C.; Huck, W. T. S.; Genzer, J.; Muller, M.; Ober, C.; Stamm, M.; Sukhorukov, G. B.; Szleifer, I.; Tsukruk, V. V.; Urban, M.; Winnik, F.; Zauscher, S.; Luzinov, I.; Minko, S., Emerging applications of stimuli-responsive polymer materials. *Nat. Mater.* **2010**, *9*, 101-113.

(30) Gerard, M.; Chaubey, A.; Malhotra, B. D., Application of conducting polymers to biosensors. *Biosens. Bioelectron.* **2002**, *17*, 345-359.
(31) Lunt, J., Large-scale production, properties and commercial applications of polylactic acid polymers. *Polym. Degrad. Stabil.* **1998**, *59*, 145-152.
(32) Yim, J. H.; Joe, S. Y.; Pang, C.; Lee, K. M.; Jeong, H.; Park, J. Y.; Ahn, Y. H.; de Mello, J. C.; Lee, S., Fully Solution-Processed Semitransparent Organic Solar Cells with a Silver Nanowire Cathode and a Conducting Polymer Anode. *ACS Nano* **2014**, *8*, 2857-2863.
(33) Wang, Y.; Di, C. A.; Liu, Y. Q.; Kajiura, H.; Ye, S. H.; Cao, L. C.; Wei, D. C.; Zhang, H. L.; Li, Y. M.; Noda, K., Optimizing Single-Walled Carbon Nanotube Films for Applications in Electroluminescent Devices. *Adv. Mater.* **2008**, *20*, 4442-4449.
(34) Alemu, D.; Wei, H. Y.; Ho, K. C.; Chu, C. W., Highly conductive PEDOT:PSS electrode by simple film treatment with methanol for ITO-free polymer solar cells. *Energy Environ. Sci.* **2012**, *5*, 9662-9671.
(35) Mengistie, D. A.; Ibrahem, M. A.; Wang, P. C.; Chu, C. W., Highly Conductive PEDOT:PSS Treated with Formic Acid for ITO-Free Polymer Solar Cells. *ACS Appl. Mater. Interfaces* **2014**, *6*, 2292-2299.
(36) Yang, T. B.; Wang, M.; Duan, C. H.; Hu, X. W.; Huang, L.; Peng, J. B.; Huang, F.; Gong, X., Inverted polymer solar cells with 8.4% efficiency by conjugated polyelectrolyte. *Energy Environ. Sci.* **2012**, *5*, 8208-8214.
(37) Dou, L. T.; You, J. B.; Yang, J.; Chen, C. C.; He, Y. J.; Murase, S.; Moriarty, T.; Emery, K.; Li, G.; Yang, Y., Tandem polymer solar cells featuring a spectrally matched low-bandgap polymer. *Nat. Photonics* **2012**, *6*, 180-185.
(38) Small, C. E.; Chen, S.; Subbiah, J.; Amb, C. M.; Tsang, S. W.; Lai, T. H.; Reynolds, J. R.; So, F., High-efficiency inverted dithienogermole-thienopyrrolodione-based polymer solar cells. *Nat. Photonics* **2012**, *6*, 115-120.
(39) He, Z. C.; Zhong, C. M.; Huang, X.; Wong, W. Y.; Wu, H. B.; Chen, L. W.; Su, S. J.; Cao, Y., Simultaneous enhancement of open-circuit voltage, short-circuit current density, and fill factor in polymer solar cells. *Adv. Mater.* **2011**, *23*, 4636-4643.
(40) Dou, L. T.; Chang, W. H.; Gao, J.; Chen, C. C.; You, J. B.; Yang, Y., A selenium-substituted low-bandgap polymer with versatile photovoltaic applications. *Adv. Mater.* **2013**, *25*, 825-831.
(41) You, J. B.; Dou, L. T.; Yoshimura, K.; Kato, T.; Ohya, K.; Moriarty, T.; Emery, K.; Chen, C. C.; Gao, J.; Li, G.; Yang, Y., A polymer tandem solar cell with 10.6% power conversion efficiency. *Nat. Commun.* **2013**, *4*, 10.
(42) Chen, H. C.; Chen, Y. H.; Liu, C. C.; Chien, Y. C.; Chou, S. W.; Chou, P. T., Prominent short-circuit currents of fluorinated quinoxaline-based copolymer solar cells with a power conversion efficiency of 8.0%. *Chem. Mat.* **2012**, *24*, 4766-4772.
(43) Yoon, S. M.; Lou, S. J.; Loser, S.; Smith, J.; Chen, L. X.; Facchetti, A.; Marks, T. J., Fluorinated copper phthalocyanine nanowires for enhancing interfacial electron transport in organic solar cells. *Nano Lett.* **2012**, *12*, 6315-6321.
(44) Cabanetos, C.; El Labban, A.; Bartelt, J. A.; Douglas, J. D.; Mateker, W. R.; Frechet, J. M. J.; McGehee, M. D.; Beaujuge, P. M., Linear side chains in benzo 1,2-b:4,5-b ' dithiophene-thieno 3,4-c pyrrole-4,6-dione polymers direct self-assembly and solar cell performance. *J. Am. Chem. Soc.* **2013**, *135*, 4656-4659.
(45) He, Z. C.; Zhong, C. M.; Su, S. J.; Xu, M.; Wu, H. B.; Cao, Y., Enhanced power-conversion efficiency in polymer solar cells using an inverted device structure. *Nat. Photonics* **2012**, *6*, 591-595.
(46) Li, R.; Di, J. T.; Yong, Z. Z.; Sun, B. Q.; Li, Q. W., Polymethylmethacrylate Coating on Aligned Carbon Nanotube-Silicon Solar Cells for Performance Improvement. *J. Mater. Chem. A* **2014**, *2*, 4140-4143.
(47) Yu, L. P.; Tune, D. D.; Shearer, C. J.; Shapter, J. G., Implementation of Antireflection Layers for Improved Efficiency of Carbon Nanotube-Silicon Heterojunction Solar Cells. *Sol. Energy* **2015**, *118*, 592-599.
(48) Tune, D. D.; Flavel, B. S.; Quinton, J. S.; Ellis, A. V.; Shapter, J. G., Single-Walled Carbon Nanotube/Polyaniline/n-Silicon Solar Cells: Fabrication, Characterization, and Performance Measurements. *ChemSusChem* **2013**, *6*, 320-327.
(49) Yu, L.; Tune, D. D.; Shearer, C. J.; Shapter, J. G., Application of Polymer Interlayers in Silicon–Carbon Nanotube Heterojunction Solar Cells. *ChemNanoMat* **2015**, *1*, 115-121.

(50) Chiang, J. C.; Macdiarmid, A. G., Polyanline - protonic acid doping of the emeraldine form to the metallic regime. *Synth. Met.* 1986, *13*, 193-205.
(51) Zielke, D.; Niehaves, C.; Lövenich, W.; Elschner, A.; Hörteis, M.; Schmidt, J., Organic-silicon solar cells exceeding 20% efficiency. *Energy Procedia* 2015, *77*, 331-339.
(52) Lin, H. J.; Li, L.; Ren, J.; Cai, Z. B.; Qiu, L. B.; Yang, Z. B.; Peng, H. S., Conducting polymer composite film incorporated with aligned carbon nanotubes for transparent, flexible and efficient supercapacitor. *Sci Rep* 2013, *3*, 6.
(53) Singh, I.; Bhatnagar, P. K.; Mathur, P. C.; Kaur, I.; Bharadwaj, L. M.; Pandey, R., Optical and electrical characterization of conducting polymer-single walled carbon nanotube composite films. *Carbon* 2008, *46*, 1141-1144.
(54) Yoshino, K.; Kajii, H.; Araki, H.; Sonoda, T.; Take, H.; Lee, S., Electrical and optical properties of conducting polymer-fullerene and conducting polymer-carbon nanotube composites. *Fullerene Sci. Technol.* 1999, *7*, 695-711.
(55) Tamburri, E.; Orlanducci, S.; Terranova, M. L.; Valentini, F.; Palleschi, G.; Curulli, A.; Brunetti, F.; Passeri, D.; Alippi, A.; Rossi, M., Modulation of electrical properties in single-walled carbon nanotube/conducting polymer composites. *Carbon* 2005, *43*, 1213-1221.
(56) Peng, C.; Zhang, S. W.; Jewell, D.; Chen, G. Z., Carbon nanotube and conducting polymer composites for supercapacitors. *Prog. Nat. Sci.* 2008, *18*, 777-788.
(57) Hou, Y.; Cheng, Y. W.; Hobson, T.; Liu, J., Design and synthesis of hierarchical MnO_2 nanospheres/carbon nanotubes/conducting polymer ternary composite for high performance electrochemical electrodes. *Nano Lett.* 2010, *10*, 2727-2733.
(58) Fan, B. H.; Mei, X. G.; Sun, K.; Ouyang, J. Y., Conducting polymer/carbon nanotube composite as counter electrode of dye-sensitized solar cells. *Appl. Phys. Lett.* 2008, *93*, 3.
(59) de Albuquerque, J. E.; Mattoso, L. H. C.; Faria, R. M.; Masters, J. G.; MacDiarmid, A. G., Study of the interconversion of polyaniline oxidation states by optical absorption spectroscopy. *Synth. Met.* 2004, *146*, 1-10.
(60) Deng, J. G.; Ding, X. B.; Zhang, W. C.; Peng, Y. X.; Wang, J. H.; Long, X. P.; Li, P.; Chan, A. S. C., Carbon nanotube-polyaniline hybrid materials. *Eur. Polym. J.* 2002, *38*, 2497-2501.
(61) Armin, A.; Velusamy, M.; Wolfer, P.; Zhang, Y. L.; Burn, P. L.; Meredith, P.; Pivrikas, A., Quantum efficiency of organic solar cells: Electro-optical cavity Considerations. *ACS Photonics* 2014, *1*, 173-181.
(62) Guillot, S. L.; Mistry, K. S.; Avery, A. D.; Richard, J.; Dowgiallo, A. M.; Ndione, P. F.; van de Lagemaat, J.; Reese, M. O.; Blackburn, J. L., Precision printing and optical modeling of ultrathin SWCNT/C-60 heterojunction solar cells. *Nanoscale* 2015, *7*, 6556-6566.
(63) Larsen, L. J.; Shearer, C. J.; Ellis, A. V.; Shapter, J. G., Solution Processed Graphene-Silicon Schottky Junction Solar Cells. *RSC Adv.* 2015, *5*, 38851-38858.

Chapter 4 Optimisation of the metal front contact design for single-walled carbon nanotube-silicon heterojunction solar cells

This Chapter has been published as “Optimization of the Metal Front Contact Design for Single-Walled Carbon Nanotube-Silicon Heterojunction Solar Cells” in Solar RRL in 2017.

Yu, L.; Grace, T.; Jazi, M. D.; Shearer, C.; Shapter, J. Optimization of the Metal Front Contact Design for Single-Walled Carbon Nanotube-Silicon Heterojunction Solar Cells. Solar RRL 2017. 1600026.

4.1 Overview

Heterojunction photovoltaic devices based on single-walled carbon nanotube transparent conducting films and silicon have been studied for more than 10 years. Until now, the typical active area sizes of these solar cells are still limited to the lab scale. However, the working area of the devices is not easy to increase to fulfil the requirement for industrial application due to the limited conductivity of the SWCNT-based transparent conducting films. In this Chapter, the optimal metal front contact grid design is determined, which can be potentially applied over a much larger active area to meet commercial demands. Gold grids in 12 different patterns acting as current collecting electrodes, are defined on the surface of the n-type silicon wafer. SWCNT-Si heterojunction devices are created with the deposition of p-type SWCNT transparent conducting electrodes on the silicon substrates covered with various grid design. Three different types of SWCNT thin film electrodes with various thickness, transparency, and sheet resistance were prepared. The influence of the active area size and the porosity of the grid patterns on the performance of the solar cells have been investigated for each individual type of SWCNT thin film. It was found that the solar cell performance was improved for all films by employing a grid-patterned electrode, and particularly, there was a large improvement in the fill factor of the devices. The greatest performance improvement (over 100%) was observed when thinner, more transparent, and less conductive SWCNT thin film electrodes were applied. The results in this Chapter indicate that application of a patterned metal front electrode is a scalable approach to fabricate solar cells with efficiency more than 10%.

4.2 Introduction

Carbon nanotube-silicon (CNT-Si) heterojunction solar cells have been investigated intensively since they are regarded as one of the potential alternatives to traditional silicon-based photovoltaics.[1-4] During the last a few years, the best efficiency of this type of solar cells has been above 17 % with the optimal heterojunction structure as well as the application of different antireflection layers.[5-6] It is worth noting that the active area sizes of most of the devices with high efficiencies are relatively small (below 0.1 cm^2), which are unlikely to be used in commercial application, both because of the difficulty in reproducibly fabricating such

devices and the reality that the output power density decreases with the increase in active area sizes for CNT-Si devices.[7-14] As a matter of fact, it was reported that the efficiency of CNT-Si devices dropped from 8.26 to 3.97 % as the active area increased from 0.06 to 2.15 cm^2.[15] Specifically, there is a higher internal series resistance when a larger transparent conducting SWCNT film is applied in such a device, and as a result, the fill factor is reduced and serious resistive power loss occurs. Under such conditions, the only transport paths for charge carriers moving from the working area to the surrounding metal electrode, including gold (Au) and silver (Ag), is the SWCNT network. This infers that travelling a longer distance is required for charge carriers over a larger porous network before they are collected and the resulting possibility of recombination is higher.[16]

The general approach to reduce the high series resistance of the SWCNT-based transparent conducting films is to increase the number of CNTs (or the thickness) in the network to provide more transport paths.[17-18] However, in the application of a window electrode in a solar cell, this approach sacrifices the optical transmittance, and results in a reduced number of excitons being produced under the sunshine because fewer photons are absorbed by the Si substrate when SWCNT electrode absorbs more. Thus, there exists a trade-off between the transmittance and the conductivity of the SWCNT thin film electrode. In the evaluation of transparent conducting films, the excellent optoelectronic properties are dependent on both high transmittance and high conductivity, which results in a high value of the figure of merit (FOM, see Section 1.2.2.1) taking both factors into consideration concurrently.[19-20] More specifically in the case of SWCNT electrodes, the large films with high transmittance normally have high sheet resistance (more than a few $k\Omega\ sq^{-1}$), which is not desirable for solar cell applications where highly transparent large films are required as the window electrodes.[21-22]

To address this issue, people are inspired by the commercial Si based solar cells where the grid patterned metal front electrode is applied to optimise light transmittance, collection of current, and the cost.[23] Recently, in order to mimic the strategy in traditional Si-based photovoltaics with p–n junctions, in which the deposition of the metallic grids are performed on the front of the top Si layer, Li et al. applied Ag nanowires on top of the surface of SWCNT-Si device (active area: 0.49 cm^2) and the efficiency was improved from 4.31 to 7.89 % (nearly a twofold improvement).[9] The incorporation of Ag nanowires in the SWCNT network can

significantly reduce the sheet resistance of the electrode film, and thus improve the performance of the devices. However, SWCNT films are required to be dense enough to avoid any undesired contact between the metallic Ag nanowires and the Si substrate since the direct contact may cause electrical shorts and then ruin the devices.[24-25] Thus, deposition of metal grids directly onto the SWCNT-Si surface (such as via physical vapour deposition or evaporation) should be avoided due to the porous nature of the SWCNT network which enables the metal particles to penetrate through. Hence, it is required to develop a new deposition approach which maintains the function of the grid in decreasing the distance for the charge carriers to travel from formation point to metal electrode.

In this Chapter, in order to prevent the undesirable direct contact between the metal grid and Si surface, photolithography was used to define the Au grids on the surface of Si wafers covered with a thermal oxide layer (SiO_2), as shown in Figure 4.1 (a). The area of the silicon dioxide not covered with Au grids was then etched and the underlying Si (active area) was then exposed to the air, as shown in Figure 4.1 (b). A SWCNT film was then deposited via filtration-transfer approach on top of the substrate to form a heterojunction solar cell device. The schematic structure of the solar cells is shown in Figure 4.1 (c) and (d). Solar cells with different metal patterns (the distance between lines and the width of the lines are defined as "a" and "b", respectively, as shown in Figure 4.1 (e)) and thicknesses of SWCNT thin films, are prepared and tested to optimise and investigate their influence on the performance.

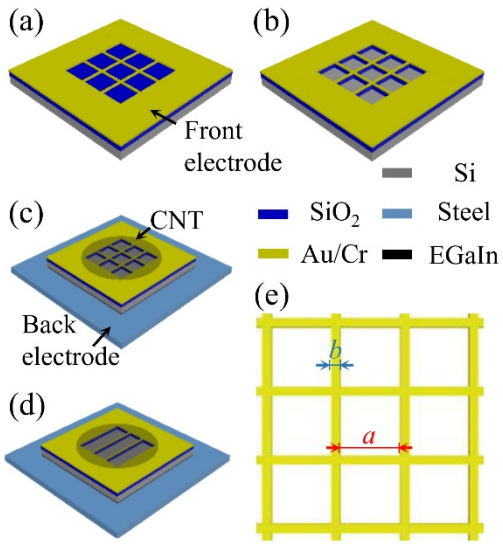

Figure 4.1 Si wafer with a layer of thermal oxide, on top of which is the Au grid pattern defined by photolithography (a) before and (b) after removing the exposed oxide layer (blue square area). (c) Schematic architecture of device patterned with Au grid after the deposition of SWCNT transparent conducting thin film electrode. (d) Schematic structure of device patterned with Au fingers with the deposition of SWCNT films (e) The definition of the parameters in the design of the grids (a is the gap distance between Au lines and b is the width of Au lines).

4.3 Experimental details

SWCNT stock dispersions were prepared with the procedure described in section 2.2.2.1.1. The preparation and characterisation of the electrode are described in sections 2.4.2 and 2.6.1.1. The methods of defining patterns on the grids are shown in section 2.5.2. In addition, device fabrication along with testing of the solar cell performance are described in sections 2.5.1 and 2.6.1.2. The designs of the metal grids were investigated by SEM while the thickness of the front metal electrode was measured by AFM.

4.4 Results and discussion

4.4.1 Preparation and characterisation of pure SWCNT transparent conducting films

Pure SWCNT films were fabricated by the filtration-transfer approach starting from a stable aqueous dispersion of SWCNT. The major goal of applying the grid patterns in CNT/Si heterojunction solar cell is to enhance the ability to collect separated holes over the entire transparent conducting film, which has the potential to provide an opportunity to use thinner films in the solar cells. Different volumes of SWCNT dispersion were used to fabricate SWCNTs TCFs in order to investigate the potential possibility of applying films with excellent electrical properties with high optical transmittance in the solar cells, with the detailed properties listed in Table 4.1 and plotted in Figure 4.2. As shown in Figure 4.2 (a), a linear relationship (Equation 4.1) between transmittance at 550 nm of the SWCNT TCFs and the volume of dispersion used for vacuum filtration was observed,

$$T = -0.0482\ V + 97.154\ (R^2 = 0.988) \qquad \text{Equation 4.1}$$

where T and V are the transmittance and the volume, respectively. In this Chapter, the transmittance of SWCNT TCFs ranges from 93 to 36%. The R_{sheet} of the "as-prepared" SWCNT TCFs before $SOCl_2$ treatment decreases with decrease in the transmittance from above 3000 Ω sq^{-1} (for T above 90%) to about 100 Ω sq^{-1} (for T less 40%). R_{sheet} of all SWCNT TCFs with different transmittances dramatically decreased after chemical doping with $SOCl_2$ by shifting the Fermi level of SWCNT into the valence band, as shown in Figure 4.2 (b). Furthermore, there is an exponential relationship between R_{sheet} and transmittance for both the as-prepared and chemically treated TCFs, as shown in Equation 4.2 and Equation 4.3,

$$R_{sheet} = 4.92 \times 10^{-5}\ e^{\frac{T}{8.39}} + 0.18\ (R^2 = 0.998) \qquad \text{Equation 4.2}$$

$$R_{sheet} = 4.40 \times 10^{-7}\ e^{\frac{T}{5.95}} + 0.12\ (R^2 = 0.988) \qquad \text{Equation 4.3}$$

where R_{sheet} and T are the sheet resistance and the transmittance of the SWCNT TCFs. The final performance of the devices is highly dependent on both of these two factors while improving one generally results in the worsening of the other. Commonly, in the TCFs community or industry, FOM is used to describe these two factors at the same time and evaluate the optoelectronic properties between different TCFs. The equations used to calculate FOM have been explained in section 1.2.2.1.[26-28]

Table 4.1 The optoelectronic properties of SWCNTs transparent conducting films fabricated with different amount of dispersions.

Volume of SWCNT dispersion (µL)	T at 550 nm (%)	R_{sheet} (Initial) (Ω sq^{-1})	R_{sheet} ($SOCl_2$) (Ω sq^{-1})	FOM (Initial)	FOM ($SOCl_2$)
100	93	3265.04 ± 32.83	2643.51 ± 0.54	1.39	1.72
200	89	2317.09 ± 14.28	1859.31 ± 1.14	1.37	1.71
300	86	1560.67 ± 7.44	821.02 ± 1.34	1.55	2.95
400	78	749.78 ± 0.18	405.78 ± 0.15	1.90	3.52
500	71	475.98	246.94	2.17	4.18

		± 0.22	± 0.01		
600	67	357.84 ± 0.05	179.48 ± 0.05	2.40	4.79
700	61	263.78 ± 0.04	134.91 ± 0.02	2.51	4.95
800	56	244.14 ± 0.56	140.35 ± 0.01	2.32	4.02
900	51	204.78 ± 1.83	114.15 ± 0.05	2.31	4.12
1000	48	188.46 ± 0.09	127.62 ± 0.05	2.22	3.29
1100	46	163.78 ± 0.04	103.83 ± 0.04	2.46	3.90
1200	42	155.04 ± 0.11	86.97 ± 0.03	2.27	4.08
1300	36	121.10 ± 0.01	64.29 ± 0.01	2.33	4.39

Normally, higher FOM values indicate better optoelectronic properties. The calculated FOM values for the TCFs both before and after chemical doping are listed in Table 4.1 and their correlation with the transmittance are plotted in Figure 4.2 (c). As the doping can cause a decrease in R_{sheet} and maintain T, optoelectronic properties (FOM values) were improved after the treatment. The general trend is that SWCNT TCFs with higher T seem to have lower FOM values than that of films with lower T. In detail, FOM increases as the transmittance reduces from about 90% to about 75%, and then fluctuates within a constant range for both treated and untreated films. Therefore, in this Chapter, SWCNT TCFs with transmittance less than 75% were not applied as the electrodes for solar cells, and TCFs fabricated with 400, 300, and 100 µL (T = 78, 86, and 93 %, as shown in Figure 4.2 (c)) were applied to solar cells in the investigation of the impact of grids on the device performance with sufficient variety in FOM.

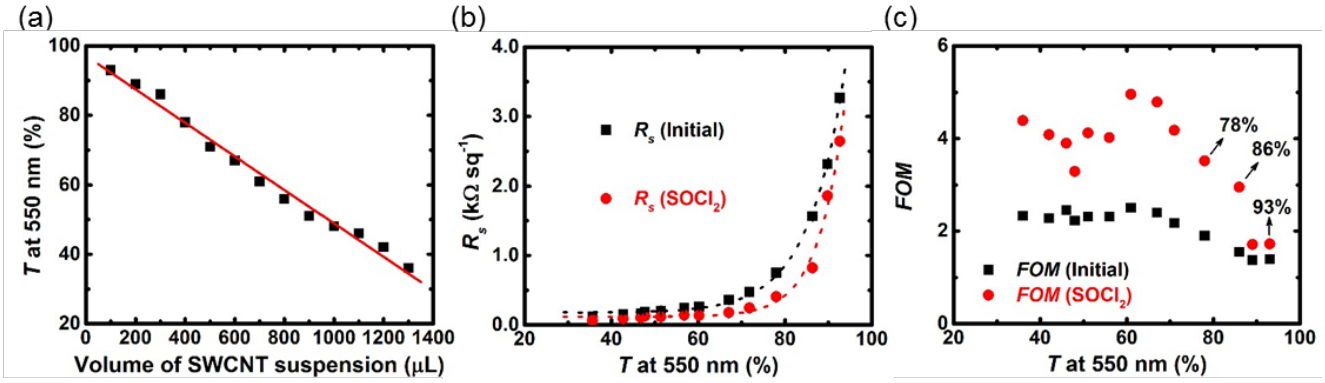

Figure 4.2 (a) The optical transmittance of SWCNT TCFs versus the volume of stock dispersion used during the vacuum filtration (the red line is the linear fit). (b) R_{sheet} of the as prepared SWCNT TCFs and the counterparts after chemical doping by $SOCl_2$ treatment correlated to the optical transmittance (the short dashed curves are the exponential fits). (c) Optoelectronic properties (FOM) of the SWCNT TCFs before and after chemical doping.

4.4.2 The influence of the active area on the device performance

The impact of the active area size on the device performance has been investigated with the application of SWCNT films (T = 78 %) on Si substrates with defined square active areas of 0.04 and 0.09 cm^2. The performance details are listed in Table 4.2 and the J–V curves under light conditions are shown in Figure 4.3 (a). The dark curves of the devices are provided in Figure 4.3 (b).

Table 4.2 Solar cell performance with SWCNT films (T = 78 %) on different types of substrates (all squares), including 0.04 cm^2 (no grid), 0.09 cm^2 (no grid), 0.09 cm^2 (fingers) and 0.09 cm^2 (grids), as shown in Figure 4.3. These values represent an average and standard deviation of 3 devices.

Area	0.04 cm^2 (No grid)	0.09 cm^2 (No grid)	0.089 cm^2 (Fingers)	0.088 cm^2 (Grid)
J_{SC} (mA cm^{-2})	24.2 ± 0.5	24.6 ± 0.5	23.8 ± 2.0	24.2 ± 0.2
V_{OC} (V)	0.539 ± 0.008	0.551 ± 0.006	0.553 ± 0.001	0.576 ± 0.004
FF	0.60 ± 0.02	0.44 ± 0.06	0.62 ± 0.03	0.68 ± 0.01

Efficiency (%)	7.88 ± 0.24	5.97 ± 0.78	8.13 ± 0.60	9.52 ± 0.09
R_{shunt} (Ω)	8.04×10^3 $\pm 1.00 \times 10^3$	4.29×10^3 $\pm 1.12 \times 10^3$	9.60×10^3 $\pm 2.30 \times 10^3$	1.60×10^4 $\pm 1.52 \times 10^3$
R_{series} (Ω)	81.1 ± 23.5	143.5 ± 9.2	74.9 ± 7.6	50.4 ± 2.2
Ideality	1.42 ± 0.02	1.52 ± 0.33	1.38 ± 0.18	1.38 ± 0.12
J_{sat} (mA cm^{-2})	9.65×10^{-6} $\pm 8.27 \times 10^{-9}$	3.36×10^{-5} $\pm 5.55 \times 10^{-5}$	2.22×10^{-6} $\pm 2.95 \times 10^{-6}$	1.86×10^{-6} $\pm 2.28 \times 10^{-6}$

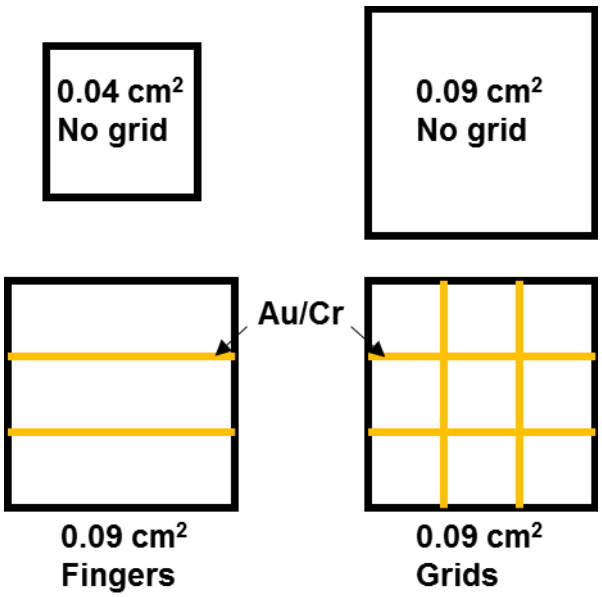

Figure 4.3 Schematics of the active area of four different substrates.

As anticipated, the efficiency shows a decreasing trend from 7.88 to 5.97 % with the increase in the size of the active area from 0.04 to 0.09 cm^2. Among all of the factors in Table 4.2, the difference mainly exists in the change of FF from 0.60 to 0.44, while J_{SC} stays relatively constant. There is a slight change in V_{OC} and this will be explored with further changes in grid design. In addition, the diode properties of devices with smaller active area (0.04 cm^2) are better than those of larger devices, with lower ideality and J_{sat}.

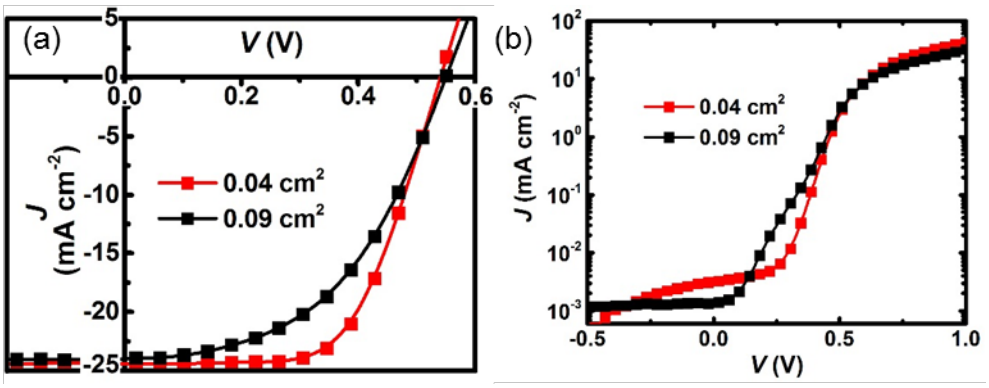

Figure 4.4 J-V curves of devices with different active area sizes (0.04 and 0.09 cm^2) with SWCNT electrodes (T = 78%) under (a) light and (b) dark conditions.

In theory, this performance degradation is due to two factors. Firstly, increase in the active area size results in an increase in the internal resistance of the SWCNT TCFs, which leads to a reduced FF and thus the dramatic loss of power. Secondly, the recombination probability increases with the increase in the transport distance for a charge carrier (hole) moving from the centre area of the SWCNT TCFs to the metal electrodes, which contributes to the decreased FF as well.[16] Thus, it is important to address the issue caused by the active area sizes when the dimensions of the devices are above 1 cm^2 in commercial applications.

4.4.3 The influence of the different front metal electrode patterns on the device performance

For this reason, in this Chapter, the application of grid structures in SWCNT/Si solar cells is investigated, and devices with different patterns on the same square area (0.09 cm^2) are fabricated. The J–V curves of devices with three different metal front electrode patterns on the same square region, including no grid, fingers and grid under light and dark conditions are shown in Figure 4.5. Further details of their performance are summarised in Table 4.2.

Among these three types of SWCNT/Si devices, solar cells with Au grid (a = 1mm, b = 0.01mm) have the best performance (9.52%, even higher than the efficiency of the counterparts with a small size of active area 0.04 cm^2) and those without any grid have the lowest efficiency (5.97%). The improved efficiency by the addition of grid patterns is due to the considerable increase in FF (from 0.44 (no grid) to 0.68 (with grid)), as shown in Figure 4.5 (a). Both J_{SC} and V_{OC} of all these three types of devices are similar since the SWCNT TCFs used

in these devices have the same transmittance. The grid-patterned devices have the lowest R_{series} (50 Ω) and the highest R_{shunt} (1.60 × 10^4 Ω), which is due to the decreased internal resistance across the TCF and suppressed recombination cases. The devices with fingers and grid also show some improvement in the diode properties seen in the lower ideality as well as J_{sat}, compared to those of the devices without grid. Thus, Au metal grids are effective in improving hole transport and collection ability by reducing the transporting distance between the location of exciton separation to the metal collector for the charge carriers.

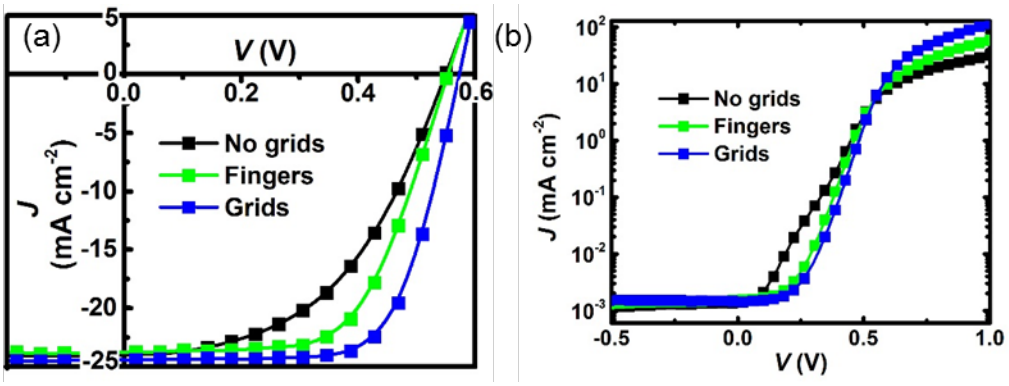

Figure 4.5 J–V curves (light) of devices with different Au front electrode patterns (no grid, fingers and grid) on the same square area (0.09 cm²) with SWCNT electrodes (T = 78%) under (a) light and (b) dark conditions.

4.4.4 Different patterns of grid structures

Since the grid pattern results in the solar cells with the best performance, the next step is to optimise the pattern of the grid electrode. In an ideal situation, the metal pattern would use a minimum amount of gold with the efficiency to be as high as possible. Before the investigation of the impact of the grid designs on the solar cell performance, 12 different grid structures were defined on both circular (0.079 cm^2) and square (0.09 cm^2) working areas during the photolithography process (refer to 2.5.2). In total, there are 24 different structures and the details are listed in Table 4.3.

The porosity parameter, (P), is generally defined as the ratio of the volume of pores to the sum volume of the solid material. It is often used to characterise porous materials and is related to many properties, such as hydraulic resistance and penetration, heat capacity, and mechanical properties.[29-31] When the grid patterns are considered to be porous materials, P of the square

or circle (P_S or P_C) can then be defined in a similar way, as shown in Equation 4.4 and Equation 4.5,

$$P_S = \frac{A_S - A_{grids}}{A_S} \qquad \text{Equation 4.4}$$

$$P_C = \frac{A_C - A_{grids}}{A_C} \qquad \text{Equation 4.5}$$

where A_{grids} is the region covered by metal grid lines and A_S (or A_C) is the area of the square (or circular) area. In this Chapter, A_S (or A_C) is 0.09 cm^2 (or 0.079 cm^2). The calculated P_S (or P_C) values are listed in Table 4.3.

Table 4.3 The details of the grid patterns (a is the spacing distance between Au lines and b is the lines width, as shown in Figure 4.1 (e)); for each a value, there are three different b values in order to prepare three different grid patterns; therefore, there are twelve different designs explored in this Chapter. When both a and b are 0, this refers to a device with no grid on the circular or square area. The active area of each design on the square (or circular) area has been shown as A_S - A_{grids} (or A_C - A_{grids}). Because at the edge of the design on the circular area is irregular, the active areas are estimated by AutoCAD 2015. P_S (or P_C) are the P values of each design for circular (or square) architectures.

a (mm)	*b* (mm)	$A_S - A_{grids}$ (cm^2)	P_S (%)	$A_C - A_{grids}$ (cm^2)	P_C (%)
1	0.1	0.072	80.0	0.064	81.0
1	0.05	0.081	90.0	0.071	89.9
1	0.01	0.088	97.8	0.077	97.5
0.5	0.1	0.062	68.9	0.054	68.4
0.5	0.05	0.075	83.3	0.065	82.3
0.5	0.01	0.087	96.7	0.075	94.9
0.25	0.1	0.044	48.9	0.040	50.6
0.25	0.05	0.062	68.9	0.054	68.4
0.25	0.01	0.083	92.2	0.073	92.4
0.01	0.1	0.022	24.4	0.020	25.3
0.01	0.05	0.040	44.4	0.035	44.3
0.01	0.01	0.074	82.2	0.065	82.3
0	0	0.090	100.0	0.079	100.0

4.4.5 Characterisation of the front metal electrode

In order to evaluate the quality of the defined grids pattern, the structure was imaged by SEM, as shown in Figure 4.6 which shows 12 different designs with certain porosity (P). The lines on the surface are denser and thicker with the decrease in the line spacing distance (a) (from 1 mm to 0.1 mm) and the increase in the line width (b) (from 0.01 mm to 0.1 mm), which results in the decrease in the P (from 97.8 % to 24.4 %). It is clearly shown that the pattern of the grids have been defined successfully on top of Si substrate after removing the photoresist in an acetone bath with the exception of some defects in the case of very thin lines in the delicate structures (the red circle). In particular, the grid lines are clear with sharp corners and they are the collectors for charge carriers, positively charged holes in CNT/Si devices.

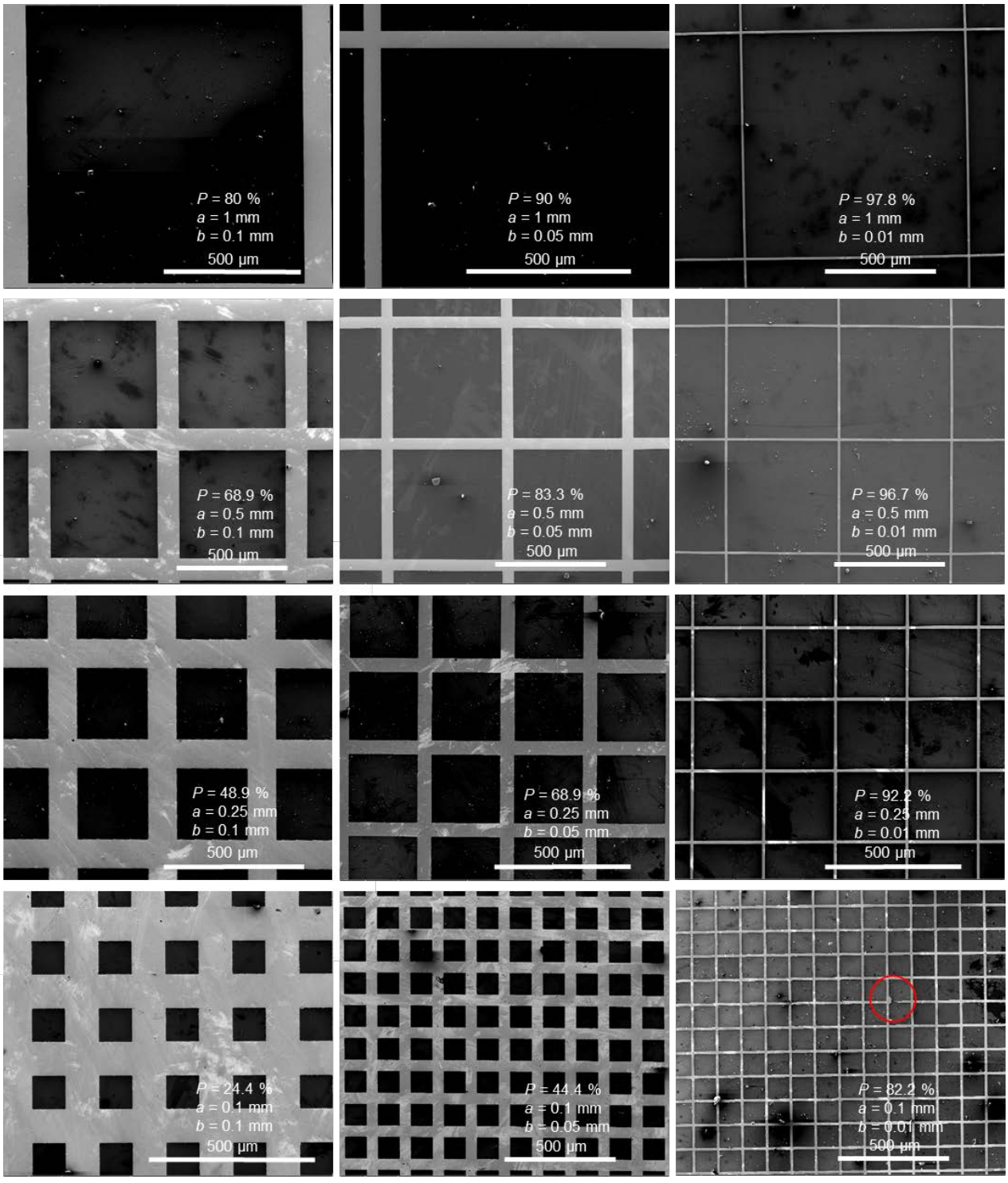

Figure 4.6 SEM images of the grid patterns with different porosity, spacing distance and width of the lines. The lines (bright regions) are the grid area (Au/Cr) and the holes are silicon dioxide surface. The red circle shows a defect. P is porosity; a is the spacing distance; and b is the width of the lines.

4.4.6 Performance of the devices with different grid patterns (square region)

The solar cell performance with SWCNT electrodes (T = 78, 86, and 93%) on Si substrates with 12 different grids patterns on the square regions are shown in Figure 4.7, with the performance of the control devices with SWCNT electrodes for each individual transmittance on square areas without grids.

As shown in Figure 4.7 (a), for grid devices with SWCNT films with T = 86%, the efficiency increases with porosity, with the best efficiency above 10%. This tendency is less obvious when SWCNT TCFs with lower transmittance (78%) are used. However, there is no clear correlation between the porosity and the efficiency when the most transparent SWCNT TCFs are applied. Because efficiency is a combined result from all three factors (J_{SC}, V_{OC}, and FF, see Equation 4.6), they all make a contribution.[32]

$$\text{Efficiency} = \frac{J_{SC} V_{OC} FF}{P_{Incident}} \qquad \text{Equation 4.6}$$

where $P_{Incident}$ is the radiation intensity of the incident beam (100 mW cm^{-2} under AM 1.5). For all non-grid devices with SWCNT TCFs (T = 78, 86, and 93%), their efficiencies are 5.97 ± 0.77, 4.73 ± 0.24, and 4.18 ± 0.08%. Compared to these values, the grid counterparts with the best performance have much higher efficiencies, namely 9.52 ± 0.09, 10.29 ± 0.31, and 9.53 ± 0.69%, which suggests that the highly transparent SWCNT TCFs can be applied with a grid metal electrode in SWCNT/Si solar cells.

Noticeably, the efficiency for non-grid devices with highly transparent SWCNT TCFs (T = 86 and 93%) is less than half that of the best grid counterparts. This is due to the dramatically decreased internal resistance of the CNT electrode where fewer frequent recombination events of the separated charge carriers occurs when grid designs are applied. There is no evident change in series resistance with the grid devices when a lower transparent films (T = 78 %) are applied (as shown in Figure 4.7 (f)), and therefore, the change in FF and PCE values is smaller than that for thinner SWCNT TCFs.

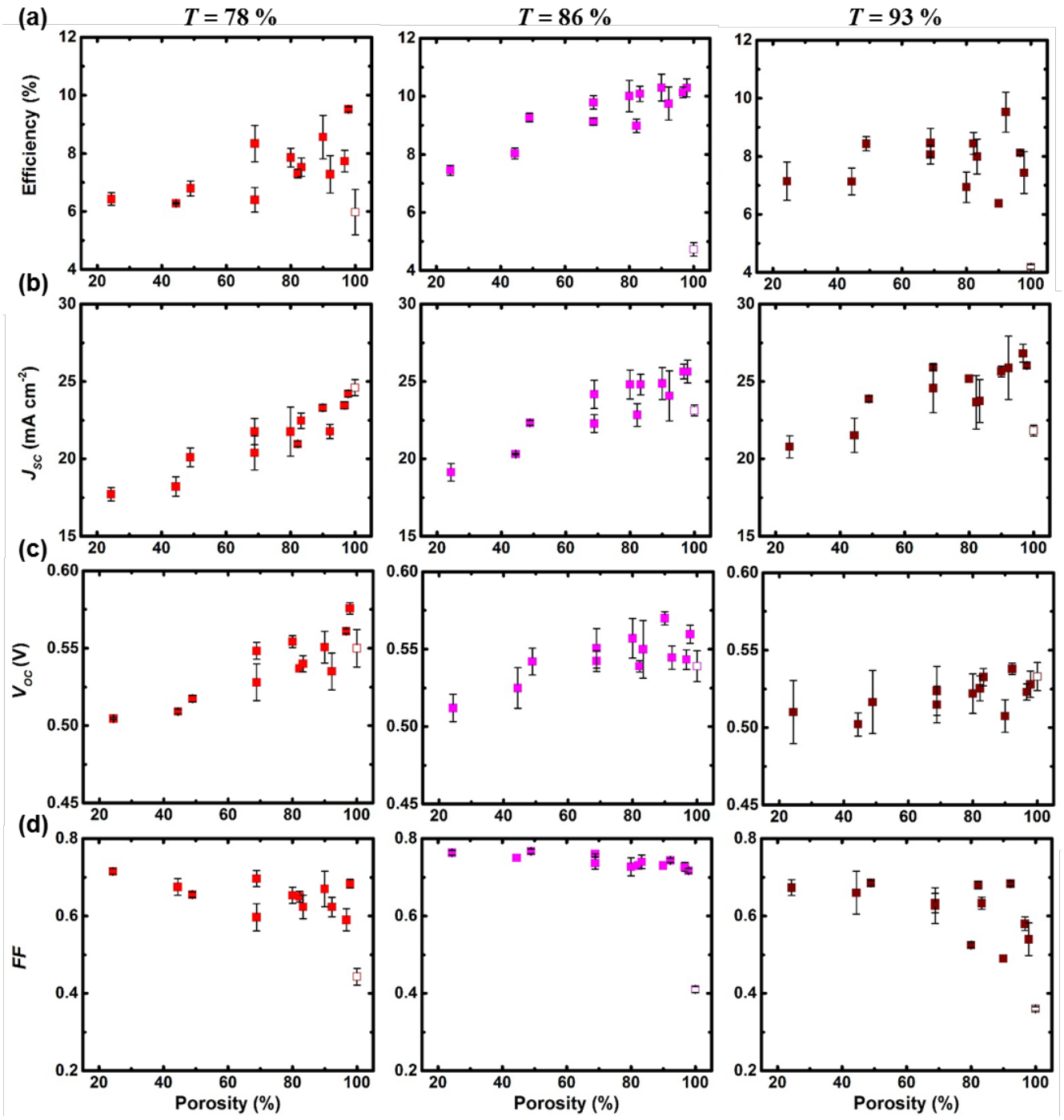
(a)
T = 78 %
T = 86 %
T = 93 %
Efficiency (%)
(b)
J_{SC} (mA cm^{-2})
(c)
V_{OC} (V)
(d)
FF
Porosity (%)
Porosity (%)
Porosity (%)

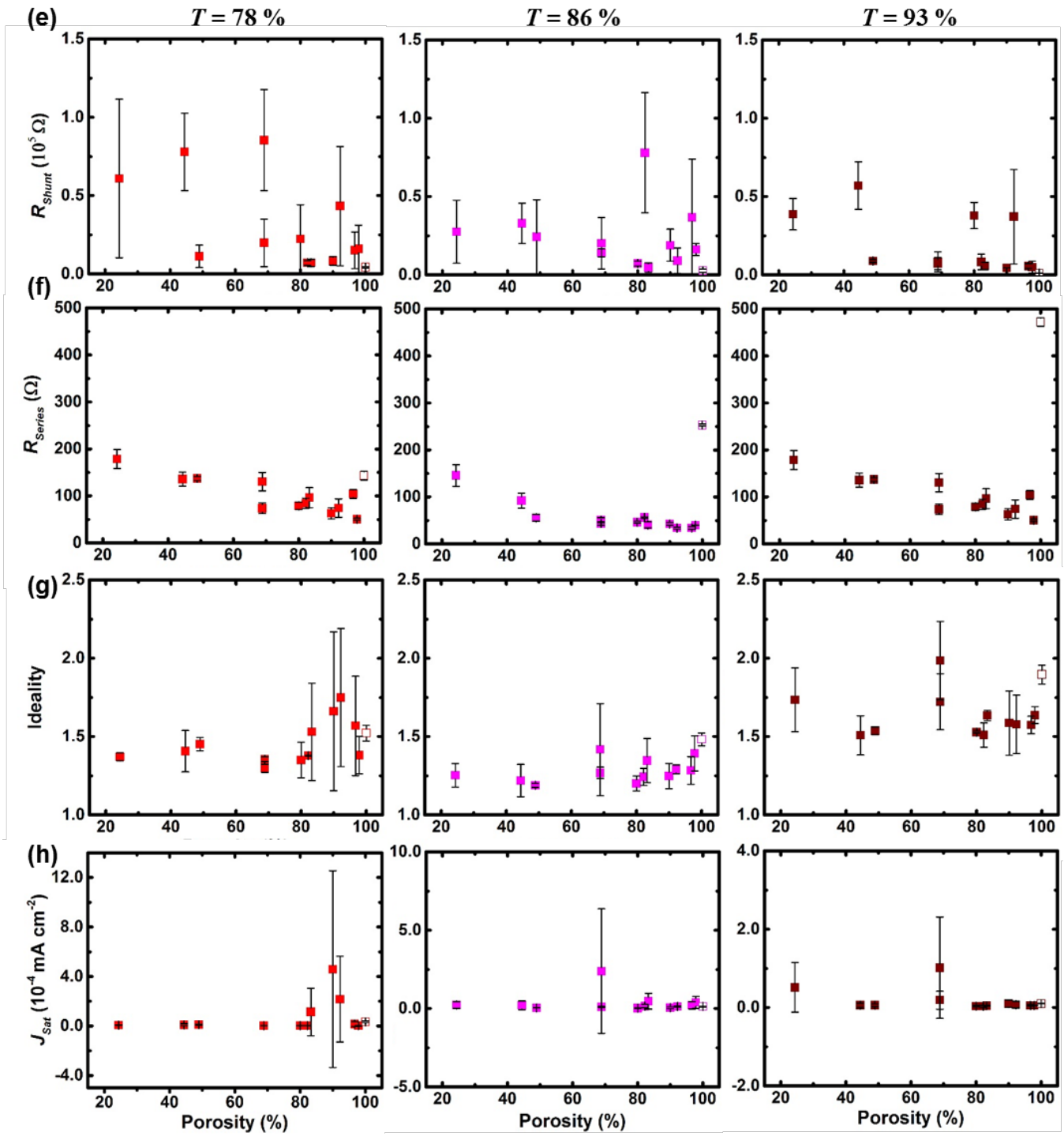

Figure 4.7 Solar cell performance with three thicknesses of SWCNT TCFs (T = 78, 86, and 93 %) on Si substrates coated with 12 patterns on *square* area. Performances of the devices with no grids are also shown (hollow data points at the porosity of 100% in each plot). (a) Efficiency, (b) J_{sc}, (c) V_{oc}, (d) FF, (e) R_{shunt}, (f) R_{series}, (g) Ideality and (h)

J_{sat}. (Values of these data points are the average with standard deviation of three devices.)

Initially, one might expect that as more Au lines are added to decrease the porosity, it will be easier to capture charge carriers due to the shorter transport distance. However, the fact is that J_{SC} decreases with decreasing porosity for grid devices fabricated with all three types of SWCNT TCFs with different transmittances, as shown in Figure 4.7 (b). This could be understood as follows; there are some Si areas near the grid lines which are not in intimate contact with the SWCNT electrode because of the film rigidity and the height difference between the surface of metal electrode and Si (the red circle in Figure 4.8 (a)), which are formed during the filtration transfer deposition of SWCNTs. However, this non-contact region is included in the so-called "input active area" during the estimation of J_{SC}, the measured current of the cell in total divided by the "input active area." Therefore, the real J_{SC} including only the "real active area" is always higher than the plotted J_{SC} to some extent. Specifically, the J_{SC} final value can be defined as Equation 4.7,

$$J_{SC} = \frac{I_{Real}}{A_{Input}} = \frac{J_{Unit\,area} A_{Real}}{A_{Input}} = J_{Unit\,area} \frac{A_{Input} - A_{Non-contact}}{A_{Input}} = J_{Unit\,area} \left(1 - \frac{A_{Non-contact}}{A_{Input}}\right) \quad \text{Equation 4.7}$$

where I_{Real} (mA) is the current produced by the intimate contact area between SWCNT electrode and Si surface; A_{Input} (cm^2) is the "input active area"; $J_{Unit\ area}$ ($mA\ cm^{-2}$) is the current density per unit area (it is assumed to be a constant value when the transmittance of SWCNT TCFs is determined), and $A_{Non\text{-}contact}$ (cm^2) is the area of Si surface which is not in contact with SWCNT electrode. As shown in Figure 4.1 (e), when the porosity of the surface decreases with either lower a (lines closer together) or higher b (wider lines), $A_{Non\text{-}contact}$ will be larger. Meantime, A_{Input} decreases with the decrease in porosity. As a result, the ratio of $A_{Non\text{-}contact}$ and A_{Input} increases. Since $J_{Unit\ area}$ is assumed to be a constant value and the term $(1 - \frac{A_{Non-contact}}{A_{Input}})$ decreases, a lower value of J_{SC} would be recorded.

In order to further investigate the influence of grid pattern on J_{SC} in solar cells applied with SWCNT films of different transmittance, J_{SC} values for non-grid and grid devices are compared and studied. For thick films (T = 78 %), the best J_{SC} for the devices with and without grids are very similar, as shown in Figure 4.7 (b). This is because the film has a high FOM and J_{SC} is not

limited by the conductivity of the film. However, for thinner SWCNT TCFs (T = 86 and 93 %), application of a pattern with high porosity considerably increases J_{SC} values compared to the control devices without a grid pattern, because these films have such high R_{sheet} that they cannot effectively transport the produced charge carriers. With the addition of metal current collectors, the poorer R_{sheet} is negated and results in better J_{SC}.

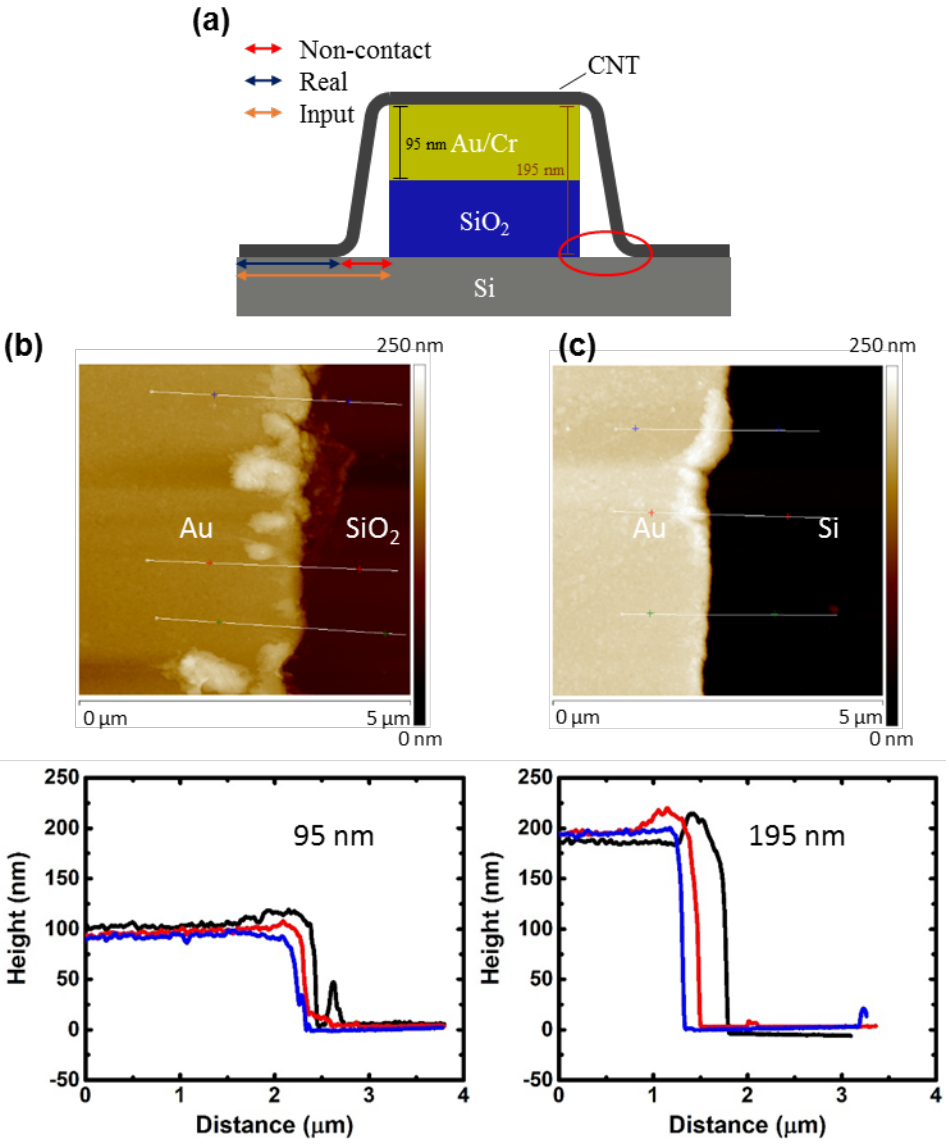

Figure 4.8 (a) Schematic cross-section view of the solar cell illustrating that there is some non-contact areas (red circle) near the edge of the Au grid lines; the distance between Au/Cr and (b) SiO_2 (before etching) or (c) Si surface (after etching) are 95nm and 195 nm, measure by AFM.

The V_{oc} of grid devices increases slightly with the increase in the porosity when the transmittance of the SWCNT films is 78 and 86 %, though the changes are barely outside the standard deviations of the measurements. The V_{oc} of the devices with high porosity is more variable but remains within 1 - 2 standard deviations for the devices with the high transmittance SWCNT TCFs (T = 93 %), as shown in Figure 4.7 (c), most likely due to lower contact area between Si and the sparse high T SWCNT films. As discussed previously, there are more contact defects for patterns with low porosity, which may lower the overall V_{oc} of the devices. In this case, the V_{oc} of the non-grid devices is comparable to those of the grid devices with high porosity.

As shown in Figure 4.7 (d), FF increases with the decrease in porosity for grid patterned devices with all three different types of SWCNT film (T = 78, 86, and 93 %). The FF of non-grid solar cells is generally much lower than those of all grid patterned counterparts, especially when highly transparent SWCNT electrodes are applied (T = 86 and 93 %). The dramatically improved performance of the grid devices is largely due to the great improvement in FF. The internal resistance of the window SWCNT electrodes decreases with the addition of the metal grids. Thus, when the grid lines are denser, the transporting distance of charge carriers between the position where excitons are separated and the grid current collector is shorter, leading to a lower probability of recombination with the improvement in FF.

From Figure 4.7 (e), there is no clear correlation between R_{shunt} of the grid patterned devices and porosity of all three types of SWCNT electrodes (T = 78 %, 86 % and 93 %). Additionally, the R_{shunt} values of the non-grid devices are similar to those of grid devices. In contrast, a clear correlation between R_{series} and porosity for grid patterned solar cells is observed, as shown in Figure 4.7 (f). The R_{series} decreases with the increase in porosity. For non-grid devices with thick SWCNT films (T = 78 %), R_{series} is slightly higher than those of grid patterned counterparts with high porosity (P > 85 %) and close to those of devices with low porosity (P < 85 %). For non-grid devices with thinner SWCNT films (T = 86 %), R_{series} is higher than those of grid devices with porosity of above 50 %. For non-grid devices with thinnest SWCNT electrodes (T = 93 %), R_{series} is higher than those of all grid patterned devices with P across the full range. All these trends suggest that grids with high porosity can dramatically reduce the R_{series} of devices, especially when highly transparent SWCNT electrodes (86 % and 93 %) are

applied, and the decrease in the porosity of the patterns normally results in increased R_{series}. Based on this view, the devices with highly porous patterns perform better than those with grids of lower porosity.

In terms of diode properties, it is expected that as the recombination of the dissociated charge carriers are suppressed with the decrease in porosity so diode properties would be improved (lower ideality and J_{sat}). However, when the porosity is low enough, the increased noncontact area could also have an important role in diode properties. Unfortunately, as shown in Figure 4.7 (g) and (h), no clear correlation between ideality and porosity, and J_{sat} and porosity is observed due to the large error bars.

4.4.7 Performance of the devices with different grid patterns (circular region)

The details of the solar cell performance on substrates with the same type of patterns but on circular areas and their control devices are shown in Figure 4.9. As shown in all of these plots, the performance (including every aspect, J_{SC}, V_{OC}, FF, Efficiency, R_{shunt}, R_{series}, ideality and J_{sat}) of the solar cells with circular regions coated with grids have a similar trend to that observed in solar cells fabricated with square areas. In addition, there is no correlation between the porosity and R_{shunt}, ideality and J_{sat} because of large error bars in these plots.

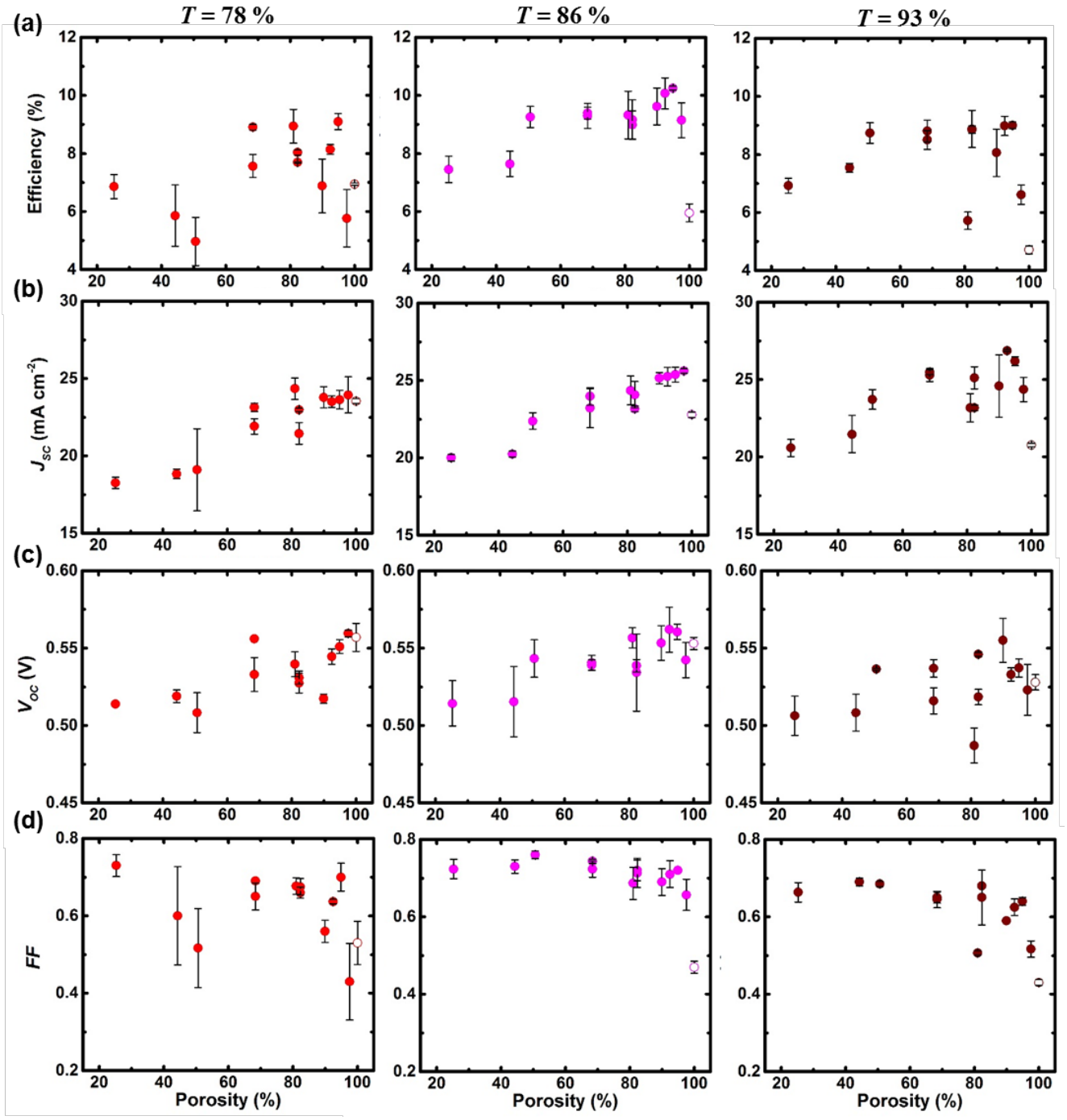
(a)
T = 78 %
T = 86 %
T = 93 %
Efficiency (%)
(b)
J_{sc} (mA cm^{-2})
(c)
V_{oc} (V)
(d)
FF
Porosity (%)
Porosity (%)
Porosity (%)

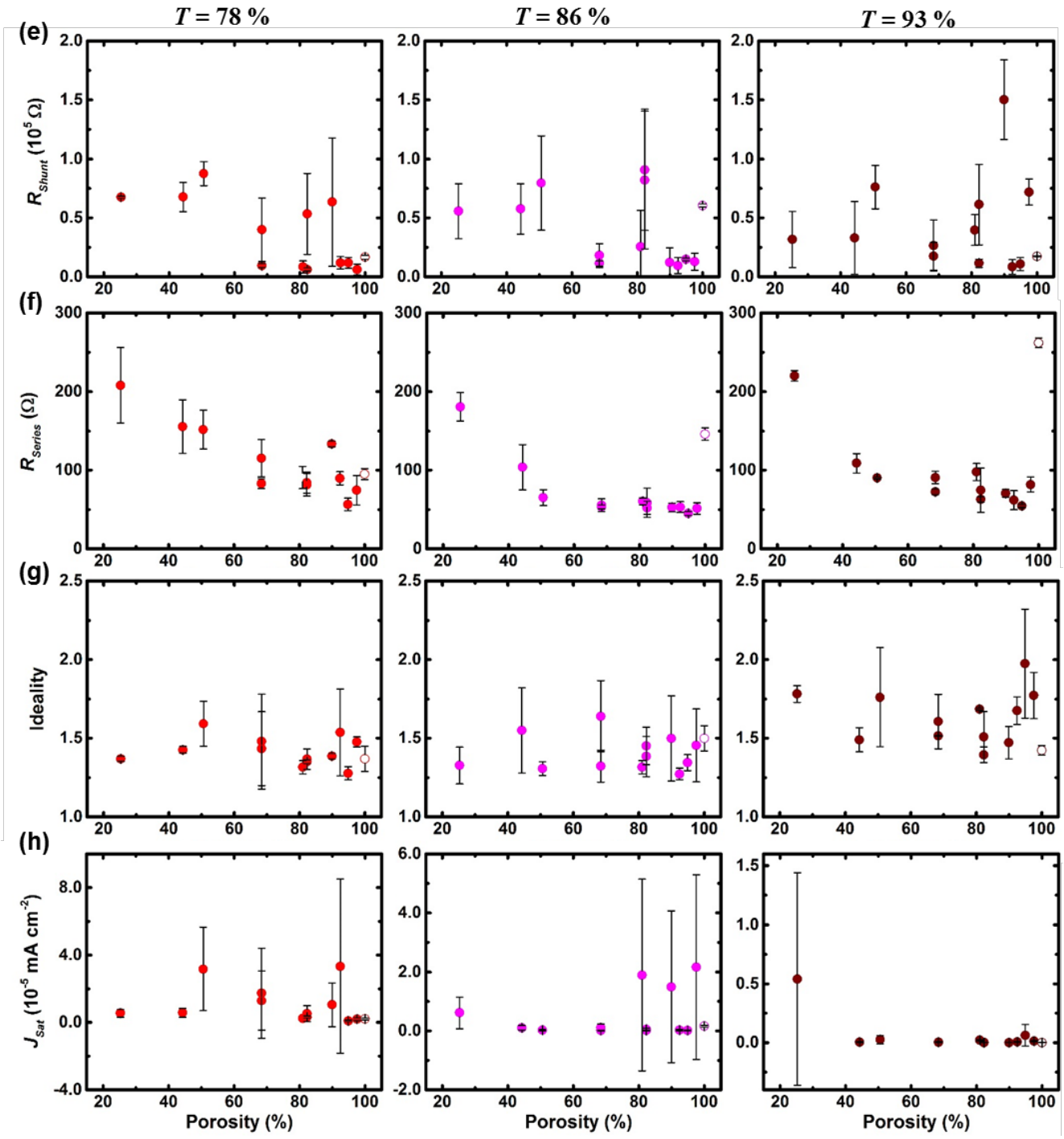

Figure 4.9 Performances of devices prepared with three different thicknesses of SWCNT electrodes (T = 78, 86 and 93 %) on Si substrates coated with 12 different metal patterns on a *circular* area. Performances of the solar cells with no grids are also shown (hollow data points at the 100 % porosity in each plot). (a) J_{SC}, (b) V_{OC}, (c) FF, (d) Efficiency, (e)

R_{shunt}, (f) R_{series}, (g) Ideality, and (h) J_{sat}. (Values of these data points are the average of 3 devices and error bars are calculated to standard deviation).

In the comparison between the control devices without grids based on circular and square area, circular-area devices show higher efficiencies as well as better diode properties with all three types of SWCNT electrodes than those of square-area counterparts (as shown in Figure 4.7 and Figure 4.9). The main reason for this fact is that the circular area is smaller than the square one (0.079 versus 0.09 cm^2) and the higher FF of circular-area devices leads to the better performance.

4.4.8 Influence of the transmittance of the SWCNT electrode on the solar cell performance

The influence of the transmittance of SWCNT electrodes on the solar cell performance with grid patterns are investigated by extracting the data points from Figure 4.7 and Figure 4.9, and they are replotted into Figure 4.10, where both circular- and square-area devices are included.

As shown in Figure 4.10 (a), with the combined effects of three factors (J_{SC}, V_{OC} and FF), when the transmittance of SWCNT electrodes is 86 % (FOM = 2.95), solar cells have the highest efficiency. Solar cells with the most transparent SWCNT films but lowest FOM have highest J_{SC} over the full porosity range (Figure 4.10 (b)), J_{SC} (T = 93 %, FOM = 1.72) > J_{SC} (T = 86 %, FOM = 2.95) > J_{SC} (T = 78 %, FOM = 3.52), which is due to the fact that more photons can penetrate through the SWCNT films. In terms of V_{OC}, as shown in Figure 4.10 (c), devices with transmittance of 78 % and 86 % perform similarly, while slightly lower V_{OC} values are observed in solar cells fabricated with the thinnest SWCNT electrode (T = 93 %). A decreased V_{OC} is generally observed with the limited contact area formed between the SWCNTs and the Si, particularly when a very thin SWCNT film containing an extremely sparse network (with high transparency and low FOM). Solar cells with SWCNT films with transmittance of 86 % have the highest FF while the FF values across the full porosity range for the devices with the other two types of SWCNT (T = 78 and 93 %) are similar, as shown in Figure 4.10 (d). There is no clear correlation observed between the R_{shunt} and the transmittance of the SWCNT films (Figure 4.10 (e)). However, as shown in Figure 4.10 (f), solar cells with SWCNTs films with transmittance of 86 % have the lowest R_{series} values among three sets of devices. In addition,

the devices with SWCNTs films with transmittance of 86 % have the best diode properties (lowest ideality as well as J_{sat}) among all three groups of data, as shown in Figure 4.10 (g) and (h).

All of these results indicate that SWCNT electrodes with a transmittance of 86 % might be the best candidate in fabrication of solar cells patterned with grid structures. For grid-free devices, the efficiency increases (from 4.18 to 5.97 %) with the decrease in the transmittance resulting in the increase in FOM of SWCNT films (from 1.72 to 3.52). Interestingly, for solar cells with grid patterns, the best performing devices are not made of the SWCNT electrode with the best FOM, which highlights the ability of grids to enable the application of the highly transparent SWCNT films.

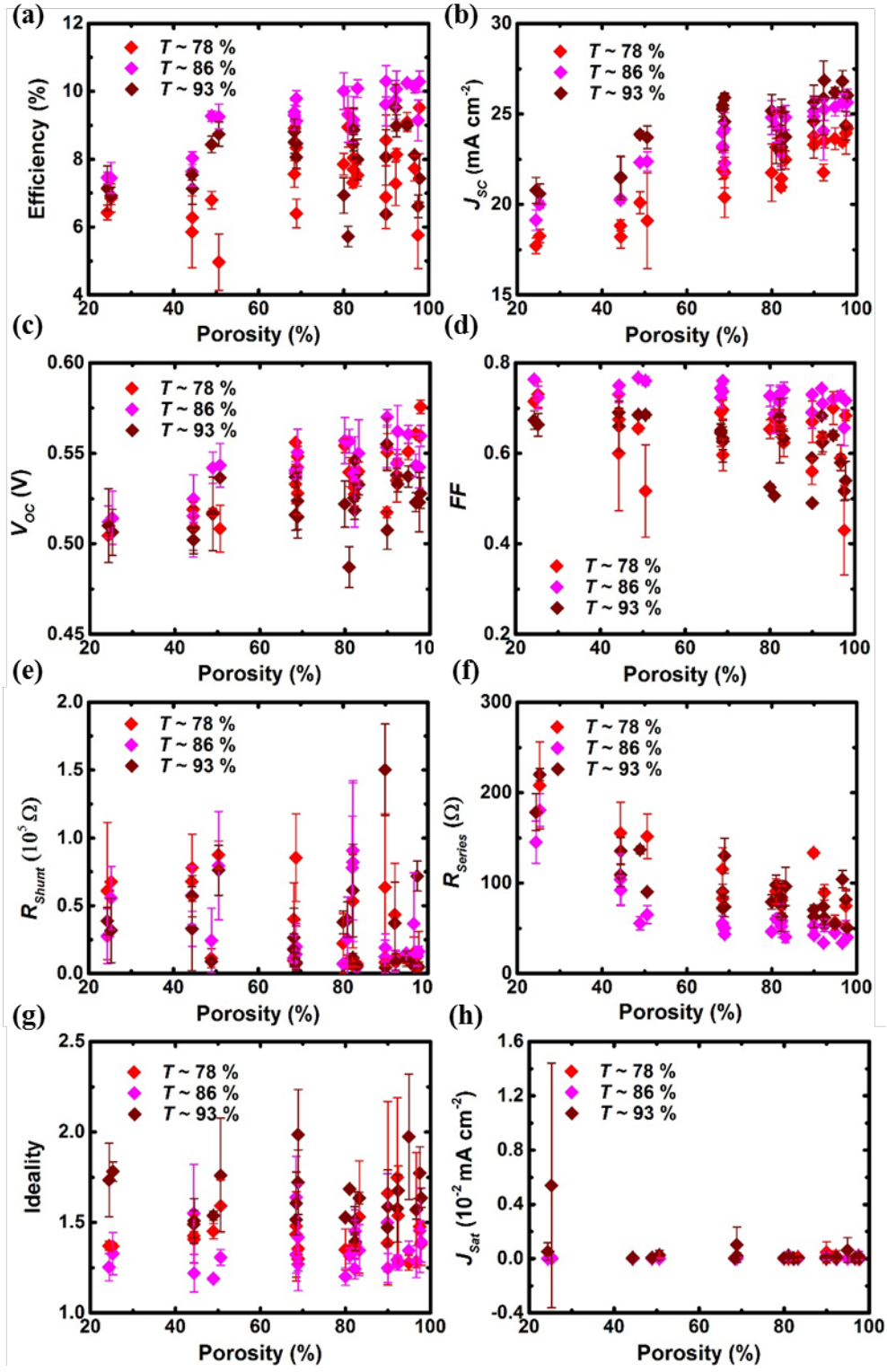

Figure 4.10 Solar cell performance versus porosity with SWCNT films of different transmittance (78 %, 86 % and 93 %). (a) Efficiency, (b) J_{SC}, (c) V_{OC}, (d) FF, (e) R_{shunt}, (f)

R_{series}, (g) Ideality, and (h) J_{sat}. Grids on both circular and square regions are included as one identical colour in these plots.

4.4.9 Summary and outlook

SWCNT/Si solar cells with high porosity metal grids generally have excellent performance. It was found that the spacing distance needs to be high (> 0.25 mm) and the width of the metal lines need to be low (about 0.01 mm) in order to satisfy the requirement for efficient charge transport and collection. An intimate contact between SWCNT film and Si at the interface is one of the key factors in achieving high efficiency. The optimised transmittance of the SWCNT electrode was found to be 86 % when the patterned grid metal electrodes were applied. The high transparency enables more light to penetrate through the TCF and to be absorbed by the Si. However, when more transparent films are applied, the porosity of the SWCNT films results in worse effective contact region at the heterojunction. It is possible that greater performance can be achieved with the patterned metal electrode when a denser, more perfect SWCNT film could be produced.

The grid design not only has improved the efficiency for thin film solar cells, but it could also be applied to devices on a larger scale. The next step is to apply the grid approach in the application of large area devices. If this was applied to commercial scale cells (where the active area > 1 m^2), further optimisation of the pattern would be needed to ensure that the thin Au grid lines were not overloaded by too much current, perhaps with the addition of thicker current collecting busbars at specific spacing. Additionally, further investigation to find the best CNT type to provide the maximum electrode conductivity would be of great value.

There is still more scope to improve CNT/Si heterojunction devices. Since the degradation of the chemical doping effect and the regrowth of the insulating layer of SiO_2 dramatically lowers the device performance within 1 week, encapsulation of the device (e.g., with polymers) is suggested.[33] Furthermore, the encapsulating layer of polymer material can act as an antireflection coating to ensure higher energy absorption by the Si surface when a polymer with appropriate refractive index is chosen and fine control over its thickness is achieved, which will further improve the efficiency. Alternatively, inorganic materials, including TiO_2, can also be used as the antireflection coating.[10] Beyond CNT-Si heterojunction solar cells, the grid

pattern has the potential to be applied to some other types of photovoltaics, such graphene silicon heterojunction solar cells.[34-37]

4.5 Conclusions

The efficiency of the SWCNT/Si solar cells decreases with increasing size of the active area. In order to address this issue and fabricate high performance large active area devices, 12 different Au grid patterns were successfully defined on top of n-type Si substrates which were then covered by p-type SWCNT thin films to fabricate SWCNT/Si heterojunction devices. The Au grids can significantly improve the device performance with the best efficiency above 10 % by applying SWCNT TCFs (T = 86 %) on grids with high porosity (above 85%). The great performance improvement is mainly due to an increase in the fill factor, which is related to the decreased series resistance and reduction in recombination events.

REFERENCES:

(1) De Nicola, F.; Salvato, M.; Cirillo, C.; Crivellari, M.; Boscardin, M.; Scarselli, M.; Nanni, F.; Cacciotti, I.; De Crescenzi, M.; Castrucci, P., Record Efficiency of Air-Stable Multi-Walled Carbon Nanotube/Silicon Solar Cells. *Carbon* 2016, *101*, 226-234.

(2) Pintossi, C.; Pagliara, S.; Drera, G.; De Nicola, F.; Castrucci, P.; De Crescenzi, M.; Crivellari, M.; Boscardin, M.; Sangaetti, L., Steering the Efficiency of Carbon Nanotube-Silicon Photovoltaic Cells by Acid Vapor Exposure: A Real-Time Spectroscopic Tracking. *ACS Appl. Mater. Interfaces* 2015, *7*, 9436-9444.

(3) Tune, D. D.; Blanch, A. J.; Krupke, R.; Flavel, B. S.; Shapter, J. G., Nanotube Film Metallicity and Its Effect on the Performance of Carbon Nanotube-Silicon Solar Cells. *Phys. Status Solidi A-Appl. Mat.* 2014, *211*, 1479-1487.

(4) Tune, D. D.; Hennrich, F.; Dehm, S.; Klein, M. F. G.; Glaser, K.; Colsmann, A.; Shapter, J. G.; Lemmer, U.; Kappes, M. M.; Krupke, R.; Flavel, B. S., The Role of Nanotubes in Carbon Nanotube-Silicon Solar Cells. *Adv. Energy Mater.* 2013, *3*, 1091-1097.

(5) Wang, F. J.; Kozawa, D.; Miyauchi, Y.; Hiraoka, K.; Mouri, S.; Ohno, Y.; Matsuda, K., Considerably Improved Photovoltaic Performance of Carbon Nanotube-Based Solar Cells Using Metal Oxide Layers. *Nat. Commun.* 2015, *6*, 6305.

(6) Shi, E. Z.; Zhang, L. H.; Li, Z.; Li, P. X.; Shang, Y. Y.; Jia, Y.; Wei, J. Q.; Wang, K. L.; Zhu, H. W.; Wu, D. H.; Zhang, S.; Cao, A. Y., TiO2-Coated Carbon Nanotube-Silicon Solar Cells With Efficiency of 15%. *Sci Rep* 2012, *2*, 884.

(7) Choi, S.; Potscavage, W. J., Jr.; Kippelen, B., Area-Scaling of Organic Solar Cells. *J. Appl. Phys.* 2009, *106*.

(8) Jeong, W.-I.; Lee, J.; Park, S.-Y.; Kang, J.-W.; Kim, J.-J., Reduction of Collection Efficiency of Charge Carriers with Increasing Cell Size in Polymer Bulk Heterojunction Solar Cells. *Adv. Funct. Mater.* 2011, *21*, 343-347.

(9) Li, X.; Jung, Y.; Huang, J.-S.; Goh, T.; Taylor, A. D., Device Area Scale-Up and Improvement of SWNT/Si Solar Cells Using Silver Nanowires. *Adv. Energy Mater.* 2014, *4*, 1400186.
(10) Shi, E.; Li, H.; Yang, L.; Zhang, L.; Li, Z.; Li, P.; Shang, Y.; Wu, S.; Li, X.; Wei, J.; Wang, K.; Zhu, H.; Wu, D.; Fang, Y.; Cao, A., Colloidal Antireflection Coating Improves Graphene-Silicon Solar Cells. *Nano Lett.* 2013, *13*, 1776-1781.
(11) Wang, F.; Kozawa, D.; Miyauchi, Y.; Hiraoka, K.; Mouri, S.; Ohno, Y.; Matsuda, K., Fabrication of Single-Walled Carbon Nanotube/Si Heterojunction Solar Cells with High Photovoltaic Performance. *ACS Photonics* 2014, *1*, 360-364.
(12) Uruena, A.; Aleman, M.; Cornagliotti, E.; Sharma, A.; Haslinger, M.; Tous, L.; Russell, R.; John, J.; Duerinckx, F.; Szlufcik, J., Progress on Large Area N-Type Silicon Solar Cells with Front Laser Doping and a Rear Emitter. *Prog. Photovoltaics* 2016, *24*, 1149-1156.
(13) Huang, H. B.; Shi, J. J.; Zhu, L. F.; Li, D. M.; Luo, Y. H.; Meng, Q. B., Two-Step Ultrasonic Spray Deposition of CH3NH3PbI3 for Efficient and Large-Area Perovskite Solar Cell. *Nano Energy* 2016, *27*, 352-358.
(14) He, Y. Y.; Lei, Y.; Yang, X. G.; Lu, K.; Liu, S. Z.; Gu, L. Y.; Zheng, Z., Using Elemental Pb Surface as a Precursor to Fabricate Large Area CH3NH3PbI3 Perovskite Solar Cells. *Appl. Surf. Sci.* 2016, *389*, 540-546.
(15) Xu, W. J.; Wu, S. T.; Li, X. M.; Zou, M. C.; Yang, L. S.; Zhang, Z. L.; Wei, J. Q.; Hu, S.; Li, Y. H.; Cao, A. Y., High-Efficiency Large-Area Carbon Nanotube-Silicon Solar Cells. *Adv. Energy Mater.* 2016, *6*, 1600095.
(16) Shi, J.; Xu, X.; Li, D.; Meng, Q., Interfaces in Perovskite Solar Cells. *Small* 2015, *11*, 2472-2486.
(17) Funde, A. M.; Nasibulin, A. G.; Syed, H. G.; Anisimov, A. S.; Tsapenko, A.; Lund, P.; Santos, J. D.; Torres, I.; Gandia, J. J.; Carabe, J.; Rozenberg, A. D.; Levitsky, I. A., Carbon Nanotube-Amorphous Silicon Hybrid Solar Cell with Improved Conversion Efficiency. *Nanotechnology* 2016, *27*.
(18) Chen, L. F.; Yu, H.; Zhong, J. S.; He, H.; Zhang, T., Harnessing Light Energy with a Planar Transparent Hybrid of Graphene/Single Wall Carbon Nanotube/N-Type Silicon Heterojunction Solar Cell. *Electrochim. Acta* 2015, *178*, 732-738.
(19) Lobiak, E. V.; Bychanok, D. S.; Shlyakhova, E. V.; Kuzhir, P. P.; Maksimenko, S. A.; Bulusheva, L. G.; Okotrub, A. V., One-Step Preparation of Multiwall Carbon Nanotube/Silicon Hybrids for Solar Energy Conversion. *J. Nanophotonics* 2016, *10*.
(20) Saini, V.; Bourdo, S. E.; Abdulrazzaq, O.; Dervishi, E.; Kannarpady, G. K.; Biris, A. S., Performance Dependence of SWCNT/N-Silicon Hybrid Solar Cells on the Charge Carrier Concentration in Silicon Substrates. *RSC Adv.* 2015, *5*, 621-627.
(21) Li, R.; Di, J. T.; Yong, Z. Z.; Sun, B. Q.; Li, Q. W., Polymethylmethacrylate Coating on Aligned Carbon Nanotube-Silicon Solar Cells for Performance Improvement. *J. Mater. Chem. A* 2014, *2*, 4140-4143.
(22) Gong, T. C.; Zhu, Y.; Xie, W. B.; Wang, N.; Zhang, J.; Ren, W. J., Study on Modification of Single-Walled Carbon Nanotubes on the Surface of Monocrystalline Silicon Solar Cells. *Appl. Opt.* 2014, *53*, 6457-6463.
(23) Kim, N.; Um, H. D.; Choi, I.; Kim, K. H.; Seo, K., 18.4%-Efficient Heterojunction Si Solar Cells Using Optimized ITO/Top Electrode. *ACS Appl. Mater. Interfaces* 2016, *8*, 11412-11417.
(24) Deb, S.; Ghosh, B., Series Resistance and Optimum Grid Design for a Thin-Film Solar-Cell of Rectangular Shape. *Sol. Cells* 1984, *13*, 145-162.
(25) Miyadera, T.; Ogo, H.; Taima, T.; Yamanari, T.; Yoshida, Y., Analytical Model for the Design Principle of Large-Area Solar Cells. *Sol. Energy Mater. Sol. Cells* 2012, *97*, 127-131.
(26) De, S.; Coleman, J. N., Are There Fundamental Limitations on the Sheet Resistance and Transmittance of Thin Graphene Films? *ACS Nano* 2010, *4*, 2713-2720.
(27) Hu, L.; Hecht, D. S.; Gruner, G., Percolation in Transparent and Conducting Carbon Nanotube Networks. *Nano Lett.* 2004, *4*, 2513-2517.
(28) Ruzicka, B.; Degiorgi, L.; Gaal, R.; Thien-Nga, L.; Bacsa, R.; Salvetat, J. P.; Forro, L., Optical and DC Conductivity Study of Potassium-Doped Single-Walled Carbon Nanotube Films. *Phys. Rev. B* 2000, *61*, R2468-R2471.

(29) Bol'shakov, M. V.; Tyshkevych, T. R., Influence of the Geometry of Metal-Wire Gauze Nets on their Porosity. *Mater. Sci.* 1999, *35*, 143-145.
(30) Belwalkar, A.; Grasing, E.; Van Geertruyden, W.; Huang, Z.; Misiolek, W. Z., Effect of Processing Parameters on Pore Structure and Thickness of Anodic Aluminum Oxide (AAO) Tubular Membranes. *J. Membr. Sci.* 2008, *319*, 192-198.
(31) Kouhikamali, R.; Abadi, S.; Hassani, M., Numerical Study of Performance of Wire Mesh Mist Eliminator. *Appl. Therm. Eng.* 2014, *67*, 214-222.
(32) Singh, P.; Ravindra, N. M., Temperature Dependence of Solar Cell Performance-an Analysis. *Sol. Energy Mater. Sol. Cells* 2012, *101*, 36-45.
(33) Yang, H.; Wang, H.; Cao, D. Y.; Sun, D. M.; Ju, X. B., Analysis of Power Loss for Crystalline Silicon Solar Module during the Course of Encapsulation. *Int. J. Photoenergy* 2015, 251615.
(34) Shen, X.; Sun, B.; Liu, D.; Lee, S.-T., Hybrid Heterojunction Solar Cell Based on Organic–Inorganic Silicon Nanowire Array Architecture. *J. Am. Chem. Soc.* 2011, *133*, 19408-19415.
(35) Li, X.; Zhu, H.; Wang, K.; Cao, A.; Wei, J.; Li, C.; Jia, Y.; Li, Z.; Li, X.; Wu, D., Graphene-On-Silicon Schottky Junction Solar Cells. *Adv. Mater.* 2010, *22*, 2743-2748.
(36) Larsen, L. J.; Shearer, C. J.; Ellis, A. V.; Shapter, J. G., Solution Processed Graphene-Silicon Schottky Junction Solar Cells. *RSC Adv.* 2015, *5*, 38851-38858.
(37) Larsen, L. J.; Shearer, C. J.; Ellis, A. V.; Shapter, J. G., Optimization and Doping of Reduced Graphene Oxide–Silicon Solar Cells. *J. Phys. Chem. C* 2016, *120*, 15648-15656.

Chapter 5 Application of a hole transporting organic interlayer in graphene oxide/single walled carbon nanotube-silicon heterojunction solar cells

This Chapter has been published as “Application of a Hole Transporting Organic Interlayer in Graphene oxide/Single walled Carbon Nanotube-Silicon Heterojunction Solar Cells” in Journal of Materials Chemistry A in 2017.

Yu, L.; Batmunkh, M.; Grace, T.; Dadkhah, M.; Shearer, C.; Shapter, J. Application of a Hole Transporting Organic Interlayer in Graphene oxide/Single walled Carbon Nanotube-Silicon Heterojunction Solar Cells. J. Mater. Chem. A 2017. 5, 8624-8634.

5.1 Overview

The widely used hole transporting material, 2,2',7,7'-tetrakis(N,N'-di-p-methoxyphenylamine)-9,9'-spirobifluorene (spiro-OMeTAD), has been integrated as an interlayer with graphene oxide/single walled carbon nanotube–silicon (GOCNT/Si) heterojunction solar cells, creating GOCNT/spiro-OMeTAD/Si solar cells. The GOCNT electrode was deposited onto a Si surface coated with spiro-OMeTAD by organic–aqueous transfer without damaging the hole transporting layer. The effect of thickness of both the organic hole transporting layer and the transparent GOCNT electrode as well as the influence of gold chloride ($AuCl_3$) doping on the performance of the solar cells are explored. Devices with power conversion efficiency about 13 % have been fabricated with the optimised organic interlayer thickness (60 nm) and the transparent GOCNT electrodes (T > 80% at 550 nm). The results in this Chapter suggest that the recombination at the heterojunction interface is significantly minimised with the addition of a hole-conducting organic interlayer. Furthermore, the spiro-OMeTAD interlayer also functioned as a protection layer for the silicon surface, leading to dramatically enhanced stability of the solar cell performance.

5.2 Introduction

Carbon nanomaterials, such as carbon nanotubes[1-5] and graphene,[6-8] are widely studied and applied into thin film solar cells due to their excellent optoelectronic properties. Graphene oxide (GO), a 2D material, is amphiphilic and contains hydroxyl and epoxy groups on the basal plane, and hydroxyl and carboxyl groups at the edge regions.[9-10] It has been combined with CNTs to create a GOCNT composite for the preparation of transparent conducting films.[11] GO can disperse the aggregated CNTs onto their surface because of its amphiphilic nature, and thus form a stable aqueous suspension.[12] Additionally, extra transport paths are provided by GO sheets within some regions where the CNTs are not connected.[13-14] More attractively in terms of processing, the GOCNT composite films can be handled in aqueous medium unlike the pure CNT films because of the hydrophobic nature-related high compatibility with water.[4]

Recently, GOCNT hybrid films have been used as a transparent top window electrode with silicon to create heterojunction photovoltaics.[15] Though the exact nature of the heterojunction

is still not clear, the heterojunction can be approximately regarded as Schottky barrier, metal–insulator–semiconductor or p–n junctions.[16] In most cases, there is a thin layer of SiO_2 between GOCNT and Si which reduces the dark current caused by electron tunnelling from Si to CNT and thus improves the diode properties.[17]

In addition, several studies have shown that the addition of a conductive polymer interlayer between the silicon surface and the thin film electrodes, such as polyaniline, poly(3-hexylthiophene-2,5-diyl) (P3HT), and poly(3,4-ethylenedioxythiophene):poly(styrene sulfonate) (PEDOT:PSS),[18-19] can enhance the performance of CNT/Si device. The main improvement of the devices is attributed to the hole transporting effect with the addition of the conductive polymers.[20] Currently, the most widely used HTL material in dye sensitised and perovskite solar cells is spiro-OMeTAD,[21-23] and it has also been integrated with graphene/silicon solar cells as an interlayer in order to improve both the hole transporting and the diode properties of the heterojunction.[20,24] Based on these studies, the organic hole transporting material, spiro-OMeTAD, can be potentially applied as an interlayer in the GOCNT/Si device to both behave as a HTL[25-27] and to improve the diode properties at the interface without significant amount absorbance of solar irradiation, as shown in Figure 5.1 (b).[28-32]

In this Chapter, the potential of applying spiro-OMeTAD as an interlayer between GOCNT transparent conducting electrode and Si (GOCNT/spiro-OMeTAD/Si) was explored and the devices without the organic interlayer were also fabricated for comparison, as shown in Figure 5.1 (c) and (d). The device performance was maximised by optimising the thickness of spiro-OMeTAD and the transmittance of GOCNT film. The effect of $AuCl_3$ doping was studied and the stability of the device performance was monitored over 2 weeks.

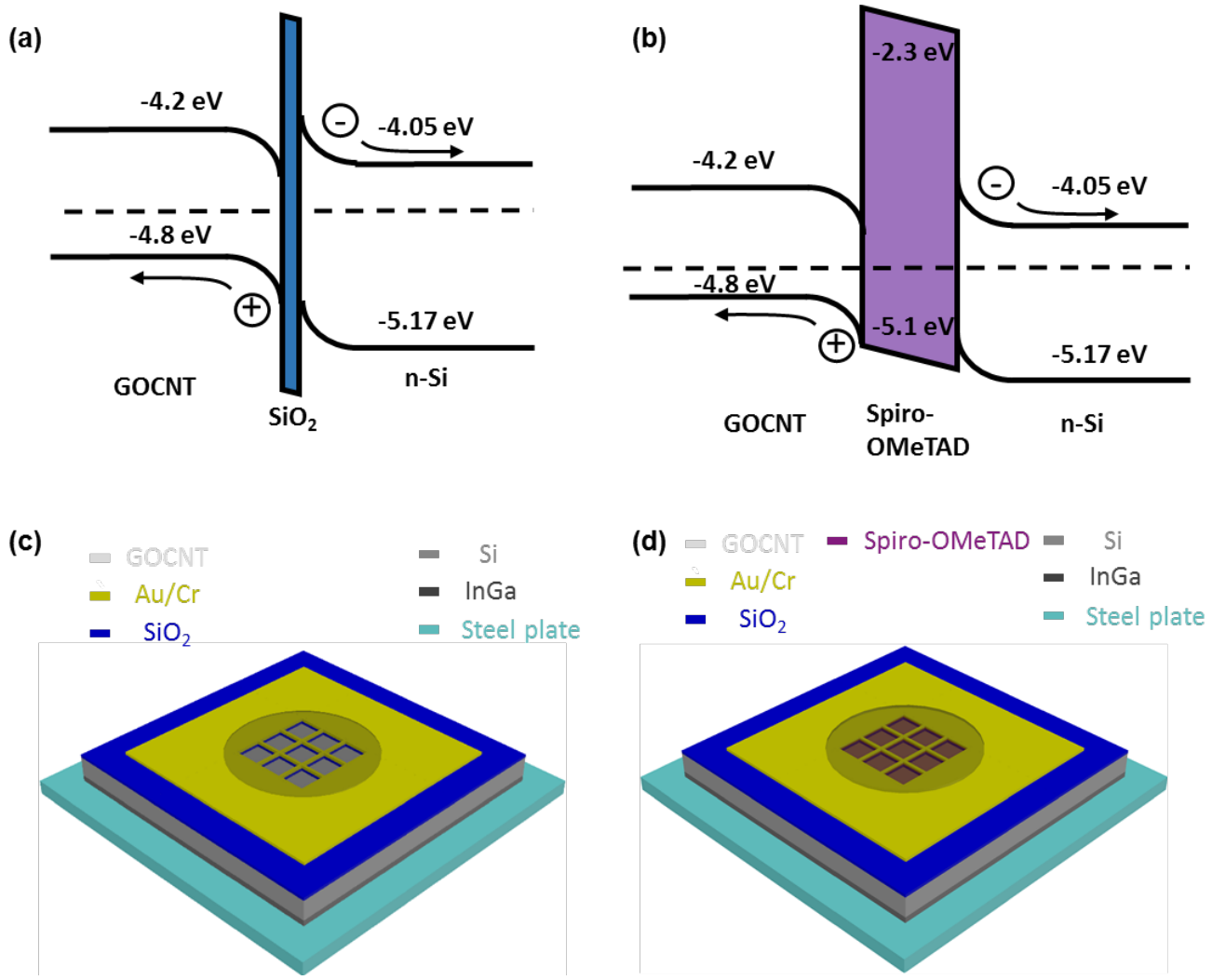

Figure 5.1 Schematic energy diagram of (a) GOCNT/Si and (b) GOCNT/spiro-OMeTAD/Si solar cell. Schematic device structures of (c) GOCNT/Si and (d) GOCNT/spiro-OMeTAD/Si devices. The band gap of GOCNT hybrid film is taken from the S_{11} peak position from the UV-Vis-NIR absorbance of the hybrid film.

5.3 Experimental details

The preparation methods of the spiro-OMeTAD and GOCNT stock solutions are described in sections 2.2.1.2 and 2.2.2.2. The fabrication and the characterisation of GOCNT TCFs are described in sections 2.4.3 and 2.6.2. The fabrication, post treatments and performance testing of the solar cells are described in sections 2.5.3.1, 2.5.3.2 and 2.6.2.

5.4 Results and discussion

5.4.1 Device preparation and characterisation

In this Chapter, the hybrid films of GOCNT were fabricated by vacuum filtration onto MCE filter membrane, which was then removed by immersing GOCNT/MCE in acetone for 90 min. Acetone can dissolve the majority of the MCE rapidly (<1 min) and the resulting flexible GOCNT film can move around in the liquid phase freely, as shown in Figure 5.2 (a). A homemade Teflon spoon was used to pick up and transfer the free-standing film from acetone to the deionised water bath. Interestingly, the GOCNT film was able to spread on the surface of water keeping its own shape, as shown in Figure 5.2 (b).

Since the spiro-OMeTAD can be easily dissolved in acetone but not water, the transfer of GOCNT from acetone into water is very important in the solar cell devices. When the GOCNT film is floating on top of the water surface, a spiro-OMeTAD coated Si substrate can pick up it with no dissolution of the spiro-OMeTAD. The amphiphilic GO sheets play an essential role in the organic-aqueous transfer process of the hybrid film. In comparison, ten pure CNT films (after dissolving MCE in acetone) were transferred in the identical manner, but most of them disintegrated and the rest crumpled immediately when contacted with the water due to the intrinsic hydrophobic nature of the CNT, as shown in Figure 5.2 (c) and (d). By integrating GO sheets into the CNT network, both the mechanical properties and the wettability of the hybrid improved because of the two dimensional nature and hydrophilic groups on GO sheets.[33-34] After pressing GOCNT hybrid film down into water phase by the Teflon spoon, it behaves in an identical manner as it did in acetone phase, which is a further piece of evidence suggesting the improved water compatibility, as shown in Figure 5.2 (d). However, this transfer approach has its own limitation. When the GOCNT hybrid film is very thin (T > 80%), the difficulty of the transfer increases dramatically. Generally, the success rate of the transfer process for hybrid films with T of 77% is above 90% but this number is about 40% for GOCNT films with T of 84% at 550 nm. In this Chapter, GOCNT films with T above 90% at 550 nm always disintegrated during the transfer process. Though increasing the GO content in the hybrid film is expected

to increase the success rate of the thin film transfer, this would dramatically sacrifice the optoelectronic properties.[15]

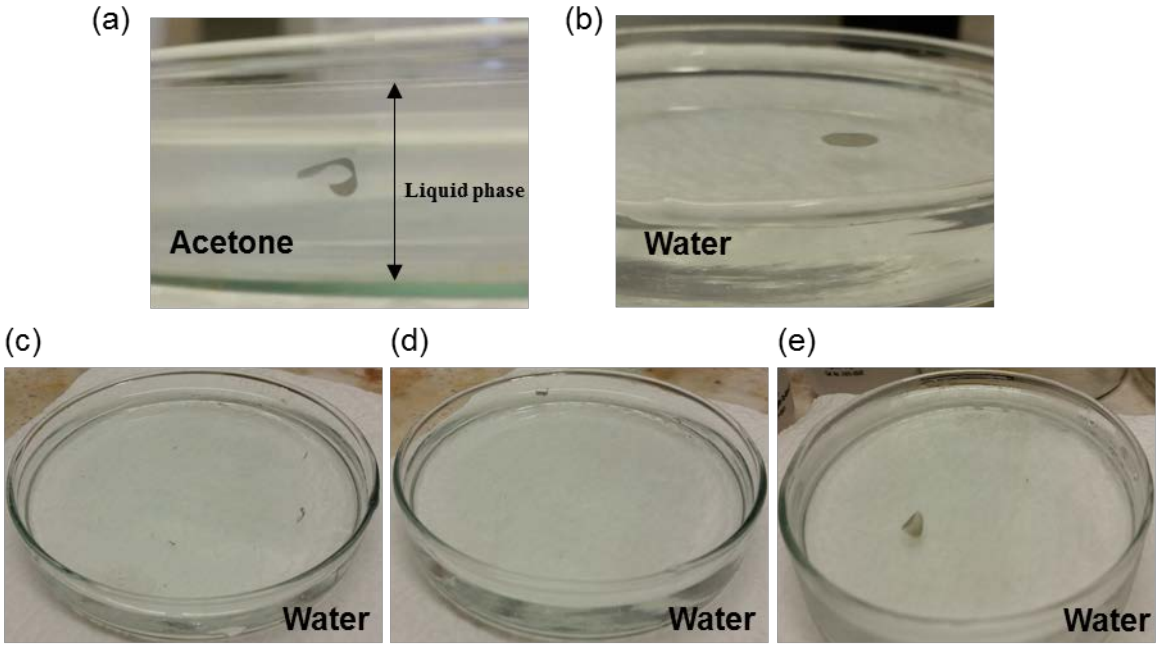

Figure 5.2 (a) GOCNT films (T = 77% at 550 nm) moving below the liquid surface in acetone after dissolving MCE in a glass Petri dish. (b) GOCNT films spreading on top of the deionised water surface after being transferred by a homemade Teflon spoon. (c) Pure CNT films broken into pieces and (d) shrunk after being transferred from acetone to deionised water. (e) GOCNT films after being pressed down into water phase.

Figure 5.3 shows the Raman spectra of pure GO, CNT and GOCNT film on glass slides. The intensity ratios of D-band to G-band (D/G ratio) for pure GO, pure CNT and GOCNT films are 1.10, 0.12 and 0.21, respectively. The D band is due to the out-of-plane vibrations and it is related to the defects on graphene sheets while G band signal is caused by the in-plane vibrations of sp^2 bonded carbon atoms. D band intensity is mainly due to the functional groups on GO sheets and a lower D/G ratio indicates lower defect content. As shown in Figure 5.3, both CNT (low-functionalised CNTs) and GO (highly functionalised GO) show typical values. The D/G ratio of GOCNT films is higher than that of pure CNT is due to the increased GO content in the films, rather than from the GO increasing the defect density of the CNTs.

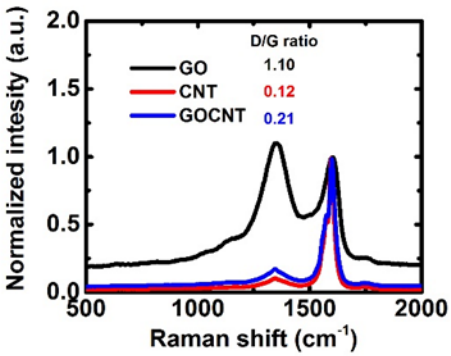

Figure 5.3 The Raman spectra of pure GO, CNT and GOCNT films on microscope glass.

As shown in Figure 5.4 (a), the transmittance (at 550 nm) of the GOCNT hybrid film has a linear correlation with the stock dispersion volume used during vacuum, as shown in Equation 5.1;

$$T = 92.64 - 0.052V \ (R^2 = 0.98) \qquad \text{Equation 5.1}$$

With higher volumes of stock dispersion, more GO sheets and CNTs are collected on the filter membrane. Then, the transmittance of the films decreases due to more light being absorbed and the resulting films are thicker and thicker. More and more percolation paths are created with the decrease in transmittance, which results in the decrease in sheet resistance, as shown in Figure 5.4 (b). In this Chapter, the p-type dopant, $AuCl_3$, is used to improve the optoelectronic properties of GOCNT hybrid films and dramatically reduce the sheet resistance (Figure 5.4 (b)). In addition, the sheet resistance has an exponential relationship with transmittance for both original and doped electrodes, as shown in Equation 5.2 and Equation 5.3.

$$R_{sheet} = 4.82 \times 10^{-1}\, e^{\frac{T}{10.59}} + 99.67 \ (R^2 = 0.92) \qquad \text{Equation 5.2}$$

$$R_{sheet} = 7.49 \times 10^{-4}\, e^{\frac{T}{6.09}} + 136.8 \ (R^2 = 0.99) \qquad \text{Equation 5.3}$$

As shown in Figure 5.4 (c), after $AuCl_3$ doping, there is a slight decrease in the transmittance of the GOCNT film with complete bleaching of S_{11} peak and a suppressed S_{22} peak in UV-Vis-NIR, which suggests that the Fermi level shifts into the valence band of semiconducting SWCNT.[35] The exact mechanism of the doping is unclear. Most researchers believe that the p-

type doping is due to the reduction of cationic Au^{3+} to Au^0 while others attribute the doping to the formation of CNT-Cl where Cl withdraws electrons from CNTs.[36]

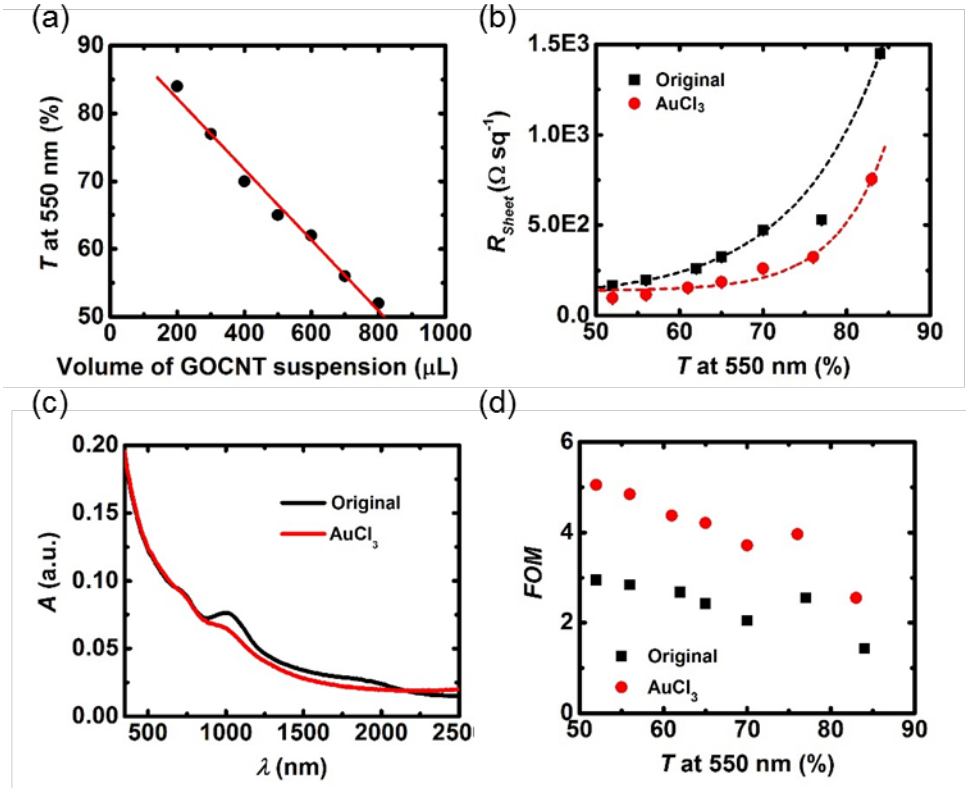

Figure 5.4 (a) Transmittance of GOCNT films at 550 nm versus the volume of stock dispersion used in vacuum filtration. (b) Sheet resistance of GOCNT films with different transmittance before and after $AuCl_3$ doping. (c) Absorbance versus wavelength for the original and $AuCl_3$ doped GOCNT films. (d) FOM of hybrid films with different transmittance before and after doping.

The ideal transparent window electrode of photovoltaics should have both high transmittance and low sheet resistance. High transmittance enables more photons to reach and be absorbed by Si surface while low sheet resistance indicates the formation of highly conductive network which can efficiently transport the separated charge carriers. Therefore, both the T and R_{sheet} have a great influence on the final efficiency of the devices, but normally improving one parameter sacrifices the other.[2] As described in section 1.2.2.1, figure of merit (FOM) is widely used to characterise and compare the optoelectronic properties of transparent conducting

electrodes with different T and R_{sheet}. Generally, lower FOM value infers worse optoelectronic properties.

As shown in Figure 5.4 (d), the FOM values are calculated for the GOCNT films correlated to T at 550 nm before and after doping. Since the sheet resistance decreased while the transmittance was maintained at a stable level after the $AuCl_3$ treatment, FOM values (optoelectronic properties) were improved, which is consistent with the results in the literature.[36] GOCNT films with low T have a higher FOM than that of films with high T. The FOM values of the hybrid films range from 2 to 5, and it is much lower than that of a rigid transparent conducting glass, such as indium tin oxide coated glass (commonly about 150).[37] The potential reasons for the low FOM values include the limited length of the CNTs (about 1 μm) and the limited number of junctions in the thin films. However, the FOM values are similar to the best CNT films applied in CNT/Si heterojunction devices.[38] The general trend is that FOM decreases with the increases in T because of the dramatically increasing R_{sheet} with the increase of T. Although thicker films (with higher FOM (lower T)) have better optoelectronic properties, it does not mean that they are appropriate for the solar cell application as the window electrode because high output of photocurrent is always linked to high T. Therefore, in this Chapter, in order to decrease the internal series resistance of solar cells resulting from the relatively poor FOM, a grid design of front metal electrode is applied over the entire active region of the devices.[39]

SEM images of pure CNT, pure GO and GOCNT are shown in Figure 5.5 (a), (b) and (c). The produced GOCNT hybrid film closely resembles that of pure CNT with only a few GO sheets observed. This finding agrees with the sheet resistance and Raman measurements in that the properties of the hybrid film are much closer to that of a pure CNT film than a pure GO film. However, even though the content of GO is low, GO sheets play an important role in creating a stable dispersion by wrapping around the CNTs as well as enhancing the mechanical properties of the film during organic-aqueous transfer.

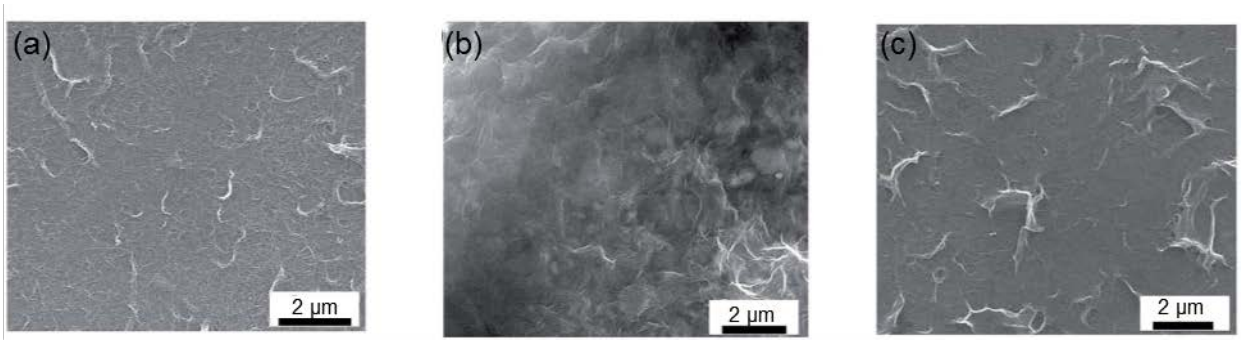

Figure 5.5 SEM images of (a) pure CNTs, (b) pure GO and (c) GOCNT.

5.4.2 Testing of the initial solar cell

Firstly, the role of GOCNT window electrode in the photovoltaics was studied with the comparison of the performance of two various types of solar cells before chemical doping (so as to exclude the dopant effect on the performance), including spiro-OMeTAD/Si and GOCNT/spiro-OMeTAD/Si. The light and dark J–V curves of these solar cells are shown in Figure 5.6 and the details are summarised in Table 5.1. By comparing the performance of these two types of devices, spiro-OMeTAD/Si has a much poorer performance (PCE = 0.05 ± 0.02%) because of the very low short circuit current density (J_{SC}), open circuit voltage (V_{OC}) and fill factor (FF). In terms of the diode properties, it also has poor performance with ideality, J_{sat} and ϕ_B of 3.67 ± 0.49, $3.15 \times 10^{-1} \pm 1.26 \times 10^{-1}$ mA cm^{-2}, and 0.61 ± 0.07 eV, which suggests that the lower efficiency might be due to the severe recombination of charge carriers after separation and it is related to the high R_{sheet} of organic layer of spiro-OMeTAD (above 10^6 Ω sq^{-1}). With the addition of GOCNT hybrid electrodes (GOCNT/spiro-OMeTAD/Si), the efficiency (9.49 ± 0.29%, which is approaching to the best SWCNT/Si solar cell before any post treatment, 12.4%)[40] has been improved dramatically, with J_{SC}, V_{OC}, and FF increasing to 26.15 ± 0.26 mA cm^{-2}, 0.550 ± 0.017 V, and 0.66 ± 0.02. The improvement in the diode properties (with ideality, J_{sat} and ϕ_B of 1.19 ± 0.06, $1.99 \times 10^{-6} \pm 1.7 \times 10^{-6}$ mA cm^{-2}, and 0.91 ± 0.01 eV) might be the reason for the performance enhancement. It indicates that the recombination is suppressed due to a much lower R_{sheet} (below 500 Ω sq^{-1}) which can collect and transport the separated charge carriers to the metal electrode rapidly by GOCNT hybrid films.

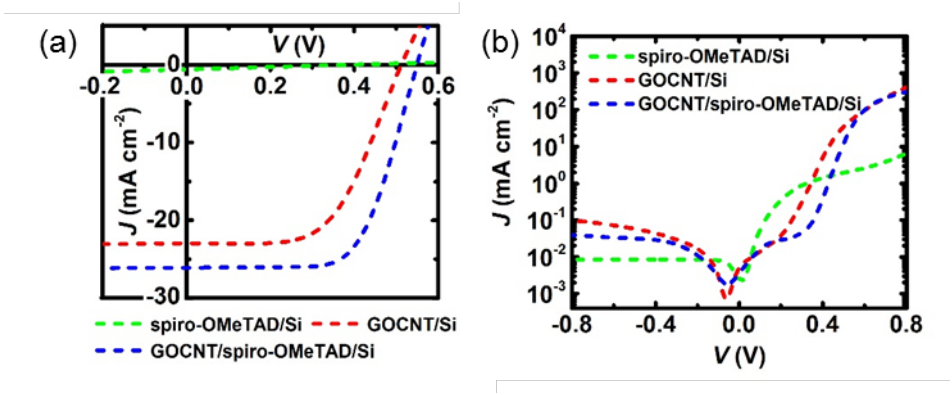

Figure 5.6 Performance of the spiro-OMeTAD/Si, GOCNT/Si and GOCNT/spiro-OMeTAD/Si devices under (a) light and (b) dark conditions before $AuCl_3$ doping.

Secondly, the function of the spiro-OMeTAD interlayer is further explored by comparing the performance of GOCNT/Si and GOCNT/spiro-OMeTAD/Si solar cells before doping to exclude the influence of the dopant. As shown in Figure 5.6 (a), (b) and Table 5.1, the performance of GOCNT/Si device (6.80 ± 0.27%) is improved with the addition of the organic interlayer to form GOCNT/spiro-OMeTAD/Si structure (9.49 ± 0.29%). The improvement with the interlayer is mainly due to the increased FF from 0.58 ± 0.03 to 0.66 ± 0.02, slight increase in J_{SC} from 23.02 ± 0.24 to 26.15 ± 0.26 mA cm^{-2} and increased V_{OC} from 0.511 ± 0.006 to 0.550 ± 0.017 V. At the same time, better diode properties were observed with a lower ideality and J_{sat}. In addition, ϕ_B of the GOCNT/Si device is about 0.1 eV lower than that of GOCNT/spiro-OMeTAD/Si solar cell and lower ϕ_B value normally indicates more serious recombination events, which is in line with the increase in FF as well as V_{OC} after the addition of interlayer. As described earlier, the GOCNT/Si interface is not an ideal Schottky junction and thus the calculated ϕ_B values are based on the assumption of a much simpler interface. Nevertheless, an increase in ϕ_B was also observed in previous reports where an organic interlayer was added in graphene/Si solar devices with the improvements in V_{OC} and FF at the same time.[28] Overall, the increased FF and V_{OC}, as well as the improved diode properties infer that the interlayer may behave as an HTL and electron blocking layer (EBL) at the same time.

Table 5.1 The performance details of light and dark J–V curves of the spiro-OMeTAD/Si, GOCNT/Si and GOCNT/spiro-OMeTAD/Si devices before and after the p-type doping of $AuCl_3$. The thickness of spiro-OMeTAD layers in the devices in this table is 90 nm and

the T of GOCNT films to be 77% before $AuCl_3$ and. The errors are calculated by the standard deviation of 3 devices of each type.

	spiro-OMeTAD/Si		GOCNT/Si		GOCNT/spiro-OMeTAD/Si	
	Original	$AuCl_3$	Original	$AuCl_3$	Original	$AuCl_3$
Efficiency (%)	0.05 ± 0.02	0.06 ± 0.02	6.80 ± 0.27	4.73 ± 0.33	9.49 ± 0.29	10.59 ± 0.27
J_{SC} (mA cm^{-2})	1.32 ± 0.14	1.29 ± 0.16	23.02 ± 0.24	24.77 ± 0.13	26.15 ± 0.26	25.22 ± 0.18
V_{OC} (V)	0.392 ± 0.002	0.392 ± 0.002	0.511 ± 0.006	0.424 ± 0.007	0.550 ± 0.017	0.576 ± 0.003
FF	0.10 ± 0.01	0.11 ± 0.01	0.58 ± 0.03	0.45 ± 0.03	0.66 ± 0.02	0.73 ± 0.01
R_{shunt} (Ω)	3.71×10^3 ± 2.52×10^3	6.41×10^3 ± 3.42×10^3	2.49×10^5 ± 8.54×10^4	6.52×10^3 ± 1.54×10^3	1.15×10^4 ± 1.67×10^4	8.22×10^4 ± 9.67×10^4
R_{series} (Ω)	6390 ± 258	6690 ± 176	72 ± 7	137 ± 12	63 ± 5	44 ± 3
Ideality	3.67 ± 0.49	3.78 ± 0.57	1.47 ± 0.07	2.55 ± 0.25	1.19 ± 0.06	1.12 ± 0.08
J_{sat} (mA cm^{-2})	3.15×10^{-1} ± 1.26×10^{-1}	3.02×10^{-1} ± 2.54×10^{-1}	6.51×10^{-5} ± 9.30×10^{-6}	4.78×10^{-2} ± 3.94×10^{-2}	1.99×10^{-6} ± 1.7×10^{-6}	3.12×10^{-6} ± 0.7×10^{-6}
ϕ_B (eV)	0.61 ± 0.07	0.61 ± 0.08	0.82 ± 0.01	0.66 ± 0.05	0.91 ± 0.01	0.90 ± 0.01

5.4.3 $AuCl_3$ doping

In order to further improve the efficiency of the devices, $AuCl_3$ was used to dope the GOCNT electrode by reducing the sheet resistance of the films. The detailed effect of the doping on the performance of the solar cells are listed in Table 5.1. $AuCl_3$ doping does not have any dramatic change to the performance of spiro-OMeTAD/Si devices, as shown in Table 5.1. After $AuCl_3$ doping, the efficiency of GOCNT/Si device decreased to 4.73 ± 0.33%, as shown in Figure 5.7 (a). The decrease in the efficiency seems to be due to the short circuits induced by Au NPs which bridges the Si with the front metal contact.[41] The short circuits cause a difference in the diode properties at the heterojunction (leading to higher ideality and J_{sat}, as shown in Figure 5.7 (b)) and the frequency of recombination at the interface is increased, which is in line with the drop of V_{OC} and FF. In contrast, with the spiro-OMeTAD applied as the interlayer in between GOCNT and Si, the performance of the device (GOCNT/spiro-OMeTAD/Si device) is improved after chemical doping to 10.59 ± 0.27%, which is close to the best SWCNT/Si

devices after post treatment with no antireflection coating, 13.7%).[42] The increased efficiency is mainly caused by the reduced R_{sheet} of GOCNT electrodes. Importantly, in this case, the diode properties (ideality and J_{sat}) stay at a same level (Table 5.1), which suggests that the short circuits do not occur since the Au NPs are physically blocked by the organic interlayer. Because of the improved efficiency, $AuCl_3$ doping is used in all subsequent experiments and the performance is signified by solid lines in J-V light/dark curves and EQE graphs.

The EQE curves of three different types of devices after $AuCl_3$ doping are shown in Figure 5.7 (c). Spiro-OMeTAD/Si devices have the lowest photocurrent output cross the whole wavelength range from 300 to 1100 nm, which is consistent with the low J_{SC} observed from the J-V curves. The GOCNT/Si devices have a broad contribution of photocurrent from 300 to 1000 nm while the GOCNT/spiro-OMeTAD/Si devices have lower photocurrent from 300 to 400 nm, which is due to the absorption of organic interlayer.[43] In the EQE curve of GOCNT/spiro-OMeTAD/Si devices, there is a bump at about 700 to 900 nm. This is probably caused by the absorption of Li-TFSI added in the spiro-OMeTAD interlayer from 400 to 600 nm.[44] The higher EQE values for GOCNT/spiro-OMeTAD/Si devices from 500 to 1000 nm could be attributed to the suppressed charge recombination at the heterojunction which leads to higher overall efficiencies.

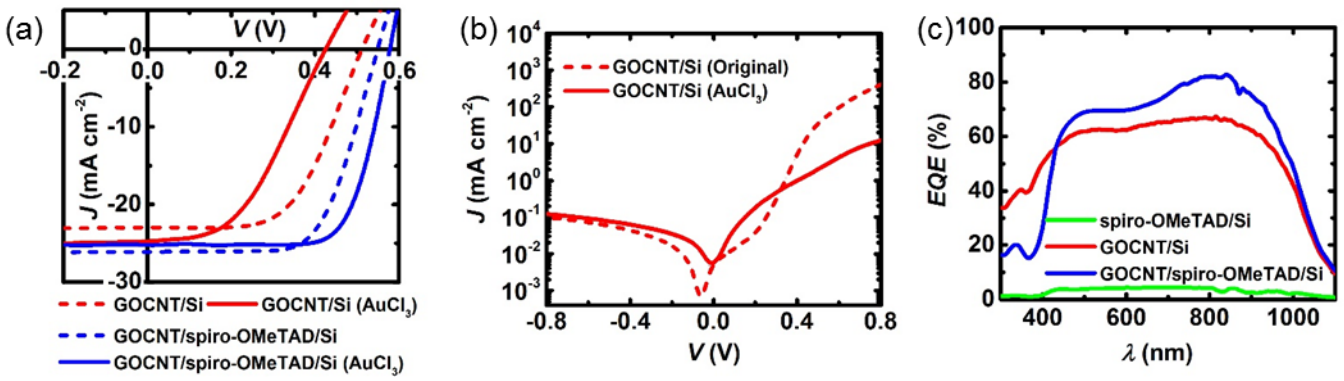

Figure 5.7 (a) J-V light curves of GOCNT/Si and GOCNT/spiro-OMeTAD/Si before and after chemical doping. (b) J-V dark curves of the GOCNT/Si device before and after $AuCl_3$ doping (c) EQE curves of the spiro-OMeTAD/Si, GOCNT/Si and GOCNT/spiro-OMeTAD/Si devices after $AuCl_3$ doping (the estimated J_{SC} values from integration of the EQE curves for the spiro-OMeTAD/Si, GOCNT/Si and GOCNT/spiro-OMeTAD/Si are 1.49

mA cm^{-2}, 24.74 mA cm^{-2} and 26.28 mA cm^{-2}). Short dash and solid curves show the performance of the devices before and after $AuCl_3$ doping respectively.

5.4.4 Optimisation of spiro-OMeTAD and GOCNT layer thickness

In order to investigate the influence of thickness of the spiro-OMeTAD interlayer, different volumes (2.5, 10, 20, 30, 40 and 80 µL) of stock solution were applied on top of the Si surface. As shown in Figure 5.8, the thicknesses of the organic films are 10, 40, 60, 90, 120, and 240 nm respectively.

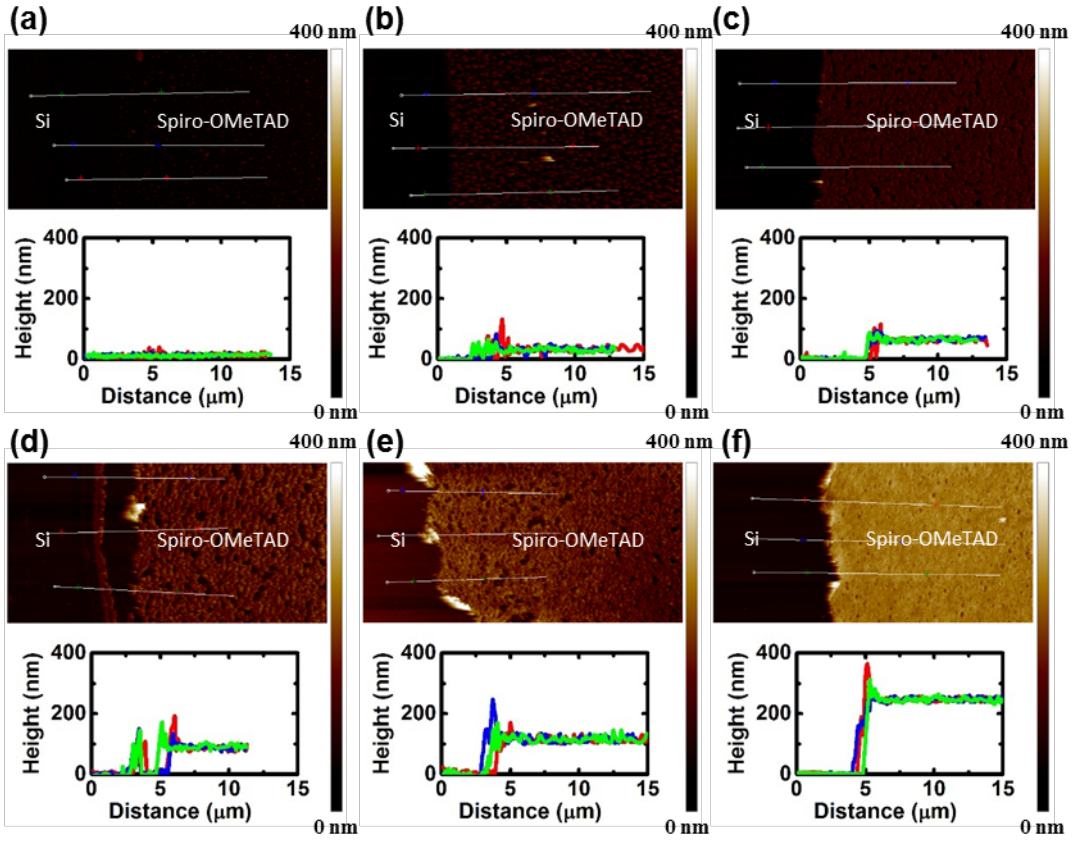

Figure 5.8 AFM height images and corresponding cross sections of spiro-OMeTAD films on Si with different stock solution volumes (a) 2.5 µL, (b) 10 µL, (c) 20 µL, (d) 30 µL, (e) 40 µL and (f) 80 µL.

GOCNT/spiro-OMeTAD/Si solar cells with different thicknesses of organic interlayer were fabricated and the details of the performance after chemical doping are shown in Figure 5.9. The J-V light curves of solar cells are shown in Figure 5.9 (a) and the device with an interlayer

thickness of 60 nm has the highest efficiency (11.41 ± 0.30%), as shown in Figure 5.9 (b). The trend of the efficiency versus thickness is like a volcano shape with the peak at 60 nm. The J_{SC} decreases from 26.84 ± 0.12 to 23.3 ± 0.19 mA cm^{-2} as the organic thickness increases from 10 to 240 nm, as shown in Figure 5.9 (c), because more light is absorbed by the interlayer with thicker interlayer and as a result, less light can be absorbed by the Si. The absorption caused by organic layer and Li-TFSI around 500 nm is clearly decreasing with decreasing thickness, which leads to higher EQE values at these wavelengths, as shown in Figure 5.9 (d). The V_{OC} has a similar volcano trend to that of efficiency, with a peak located at 60 nm (Figure 5.9 (e)). In a similar manner, the maximum FF of devices is located at 60 nm interlayer thickness with a significant decrease for both thinner and thicker films (Figure 5.9 (f)). This improvement in FF is due to the fact that a better heterojunction and suppressed recombination is realised with thicker films (except when it is very thick, 240 nm) though more light is absorbed by the interlayer. However, when the interlayer is extremely thick (240 nm), the transporting capability of the holes from the Si to GOCNT hybrid electrode could be limited. The diode properties of devices are evaluated from the J–V dark curves, as shown in Figure 5.9 (g)–(i). Due to the relatively large error bars, a clear trend is difficult to observe for all of these solar cells. Nevertheless, solar cells with the interlayer thickness of 40, 60 and 90 nm perform very similarly and they are better than devices with interlayer thickness of 10, 120 and 240 nm. Therefore, when the thickness of the interlayer is 60 nm, it is thick enough to create a good heterojunction and physically protect the Si surface and at the same time allows a large number of photons to pass through while still being thick enough to effectively pass the charge carriers to the GOCNT electrode. Thus, such devices have the best performance.

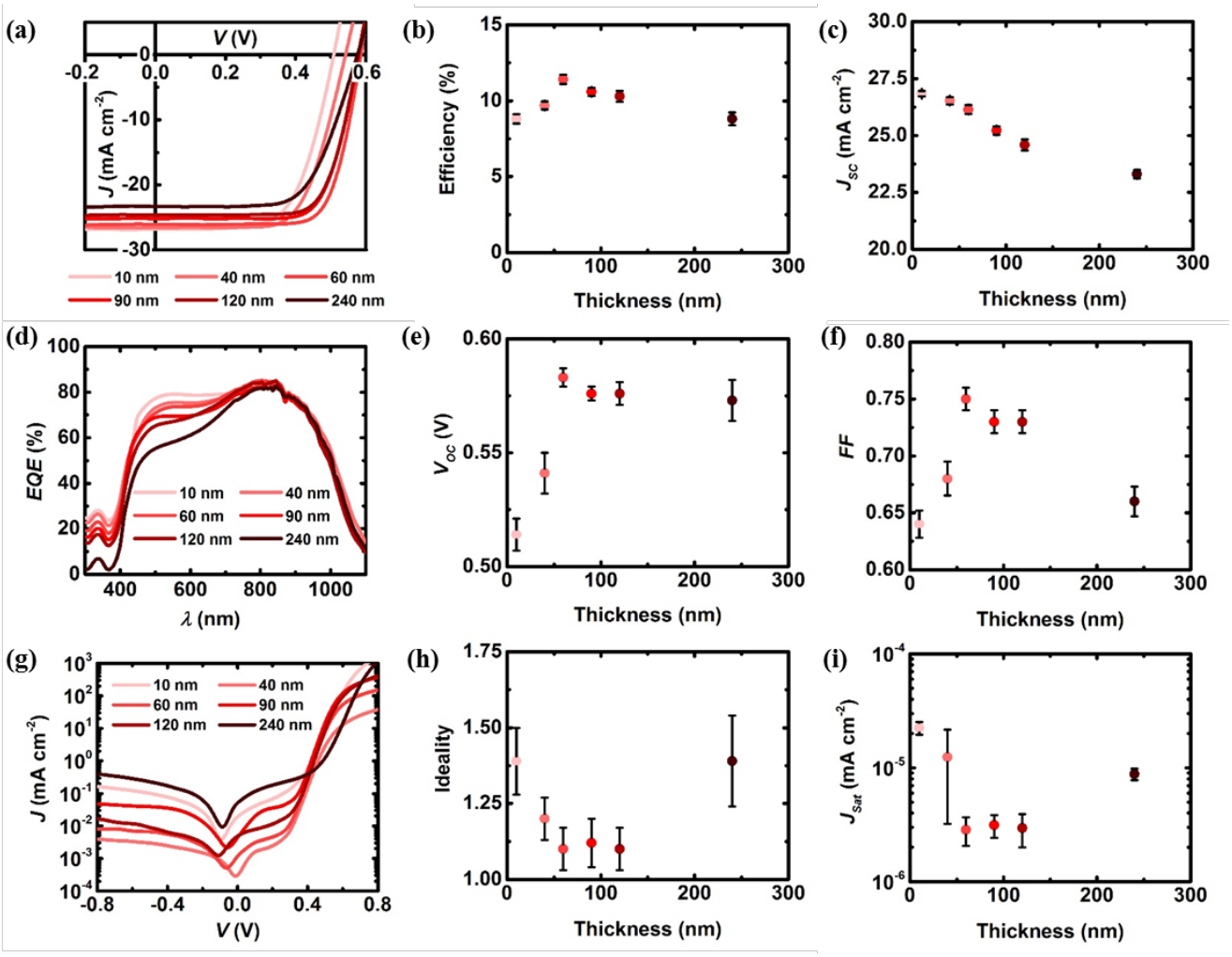

Figure 5.9 The performance of GOCNT/spiro-OMeTAD/Si devices as a function of the organic interlayer thickness after chemical doping (a) J-V light curves, (b) efficiency, (c) J_{SC}, (d) EQE (the estimated J_{SC} values of the devices with interlayer thickness of 10, 40, 60, 90, 120, 240 nm are 28.20 mA cm^{-2}, 27.37 mA cm^{-2}, 27.18 mA cm^{-2}, 26.28 mA cm^{-2}, 25.74 mA cm^{-2}, and 24.40 mA cm^{-2}), (e) V_{OC}, (f) FF, (g) J-V dark curves, (h) ideality and (i) J_{sat}. The performance of devices was tested after chemical doping with the GOCNT transmittance of 77 %.

As described in section 5.4.1, a lower FOM is achieved with higher T which is closely linked to high output of photocurrent and therefore the resulting efficiency. Thus, in this Chapter, with the optimised thickness of spiro-OMeTAD fixed at 60 nm, GOCNT films with different T (56%, 65% and 76% and 83%) were then applied to prepare GOCNT/spiro-OMeTAD/Si solar cells to

study the impact on the solar cell performance. The details of the performance are shown in Figure 5.10. As shown in Fig. 5.10(a) and (b), the solar cell efficiency increases with the increase of GOCNT transmittance from 8.52 ± 0.56% to 12.83 ± 0.22%. Noticeably, with the increase in the transmittance of GOCNT, there is a dramatic improvement in J_{SC} from 19.97 ± 0.16 mA cm^{-2} to 28.1 ± 0.21 mA cm^{-2} while both V_{OC} and FF are stable at about 0.575 V and 0.75. The diode properties of the GOCNT/spiro-OMeTAD/Si with GOCNT films of different transmittance are similar, with ideality, J_{sat} and ϕ_B stabilised around 1.2, 10^{-6} mA cm^{-2} and 0.92 eV, as shown in Figure 5.10 (c).

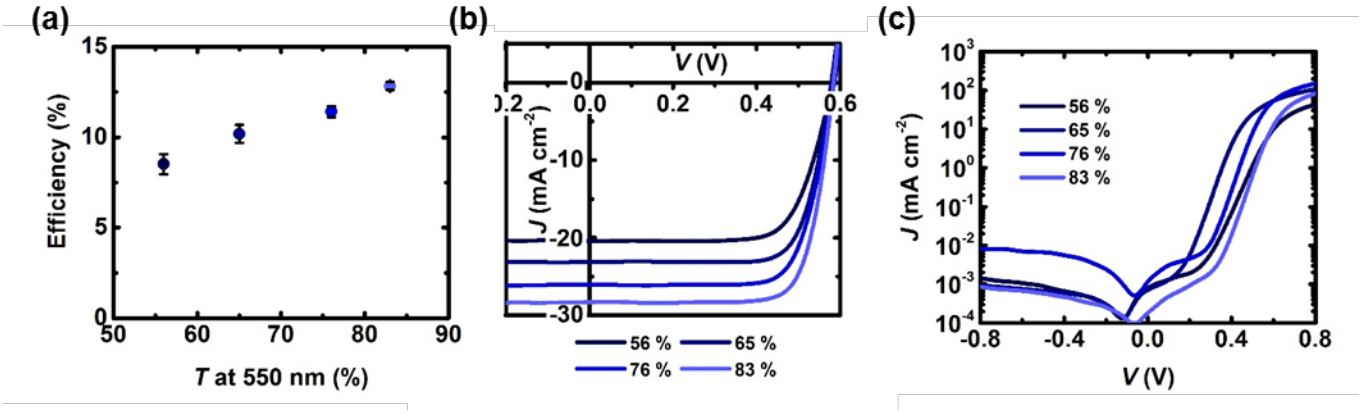

Figure 5.10 (a) Efficiency, J–V light (b) and (c) dark curves of the GOCNT/spiro-OMeTAD/Si devices after chemical doping with various T of GOCNT. The thickness of the organic interlayer in these devices is fixed at 60 nm.

Combining all the results with the transmittance of GOCNT electrodes, the transmittance of window electrode does not have a significant influence on the heterojunction properties (with relatively constant FF and V_{OC}) but dramatically impacts the number of photons passing through the electrode and therefore the number of excitons produced at the heterojunction which is related to J_{SC}. This result shows that the best performing solar cell is fabricated with thin GOCNT films and this is different from most other reported results which generally show an optimised transmittance between 50 and 70%.[15,45] This finding highlights the necessity for the creation of a conformal heterojunction across the interface (which is difficult to realise with thin and sparse CNT films) in these heterojunction devices. This is an ideal case where the quantity of potentially expensive CNT is minimised. Unfortunately, in this study, the transmittance of GOCNT hybrid films is limited by the transfer method, in which films with T

above 90% at 550 nm could not be prepared to fabricate solar devices. However, it is expected that devices with GOCNT films of about 90% transmittance would exhibit even better performance following previous work increasing CNT film T in devices.[39]

5.4.5 The stability of Photovoltaics

Finally, the device stability over 2 weeks was investigated, as shown in Figure 5.11. Generally, the performance of CNT/Si heterojunction solar cells degrades within several days because of both the formation of a thick (>2 nm) SiO_2 layer at the heterojunction which limits the transport of charge carrier and the unstable doping effect on the CNTs which reduce film conductivity.[46-48] In order to only observe the degradation from the SiO_2 formed at the interface, the change of efficiency of GOCNT/Si was compared with that of GOCNT/sprio-OMeTAD/Si (red circles and blue open triangles in Figure 5.11 (a)). The performance of the device without the conformal spiro-OMeTAD interlayer decreases by about 30% within 14 days while the device with the organic interlayer only decreases by about 10 %. This suggests that the organic interlayer limits the growth of unwanted SiO_2 at the heterojunction.[49]

In order to investigate the stability of chemical doping, the performance degradation of GO/spiro-OMeTAD/Si with and without doping are compared, as shown by the blue series in Figure 5.11, and it is obvious that efficiency decreases more over two weeks when chemical dopant is employed. In several previous reports, similar behaviour of the performance degradation was observed with few layer graphene doped with $AuCl_3$.[50-52] Because of the difference in the surface energy between the Au nanoparticles and the graphitic structure, the Au nanoparticles tend to form aggregates. In addition, if some of the doping effect is due to Cl^- bonded on the surface, these reactive groups are likely to be removed from the surface due to the reaction with air. The reduction in solar cell performance with doping is closely related to the decrease in film FOM (Figure 5.11 (b)), which infers that there is a strong correlation between GOCNT film conductivity and photovoltaic performance. Besides the changes to the GOCNT film and Si interface, the other potential reason is the degradation of the conductivity of the organic interlayer as the accumulation of Li-TFSI occurs.[53] Overall, the GOCNT/spiro-OMeTAD/Si device before the chemical doping (hollow blue triangles) has the best stability in efficiency over 15 days, which is comparable to the most stable CNT/Si heterojunction devices with the application of polymeric encapsulating coatings.[17]

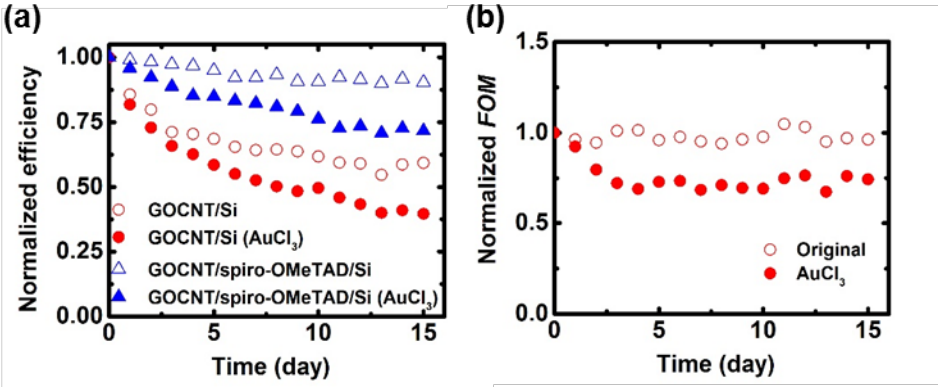

Figure 5.11 Degradation of the solar cell performance: (a) efficiency and (b) FOM of the GOCNT hybrid films. The properties of the devices or hybrid films before and after chemical doping are characterised by the hollow and solid data points.

5.5 Conclusions

GOCNT/spiro-OMeTAD/Si solar cells have been fabricated by the application of organic material spiro-OMeTAD between GOCNT and Si layers. $AuCl_3$ was an effective p-type dopant and can improve the FOM of the GOCNT TCFs. With the optimal thickness of spiro-OMeTAD and transmittance of GOCNT film, solar cells with efficiency of 12.83 ± 0.22% have been fabricated. The organic interlayer plays several important roles in the heterojunction solar cells. It can not only act as an HTL to enhance the properties of heterojunction by supressing recombination of charge carriers, but also behaves as a protective coating which physically limits short circuits due to Au nanoparticles as well as preventing atmospheric interaction with the Si substrate to limit SiO_2 growth.

REFERENCES:

(1) Shastry, T. A.; Hersam, M. C., Carbon Nanotubes in Thin-Film Solar Cells. *Adv. Energy Mater.* 2016, 1601205.

(2) Yu, L.; Shearer, C.; Shapter, J., Recent Development of Carbon Nanotube Transparent Conductive Films. *Chem. Rev.* 2016, 13413-13453.

(3) Batmunkh, M.; Biggs, M. J.; Shapter, J. G., Carbon Nanotubes for Dye-Sensitized Solar Cells. *Small* 2015, *11*, 2963-2989.

(4) Yadav, S.; Kumar, V.; Arora, S.; Singh, S.; Bhatnagar, D.; Kaur, I., Fabrication of Ultrathin, Free-Standing, Transparent and Conductive Graphene/Multiwalled Carbon Nanotube Film with Superior Optoelectronic Properties. *Thin Solid Films* **2015**, *595, Part A*, 193-199.
(5) Gao, G.; Yu, L.; Vinu, A.; Shapter, J. G.; Batmunkh, M.; Shearer, C. J.; Yin, T.; Huang, P.; Cui, D., Synthesis of Ultra-Long Hierarchical ZnO Whiskers in a Hydrothermal System for Dye-Sensitised Solar Cells. *RSC Adv.* **2016**, *6*, 109406-109413.
(6) Loh, K. P.; Tong, S. W.; Wu, J. S., Graphene and Graphene-Like Molecules: Prospects in Solar Cells. *J. Am. Chem. Soc.* **2016**, *138*, 1095-1102.
(7) Li, X.; Zhu, H.; Wang, K.; Cao, A.; Wei, J.; Li, C.; Jia, Y.; Li, Z.; Li, X.; Wu, D., Graphene-On-Silicon Schottky Junction Solar Cells. *Adv. Mater.* **2010**, *22*, 2743-2748.
(8) Batmunkh, M.; Shearer, C. J.; Biggs, M. J.; Shapter, J. G., Solution Processed Graphene Structures for Perovskite Solar Cells. *J. Mater. Chem. A* **2016**, *4*, 2605-2616.
(9) Zhi-Jia, L.; Hong-Zhang, G.; Xing, Z.; Baotan, D.; Er-Xiong, D.; Jing, W.; Zhanguo, L.; Baoquan, S.; Jie, W.; Juncheng, L., A Timesaving, Low-Cost, High-Yield Method for the Synthesis of Ultrasmall Uniform Graphene Oxide Nanosheets and their Application in Surfactants. *Nanotechnology* **2016**, *27*, 055601.
(10) Kim, J.; Cote, L. J.; Huang, J., Two Dimensional Soft Material: New Faces of Graphene Oxide. *Accounts Chem. Res.* **2012**, *45*, 1356-1364.
(11) Da, S.-X.; Wang, J.; Geng, H.-Z.; Jia, S.-L.; Xu, C.-X.; Li, L.-G.; Shi, P.-P.; Li, G., High Adhesion Transparent Conducting Films Using Graphene Oxide Hybrid Carbon Nanotubes. *Appl. Surf. Sci.* **2017**, *392*, 1117-1125.
(12) Huang, J.-Q.; Xu, Z.-L.; Abouali, S.; Akbari Garakani, M.; Kim, J.-K., Porous Graphene Oxide/Carbon Nanotube Hybrid Films as Interlayer for Lithium-Sulfur Batteries. *Carbon* **2016**, *99*, 624-632.
(13) Lin, J.-Y.; Su, A.-L.; Chang, C.-Y.; Hung, K.-C.; Lin, T.-W., Molybdenum Disulfide/Reduced Graphene Oxide–Carbon Nanotube Hybrids as Efficient Catalytic Materials in Dye-Sensitized Solar Cells. *ChemElectroChem* **2015**, *2*, 720-725.
(14) Kim, T.; Park, J.; Sohn, J.; Cho, D.; Jeon, S., Bioinspired, Highly Stretchable, and Conductive Dry Adhesives Based on 1D–2D Hybrid Carbon Nanocomposites for All-in-One ECG Electrodes. *ACS Nano* **2016**, *10*, 4770-4778.
(15) Yu, L.; Tune, D.; Shearer, C.; Shapter, J., Heterojunction Solar Cells Based on Silicon and Composite Films of Graphene Oxide and Carbon Nanotubes. *ChemSusChem* **2015**, *8*, 2940-2947.
(16) De Nicola, F.; Salvato, M.; Cirillo, C.; Crivellari, M.; Boscardin, M.; Passacantando, M.; Nardone, M.; De Matteis, F.; Motta, N.; De Crescenzi, M.; Castrucci, P., 100% Internal Quantum Efficiency in Polychiral Single-Walled Carbon Nanotube Bulk Heterojunction/Silicon Solar Cells. *Carbon* **2017**, *114*, 402-410.
(17) Jia, Y.; Li, P.; Gui, X.; Wei, J.; Wang, K.; Zhu, H.; Wu, D.; Zhang, L.; Cao, A.; Xu, Y., Encapsulated Carbon Nanotube-Oxide-Silicon Solar Cells with Stable 10% Efficiency. *Appl. Phys. Lett.* **2011**, *98*, 133115.
(18) Yu, L.; Tune, D. D.; Shearer, C. J.; Shapter, J. G., Application of Polymer Interlayers in Silicon–Carbon Nanotube Heterojunction Solar Cells. *ChemNanoMat* **2015**, *1*, 115-121.
(19) Tune, D. D.; Flavel, B. S.; Quinton, J. S.; Ellis, A. V.; Shapter, J. G., Single-Walled Carbon Nanotube/Polyaniline/n-Silicon Solar Cells: Fabrication, Characterization, and Performance Measurements. *ChemSusChem* **2013**, *6*, 320-327.
(20) Xu, D.; Yu, X.; Gao, D.; Mu, X.; Zhong, M.; Yuan, S.; Xie, J.; Ye, W.; Huang, J.; Yang, D., Room-Temperature Processed, Air-Stable and Highly Efficient Graphene/Silicon Solar Cells with an Organic Interlayer. *J. Mater. Chem. A* **2016**, *4*, 11284-11291.
(21) Lee, J.; Menamparambath, M. M.; Hwang, J. Y.; Baik, S., Hierarchically Structured Hole Transport Layers of Spiro-OMeTAD and Multiwalled Carbon Nanotubes for Perovskite Solar Cells. *ChemSusChem* **2015**, *8*, 2358-2362.
(22) Li, M. H.; Hsu, C. W.; Shen, P. S.; Cheng, H. M.; Chi, Y.; Chen, P.; Guo, T. F., Novel Spiro-Based Hole Transporting Materials for Efficient Perovskite Solar Cells. *Chem. Commun.* **2015**, *51*, 15518-15521.

(23) Bachilo, S. M.; Strano, M. S.; Kittrell, C.; Hauge, R. H.; Smalley, R. E.; Weisman, R. B., Structure-assigned optical spectra of single-walled carbon nanotubes. *Science* 2002, *298*, 2361-2366.
(24) Tune, D. D.; Flavel, B. S.; Krupke, R.; Shapter, J. G., Carbon Nanotube-Silicon Solar Cells. *Adv. Energy Mater.* 2012, *2*, 1043-1055.
(25) Yuan, Z.; Wu, Z.; Bai, S.; Xia, Z.; Xu, W.; Song, T.; Wu, H.; Xu, L.; Si, J.; Jin, Y.; Sun, B., Hot-Electron Injection in a Sandwiched TiOx-Au-TiOx Structure for High-Performance Planar Perovskite Solar Cells. *Adv. Energy Mater.* 2015, *5*, 1500038.
(26) Abrusci, A.; Stranks, S. D.; Docampo, P.; Yip, H.-L.; Jen, A. K. Y.; Snaith, H. J., High-Performance Perovskite-Polymer Hybrid Solar Cells via Electronic Coupling with Fullerene Monolayers. *Nano Lett.* 2013, *13*, 3124-3128.
(27) Chen, H.-W.; Huang, T.-Y.; Chang, T.-H.; Sanehira, Y.; Kung, C.-W.; Chu, C.-W.; Ikegami, M.; Miyasaka, T.; Ho, K.-C., Efficiency Enhancement of Hybrid Perovskite Solar Cells with MEH-PPV Hole-Transporting Layers. *Sci Rep* 2016, *6*, 34319.
(28) He, H.; Yu, X.; Wu, Y.; Mu, X.; Zhu, H.; Yuan, S.; Yang, D., 13.7% Efficiency Graphene-Gallium Arsenide Schottky Junction Solar Cells with a P3HT Hole Transport Layer. *Nano Energy* 2015, *16*, 91-98.
(29) Ruan, K.; Ding, K.; Wang, Y.; Diao, S.; Shao, Z.; Zhang, X.; Jie, J., Flexible Graphene/Silicon Heterojunction Solar Cells. *J. Mater. Chem. A* 2015, *3*, 14370-14377.
(30) Wang, S.; Yuan, W.; Meng, Y. S., Spectrum-Dependent Spiro-OMeTAD Oxidization Mechanism in Perovskite Solar Cells. *ACS Appl. Mater. Interfaces* 2015, *7*, 24791-24798.
(31) Zhang, K.; Wang, L.; Liang, Y.; Yang, S.; Liang, J.; Cheng, F.; Chen, J., A Thermally and Electrochemically Stable Organic Hole-Transporting Material with an Adamantane Central Core and Triarylamine moieties. *Synth. Met.* 2012, *162*, 490-496.
(32) Yang, L.; Yu, X.; Xu, M.; Chen, H.; Yang, D., Interface Engineering for Efficient and Stable Chemical-Doping-Free Graphene-on-Silicon Solar Cells by Introducing a Graphene Oxide Interlayer. *J. Mater. Chem. A* 2014, *2*, 16877-16883.
(33) Wang, Y. Y.; Colas, G.; Filleter, T., Improvements in the Mechanical Properties of Carbon Nanotube Fibers through Graphene Oxide Interlocking. *Carbon* 2016, *98*, 291-299.
(34) Rasuli, R.; Mokarian, Z.; Karimi, R.; Shabanzadeh, H.; Abedini, Y., Wettability Modification of Graphene Oxide by Removal of Carboxyl Functional Groups Using Non-Thermal Effects of Microwave. *Thin Solid Films* 2015, *589*, 364-368.
(35) Tey, J. N.; Ho, X.; Wei, J., Effect of doping on single-walled carbon nanotubes network of different metallicity. *Nanoscale Res. Lett.* 2012, *7*, 548-548.
(36) Kim, S. M.; Kim, K. K.; Jo, Y. W.; Park, M. H.; Chae, S. J.; Duong, D. L.; Yang, C. W.; Kong, J.; Lee, Y. H., Role of Anions in the AuCl3-Doping of Carbon Nanotubes. *ACS Nano* 2011, *5*, 1236-1242.
(37) Duta, M.; Anastasescu, M.; Calderon-Moreno, J. M.; Predoana, L.; Preda, S.; Nicolescu, M.; Stroescu, H.; Bratan, V.; Dascalu, I.; Aperathitis, E.; Modreanu, M.; Zaharescu, M.; Gartner, M., Sol-Gel versus Sputtering Indium Tin Oxide Films as Transparent Conducting Oxide Materials. *J. Mater. Sci.: Mater. Electron.* 2016, *27*, 4913-4922.
(38) Li, J. Y.; Zhu, Y.; Wang, X.; Wang, N.; Zhang, J., Light-Induced Vibration Characteristics of Free-Standing Carbon Nanotube Films Fabricated by Vacuum Filtration. *J. Appl. Phys.* 2014, *116*, 023101.
(39) Yu, L.; Grace, T.; Jazi, M. D.; Shearer, C.; Shapter, J., Optimization of the Metal Front Contact Design for Single-Walled Carbon Nanotube-Silicon Heterojunction Solar Cells. *Solar RRL* 2017, *1*, 1600026.
(40) Wang, F. J.; Kozawa, D.; Miyauchi, Y.; Hiraoka, K.; Mouri, S.; Ohno, Y.; Matsuda, K., Fabrication of Single-Walled Carbon Nanotube/Si Heterojunction Solar Cells with High Photovoltaic Performance. *ACS Photonics* 2014, *1*, 360-364.
(41) Li, X.; Jung, Y.; Huang, J.-S.; Goh, T.; Taylor, A. D., Device Area Scale-Up and Improvement of SWNT/Si Solar Cells Using Silver Nanowires. *Adv. Energy Mater.* 2014, *4*, 1400186.

(42) Harris, J. M.; Semler, M. R.; May, S.; Fagan, J. A.; Hobbie, E. K., Correction to “Nature of Record Efficiency Fluid-Processed Nanotube–Silicon Heterojunctions”. *J. Phys. Chem. C* 2015, *119*, 23293-23293.
(43) Noh, J. H.; Jeon, N. J.; Choi, Y. C.; Nazeeruddin, M. K.; Gratzel, M.; Seok, S. I., Nanostructured TiO2/CH3NH3PbI3 Heterojunction Solar Cells Employing Spiro-OMeTAD/Co-Complex as Hole-Transporting Material. *J. Mater. Chem. A* 2013, *1*, 11842-11847.
(44) Abate, A.; Leijtens, T.; Pathak, S.; Teuscher, J.; Avolio, R.; Errico, M. E.; Kirkpatrik, J.; Ball, J. M.; Docampo, P.; McPherson, I.; Snaith, H. J., Lithium salts as "redox active" p-type dopants for organic semiconductors and their impact in solid-state dye-sensitized solar cells. *Phys. Chem. Chem. Phys.* 2013, *15*, 2572-2579.
(45) Tune, D. D.; Shapter, J. G., Effect of nanotube film thickness on the performance of nanotube-silicon hybrid solar cells. *Nanomaterials* 2013, *3*, 655-673.
(46) Cui, K.; Maruyama, S., Carbon Nanotube-Silicon Solar Cells: Improving Performance for Next-Generation Energy Systems. *IEEE Nanotechnol. Mag.* 2016, *10*, 34-C33.
(47) Hellstrom, S. L.; Vosgueritchian, M.; Stoltenberg, R. M.; Irfan, I.; Hammock, M.; Wang, Y. B.; Jia, C.; Guo, X.; Gao, Y.; Bao, Z., Strong and Stable Doping of Carbon Nanotubes and Graphene by MoOx for Transparent Electrodes. *Nano Lett.* 2012, *12*, 3574-3580.
(48) Hedman, D.; Reza Barzegar, H.; Rosén, A.; Wågberg, T.; Andreas Larsson, J., On the Stability and Abundance of Single Walled Carbon Nanotubes. *Sci Rep* 2015, *5*, 16850.
(49) Larsen, L. J.; Shearer, C. J.; Ellis, A. V.; Shapter, J. G., Solution processed graphene-silicon Schottky junction solar cells. *RSC Adv.* 2015, *5*, 38851-38858.
(50) Abdullah-Al-Galib, M.; Hou, B.; Shahriad, T.; Zivanovic, S.; Radadia, A. D., Stability of Few Layer Graphene Films Doped with Gold (III) Chloride. *Appl. Surf. Sci.* 2016, *366*, 78-84.
(51) Ki Kang, K.; Alfonso, R.; Yumeng, S.; Hyesung, P.; Lain-Jong, L.; Young Hee, L.; Jing, K., Enhancing the Conductivity of Transparent Graphene Films via Doping. *Nanotechnology* 2010, *21*, 285205.
(52) Güneş, F.; Shin, H.-J.; Biswas, C.; Han, G. H.; Kim, E. S.; Chae, S. J.; Choi, J.-Y.; Lee, Y. H., Layer-by-Layer Doping of Few-Layer Graphene Film. *ACS Nano* 2010, *4*, 4595-4600.
(53) Hawash, Z.; Ono, L. K.; Raga, S. R.; Lee, M. V.; Qi, Y., Air-Exposure Induced Dopant Redistribution and Energy Level Shifts in Spin-Coated Spiro-MeOTAD Films. *Chem. Mat.* 2015, *27*, 562-569.

Chapter 6 Insights into Chemical Doping to Engineer the Graphene Oxide Carbon Nanotube / Silicon Photovoltaic Heterojunction Interface

This Chapter has been published as “Insights into Chemical Doping to Engineer the Carbon Nanotube/Silicon Photovoltaic Heterojunction Interface” in Journal of Materials A in 2017.

Yu, L.; Grace, T.; Batmunkh, M.; Dadkhah, M.; Shearer, C.; Shapter, J. Insights into Chemical Doping to Engineer the Carbon Nanotube/Silicon Photovoltaic Heterojunction Interface. J. Mater. Chem. A 2017. 5, 24247-24256.

6.1 Overview

Hybrids of graphene oxide and single-wall carbon nanotubes (GOCNT) have been applied to fabricate solar cells with silicon (Si) because of their compatibility with processing in both aqueous and organic conditions. In these photovoltaics, GOCNT films need to be both conducting and transparent. The optoelectronic properties of the hybrid electrodes are improved by different methods, including hybridisation with silver nanowires (AgNWs) and p-type doping with $CuCl_2$, $AuCl_3$, $SOCl_2$, HCl, H_2SO_4, HNO_3 and $HClO_4$. The UV-Vis-NIR spectrum, Raman spectrum, and sheet resistance of the hybrids were analysed and used to evaluate the properties of the treated films. The incorporation of AgNWs was the most effective way to improve the optoelectronic properties of the GOCNT hybrids, which resulted in an over 600 % improvement in the figure of merit (FOM). However, GOCNT/Si heterojunction photovoltaic devices with HNO_3 doped GOCNT hybrid films had the highest solar photocurrent conversion efficiency (11.38 ± 0.26 %). In addition, $CuCl_2$ and HCl doped films have the best electrode stability in FOM and solar cells made with such films have the most stable efficiency. This report suggests that there is a strong correlation between the electronegativity of the active elements in the dopants and the optoelectronic properties of the films as well as the solar cell performance.

6.2 Introduction

Carbon nanotubes (CNTs) have been regarded as the ideal material for the preparation of transparent and conductive thin films,[1-7] because of their unique optical and excellent electrical properties. However, their compatibility with aqueous processing is limited by the hydrophobicity and the strong van der Waals interaction between individual nanotubes.[8-11] Various dispersing agents containing both hydrophobic and hydrophilic moieties, such as polymers,[12] porphyrins,[13] cellulose derivatives,[14] surfactants[15] and single stranded DNA sequences[16] are commonly used to solve this issue, but the CNT films prepared from these aqueous dispersions usually do not have high figure of merit (FOM).[17]

Graphene oxide (GO) has been shown to be able to both disperse CNTs in water and improve the compatibility of the as-prepared film in aqueous medium because of its amphiphilic nature.[18-21] These hybrid films of GO and CNTs (GOCNT) have been applied as transparent

window electrodes and placed on top of silicon to fabricate graphene oxide carbon nanotube/silicon heterojunction photovoltaics (GOCNT/Si).[22] The working mechanism of GOCNT/Si solar cells has been described in section 5.2.

Generally, solar cells fabricated with as-deposited GOCNT films show mediocre performance as a result of the high sheet resistance and low native p-doping. The optoelectronic properties for CNT based window electrodes can be improved to satisfy the practical applications by chemical doping.[23] HCl,[24] HNO_3,[25] H_2SO_4,[26] $SOCl_2$,[27] $AuCl_3$,[28] and $CuCl_2$[29] are the most frequently used p-type dopants. Both the conductivity of individual CNTs and the contact resistance between CNTs play a role in the final sheet resistance (R_{sheet}) of CNT based films.[30] The shifting of Fermi level caused by the chemical doping can result in an increase in the density of charge carriers and the reduction in the Schottky barrier height between metallic and semiconducting species. Thus, the optical absorption peaks due to the first and second interband transitions in SWCNTs are suppressed to certain degree (as shown in Figure 1.18).[31] Recently, the efficiency of SWCNT/Si devices was improved by nearly two-fold from 4.31 to 7.89 % with a bilayer structure of AgNWs/SWCNTs as the top window electrode, where the major improvement was from the dramatic improvement of the optoelectronic properties after the addition of AgNWs top layer and highly conducting paths provided by AgNWs through CNT networks.[32-33]

In this Chapter, a few commonly used p-type dopants as well as AgNWs are used to enhance the optoelectronic properties of the GOCNT based transparent conducting films. As shown in Figure 6.1, bath doping could be used due to the previously developed organic-aqueous transfer process which makes films available for bath processing.[17] This method extends the doping period compared to simple drop doping (by dropping the chemicals on the films) and eliminates the effect of the chemicals on the metal coated Si substrates. Due to the limited dispersity of AgNWs in water, they could not be processed this way and were collected with GOCNTs on the filter paper. The treated films were then placed on the n-type Si to form GOCNT/Si heterojunction devices. Both the efficiency and the stability of the solar cells were measured and compared.

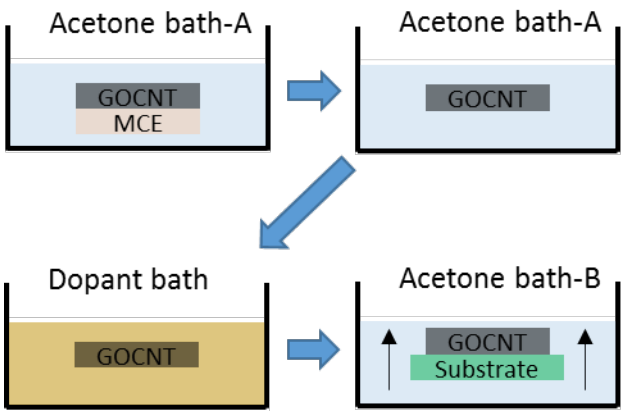

Figure 6.1 Schematic of bath doping process. MCE represents the mixed cellulose ester membrane and the substrate can be glass or Si coated with metal electrode. The MCE dissolves in acetone and GOCNT films are then transferred to a dopant bath to perform chemical doping, after which the film is transferred to a second, clean acetone bath before being picked up with the substrate.

6.3 Experimental details

6.3.1 Preparation of stock solutions

GO was prepared following the improved synthesis based on Hummers' approach reported by Marcano et al. as shown in section 2.1.1.3.[34] The final concentration of the GO suspension was controlled to be 1 mg mL^{-1}. The GOCNT suspension was fabricated by following the procedure described in section 2.2.2.2 with the GO dispersion prepared before.

AgNWs were synthesised by following the procedures described in section 2.2.1.4.[35] The final concentration of AgNWs in deionised water is kept at 0.2 mg mL^{-1}. The redox colloidal solution was prepared by following the procedures shown in section 2.2.1.5.[29] $AuCl_3$ solution was prepared by dissolving 118 mg of $HAuCl_4 \cdot 3H_2O$ (99.0 %, Sigma-Aldrich) in 30 mL of acetone at room temperature with gentle vortex mixing to prepare 10 mM $AuCl_3$ solution. 10 % v/v $SOCl_2$ (99.0 %, Sigma-Aldrich) was prepared by diluting pure $SOCl_2$ with benzene. 10 wt % HCl (32.0 %, RCI Labscan), 10 wt % HNO_3 (70.0 %, RCI Labscan), 10 wt % H_2SO_4 (98.0 %, RCI Labscan) and 10 wt % $HClO_4$ (70.0 %, Merck) were prepared by diluting the acid with deionised water.

6.3.2 Fabrication and treatment of hybrid films

The preparation of GOCNT hybrid films follows the procedure in section 2.4.3 with minor changes as follows.[17] In detail, the free-floating GOCNT films were transferred by a homemade Teflon spoon from the acetone bath to one of the dopant baths, including $CuCl_2$, $AuCl_3$, $SOCl_2$, HCl, HNO_3, H_2SO_4 and $HClO_4$. The doping period was 30 min and then the films were transferred to a fresh acetone bath and ready to be picked up with an as-fabricated Si substrate to fabricate solar cells or with a glass. As a control experiment, the hybrid films were picked up after the removal of the MCE in acetone bath.

In terms of the devices based on AgNWs, AgNWs-GOCNT films were prepared by filtering a mixture of 150 µL GOCNT suspension and 50 µL AgNWs stock solution diluted to 100 mL with deionised water. The reduced amount of GOCNT solution was required to keep the transmittance at 550 nm (*T*) the same as that of the hybrid films with no AgNWs. After the MCE is dissolved in the first acetone bath, the AgNWs-GOCNT films were then picked up as described before.

6.3.3 Fabrication and performance measurement of the solar cells

The fabrication and performance testing of the solar cells are described in sections 2.5.3.1 and 2.6.2.

6.4 Results and discussion

6.4.1 Hybridisation/Doping influence on the optoelectronic properties of hybrid films

In this Chapter, in order to enhance the optoelectronic properties of GOCNT hybrid films and apply them to solar cells, the effect of 8 different types of materials either by hybridisation (AgNWs) or p-type doping ($CuCl_2$, $AuCl_3$, $SOCl_2$, HCl, H_2SO_4, HNO_3 and $HClO_4$) were studied. The working mechanisms of dopants and AgNWs are summarised and listed in Table 6.1.

Table 6.1 Working mechanisms of different materials (by either incorporation or p-type doping) to enhance the optoelectronic properties of the hybrid films. The sum of the

electronegativity of the active elements (bold) in these materials are calculated based on the Pauling scale.[36]

Materials (sum of electronegativity)	Working mechanisms
AgNWs (1.93)	The incorporated AgNWs act as the additional charge transport paths to bridge the less conductive GOCNT network which is considered as a mechanical support.[32]
$CuCl_2$ (8.22)	Instant electron transfer from CNTs to Cu^{2+} in $CuCl_2$ which is reduced to Cu^{1+} with the less active Cu^{2+} in $Cu(OH)_2$ providing long-term charge transfer effect on the CNTs.[29] Furthermore, it is also possible that CNT-Cl is formed by the doping where Cl withdraws electrons from CNTs.[28]
$AuCl_3$ (12.02)	The doping mechanism is not completely clear. Some reports suggest the reduction of cationic Au^{3+} to Au nanoparticles results in the p-type doping while others attribute the doping to the creation of CNT-Cl where electron transfer from CNT to Cl happens.[28]
SO**Cl_2** (6.32)	The doping effect is due to the decomposition of the molecules, $2SOCl_2 + 4e^- \rightarrow S + SO_2 + 4\ Cl^-$, which withdraws electrons from CNTs[27] caused by adsorption of SO_2 and possible formation of CNT-Cl.
H_2**SO_4** (16.54)	The intercalated SO_3^-/SO_4^{2-} withdraws electrons from CNT and causes the shifting of Fermi level with the formation of more holes in the valence band. Furthermore, it could also remove some dispersants and thus results in the reduction in the contact resistance between CNTs.[37]
H**NO_3** (13.46)	Electrons are transferred from the surface of CNTs to the absorbed molecules with NO_3^- groups which shifts the Fermi level to the valence band. A better contact is also formed by the removal of impurities, such as metal catalysts and amorphous carbon.[37-38]
H**Cl** (3.44)	The mechanism is similar to that of HNO_3 and H_2SO_4 by intercalation. The doping is able to shift the Fermi level into the valence band.[37]
H**ClO_4** (16.92)	ClO_4^- groups might withdraw electrons from the surface of CNTs and result in the downshift of Fermi level of CNTs into their valence band.

XPS analysis (Figure 6.2) shows that the GOCNT C 1s spectrum is very similar to that of the CNT starting material (peak is centred at 284.4 eV) meaning that the amount of GO in the film is small. GO would be easily observed with another strong C1s peak centred at 287.5 – 280 eV from the contribution of C-OH, C=O and O=C-OH.[39] The limited amount of GO in the films suggested that the influence of the p-type doping must be mainly on CNTs rather than GO.

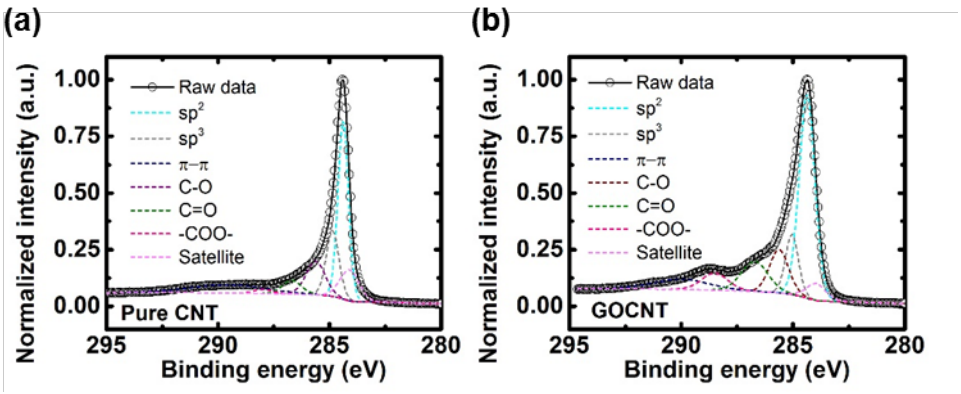

Figure 6.2 Fitting of C 1s peak for (b) pure CNT and (c) GOCNT hybrid films.

Optoelectronic properties (UV-Vis-NIR absorbance and sheet resistance) of the prepared and modified GOCNT films on microscope slides were studied. As shown in Figure 6.3 (a), the absorbance at 550 nm of all the GOCNT films are very close and therefore the visible transmittance of these films can be regarded as the same (80 %). Additionally, the untreated film has two broad optical absorption peaks at about 1945 nm (S_{11}) (shown in the inset of Figure 6.3 (a)) and 1010 nm (S_{22}), which is consistent with arc discharge SWCNTs with large diameters.[40] The S_{11} peak remains and a wide absorption feature above 1000 nm is observed for the GOCNT networks incorporated with AgNWs, which implies the existence of AgNWs in the hybrid and indicates that AgNW probably is not a p-type dopant for SWCNTs.[41] Oppositely, both S_{11} and S_{22} peaks are suppressed to various degrees after the treatment by p-type dopants on GOCNT films (the degree of the S_{11} and S_{22} suppression: $HNO_3 \approx H_2SO_4 \approx SOCl_2 \approx AuCl_3 \approx CuCl_2 > HCl$, as shown in Figure 6.3 (b)-(d)),[42] which results from the shift of Fermi level of SWCNT into the valence band and electrons transferred from CNTs to dopants.[43] As shown in Figure 6.1 (b) and (c), there is a lower population of electrons in the valence band after doping, which is responsible for the suppressed S_{11} peak.

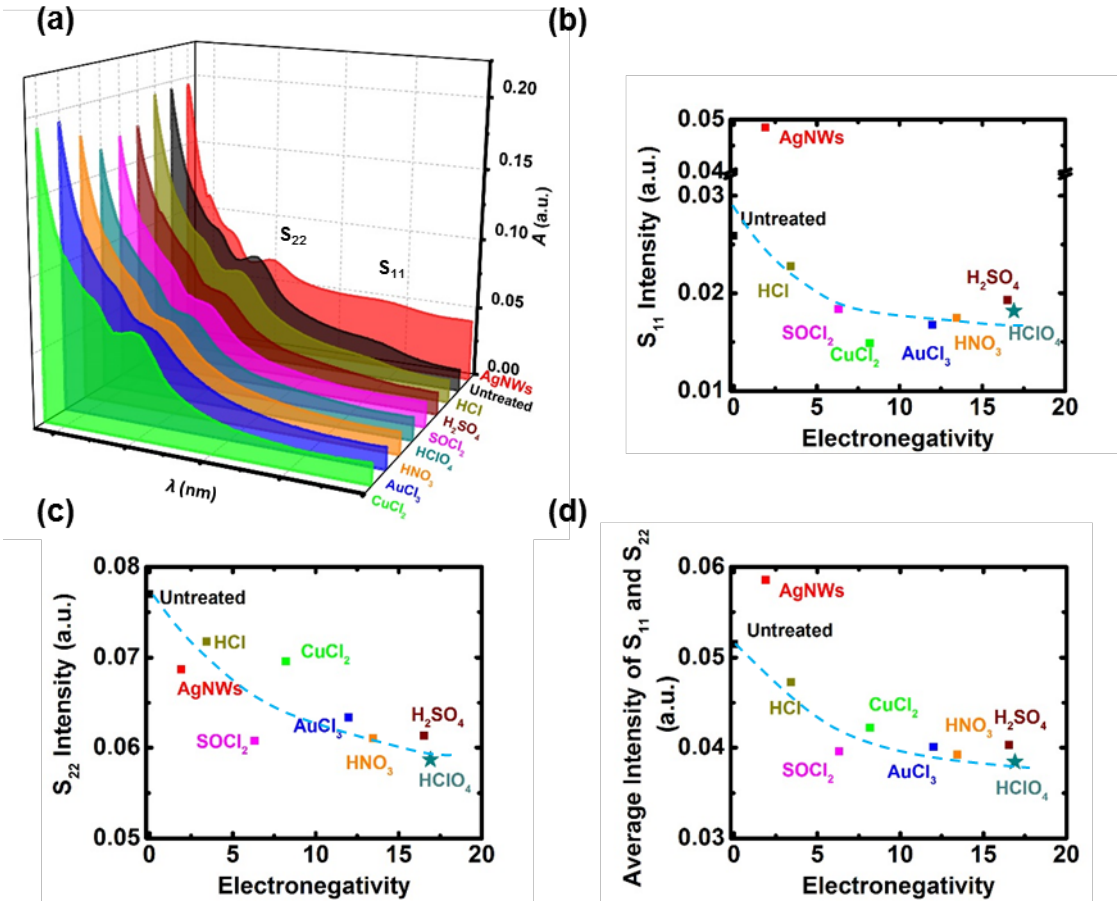

Figure 6.3 (a) UV-Vis-NIR spectra of the untreated, AgNWs hybridised, $CuCl_2$, $AuCl_3$, $SOCl_2$, HCl, H_2SO_4, HNO_3 and $HClO_4$ doped GOCNT hybrid films. (b) S_{11}, (c) S_{22} and (d) the averaged intensity of S_{11} and S_{22} in the UV-Vis-NIR spectra as a function of electronegativity for the hybrid films. The trend lines in these figures are used to guide the eye.

Raman spectra provide further support that p-doping occurs, as shown in Figure 6.4. The G/D ratio of all the films are very close (about 4), which indicates that both hybridisation of AgNWs and p-type doping do not result in structural defects on the SWCNTs.[44] The untreated film has an evident metallic contribution on the low wavenumber side of the G peak (Breit-Wigner-Fano (BWF) peak), which is due to the strong electron-phonon interactions in metallic SWCNTs (Figure 6.4 (b)).[45-46] After p-type doping, there is a reduction in the metallic contribution in the G band (Noticeably, the reduction of BWF intensity is more evident in hybrid films after treatment with higher electronegativity species, as shown in Figure 6.4 (b) and (c), with a blue

shift of the G peak position to a certain extent. In addition, the position of G band for films treated by dopants with active elements of higher electronegativity seems to shift further, as shown in Figure 6.4 (b) and (d)), which indicates that CNT stiffening leads to higher phonon energies after electron transfer from SWCNTs to dopants.[47-48]

However, GOCNT films incorporated with AgNWs behave in a different manner compared to the p-typed dopants. These films have a broader BWF peak and a red shift in the G band position is observed with a similar BWF intensity as that of the untreated film. Thus, AgNWs might have a different working mechanism in GOCNT films.

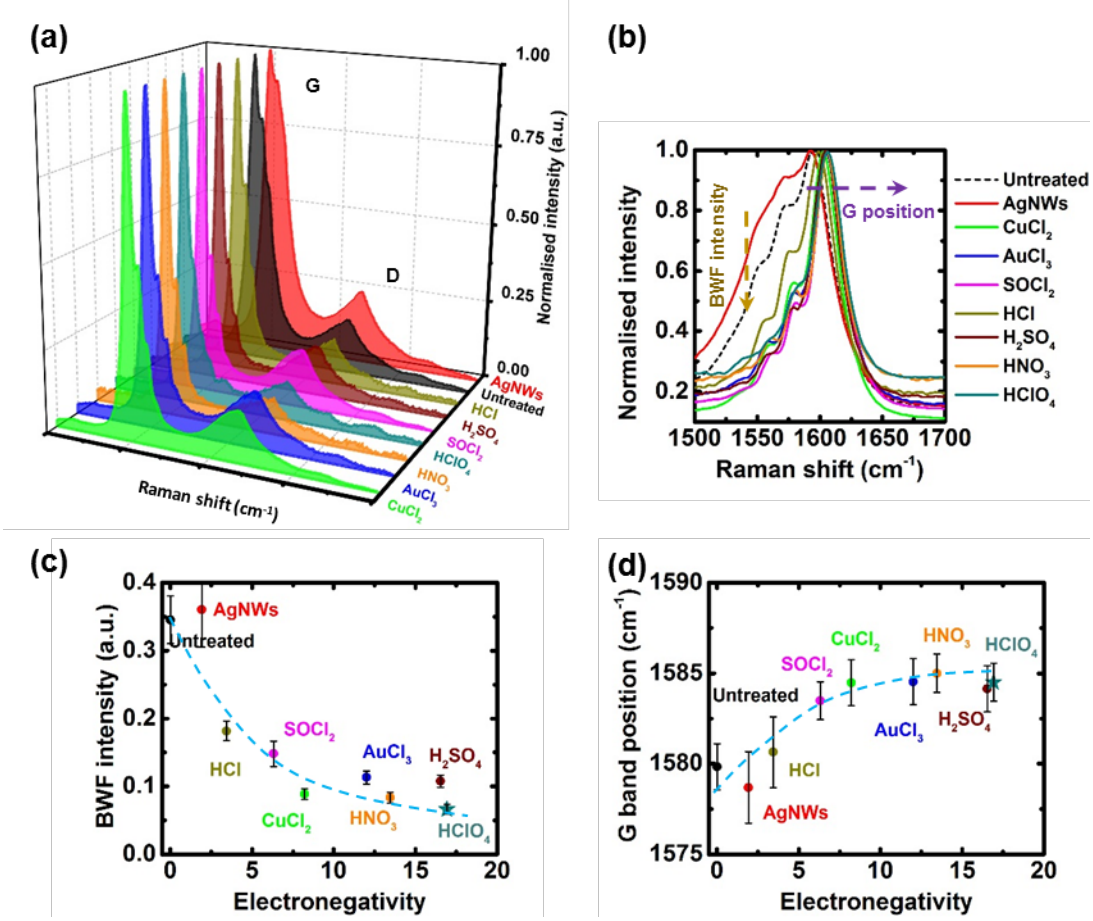

Figure 6.4 (a) Raman spectra of the untreated, AgNWs incorporated, $CuCl_2$, $AuCl_3$, $SOCl_2$, HCl, H_2SO_4, HNO_3 and $HClO_4$ doped hybrid films. (b) An expanded view of Raman G band from 1500 to 1700 cm^{-1}. (c) BWF peak intensity[49-50] of hybrid films. (d) G band position versus electronegativity after being treated with different materials. The dashed lines in (c) and (d) are added to highlight a trend.

The measured R_{sheet} and calculated FOM as a function of the sum of electronegativity of the active species of the materials are used to further study the impact of the hybridisation and p-type doping on the optoelectronic properties, Figure 6.5. The untreated film has the highest R_{sheet} with the lowest FOM while AgNWs incorporated GOCNT film has the lowest R_{sheet} (120 Ω sq^{-1} (AgNWs-GOCNT hybrids) versus above 350 Ω sq^{-1} for p-doped GOCNT films) with the highest FOM (12 (AgNWs-GOCNT hybrids) versus less than 4 for p-doped GOCNT films), which implies that the hybridisation of AgNWs can significantly improve the optoelectronic properties of GOCNT hybrid films. Our FOM value for AgNWs hybridised GOCNT films is much lower than that of the literature value (above 90). This is likely due to the much higher content of AgNWs in the previous report (only 6 wt% SWCNT and the absorption peaks of SWCNTs were not observed in the UV-Vis-NIR spectrum for the hybrid at all)[51] than that of film in this study. It seems that the R_{sheet}/FOM of the p-type doped GOCNT films decreases/increases exponentially with electronegativity. It is not surprising that molecules with more and/or higher electronegativity atoms have stronger doping effect on GOCNT films since the nature of p-type doping is to withdraw electrons from CNTs to adsorbed dopant molecules. A dopant which has not been reported in previous study, $HClO_4$, was used to test the validity of this correlation. It is shown that both the R_{sheet} and FOM of GOCNT films after $HClO_4$ doping (electronegativity sum = 16.92) fit well in the correlation found before, as shown in Figure 6.5 (the star). Additionally, the bleaching of S_{11} in the UV-Vis-NIR as well as the upshifting of G band in Raman spectrum suggested the p-doping nature of $HClO_4$ treatment (Figure 6.3 and Figure 6.4) are observed in line with the predictions.

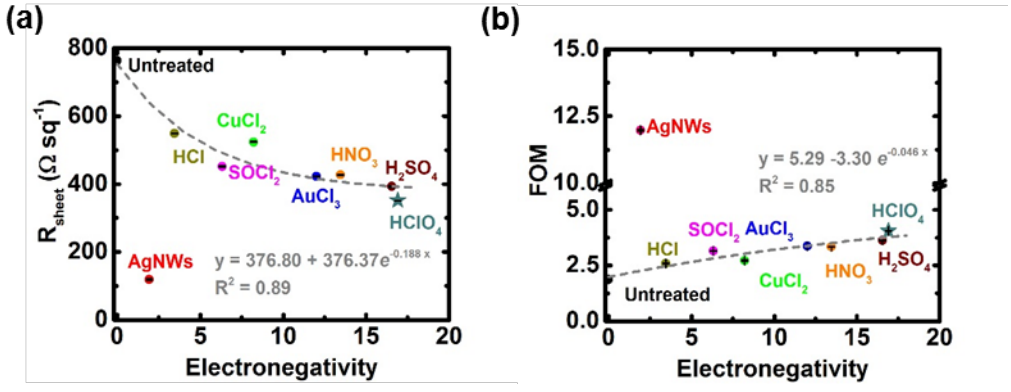

Figure 6.5 (a) R_{sheet} and (b) FOM as a function of the electronegativity of the active elements. The exponential fits in the figures do not consider the AgNWs-GOCNT data

point because the incorporation of AgNWs has a different working mechanism on GOCNT films – it does not shift the Fermi level but rather changes the transporting ability of the charge carriers though the network).

Overall, the incorporation of AgNWs into GOCNT network is the best way to improve the optoelectronic properties while substances with active elements of higher electronegativity values are better p-type dopants than those with lower values. Since the working mechanism of AgNWs, the creation of more conductive metallic paths between less conductive GOCNT networks, is different from that of p-type dopants, it does not fit the trend line found in this Chapter. In addition, we used a measure of electronegativity as opposed to redox potentials since in many cases there are more than one doping mechanisms suggested and the sum of electronegativity was used to take account of all means of interaction.

6.4.2 Performance of solar cells

Figure 6.6 (a) and (b) show the J-V curves of GOCNT/Si solar cells in which GOCNT films are treated with AgNWs and different p-type dopants under light and dark conditions with the detailed parameters plotted in Figure 6.6 (c)-(l). The solar cell efficiency increases with the electronegativity for the samples with p-type doped GOCNT films, as shown in Figure 6.6 (c). It is worth mentioning that the devices with GOCNT films of the best optoelectronic properties (AgNWs-GOCNT) do not have the best efficiency. For further details, all of these devices have short circuit current density (J_{SC}) that are very similar (the averaged values for each type are within the range from 26 to 27 mA cm^{-2}), which is further supported by the fact that both the shape and the signal intensity in EQE curves are similar, as shown in Figure 6.6 (d) and (e). In addition, both open circuit voltage (V_{OC}) and fill factor (FF) increase with the electronegativity (Figure 6.6 (f) and (g)). Thus, the trend in the solar cell efficiency is probably from the combination effect of V_{OC} and FF. The reason for the inconsistency in the V_{OC} of AgNWs and $AuCl_3$ treated devices (relatively larger error bars compared to those of other devices) is the non-ideal short circuits resulting from the metal nanowires/nanoparticles which bridges the front metal electrode (Au/Cr) with the Si layer, and it has been observed previously in other reports (see section 5.4.2).[17,32] Shunt resistance (R_{shunt}) of the devices increases with the electronegativity and series resistance (R_{series}) has a decreasing correlation with the electronegativity, as shown in Figure 6.6 (h) and (i).

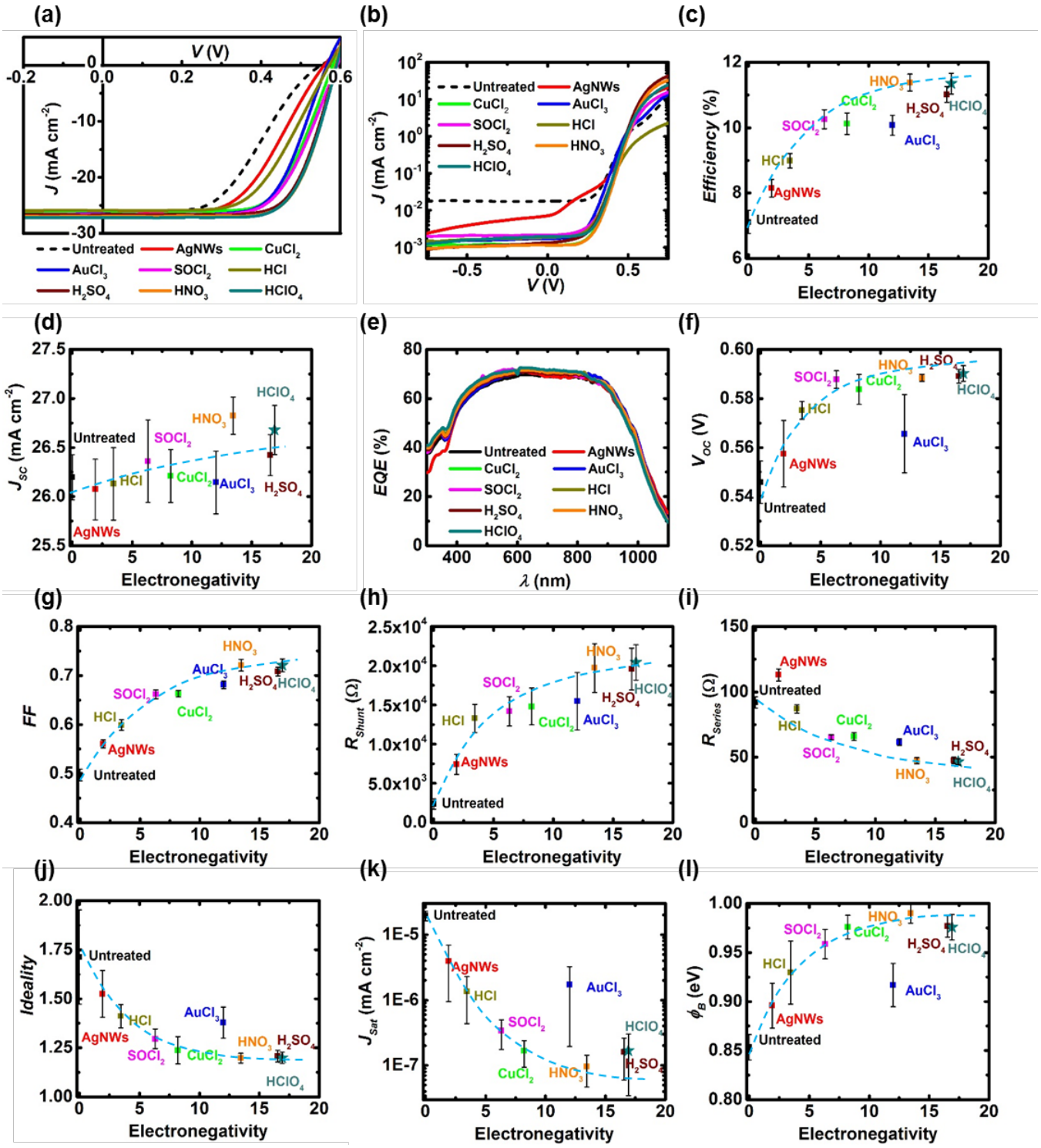

Figure 6.6 Performance of the devices based on GOCNT films treated with different materials (a) J-V light curves, (b) J-V dark curves, (c) Efficiency, (d) J_{SC}, (e) EQE, (f) V_{OC},

(g) FF, (h) R_{shunt}, (i) R_{series}, (j) Ideality, (k) J_{sat} and (l) ϕ_B. The blue trend lines in (c), (d), (f)-(l) are used to guide the eye.

In terms of the diode properties, because of the relatively large error bars, there is no clear trend in ideality, J_{sat} and ϕ_B (Figure 6.6 (j) - (l)). However, devices with untreated GOCNT films generally have poorest diode performance (the highest ideality and J_{sat} and the lowest ϕ_B) while devices with p-doped films by dopants with a high total electronegativity, such as HNO_3 and H_2SO_4, have excellent diode properties (with ideality approaching to 1 and increasing ϕ_B).

Solar cells with $HClO_4$ treated GOCNT films were fabricated to test the validity of the correlation between the efficiency and the sum of the active element electronegativity in the dopants, and the results (the star) seem to fit well in Figure 6.6 (c). Furthermore, most of the other parameters of the $HClO_4$ treated devices, including J_{SC}, V_{OC}, FF, R_{shunt}, R_{series}, ideality, J_{sat}, and ϕ_B, fit the general trends created by other dopants, as shown in Figure 6.6. The improvement in V_{OC}, FF, ideality and ϕ_B infers that a better junction has been created between Si and GOCNT film after different treatments with the enhanced optoelectronic properties as well as the creation of a better contact.

Overall, dopants with higher electronegativity values for the active elements enable the solar cells to have better efficiency (HNO_3 treated devices have the highest efficiency among them, 11.38 ± 0.26 %) as well as the better diode properties while the films with the best optoelectronic properties (AgNWs-GOCNT) result in the devices with efficiency just higher than the control devices (8.14 ± 0.27 % versus 7.11 ± 0.35 %). This implies that the optoelectronic properties of the transparent conducting window electrodes is not the only determining factor in the solar cell performance. Because the charge transport through the GOCNT network was dramatically enhanced by the incorporation of AgNWs while the improvement in the FOM from p-type dopants is largely from an increased density of free charge carriers,[47] it is then suggested that the density of free charge carriers plays a more important role in the solar cell performance. Additionally, the role of the GOCNT networks is far more than a window electrode to transport the separated holes, and it contributes to the electron-hole pair separation by creating a p-n or Schottky junction between Si.

6.4.3 Stability of the treatment and the device performance

Since the instability of chemical doping is one of the main issues in industrial application, normalised FOM and solar cell efficiency as a function of time were studied, as shown in Figure 6.7. As shown in Figure 6.7 (a), the untreated films have the most stable optoelectronic properties over 10 days while GOCNT films treated with AgNWs, HNO_3 and $AuCl_3$ are the most unstable samples (retaining about 70 % of the original value after 10 days). The main reason of FOM degradation for AgNWs hybridised GOCNT is the oxidation of the metal nanowire,[52] while the serious desorption of physisorbed NO_2 and HNO_3 molecules[38] and the aggregation of Au nanoparticles[53] as well as the desorption of Cl^- reacting with air are the potential reasons for the FOM degradation of GOCNT films treated with HNO_3 and $AuCl_3$.[28] The stability of $SOCl_2$ doping is slightly better than the aforementioned three but worse than that of $CuCl_2$. The better stability of $CuCl_2$ treated GOCNT films is caused by the fact that Cu^{2+} hydroxide in the redox dopant can persistently withdraw electrons from CNTs over the long term.[29] HCl is a very stable dopant as well, but it is the least effective doping approach on GOCNT. GOCNT films doped with H_2SO_4 are quite stable for the first 5 days and then degrade rapidly, which is due to desorption of HSO_4^- and H_2SO_4 molecules consistent with previous studies.[37]

The solar cell performance degradation is shown in Figure 6.7 (b) and the normalised efficiency divided by FOM is plotted in Figure 6.7 (c) in order to study the influence of the electrode degradation on the solar cell performance. In a typical GOCNT/Si device, there are two main degradation mechanisms, namely, the degradation of the optoelectronic properties of GOCNT films and the growth of the insulating oxide layers (SiO_x) between Si and GOCNT electrode. The untreated devices have an efficiency of about 75 % of their original state after 10 days (this is close to previous reports),[17] which is solely caused by the growth of oxide layer. Solar cells with GOCNT films doped with the three most stable dopants ($CuCl_2$, $SOCl_2$ and HCl) show a similar stability as that of the control devices, but when the least stable four dopants (AgNW, HNO_3, $AuCl_3$ and $HClO_4$) are used, the devices degrade to about 65 % efficiency of their original state, which suggests that the main reason for the degradation may be due to the SiO_2 growth rather than the degradation of the window electrode optoelectronic properties. This is further supported by the fact that the treated devices have slightly higher values of the

normalised efficiency divided by FOM (about 0.8) than that of the untreated devices (about 0.75) after 10 days with the exception of H_2SO_4 treated solar cells, as shown in Figure 6.7 (c). H_2SO_4 doped solar cells degrade to about 35 % efficiency of its starting point within 5 days but the doping is very stable for the first 5 days. Furthermore, such devices have a much lower value of the normalised efficiency divided by FOM than that of untreated samples. Both results suggest that the oxidation rate of the Si might be faster for the devices with the H_2SO_4 treated electrodes because of the presence of oxidising species (HSO_4^- and H_2SO_4).

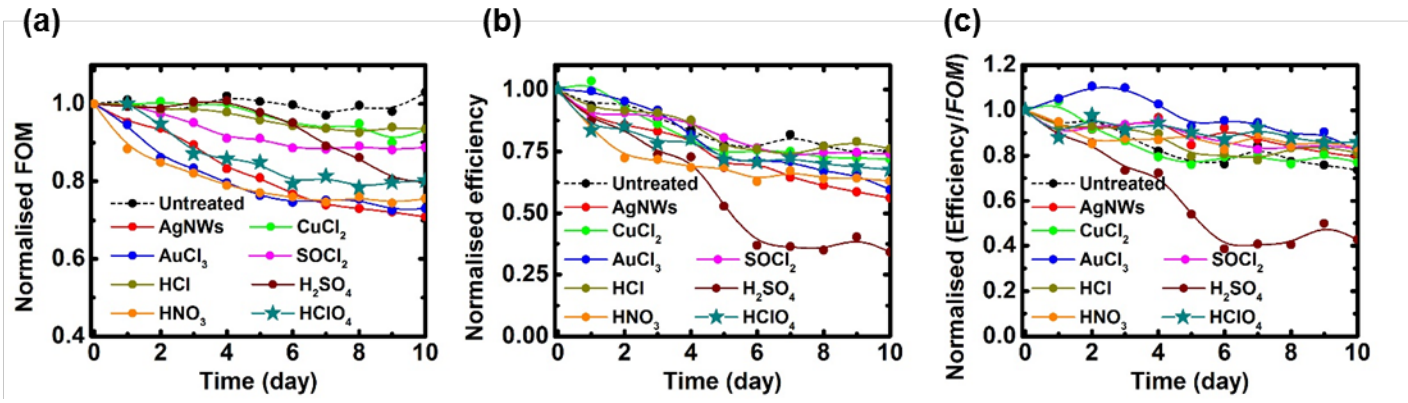

Figure 6.7 Degradation of (a) FOM, (b) solar cell efficiency and (c) normalised efficiency divided by FOM (when the value stays at 1 with increasing time, it indicates that the FOM degradation is the only reason of the performance degradation of the solar cells. Lower values means more serious oxidation effect on the performance degradation). The trend lines in the figures are used to guide the eye.

Various doping approaches have been widely studied and applied to CNT based transparent conducting films to enhance the optoelectronic properties. As shown in this Chapter, the FOM of GOCNT electrodes are improved by different dopants and the fabricated devices have improved performance compared to that of the control samples. The bath doping processing shows excellent compatibility in the terms of dopants, doping periods and the limited adverse effect on the substrates. Based on the results in this Chapter, atoms of high electronegativity are required for an ideal dopant. However, the instability of the doping and the devices is still a concern which must be addressed before any practical application.

6.5 Conclusions

The optoelectronic properties of GOCNT films were enhanced by different approaches, including incorporation of AgNWs, and p-type dopants ($CuCl_2$, $AuCl_3$, $SOCl_2$, HCl, H_2SO_4, HNO_3, and $HClO_4$). These films were used as the window electrodes in GOCNT/Si heterojunction devices to study both the performance and stability. Among these various materials, AgNWs are the most effective to improve the FOM while p-type dopants with a high electronegativity of the active atoms, such as HNO_3, H_2SO_4 and $HClO_4$, improve the solar cell efficiency significantly and the best performance is recorded for HNO_3 doping (11.38 ± 0.26 % vs. 7.11 ± 0.35 % before doping). In addition, $CuCl_2$ and HCl have the most stable chemical doping approach and the fabricated devices show the best stability over 10 days.

REFERENCES:

(1) Zhang, Y. Q.; Yang, L. L.; Ge, Y., Transparent Strain Sensors Through Randomly Self-Assembly of Single Walled Carbon Nanotubes at the Air/Water Interface. *J. Nanosci. Nanotechnol.* 2017, *17*, 4931-4935.

(2) Yu, Y.; Luo, Y. F.; Guo, A.; Yan, L. J.; Wu, Y.; Jiang, K. L.; Li, Q. Q.; Fan, S. S.; Wang, J. P., Flexible and transparent strain sensors based on super-aligned carbon nanotube films. *Nanoscale* 2017, *9*, 6716-6723.

(3) Pyo, S.; Kim, W.; Jung, H. I.; Choi, J.; Kim, J., Heterogeneous Integration of Carbon-Nanotube-Graphene for High-Performance, Flexible, and Transparent Photodetectors. *Small* 2017, *13*, 1700918.

(4) Kim, Y.; Lee, H. R.; Saito, T.; Nishi, Y., Ultra-thin and high-response transparent and flexible heater based on carbon nanotube film. *Appl. Phys. Lett.* 2017, *110*, 153301.

(5) He, Y.; Jin, H. H.; Qiu, S.; Li, Q. W., A novel strategy for high-performance transparent conductive films based on double-walled carbon nanotubes. *Chem. Commun.* 2017, *53*, 2934-2937.

(6) Zhang, X. L.; Aitola, K.; Hagglund, C.; Kaskela, A.; Johansson, M. B.; Sveinbjornsson, K.; Kauppinen, E. I.; Johansson, E. M. J., Dry-Deposited Transparent Carbon Nanotube Film as Front Electrode in Colloidal Quantum Dot Solar Cells. *ChemSusChem* 2017, *10*, 434-441.

(7) Pillai, S. K. R.; Wang, J.; Wang, Y. L.; Sk, M. M.; Prakoso, A. B.; Rusli; Chan-Park, M. B., Totally embedded hybrid thin films of carbon nanotubes and silver nanowires as flat homogenous flexible transparent conductors. *Sci Rep* 2016, *6*, 38453.

(8) Zhang, X.; Zhou, W. X.; Chen, X. K.; Liu, Y. Y.; Chen, K. Q., Significant decrease in thermal conductivity of multi-walled carbon nanotube induced by inter-wall van der Waals interactions. *Phys. Lett. A* 2016, *380*, 1861-1864.

(9) Weck, P. F.; Kim, E.; Wang, Y. F., van der Waals forces and confinement in carbon nanopores: Interaction between CH4, COOH, NH3, OH, SH and single-walled carbon nanotubes. *Chem. Phys. Lett.* 2016, *652*, 22-26.

(10) Rong, Q. Y.; Shao, C.; Bao, H., Molecular dynamics study of the interfacial thermal conductance of multi-walled carbon nanotubes and van der Waals force induced deformation. *J. Appl. Phys.* 2017, *121*, 054302.

(11) Liu, Y. D.; Wang, F. Q.; Liu, Y. J.; Wang, X. Z.; Xu, Y. B.; Zhang, R., Charge transfer at carbon nanotube-graphene van der Waals heterojunctions. *Nanoscale* 2016, *8*, 12883-12886.

(12) Lee, T.; Kim, S.; Kim, H.; Kim, B. S.; Lee, Y. S.; Han, J. H.; Paik, H. J., The effect of thermal treatment on polymer-dispersed single-walled carbon nanotube transparent conductive film. *Compos. Sci. Technol.* 2015, *121*, 95-103.

(13) Ahmed, M. S.; Jeong, H.; You, J. M.; Jeon, S., Electrocatalytic reduction of dioxygen at a modified glassy carbon electrode based on Nafion (R)-dispersed single-walled carbon nanotubes and cobalt-porphyrin with palladium nanoparticles in acidic media. *Electrochim. Acta* 2011, *56*, 4924-4929.

(14) Vlasov, D. V.; Kryshtob, V. I.; Vlasova, T. V.; Bokova, S. N.; Shkarova, O. P.; Obraztsova, E. D.; Apresyan, L. A.; Konov, V. I., Synthesis of Composites with Alternating Layers of Poly(vinyl chloride) and Single-Wall Carbon Nanotubes Homogeneously Dispersed in Carboxymethyl Cellulose. *Polym. Sci. Ser. A* 2012, *54*, 34-38.

(15) Chen, S. J.; Qiu, C. Y.; Korayem, A. H.; Barati, M. R.; Duan, W. H., Agglomeration process of surfactant-dispersed carbon nanotubes in unstable dispersion: A two-stage agglomeration model and experimental evidence. *Powder Technol.* 2016, *301*, 412-420.

(16) Ao, G. Y.; Streit, J. K.; Fagan, J. A.; Zheng, M., Differentiating Left- and Right-Handed Carbon Nanotubes by DNA. *J. Am. Chem. Soc.* 2016, *138*, 16677-16685.

(17) Yu, L.; Batmunkh, M.; Grace, T.; Dadkhah, M.; Shearer, C.; Shapter, J., Application of a Hole Transporting Organic Interlayer in Graphene oxide/Single walled Carbon Nanotube-Silicon Heterojunction Solar Cells. *J. Mater. Chem. A* 2017, 8624-8634.

(18) Yang, Y. J.; Li, W. K., CTAB functionalized graphene oxide/multiwalled carbon nanotube composite modified electrode for the simultaneous determination of ascorbic acid, dopamine, uric acid and nitrite. *Biosens. Bioelectron.* 2014, *56*, 300-306.

(19) Yang, C. Y.; Shen, J. L.; Wang, C. Y.; Fei, H. J.; Bao, H.; Wang, G. C., All-solid-state asymmetric supercapacitor based on reduced graphene oxide/carbon nanotube and carbon fiber paper/polypyrrole electrodes. *J. Mater. Chem. A* 2014, *2*, 1458-1464.

(20) Wang, L. N.; Jia, X. L.; Li, Y. F.; Yang, F.; Zhang, L. Q.; Liu, L. P.; Ren, X.; Yang, H. T., Synthesis and microwave absorption property of flexible magnetic film based on graphene oxide/carbon nanotubes and Fe3O4 nanoparticles. *J. Mater. Chem. A* 2014, *2*, 14940-14946.

(21) Sun, G. Z.; Zhang, X.; Lin, R. Z.; Yang, J.; Zhang, H.; Chen, P., Hybrid Fibers Made of Molybdenum Disulfide, Reduced Graphene Oxide, and Multi-Walled Carbon Nanotubes for Solid-State, Flexible, Asymmetric Supercapacitors. *Angew. Chem.-Int. Edit.* 2015, *54*, 4651-4656.

(22) Yu, L.; Tune, D.; Shearer, C.; Shapter, J., Heterojunction Solar Cells Based on Silicon and Composite Films of Graphene Oxide and Carbon Nanotubes. *ChemSusChem* 2015, *8*, 2940-2947.

(23) Maiti, U. N.; Lee, W. J.; Lee, J. M.; Oh, Y.; Kim, J. Y.; Kim, J. E.; Shim, J.; Han, T. H.; Kim, S. O., 25th Anniversary Article: Chemically Modified/Doped Carbon Nanotubes & Graphene for Optimized Nanostructures & Nanodevices. *Adv. Mater.* 2014, *26*, 40-67.

(24) Yun, D. J.; Jeong, Y. J.; Ra, H.; Kim, J. M.; Park, J. H.; Park, S.; An, T. K.; Seol, M.; Park, C. E.; Jang, J.; Chung, D. S., Effective Way To Enhance the Electrode Performance of Multiwall Carbon Nanotube and Poly(3,4-ethylenedioxythiophene): Poly(styrene sulfonate) Composite Using HCl-Methanol Treatment. *J. Phys. Chem. C* 2016, *120*, 10919-10926.

(25) Li, Y.; Li, H.; Petz, A.; Kunsagi-Mate, S., Reducing structural defects and improving homogeneity of nitric acid treated multi-walled carbon nanotubes. *Carbon* 2015, *93*, 515-522.

(26) Ogino, S.; Itoh, T.; Mabuchi, D.; Yokoyama, K.; Motomiya, K.; Tohji, K.; Sato, Y., In Situ Electrochemical Raman Spectroscopy of Air-Oxidized Semiconducting Single-Walled Carbon Nanotube Bundles in Aqueous Sulfuric Acid Solution. *J. Phys. Chem. C* 2016, *120*, 7133-7143.

(27) Kim, D. H.; Lee, J. K.; Huh, J. H.; Kim, Y. H.; Kim, G. T.; Roth, S.; Dettlaff-Weglikowska, U., Effect of SOCl2 doping on electronic properties of single-walled carbon nanotube thin film transistors. *Phys. Status Solidi B* 2011, *248*, 2668-2671.

(28) Kim, S. M.; Kim, K. K.; Jo, Y. W.; Park, M. H.; Chae, S. J.; Duong, D. L.; Yang, C. W.; Kong, J.; Lee, Y. H., Role of Anions in the AuCl3-Doping of Carbon Nanotubes. *ACS Nano* 2011, *5*, 1236-1242.
(29) Cui, K.; Qian, Y.; Jeon, I.; Anisimov, A.; Matsuo, Y.; Kauppinen, E. I.; Maruyama, S., Scalable and Solid-State Redox Functionalization of Transparent Single-Walled Carbon Nanotube Films for Highly Efficient and Stable Solar Cells. *Adv. Energy Mater.* 2017, *7*, 1700449.
(30) Yu, L.; Shearer, C.; Shapter, J., Recent Development of Carbon Nanotube Transparent Conductive Films. *Chem. Rev.* 2016, *116*, 13413-13453.
(31) Kim, K. K.; Kim, S. M.; Lee, Y. H., Chemically Conjugated Carbon Nanotubes and Graphene for Carrier Modulation. *Accounts Chem. Res.* 2016, *49*, 390-399.
(32) Li, X.; Jung, Y.; Huang, J.-S.; Goh, T.; Taylor, A. D., Device Area Scale-Up and Improvement of SWNT/Si Solar Cells Using Silver Nanowires. *Adv. Energy Mater.* 2014, *4*, 1400186.
(33) Lee, J.; Woo, J. Y.; Kim, J. T.; Lee, B. Y.; Han, C. S., Synergistically Enhanced Stability of Highly Flexible Silver Nanowire/Carbon Nanotube Hybrid Transparent Electrodes by Plasmonic Welding. *ACS Appl. Mater. Interfaces* 2014, *6*, 10974-10980.
(34) Marcano, D. C.; Kosynkin, D. V.; Berlin, J. M.; Sinitskii, A.; Sun, Z.; Slesarev, A.; Alemany, L. B.; Lu, W.; Tour, J. M., Improved Synthesis of Graphene Oxide. *ACS Nano* 2010, *4*, 4806-4814.
(35) Yang, C.; Tang, Y.; Su, Z.; Zhang, Z.; Fang, C., Preparation of Silver Nanowires via a Rapid, Scalable and Green Pathway. *J. Mater. Sci. Technol.* 2015, *31*, 16-22.
(36) Housecroft, C.; Sharpe, A. G. *Inorganic Chemistry*; Pearson Education Limited, 2007.
(37) Graupner, R.; Abraham, J.; Vencelova, A.; Seyller, T.; Hennrich, F.; Kappes, M. M.; Hirsch, A.; Ley, L., Doping of Single-Walled Carbon Nanotube Bundles by Bronsted acids. *Phys. Chem. Chem. Phys.* 2003, *5*, 5472-5476.
(38) Shin, D. W.; Lee, J. H.; Kim, Y. H.; Yu, S. M.; Park, S. Y.; Yoo, J. B., A Role of HNO3 on Transparent Conducting Film with Single-Walled Carbon Nanotubes. *Nanotechnology* 2009, *20*, 475703.
(39) Yang, D.; Velamakanni, A.; Bozoklu, G.; Park, S.; Stoller, M.; Piner, R. D.; Stankovich, S.; Jung, I.; Field, D. A.; Ventrice, C. A.; Ruoff, R. S., Chemical analysis of graphene oxide films after heat and chemical treatments by X-ray photoelectron and Micro-Raman spectroscopy. *Carbon* 2009, *47*, 145-152.
(40) Fagan, J. A.; Haroz, E. H.; Ihly, R.; Gui, H.; Blackburn, J. L.; Simpson, J. R.; Lam, S.; Walker, A. R. H.; Doorn, S. K.; Zheng, M., Isolation of > 1 nm Diameter Single-Wall Carbon Nanotube Species Using Aqueous Two-Phase Extraction. *ACS Nano* 2015, *9*, 5377-5390.
(41) Jing, M. X.; Han, C.; Li, M.; Shen, X. Q., High performance of carbon nanotubes/silver nanowires-PET hybrid flexible transparent conductive films via facile pressing-transfer technique. *Nanoscale Res. Lett.* 2014, *9*.
(42) Naumov, A. V.; Ghosh, S.; Tsyboulski, D. A.; Bachilo, S. M.; Weisman, R. B., Analyzing Absorption Backgrounds in Single-Walled Carbon Nanotube Spectra. *ACS Nano* 2011, *5*, 1639-1648.
(43) Liu, X. D.; Chen, C. X.; Wei, L. M.; Hu, N. T.; Song, C. J.; Liao, C. H.; He, R.; Dong, X. S.; Wang, Y.; Liu, Q. R.; Zhang, Y. F., A p-i-n junction diode based on locally doped carbon nanotube network. *Sci Rep* 2016, *6*, 23319.
(44) Dresselhaus, M. S.; Jorio, A.; Hofmann, M.; Dresselhaus, G.; Saito, R., Perspectives on Carbon Nanotubes and Graphene Raman Spectroscopy. *Nano Lett.* 2010, *10*, 751-758.
(45) Dresselhaus, M. S.; Dresselhaus, G.; Saito, R.; Jorio, A., Raman spectroscopy of carbon nanotubes. *Phys. Rep.* 2005, *409*, 47-99.
(46) Brown, S. D. M.; Jorio, A.; Corio, P.; Dresselhaus, M. S.; Dresselhaus, G.; Saito, R.; Kneipp, K., Origin of the Breit-Wigner-Fano lineshape of the tangential G-band feature of metallic carbon nanotubes. *Phys. Rev. B* 2001, *63*, 155414.
(47) Rao, A. M.; Eklund, P. C.; Bandow, S.; Thess, A.; Smalley, R. E., Evidence for charge transfer in doped carbon nanotube bundles from Raman scattering. *Nature* 1997, *388*, 257-259.

(48) Voggu, R.; Rout, C. S.; Franklin, A. D.; Fisher, T. S.; Rao, C. N. R., Extraordinary sensitivity of the electronic structure and properties of single-walled carbon nanotubes to molecular charge-transfer. *J. Phys. Chem. C* 2008, *112*, 13053-13056.
(49) Hasdeo, E. H.; Nugraha, A. R. T.; Dresselhaus, M. S.; Saito, R., Breit-Wigner-Fano line shapes in Raman spectra of graphene. *Phys. Rev. B* 2014, *90*, 245140.
(50) Shin, H.-J.; Kim, S. M.; Yoon, S.-M.; Benayad, A.; Kim, K. K.; Kim, S. J.; Park, H. K.; Choi, J.-Y.; Lee, Y. H., Tailoring Electronic Structures of Carbon Nanotubes by Solvent with Electron-Donating and -Withdrawing Groups. *J. Am. Chem. Soc.* 2008, *130*, 2062-2066.
(51) Tokuno, T.; Nogi, M.; Jiu, J.; Suganuma, K., Hybrid Transparent Electrodes of Silver Nanowires and Carbon Nanotubes: A Low-Temperature Solution Process. *Nanoscale Res. Lett.* 2012, *7*, 1-7.
(52) Moon, I. K.; Kim, J. I.; Lee, H.; Hur, K.; Kim, W. C.; Lee, H., 2D Graphene Oxide Nanosheets as an Adhesive Over-Coating Layer for Flexible Transparent Conductive Electrodes. *Sci Rep* 2013, *3*, 1112.
(53) Abdullah-Al-Galib, M.; Hou, B.; Shahriad, T.; Zivanovic, S.; Radadia, A. D., Stability of Few Layer Graphene Films Doped with Gold (III) Chloride. *Appl. Surf. Sci.* 2016, *366*, 78-84.

Chapter 7 Pyramid-Textured Antireflective Silicon Surface in Graphene Oxide/Single-Wall Carbon Nanotube Silicon Heterojunction Solar Cells

7.1 Overview

Antireflection layers in photovoltaics are commonly used to enhance light absorption and thus improve the photocurrent. In this Chapter, pyramid structures are formed on Si surfaces via a traditional alkaline solution based reaction. The coverage of the pyramids on the surface was dependent on the reaction time so that the reflectance of the surface decreases with the reaction time. Heterojunction solar cells based on p-type GOCNT and n-type Si were fabricated via a floating transfer approach. The highest efficiency of the solar cell was over 13 %, in which Si substrates with the highest coverage of pyramids (99.9 %) were applied. It is determined that the improved performance is a combined effect of decreased reflectance and increased effective heterojunction area per unit illumination area.

7.2 Introduction

The record efficiency of the crystalline silicon based photovoltaics has been improved to above 25 %[1-3] by several groups with different designs, such as top/rear contacted heterojunctions,[4] top/rear contacted device using front homojunction emitter and rear contact with thin oxide passivation,[5] interdigitated back contact,[6] and heterojunction interdigitated back contact.[7] The best solar cell has the efficiency of 26.6 %, confirmed by Fraunhofer Institute for Solar Energy System Callab independently, in which a heterojunction interdigitated back contact design was used.[8-9]

Different approaches of surface texturing,[10-13] including tiler's pattern,[14] perpendicular grooves,[15] honeycomb texture,[16] and prism pyramidal structures,[17] were applied to enhance the light trapping in most of these studies targeting the high efficiency solar cells.[18] Among them, random pyramidal texturing via a mixture of an alkaline (for example, NaOH and KOH) and isopropyl alcohol (IPA) is the most mature technique used in the industrial fabrication of Si based solar cells.[19-20] In detail, alkaline is important in forming upright pyramidal structures and IPA is used to improve the surface wettability and the uniformity of the reaction across the Si surface by controllably nucleating the texturing process.[21] Some additives, including potassium silicate, has been shown recently to improve the throughput.[22]

In the last a few years, carbon nanomaterials, such as carbon nanotubes (CNTs),[23-28] graphene[29-35] and graphene oxide (GO),[36-37] have been applied to create heterojunction solar cells with Si and thus reduce the fabrication cost as well as the consumption of the semiconductors. Such a device is created by n-type Si with a GOCNT hybrid film (GOCNT/Si), whose working mechanism has been explained in section 5.1.

Different antireflection layers, such as polymethylmethacrylate,[38] polydimethylsiloxane,[39] and TiO_2[40] have been used to reduce the reflection of Si and thus improve the photocurrent output. However, planar Si were used in these reports. The optical reflection could be reduced by the "double-bounce" effect with a textured Si surface, and in addition, the surface area at the interface (compared to planar Si) might increase at the same time, as shown in Figure 7.1.

In this Chapter, randomly distributed pyramids are formed on Si via anisotropically etching a planar Si surface by a mixed solution of NaOH and IPA. A previously developed floating transfer process is used to fabricate GOCNT/Si solar cells, where transparent conducting films of GOCNT hybrids are placed on the pyramid-textured Si surface, as shown in Figure 7.1.[36] The impact of the reaction time of etching on both the surface reflection and the coverage of pyramid across the Si surface as well as on the solar cell performance has been studied.

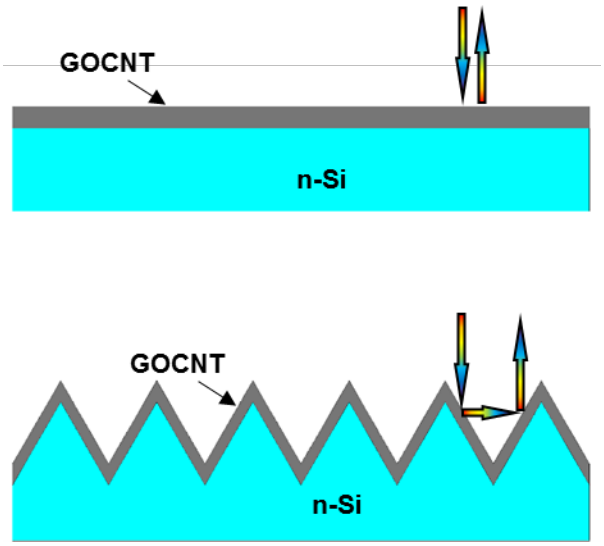

Figure 7.1 Schemes of GOCNT/Si heterojunction with planar and pyramidal Si surface.

7.3 Experimental details

The preparation of Si etching and GOCNT stock solution are described in sections 2.2.1.6 and 2.2.2.2. The preparation of GOCNT films and their characterisation are described in sections 2.4.3 and 2.6.2. The fabrication, chemical doping and measurement of the device performance are described in sections 2.5.3.1, 2.5.3.2 and 2.6.2.

7.4 Results and discussion

7.4.1 Creation of pyramid structure on Si surface

In this Chapter, conventional alkaline based chemical wet etching was applied to create the micro-structures on the planar Si surfaces, where the etch rate of the {1 0 0} and {1 1 0} facets is much higher than that of {1 1 1} surface. As a result, pyramid structures on the {1 1 0} facet are created due to such strong dependence of etching rates.[41] In order to explore the impact of the reaction time on the pyramid coverage on the Si surface, the etching duration was controlled to be 5, 15, 25, 35 and 45 min and the top-view SEM images of the etched surfaces are shown in Figure 7.2 (a) - (e). As shown in Figure 7.2 (a), for 5 min the base size of the pyramid structures is below 3 μm on a side and the surface coverage is below 5 %. As the reaction duration extends from 5 to 25 min, the side of the largest pyramid increases to about 20 μm and the surface coverage is up to above 80 %. However, the pyramid size is not homogeneous across the entire Si surface, as shown in Figure 7.2 (b) and (c). After 25 min, the number of large pyramids increases with the largest size remaining at about 20 μm on a side while the surface coverage increases to nearly 100 % after 45 min (Figure 7.2 (d) and (e)). This is consistent with the previous literature which shows the distribution of the pyramids becomes more uniform with increasing reaction time.[42-43] Importantly, the actual surface area increases with the reaction time when a larger number of pyramids are created on a planar surface. Furthermore, if it is assumed that all pyramids have the exact same base angle, the increase in the surface area solely depends on the surface coverage but not the pyramid size.[44-46] Therefore, the surface area of the Si will approach the maximum possible after 45 min.

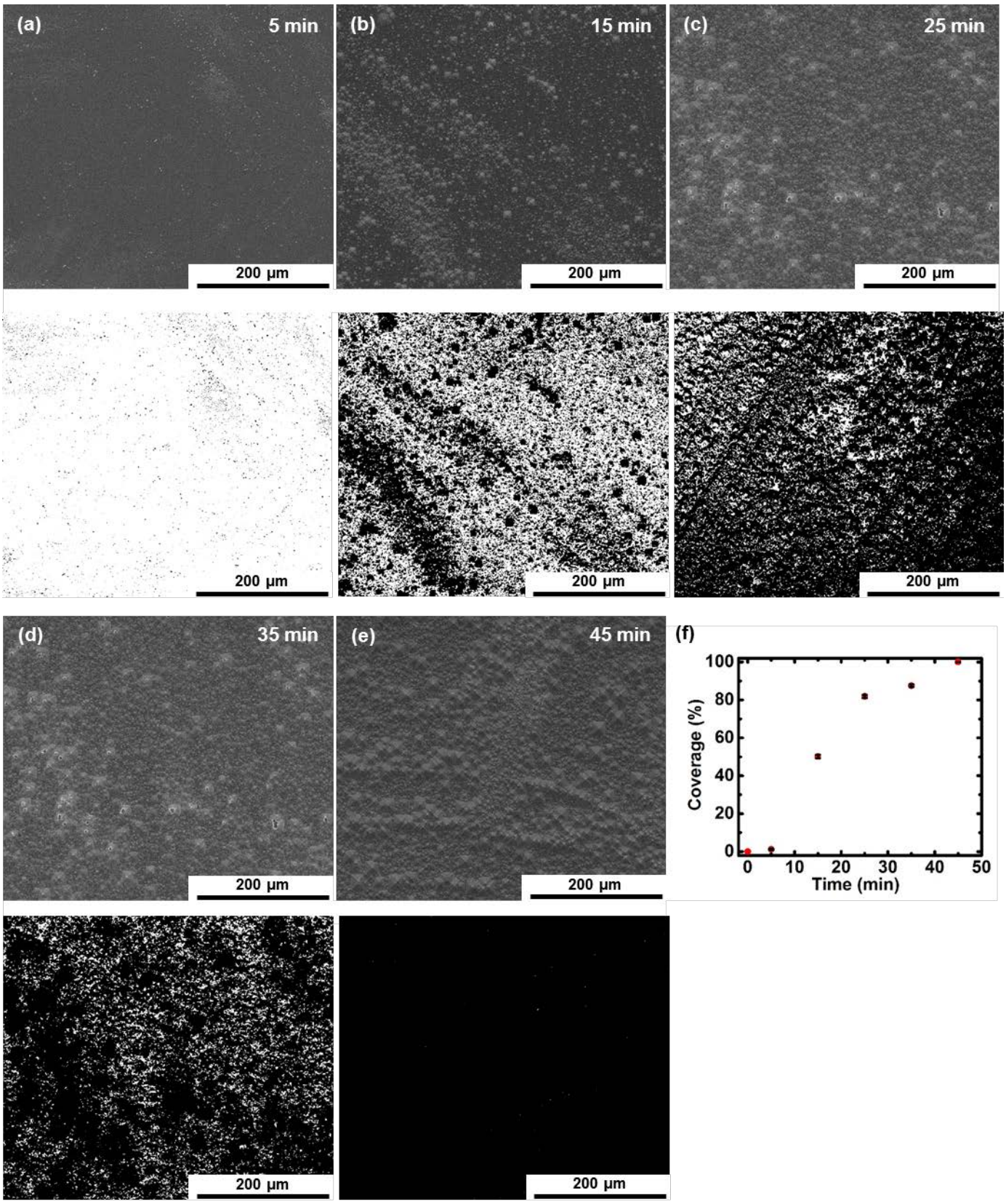
(a)
5 min
200 µm
(b)
15 min
200 µm
(c)
25 min
200 µm
200 µm
200 µm
200 µm
(d)
35 min
200 µm
(e)
45 min
200 µm
(f)
Coverage (%)
Time (min)
0
20
40
60
80
100
0
10
20
30
40
50
200 µm
200 µm

Figure 7.2 SEM images of Si surface with pyramid structure for different reaction time: (a) 5 min, (b) 15 min, (c) 25 min, (d) 35 min and (e) 45 min. (f) Surface coverage of pyramid structure as a correlation of the etching time. All these images are top views with the same magnification. In each plot (from (a) to (e)), the top image is the original SEM image while the bottom one is used to estimate the coverage of the pyramid structures after different reaction times by comparing the percentage of the pixels from the pyramids to the total pixels in the SEM images using manual thresholding from imageJ software (NIH).

The Si surface reflectance spectra with various coverages are shown in Figure 7.3. It is consistent that the overall reflectance of the surface reduces through the visible and near infrared range (from 300 to 1100 nm) as the surface coverage increases.[42] However, the surface reflectance at near full coverage (99.9 %) is higher in previous study (18 % versus 13 % as the lowest reflectance),[42,45] which might be caused by the inhomogeneity of the pyramid size and it results in a more serious light scattering in the previous report.

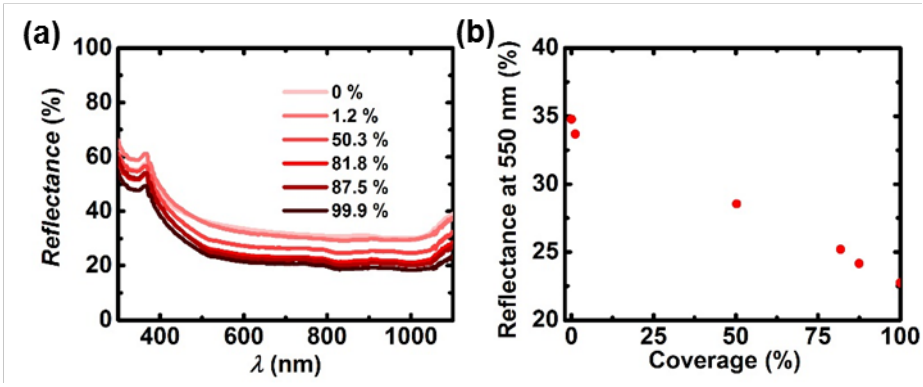

Figure 7.3 (a) Si surface reflectance as a function of wavelength with different pyramid coverage. (b) Reflectance of silicon surface at 550 nm as a function of the surface coverage of pyramids.

7.4.2 Characterisation of hybrid films and its deposition on surface

In order to estimate the optoelectronic properties, namely the transparency and the sheet resistance of GOCNT films acting as the window electrodes for the solar cells, a UV-Vis-NIR spectrometer and the four point probe were used to study these properties with the results shown in Figure 7.4, and listed in Table 7.1. The optical transmittance (calculated from the

absorbance at 550 nm) of both films is about 80 %. After $SOCl_2$ chemical doping, the S_{11} peak was completely bleached with a suppressed S_{22} peak because the Fermi level shifts into the valence band.[47] As a result, as shown in Table 7.1, the R_{sheet} reduced from 800 to about 500 $\Omega\ sq^{-1}$ and the FOM was improved from 1.9 to 2.9 (higher FOM values commonly indicate better optoelectronic properties).[48]

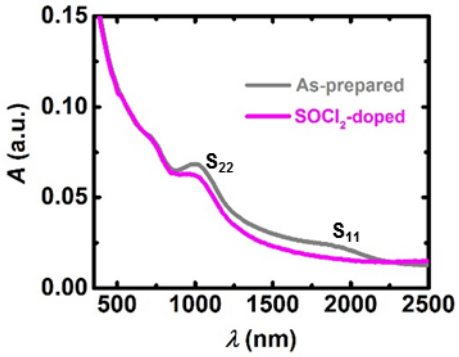

Figure 7.4 UV-Vis-NIR spectra of the GOCNT films before and after chemical doping by $SOCl_2$.

Table 7.1 Sheet resistance and figure of merit of the GOCNT films before and after chemical doping by $SOCl_2$.

	R_{sheet} ($\Omega\ sq^{-1}$)	FOM
As-prepared	813 ± 6	1.87 ± 0.01
$SOCl_2$-doped	523 ± 2	2.88 ± 0.01

The most obvious concern using a textured Si surface in a GOCNT/Si heterojunction solar cell is that the hybrid film will not conform to the roughened surface. In this Chapter, a previously developed floating transfer method is used to form the GOCNT/Si heterojunction to create an intimate contact between the GOCNT electrode and the textured Si to realise efficient separation of electron-hole pairs, as shown in Figure 7.5 (a) and (b). The floating transfer approach has many benefits when compared to other liquid processing methods (including spray coating,[49] spin coating,[50-51] Mayer rod coating[52] and electrophoretic deposition[53]): (a) room temperature processing, (b) compatibility with almost any substrate, (c) compatibility with surfaces with complex structures, (d) compatibility with most liquid film doping processes, (e)

ability to prepare hole-free films of large sizes. However, it is not appropriate in the preparation of ultrathin films (T > 90 %) because of the dramatically decreased mechanical properties of the networks for thin films. The floating transfer should be ideal to create an intimate contact between the transparent hybrid films and the textured Si surface when the transparency is below 85 %. While most of the pyramids are covered and interconnected by the GOCNT film, there are still some defects where the GOCNT film is broken at joints between two neighbouring pyramids, as highlighted in the red dashed circles in Figure 7.5 (c) and (d).

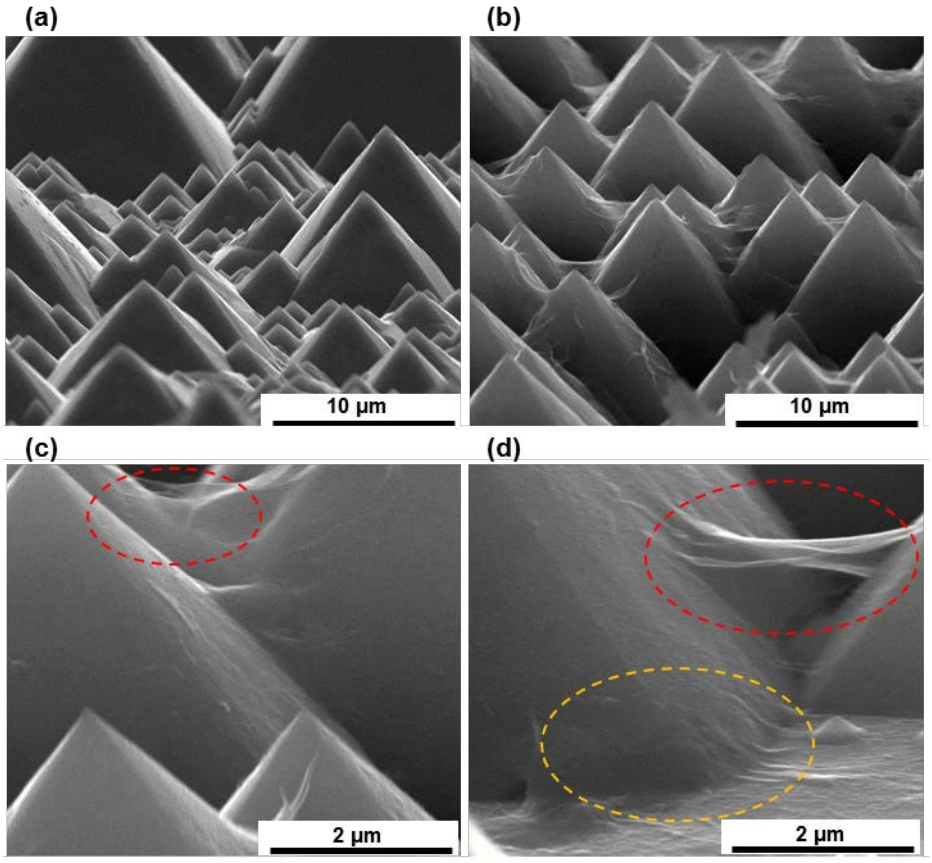

Figure 7.5 Side view SEM images of (a) bare Si pyramids. (b), (c) and (d) GOCNT films coated textured Si surface.

7.4.3 Solar cell performance

After it was confirmed that the surface texture decreases the reflection and hybrid electrodes can form a conformal contact with the roughened surface, GOCNT/Si heterojunction solar cells were fabricated by depositing GOCNT films on the textured Si surface. The current density versus voltage (J-V curves) of the solar cells with different coverages of pyramids are plotted in Figure 7.6 (a). The solar cell efficiency increases from 10.18 ± 0.33 % to 13.01 ± 0.32 % with the pyramid coverage increasing from 0 to 99.9 %, as shown in Figure 7.6 (b). The major reason of such improvement is the dramatically increased short circuit current density (J_{SC}) from 26.15 $\pm$ 0.22 to 33.75 $\pm$ 0.26 mA cm^{-2} with the increase in pyramid coverage while there is no obvious change in the open circuit voltage (V_{OC}) and fill factor (FF), as shown in Figure 7.6 (c), (e) and (f). The increase in J_{SC} indicates that there is an increase in the number of charge carriers produced by the devices, and it is further supported by the external quantum efficiency (EQE) curves shown in Figure 7.6 (d) (higher surface coverage corresponds to higher values of EQE over the full wavelength range). The increased J_{sc} was caused by the reduced surface reflection as well the increase in the interface area. The decrease in the reflection resulted in an increased number of photons absorbed by Si and thus more excitons are created. The improvement in the interface area has a dual benefit. It can absorb a higher number of photons and again produce more excitons while the larger interfacial area also results in more effective separation of the excitons into electrons and holes. Unfortunately, there is no clear relationship between shunt resistance (R_{shunt})/the series resistance (R_{series}) and the coverage of pyramids, as shown in Figure 7.6 (g) and (h).

The diode properties of the devices are estimated with the measured J-V curves under dark conditions, as shown in Figure 7.6 (i). Though there is no obvious trend in the ideality as a correlation to the surface coverage of pyramids because of the large errors, the general change is that the ideality increases with the coverage, as shown in Figure 7.6 (j). This might be partially caused by a poorer conformal contact between GOCNT and Si when roughness of the surface is increased. In addition, as shown in Figure 7.6 (k), the reverse saturation current (J_{sat}) increases with the surface coverage, which is possibly due to the less ideal heterojunction quality resulting from the increase in the surface roughness. The other potential possibility is that the illumination area which is used for the estimation of the solar cell performance is smaller than the actual interfacial area. This mismatch leads to the overestimation of both the ideality and J_{sat} since poorer dark curves might be recorded for the same illumination area

value in the case of devices with pyramidal Si surface. Such mismatch results in the overestimation of both the ideality and J_{sat} because poorer dark J-V curves are recorded while using the same illumination area for devices with higher coverage of pyramids though the influence of this is slight very slight. Therefore, the diode properties of devices become worse as the pyramid coverage increases which is mainly caused by recombination events contributed by the increase in the surface roughness with slight influence from the mismatch between the contact and the illumination area.

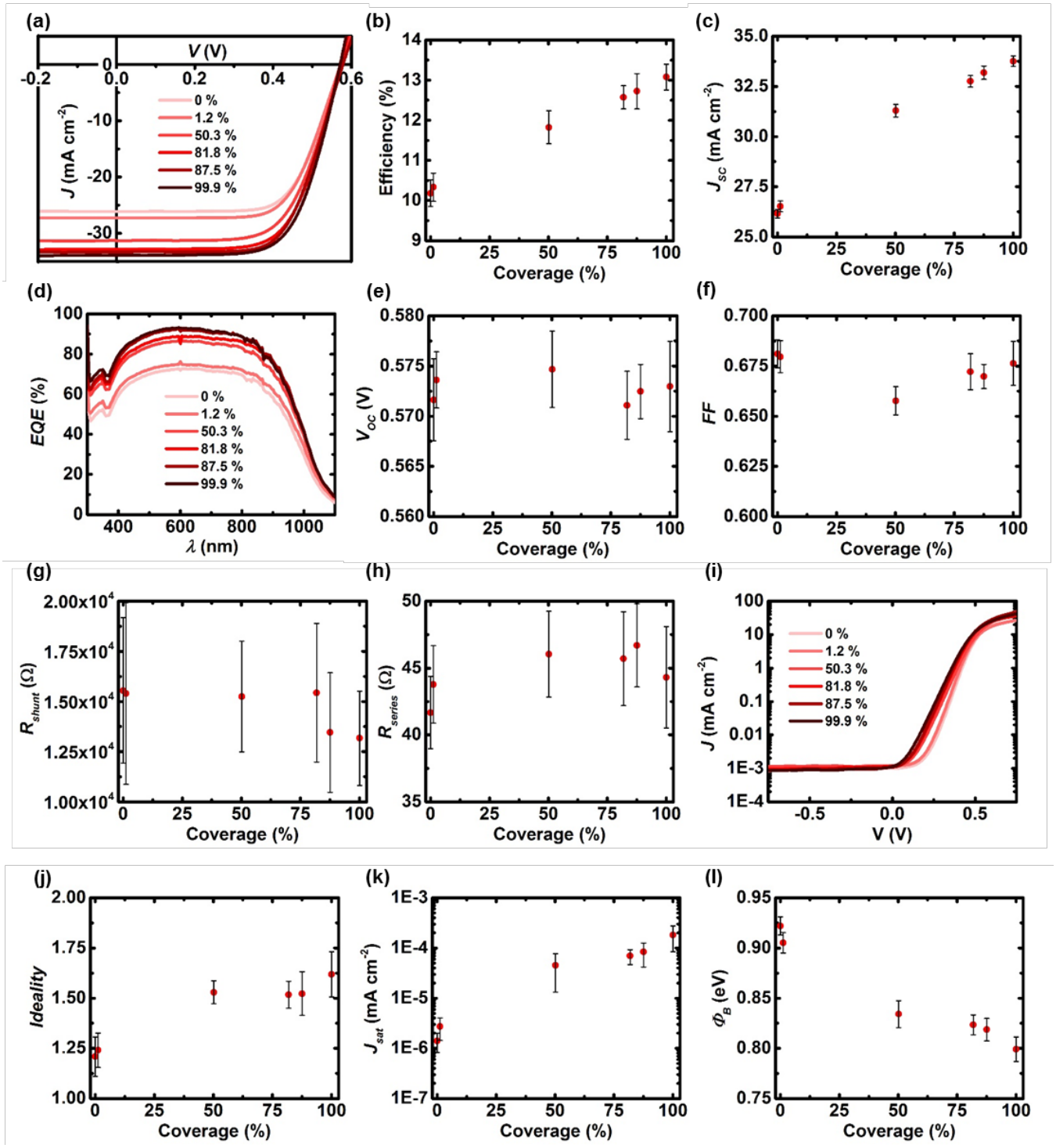

Figure 7.6 The detailed solar cell performance: J-V curves under (a) light and (i) dark conditions, (d) EQE curves, (b) Efficiency, (c) J_{SC}, (e) V_{OC}, (f) FF, (g) R_{shunt}, (h) R_{series}, (j) Ideality, (k) J_{sat} and (l) ϕ_B as a function of the coverage of pyramids on the Si surface.

7.4.4 Source of the improvement in solar cell performance

As shown in Figure 7.6, the main contribution to the increase in efficiency with the pyramid coverage is the dramatically increased J_{SC}, which further suggests that an increased number of produced charge carriers was the main source of the improvement in the solar cell performance. Generally, the decrease in the reflection results in a higher number of photons absorbed by the Si surface with high surface coverage, as shown in Figure 7.7 (a), where the values for number of photons absorbed by Si (N) are calculated by Equation 7.1 when it is assumed that the loss of incident energy is due to the surface reflection alone.

The normalised values (X/X_0, in which X is the value at a certain coverage and X_0 is the value for the initial flat Si surface) of different parameters are plotted in Figure 7.7 (b). Noticeably, there is a mismatch between the increased number of photons and the J_{SC} improvement - the improvement in J_{SC} is higher, which suggests that some other factors rather than the reduced reflection of the surface contribute to such performance improvement. The most likely factor is the increase in the contact area between hybrid films and textured Si surface as the surface coverage of pyramids increases. If the internal quantum efficiency is assumed to be 100 %, the actual contact area (A_{Total}) at various coverages is calculated by Equation 7.2 and plotted in Figure 7.7 (b). The results show that A_{Total} increased to 1.1 times of the initial area for flat Si surface when the coverage is at 50 %, but it remains at this level with further increases in the pyramid coverage. This is probably because it is more difficult to create a perfectly conformal contact between GOCNT films and pyramid surfaces with the increase in the surface roughness.

Equation 7.3 (rearranged in Equation 7.4) is used to understand the impact of the imperfect contact and it is assumed that all the pyramids have the same base angle (50°).[54] As shown in Figure 7.7 (c), the coverage factor decreases with surface coverage in a linear relationship and it suggests that even though the floating transfer approach is able to cover some complex structures, the ability for the GOCNT layer to form a perfect conformal coverage to the pyramid structure is decreased in the case of high surface roughness. When the coverage is low, most of the structures are likely separated by some flat region and the hybrid film can cover the corner the pyramids (highlighted by the yellow dashed circle in Figure 7.5 (d)). In contrast, when the pyramid coverage is high, most of the pyramids are connected with each other and

the hybrid films start to fall apart at the bottom of the valleys between two pyramids and the intimate contact between the GOCNT films and the silicon is poorer.

$$N = N_{AM1.5}\, T\, (1 - R_{Si}) \qquad \text{Equation 7.1}$$

$$\frac{J_{SC}}{J_{SC_0}} = \frac{N}{N_0}\frac{A_{Total}}{A_0} \qquad \text{Equation 7.2}$$

$$A_{Total} = \frac{A_0\ Coverage}{\cos 50^\circ} CF + A_0\ (1 - Coverage) \qquad \text{Equation 7.3}$$

$$CF = [A_{Total} - A_0\ (1 - Coverage)]\frac{\cos 50^\circ}{A_0\ Coverage} \qquad \text{Equation 7.4}$$

N and $N_{AM1.5}$ (photons s^{-1} m^{-2}) are the number of photons reaching Si surface at different pyramid coverage and the number of photons from the incident light beam (these values are calculated by the integration from 300 to 1100 nm); T (%) is the transmittance of the hybrid films after chemical doping; R_{Si} (%) is the reflectance of the Si surface with various pyramid coverage; J_{SC_0} (mA cm^{-2}) and N_0 are the current density and the number of photons reaching Si surface at zero coverage (the initial state); A_{Total} and A_0 (cm^2) are the actual contact area between GOCNT films and Si at different pyramid coverage and zero coverage (A_0 = 0.087 cm^2); CF is the coverage factor describing the percentage of the pyramid surface area covered by GOCNT films tightly; and Coverage (%) is the surface pyramid coverage.

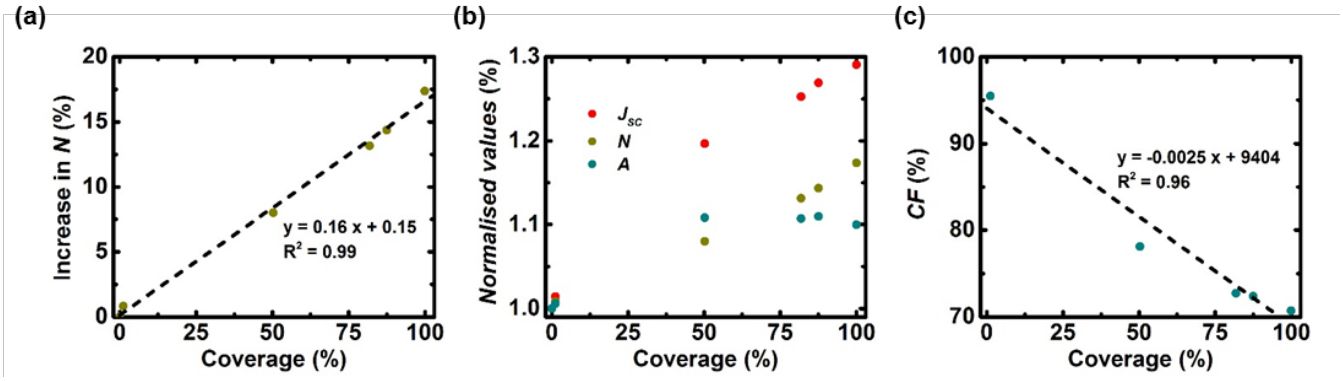

Figure 7.7 (a) The increase in the number of photons absorbed by Si surface, (b) normalised J_{SC}, N and A, and (c) CF as a correlation with the surface coverage of pyramids.

There are three assumptions in the previous calculation, (a) the light scattered from the surface is 0 %; (b) the internal quantum efficiency is 100 % and (c) the base angles of all the pyramids are the same. Deviations from these assumptions would yield lower photocurrent improvement due to the decrease in the reflectance, suggesting that the calculated A_{Total} is lower than the actual value which would further imply that the increased area has a higher contribution than the calculated results in all cases, and the CF values are expected to be higher than those in Figure 7.7 (c). However, the general trend in these plots can probably remain the same.

The highest efficiency in this Chapter is above 13 %, which is one of the highest values among the class of carbon nanomaterials/Si heterojunction photovoltaics, including graphene/Si and CNT/Si solar cells.[29,33,36] The theme of this Chapter is to decrease the reflection of Si and improve the actual heterojunction area between GOCNT and Si to increase the number of charge carriers produced in the fixed illumination area. Thus, the nanostructure on the surface has a strong influence on these 2 factors. If both the reflectance of the pyramid surface (above 15 %) can be further decreased and the coverage of GOCNT on the Si structure is further improved, higher efficiency solar cells would be fabricated.

7.5 Conclusions

A traditional solution based approach was used to create pyramid structures on Si surface with various coverages from 0 to 99.9 % with different reaction duration from 0 to 45 min. The surface reflectance decreased with the surface coverage of pyramids and the surface with the highest coverage (99.9 %) had reflectance below 20 % in the visible and near infrared range. GOCNT/Si heterojunction solar cells were created by picking up floating GOCNT transparent hybrid films from an acetone bath with pyramid-covered Si surfaces. Solar cells with the highest pyramid coverage had the best performance (13.01 ± 0.32 %) because of the increased actual contact area between GOCNT and Si which helps to produce and extract more charge carriers and at the same time a higher number of photons are absorbed at the heterojunction with the decreased reflectance of the textured Si.

REFERENCES:

(1) Green, M. A., The Path to 25% Silicon Solar Cell Efficiency: History of Silicon Cell Evolution. *Prog. Photovoltaics* 2009, *17*, 183-189.

(2) Ho, W. J.; Hsieh, M. L.; Lee, Y. Y.; Liu, J. J.; Syu, J. K.; Lai, Q. R.; Yu, C. M., Efficiency improvement of 25.7% using a voltage biasing transparent electrode for MIS transistor-based silicon solar cells. *Surf. Coat. Technol.* 2013, *231*, 447-451.

(3) Hermle, M.; Feldmann, F.; Eisenlohr, J.; Benick, J.; Richter, A.; Lee, B.; Stradins, P.; Rohatgi, A.; Glunz, S. W.; Ieee In *2015 Ieee 42nd Photovoltaic Specialist Conference*, 2015.

(4) Adachi, D.; Hernandez, J. L.; Yamamoto, K., Impact of carrier recombination on fill factor for large area heterojunction crystalline silicon solar cell with 25.1% efficiency. *Appl. Phys. Lett.* 2015, *107*, 233506.

(5) Glunz, S. W. In *European Photovoltaic Solar Energy Conference* Hamburg, 2015.

(6) Smith, D. D.; Reich, G.; Baldrias, M.; Reich, M.; Boitnott, N.; Bunea, G.; Ieee In *2016 Ieee 43rd Photovoltaic Specialists Conference*, 2016.

(7) Masuko, K.; Shigematsu, M.; Hashiguchi, T.; Fujishima, D.; Kai, M.; Yoshimura, N.; Yamaguchi, T.; Ichihashi, Y.; Mishima, T.; Matsubara, N.; Yamanishi, T.; Takahama, T.; Taguchi, M.; Maruyama, E.; Okamoto, S., Achievement of More Than 25% Conversion Efficiency With Crystalline Silicon Heterojunction Solar Cell. *IEEE J. Photovolt* 2014, *4*, 1433-1435.

(8) Yoshikawa, K.; Yoshida, W.; Irie, T.; Kawasaki, H.; Konishi, K.; Ishibashi, H.; Asatani, T.; Adachi, D.; Kanematsu, M.; Uzu, H.; Yamamoto, K., Exceeding conversion efficiency of 26% by heterojunction interdigitated back contact solar cell with thin film Si technology. *Sol. Energy Mater. Sol. Cells* 2017.

(9) Yoshikawa, K.; Kawasaki, H.; Yoshida, W.; Irie, T.; Konishi, K.; Nakano, K.; Uto, T.; Adachi, D.; Kanematsu, M.; Uzu, H.; Yamamoto, K., Silicon heterojunction solar cell with interdigitated back contacts for a photoconversion efficiency over 26%. *Nat. Energy* 2017, *2*, 17032.

(10) Joseph, S.; Joseph, J., Influence of periodic texture profile and parameters for enhanced light absorption in amorphous silicon ultra-thin solar cells. *Appl. Opt.* 2017, *56*, 5013-5022.

(11) Eisenhauer, D.; Koppel, G.; Jager, K.; Chen, D. T.; Shargaieva, O.; Sonntag, P.; Amkreutz, D.; Rech, B.; Becker, C., Smooth anti-reflective three-dimensional textures for liquid phase crystallized silicon thin-film solar cells on glass. *Sci Rep* 2017, *7*.

(12) Feng, Z. Z.; Jia, R.; Dou, B. F.; Li, H. F.; Jin, Z.; Liu, X. Y.; Li, F.; Zhang, W.; Wu, C. Y., Enhanced properties of silicon nano-textured solar cells enabled by controlled ZnO nanorods coating. *Sol. Energy* 2015, *115*, 770-776.

(13) Zhao, J. H.; Wang, A. H.; Green, M. A.; Ferrazza, F., 19.8% efficient "honeycomb'' textured multicrystalline and 24.4% monocrystalline silicon solar cells. *Appl. Phys. Lett.* 1998, *73*, 1991-1993.

(14) Campbell, P.; Green, M. A., Light trapping properties of pytamidally textured surfaces. *J. Appl. Phys.* 1987, *62*, 243-249.

(15) Lauermann, T.; Frohlich, B.; Hahn, G.; Terheiden, B.; Ieee, Design Considerations for Industrial Rear Passivated Solar Cells. *2012 38th Ieee Photovoltaic Specialists Conference (Pvsc)* 2012, 1710-1715.

(16) Zhao, J. H.; Wang, A. H.; Campbell, P.; Green, M. A., A 19.8% efficient honeycomb multicrystalline silicon solar cell with improved light trapping. *IEEE Trans. Electron Devices* 1999, *46*, 1978-1983.

(17) Brendel, R.; Ieee In *Conference Record of the Twenty Third Ieee Photovoltaic Specialists Conference - 1993*, 1993.

(18) Zin, N.; McIntosh, K.; Kho, T.; Franklin, E.; Fong, K.; Stocks, M.; Wang, E. C.; Ratcliff, T.; Blakers, A.; Ieee In *2016 Ieee 43rd Photovoltaic Specialists Conference*, 2016.

(19) Nijdam, A. J.; van Veenendaal, E.; Cuppen, H. M.; van Suchtelen, J.; Reed, M. L.; Gardeniers, J. G. E.; van Enckevort, W. J. P.; Vlieg, E.; Elwenspoek, M., Formation and stabilization of pyramidal etch hillocks on

silicon {100} in anisotropic etchants: Experiments and Monte Carlo simulation. *J. Appl. Phys.* **2001**, *89*, 4113-4123.

(20) Basu, P. K.; Khanna, A.; Hameiri, Z., The effect of front pyramid heights on the efficiency of homogeneously textured inline-diffused screen-printed monocrystalline silicon wafer solar cells. *Renew. Energ.* **2015**, *78*, 590-598.

(21) Verlinden, P.; Evrard, O.; Mazy, E.; Crahay, A., The surface texturization of solar cells - A new method using V-grooves with controllable sidewall angles. *Sol. Energy Mater. Sol. Cells* **1992**, *26*, 71-78.

(22) Basu, P. K.; Sarangi, D.; Shetty, K. D.; Boreland, M. B., Liquid silicate additive for alkaline texturing of mono-Si wafers to improve process bath lifetime and reduce IPA consumption. *Sol. Energy Mater. Sol. Cells* **2013**, *113*, 37-43.

(23) Fan, Q. X.; Zhang, Q.; Zhou, W. B.; Xia, X. G.; Yang, F.; Zhang, N.; Xiao, S. Q.; Li, K. W.; Gu, X. G.; Xiao, Z. J.; Chen, H. L.; Wang, Y. C.; Liu, H. P.; Zhou, W. Y.; Xie, S. S., Novel approach to enhance efficiency of hybrid silicon-based solar cells via synergistic effects of polymer and carbon nanotube composite film. *Nano Energy* **2017**, *33*, 436-444.

(24) Xu, W. J.; Wu, S. T.; Li, X. M.; Zou, M. C.; Yang, L. S.; Zhang, Z. L.; Wei, J. Q.; Hu, S.; Li, Y. H.; Cao, A. Y., High-Efficiency Large-Area Carbon Nanotube-Silicon Solar Cells. *Adv. Energy Mater.* **2016**, *6*, 1600095.

(25) Stolz, B. W.; Tune, D. D.; Flavel, B. S., The effect of dry shear aligning of nanotube thin films on the photovoltaic performance of carbon nanotube-silicon solar cells. *Beilstein J. Nanotech.* **2016**, *7*, 1486-1491.

(26) Grace, T.; Yu, L. P.; Gibson, C.; Tune, D.; Alturaif, H.; Al Othman, Z.; Shapter, J., Investigating the Effect of Carbon Nanotube Diameter and Wall Number in Carbon Nanotube/Silicon Heterojunction Solar Cells. *Nanomaterials* **2016**, *6*, 52.

(27) Funde, A. M.; Nasibulin, A. G.; Syed, H. G.; Anisimov, A. S.; Tsapenko, A.; Lund, P.; Santos, J. D.; Torres, I.; Gandia, J. J.; Carabe, J.; Rozenberg, A. D.; Levitsky, I. A., Carbon nanotube-amorphous silicon hybrid solar cell with improved conversion efficiency. *Nanotechnology* **2016**, *27*.

(28) De Nicola, F.; Salvato, M.; Cirillo, C.; Crivellari, M.; Boscardin, M.; Scarselli, M.; Nanni, F.; Cacciotti, I.; De Crescenzi, M.; Castrucci, P., Record efficiency of air-stable multi-walled carbon nanotube/silicon solar cells. *Carbon* **2016**, *101*, 226-234.

(29) Xu, D. K.; He, J.; Yu, X. G.; Gao, D. C.; Ma, L. L.; Mu, X. H.; Zhong, M. Y.; Xu, Y.; Ye, J. C.; Xu, M. S.; Yang, D. R., Illumination-Induced Hole Doping for Performance Improvement of Graphene/n-Silicon Solar Cells with P3HT Interlayer. *Adv. Electron. Mater.* **2017**, *3*, 1600516.

(30) Shin, D. H.; Kim, J. H.; Kim, J. H.; Jang, C. W.; Seo, S. W.; Lee, H. S.; Kim, S.; Choi, S. H., Graphene/porous silicon Schottky-junction solar cells. *J. Alloy. Compd.* **2017**, *715*, 291-296.

(31) Patel, K.; Tyagi, P. K., P-type multilayer graphene as a highly efficient transparent conducting electrode in silicon heterojunction solar cells. *Carbon* **2017**, *116*, 744-752.

(32) Jiang, X. Y.; Wang, Z. L.; Han, W. H.; Liu, Q. M.; Lu, S. Q.; Wen, Y. X.; Hou, J.; Huang, F.; Peng, S. L.; He, D. Y.; Cao, G. Z., High performance silicon-organic hybrid solar cells via improving conductivity of PEDOT:PSS with reduced graphene oxide. *Appl. Surf. Sci.* **2017**, *407*, 398-404.

(33) Huang, K.; Yan, Y. C.; Yu, X. G.; Zhang, H.; Yang, D. R., Graphene coupled with Pt cubic nanoparticles for high performance, airstable graphene-silicon solar cells. *Nano Energy* **2017**, *32*, 225-231.

(34) Ding, K.; Zhang, X. J.; Xia, F. F.; Wang, R. B.; Kuang, Y. W.; Duhm, S.; Jie, J. S.; Zhang, X. H., Surface charge transfer doping induced inversion layer for high-performance graphene/silicon heterojunction solar cells. *J. Mater. Chem. A* **2017**, *5*, 285-291.

(35) Diao, S. L.; Zhang, X. J.; Shao, Z. B.; Ding, K.; Jie, J. S.; Zhang, X. H., 12.35% efficient graphene quantum dots/silicon heterojunction solar cells using graphene transparent electrode. *Nano Energy* **2017**, *31*, 359-366.

(36) Yu, L.; Batmunkh, M.; Grace, T.; Dadkhah, M.; Shearer, C.; Shapter, J., Application of a Hole Transporting Organic Interlayer in Graphene oxide/Single walled Carbon Nanotube-Silicon Heterojunction Solar Cells. *J. Mater. Chem. A* 2017, 8624-8634.
(37) Yu, L.; Tune, D.; Shearer, C.; Shapter, J., Heterojunction Solar Cells Based on Silicon and Composite Films of Graphene Oxide and Carbon Nanotubes. *ChemSusChem* 2015, *8*, 2940-2947.
(38) Li, R.; Di, J.; Yong, Z.; Sun, B.; Li, Q., Polymethylmethacrylate Coating on Aligned Carbon Nanotube–Silicon Solar Cells for Performance Improvement. *J. Mater. Chem. A* 2014, *2*, 4140.
(39) Jia, Y.; Li, P.; Gui, X.; Wei, J.; Wang, K.; Zhu, H.; Wu, D.; Zhang, L.; Cao, A.; Xu, Y., Encapsulated Carbon Nanotube-Oxide-Silicon Solar Cells with Stable 10% Efficiency. *Appl. Phys. Lett.* 2011, *98*, 133115.
(40) Shi, E. Z.; Zhang, L. H.; Li, Z.; Li, P. X.; Shang, Y. Y.; Jia, Y.; Wei, J. Q.; Wang, K. L.; Zhu, H. W.; Wu, D. H.; Zhang, S.; Cao, A. Y., TiO_2-coated carbon nanotube-silicon solar cells with efficiency of 15%. *Sci Rep* 2012, *2*, 884.
(41) Seidel, H.; Csepregi, L.; Heuberger, A.; Baumgartel, H., ANISOTROPIC ETCHING OF CRYSTALLINE SILICON IN ALKALINE-SOLUTIONS .1. ORIENTATION DEPENDENCE AND BEHAVIOR OF PASSIVATION LAYERS. *J. Electrochem. Soc.* 1990, *137*, 3612-3626.
(42) Singh, P. K.; Kumar, R.; Lal, M.; Singh, S. N.; Das, B. K., Effectiveness of anisotropic etching of silicon in aqueous alkaline solutions. *Sol. Energy Mater. Sol. Cells* 2001, *70*, 103-113.
(43) Jiang, Y. J.; Zhang, X. D.; Wang, F. Y.; Zhao, Y., Optimization of a silicon wafer texturing process by modifying the texturing temperature for heterojunction solar cell applications. *RSC Adv.* 2015, *5*, 69629-69635.
(44) Manzoor, S.; Filipic, M.; Topic, M.; Holman, Z.; Ieee In *2016 Ieee 43rd Photovoltaic Specialists Conference*, 2016.
(45) Han, Y. G.; Yu, X. G.; Wang, D.; Yang, D. R., Formation of Various Pyramidal Structures on Monocrystalline Silicon Surface and Their Influence on the Solar Cells. *J. Nanomater.* 2013, 716012.
(46) Mackel, H.; Holst, H.; Lohmann, M.; Wefringhaus, E.; Altermatt, P. P., Detailed Analysis of Random Pyramid Surfaces With Ray Tracing and Image Processing. *IEEE J. Photovolt* 2016, *6*, 1456-1465.
(47) Kim, D. H.; Lee, J. K.; Huh, J. H.; Kim, Y. H.; Kim, G. T.; Roth, S.; Dettlaff-Weglikowska, U., Effect of SOCl2 doping on electronic properties of single-walled carbon nanotube thin film transistors. *Phys. Status Solidi B* 2011, *248*, 2668-2671.
(48) Yu, L.; Shearer, C.; Shapter, J., Recent Development of Carbon Nanotube Transparent Conductive Films. *Chem. Rev.* 2016, 13413-13453.
(49) Tuukkanen, S.; Valimaki, M.; Lehtimaki, S.; Vuorinen, T.; Lupo, D., Behaviour of One-Step Spray-Coated Carbon Nanotube Supercapacitor in Ambient Light Harvester Circuit with Printed Organic Solar Cell and Electrochromic Display. *Sci Rep* 2016, *6*, 22967.
(50) Pichumani, M.; Bagheri, P.; Poduska, K. M.; Gonzalez-Vinas, W.; Yethiraj, A., Dynamics, Crystallization and Structures in Colloid Spin CoatingDynamics, crystallization and structures in colloid spin coating. *Soft Matter* 2013, *9*, 3220-3229.
(51) Toolan, D. T. W.; Hodgkinson, R.; Howse, J. R., Stroboscopic Microscopy-Direct Imaging of Structure Development and Phase Separation During Spin-Coating. *J. Polym. Sci. Part B Polym. Phys.* 2014, *52*, 17-25.
(52) Wang, J.; Liang, M. H.; Fang, Y.; Qiu, T. F.; Zhang, J.; Zhi, L. J., Rod-Coating: Towards Large-Area Fabrication of Uniform Reduced Graphene Oxide Films for Flexible Touch Screens. *Adv. Mater.* 2012, *24*, 2874-2878.
(53) An, Q.; Rider, A. N.; Thostenson, E. T., Hierarchical Composite Structures Prepared by Electrophoretic Deposition of Carbon Nanotubes onto Glass Fibers. *ACS Appl. Mater. Interfaces* 2013, *5*, 2022-2032.
(54) Baker-Finch, S. C.; McIntosh, K. R., Reflection distributions of textured monocrystalline silicon: implications for silicon solar cells. *Prog. Photovoltaics* 2013, *21*, 960-971.

Chapter 8 Postsynthesis Separation of Single-chirality Single Walled Carbon Nanotubes

8.1 Overview

Preparation of single chirality species of single walled carbon nanotubes is one of the top challenges in the nanocarbon field. In the past 15 years, great progress has been achieved in the preparation of single-chirality species via both chirality-specific growth and post synthesis separation methods. As a result, the application of the single-chirality enriched SWCNTs in various fields, such as photovoltaics and biological imaging, has been a new topic in carbon nanotube research. Overall, single-chirality SWCNT species are successfully separated from a commercial parent soot containing a wide distribution of species by both methods (gel chromatography and aqueous two phase extraction (ATPE)).

8.2 Introduction

Due to the unique properties of SWCNTs,[1] such as mechanical strength, chemical stability, electronic conductivity and so on, they have been intensively studied and have great potential to be applied in different fields,[2] including nano-composites, energy harvesting, medical and biological applications.[3-5] Currently, industrial scale manufacturing of CNT has been achieved[6-8] and there are several commercialised CNT-based products.[9-11] However, one of the key issues in these products is the inhomogeneity of the structure and properties caused by the wide distribution of CNT length and chirality.[12]

Many properties of SWCNTs are chirality dependent, such as electronic band structure and optical absorption.[13] For instance, two-thirds of SWCNTs are semiconductors ($n - m \neq 3q$ and q is an integer) while the rest one-third of SWCNTs are metals ($n - m = 3q$).[14] In these semiconductors, the bandgaps are inversely proportional to the diameter of the nanotubes.[15] In addition, the optical absorption is determined by the bandgaps and/or the van Hove singularities for both semiconducting and metallic carbon nanotubes.[16-17] Therefore, it is important to have control over the chirality of SWCNTs for different applications.[18] For example, in the fabrication of the biologically transparent electronic devices (such as transistors) which absorb limited light in the visible range, the potentially ideal materials are SWCNTs with the absorption of S_{11} and S_{22} located above 700 nm.[19-22]

Nowadays, with the continuous efforts in this field, people have the ability to prepare single chirality enriched SWCNTs by either direct growth[7,23-37] or post synthesis.[16,38-54] In terms of the purity, post synthesis purification methods seem to be better than the direct growth. Among these purification approaches, gel chromatography, in which allyl dextran-based polymer beads are used as the stationary phase having different affinities to various surfactant-coated SWCNTs with different chiralities, has the potential to be applied on an industrial scale.[49] The adsorption of surfactant-suspended SWCNTs onto the gel beads is highly dependent on the chirality and the selection of the mobile phase as well as the type of surfactant. In addition, the temperature of the separation also plays an import role in the adsorption.[47] More than 10 types of semiconducting SWCNT species were separated with good control over the type and concentration of the surfactant and the temperature, and the separated SWCNTs have a purity up to 93 % with high yield.[45] In addition, simultaneous separation of single-chirality species and enantiomer purification are realised by the same method.[47] Recently, the same group optimised the procedure and demonstrated the separation of highly pure single-chirality SWCNTs on a milligram scale.[49] The second very interesting approach to obtain high-purity single-chirality SWCNTs is an aqueous two-phase separation or aqueous two-phase extraction technique, which link the carbon nanomaterials with biological materials. [54] This approach is derived from deoxyribonucleic acid (DNA)-based separation via ion-exchange chromatography by replacing the ion-exchange resin with polymer two-phase systems as the separation media, where two separate but permeable aqueous phases with slight differences are created.[40] As a result, dispersed SWCNTs of various chiralities partition into two phases due to the different hydration energy in the two phases, which is exploited to achieve the separation of SWCNTs. In fact, this approach is compatible to both DNA and surfactant dispersed SWCNTs to purify high purity single species.[52-53] Overall, this ATPE based method is efficient and easy to scale up.

In this Chapter, both gel chromatography and DNA-based ATPE approaches are used to separate SWCNTs from a mixed soot either by electronic properties (metals and semiconductors) and/or single-chirality species. Surfactants are used to prepare the SWCNT dispersion for gel chromatography separation while DNA sequences are used to fabricate CNT suspension for ATPE method. Overall, gel chromatography is able to separate SWCNTs into metal and semiconductors and 6 individual semiconducting species are purified while more

than 10 different SWCNT species are purified with different electronic properties by the ATPE approach.

8.3 Experimental details

8.3.1 Metal/semiconductor separation by gel chromatography

The preparation of the dispersion and the procedure of the separation are described in sections 2.2.2.1.2 and 2.3.1.1, respectively. The purity of these fractions are evaluated by UV-Vis-NIR spectra (refer to 2.6.3).

8.3.2 Single-chirality SWCNT separation by gel chromatography

The preparation of the SWCNT dispersion and the separation of single-chirality SWCNT are described in sections 2.2.2.1.3 and 2.3.1.2. The purity of the separated fractions are assessed by UV-Vis-NIR spectrometer (refer to 2.6.3).

8.3.3 Single-chirality SWCNT separation by ATPE

The dispersion of the SWCNTs and aqueous solutions used in ATPE were prepared as described in sections 2.2.2.3 and 2.2.1.7. The ATPE separation procedure is described in section 2.3.1.3 with the evaluation of the purity by UV-Vis-NIR spectroscopy (refer to 2.6.3).

8.4 Results and discussion

8.4.1 Separation of metallic and semiconducting SWCNTs

The separation of metallic and semiconducting SWCNTs was done with a gel chromatography approach. As shown in the dark trace in Figure 8.1, the parent CNT dispersion (HiPco SWCNTs, in 0.5 wt% SDS aqueous solution) contains a wide distribution of many chiralities with many absorption features through S_{11} (900 - 1350 nm) and S_{22} (500 - 850 nm) overlapped with M_{11} (400 - 600 nm). Since some metallic species have weak affinity to the dextran-based gel beads due to the high coverage of surfactant, they are not bound to the gel and are easily

flushed out of the gel bed by 0.5 wt% SDS aqueous solution. The UV-Vis-NIR spectrum of the metal enriched fraction (the red trace in Figure 8.1) has several peaks with high intensity in the range of 400 to 600 nm (M_{11}) while there are still some semiconducting impurities which absorb at above 900 nm. It is difficult to assign these peaks to specific species with UV-Vis-NIR spectra when the fraction contains many chiral species. By increasing the concentration of SDS aqueous solution to 1 wt%, both strong-bound metallic species and weak-bound semiconducting species are flushed out of the gel bed. This is indicated by the blue trace in Figure 8.1, where absorption peaks of both metallic species (M_{11}) and semiconducting species (S_{11} and S_{22}) are observed. After this step, most of the metallic species in the parent suspension are removed from the gel bed with some larger diameter semiconducting species, including (10,3) and (8,6). In order to collect a semiconducting SWCNT enriched fraction, 0.5 wt% DOC aqueous solution is used to flush the gel bed and elute the strong-bound semiconducting SWCNTs, as shown in the pink trace in Figure 8.1, where very low metallic SWCNT peak intensity (M_{11}) and strong semiconducting species peaks (S_{11} and S_{22}) are observed.

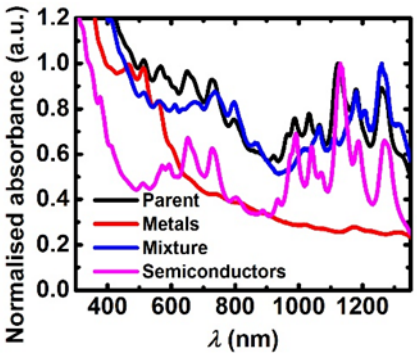

Figure 8.1 UV-Vis-NIR spectra of different fractions in the separation of metallic and semiconducting SWCNT species. The spectra of parent, mixture and semiconductors are normalised at the strongest S_{11} peak while the metallic spectrum is normalised at the strongest M_{11} peak.

Overall, based on the affinity difference of metallic and semiconducting SWCNTs to the gel beads, tuning the concentration and type of the surfactant (and the resulting coverage on the SWCNTs) enables the separation of metallic and semiconducting species from the parent suspension.

8.4.2 Single-chirality SWCNT separation by gel chromatography

Since the separation of SWCNT by chiral angles can be done by a two-surfactant system (SC/SDS)[45,47] and DOC shows is effective in the diameter separation of SWCNTs due to its stronger affinity with small diameter species,[55-56] in this section, single-chirality separation of SWCNTs is achieved with the combination of chiral angle and diameter selectivity in a three-surfactant system (SC/SDS/DOC). The mechanism is described as follows: ideally, the loading of the SWCNTs to the gel bed is performed with SC/SDS system and desorption of the SWCNTs out of the gel bed is conducted by SC/SDS/DOC system. During the loading process, under a certain concentration of the surfactant, SWCNTs with specific chiral angles were adsorbed while the species with different chiral angles are not bound to the gel. Then, the absorbed SWCNTs are eluted out of the gel bed into fractions of different diameter species by continually increasing the concentration of DOC in SC/SDS/DOC system. The surfactant concentration in the unbound fraction from the loading process can then be diluted to another level and the diluted fraction is loaded to the subsequent gel bed to repeat the chiral angle and diameter separation in a similar manner, as shown in Figure 8.2 (a). Single-chiral species can eventually be separated by repeating the described process several times.

As shown in Figure 8.2 (b), the unbound suspension is a mixture of many chiral species, which absorbs light throughout the entire wavelength range from 300 to 1350 nm by E_{11}, E_{22} and E_{33}. After the collection of the unbound SWCNTs, aqueous solutions with increasing DOC concentration but constant SC and SDS concentration are used to flush the gel bed to elute the adsorbed SWCNTs step by step. The first three fractions (0.5 wt% SC 2 wt% SDS 0.04 wt% DOC, 0.5 wt% SC 2 wt% SDS 0.08 wt% DOC and 0.5 wt% SC 2 wt% SDS 0.12 wt% DOC) seem to have very similar absorbance features to the parent suspension. This is possibly due to the fact that the concentration of DOC is not high enough to elute any specific chiral species but there are still some SWCNTs being eluted out with the aqueous medium ("background"). As a matter of fact, the actual intensities of the spectral signals are extremely low (Absorbance < 0.05). All the rest of these fractions contain different SWCNT species due to their various absorbance features in the spectra, as shown in Figure 8.2 (a). However, there are no single-chirality species collected from this column while the majority of the species in the 4th (0.5 wt% SC 2 wt% SDS 0.16 wt% DOC) and the 6th fractions are (7,3) (S_{11} = 999 nm

and S_{22} = 509 nm) and (7,6) (S_{11} = 1145 nm and S_{22} = 657 nm).[57-58] In addition, the S_{11} and S_{22} values showed are not exactly where these species absorb energy due to the impurity species which have the potential to shift the peak position. For instance, in the spectrum of 4th fraction, the tail of the (7,3) peak below 1000 nm is from the impurity ((6,5) S_{11} = 975 nm, and its S_{22} peak is observed at 568 nm).[57-58] Similarly, the tail (from 1160 to 1200 nm) of the (7,6) peak in the spectrum of the 6th fraction is caused by (8,6) whose S_{11} is at 1172 nm (and the S_{22} is at 722 nm).[58] The summarised information of the main species in each fraction are shown in Table 8.1.

Table 8.1 Summary of the main species in different factions from the 1st, 2nd and 3rd columns during gel chromatography-based separation.

Column Number (SC and SDS concentration)	Concentration of DOC (wt%)	Composition of the species	S_{11} (nm)	S_{22} (nm)
1 st 0.5 wt% SC 2 wt% SDS	0.04; 0.08; 0.12; 0.20; 0.28; 0.32 and 0.36	complex	n.a.	n.a.
	0.16	Mainly (7,3)	999	509
		(7,6)	1145	657
	0.24	Mainly (7,6)	1145	657
		(8,6)	1172	722
2 nd 0.5 wt% SC 1 wt% SDS	0.02; 0.04; 0.08; 0.10; 0.12; 0.16 and 0.20	complex	n.a.	n.a.
	0.06	Highly pure (7,3)	1000	508
	0.14	Mainly (9,4)	1114	727
		(11,1)	1270	612
		(10,3)	1270	645
	0.18	Highly pure (10,3)	1270	645
3 rd 0.5 wt% SC 0.5 wt% SDS	0.01; 0.05; 0.06; 0.07; 0.09 and 0.10	complex	n.a.	n.a.
	0.02	Highly pure (6,4)	883	583
	0.03	Highly pure (6,5)	980	569
	0.04	Mainly (8,7)	1290	739
	0.08	Highly pure (8,6)	1175	719

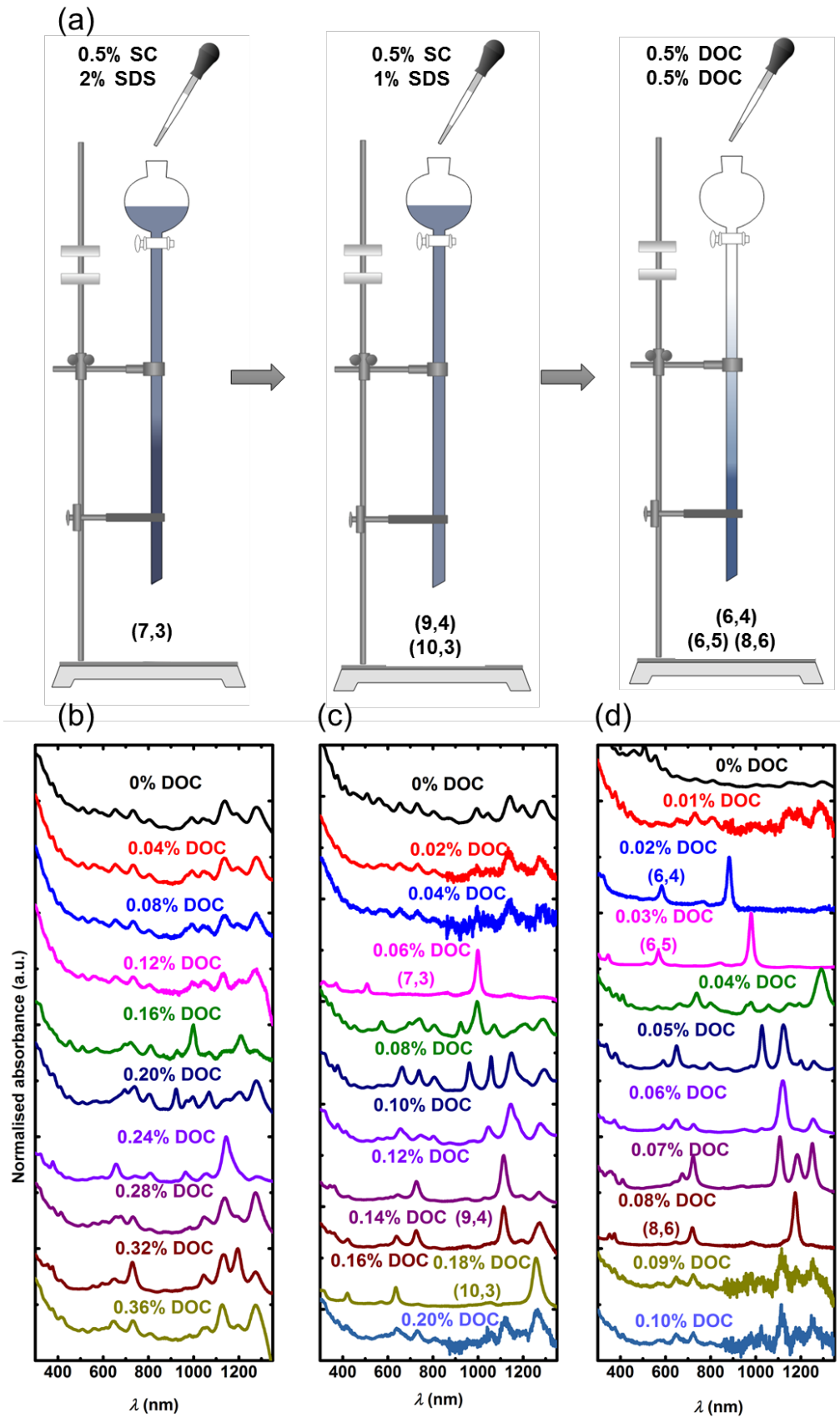
(a)
0.5% SC
2% SDS
(7,3)
0.5% SC
1% SDS
(9,4)
(10,3)
0.5% DOC
0.5% DOC
(6,4)
(6,5) (8,6)
(b)
0% DOC
0.04% DOC
0.08% DOC
0.12% DOC
0.16% DOC
0.20% DOC
0.24% DOC
0.28% DOC
0.32% DOC
0.36% DOC
Normalised absorbance (a.u.)
400 600 800 1000 1200
λ (nm)
(c)
0% DOC
0.02% DOC
0.04% DOC
0.06% DOC
(7,3)
0.08% DOC
0.10% DOC
0.12% DOC
0.14% DOC (9,4)
0.16% DOC 0.18% DOC
(10,3)
0.20% DOC
400 600 800 1000 1200
λ (nm)
(d)
0% DOC
0.01% DOC
0.02% DOC
(6,4)
0.03% DOC
(6,5)
0.04% DOC
0.05% DOC
0.06% DOC
0.07% DOC
0.08% DOC
(8,6)
0.09% DOC
0.10% DOC
400 600 800 1000 1200
λ (nm)

Figure 8.2 (a) The process of the separation, (b) Normalised UV-Vis-NIR spectra (at the maximum of E_{11} absorbance) of separated SWCNTs fractions from the (b) 1st, (c) 2nd, and (d) 3rd column. The concentration of SC and SDS are 0.5 and 2 wt% (1st)/1 wt% (2nd)/0.5 wt% (3rd) while DOC concentration ranges from 0 to 0.36 wt% (1st)/0.20 wt% (2nd)/0.10 wt% (3rd) with a step of 0.04 wt% (1st)/0.02 wt% (2nd)/0.01 wt% (3rd). The poor signal to noise ratio of the spectra in some of the plots is due to the low CNT concentration of these particular fractions.

As shown in Figure 8.2 (c), the unbound fraction has a higher metallic content than in the parent suspension (relatively higher M_{11} intensity from 400 – 600 nm). In the first two fractions (0.5 wt% SC 1 wt% SDS 0.02 wt% DOC and 0.5 wt% SC 1 wt% SDS 0.04 wt% DOC), the DOC concentration is too low to be able to elute any specific chiral species, which is a very similar situation observed in the previous column. Besides, the low signal-to-noise ratio in the IR region shows ever lower concentration of CNT in these fractions (absorbance < 0.02) than that in the previous column. The third fraction is a relatively pure (7,3) fraction (S_{11} = 1000 nm and S_{22} = 508 nm).[57-58] With the increase in the DOC concentration of the flushing aqueous solutions, more and more semiconducting SWCNTs are eluted from the 4th to 6th fractions. In the 7th fraction, (9,4) is eluted out of the gel bed with small amount of (11,1) and (10,3).[57-58] Further increase in the DOC concentration flushes the 9th fraction mainly containing (10,3) out of the gel bed. Any increase in the DOC concentration is very difficult to elute enough SWCNTs (the 10th fraction has a very low signal (absorbance < 0.015) with a low signal-to-noise ratio). Overall, as the concentration of DOC increases, the diameter of the SWCNTs in the fractions increases (since the diameter of the SWCNT is in a reverse proportional relationship to the E_{11} absorbance position).

As shown in Figure 8.2 (d), the unbound fraction is enriched with metallic SWCNTs, with limited signal intensity above 800 nm. Small-diameter semiconducting species, (6,4) (S_{11} = 883 nm and S_{22} = 583 nm), is eluted at the 2nd fraction.[57-58] Slightly larger species (6,5) (S_{11} = 980 nm and S_{22} = 569 nm)[57-58] is eluted out of the gel bed at the next fraction. The next single-chiral species, (8,6) (S_{11} = 1175 nm and S_{22} = 719 nm),[57-58] is collected at the 8th fraction. Further increase in the DOC concentration does not elute sufficient SWCNTs. The overall

trend is that the dimeter of the eluted SWCNTS increases with the concentration of DOC, which is very similar to that is observed from the 2nd column.

In summary, metal/semiconductor separation is achieved by the three-surfactant system (SC/SDS/DOC) due to much lower affinity of metallic species to the gel bed. More importantly, this system takes the advantages of surfactant selectivity on both chiral angle and diameter of semiconducting SWCNTs to yield single-chiral species, including (7,3), (9,4), (10,3), (6,4), (6,5) and (8,6). The concentration and the yield of these species are estimated by the absorbance spectra and shown in Table 8.2 (~3 mL of each of these species were collected).[59] Among them, (6,5) has the highest yield while the yield of (7,3) and (6,4) are below 0.2 µg.

Table 8.2 Estimated concentration and yield based on UV-Vis-NIR spectra of the single-chirality species separated by gel chromatography (about 3 mL of each species can be collected during each experiment).

Species	Estimated concentration* (µg mL^{-1})	Mass (µg)
(7,3)	4.6×10^{-2}	0.14
(9,4)	7.3×10^{-1}	2.19
(10,3)	4.7×10^{-1}	1.41
(6,4)	5.3×10^{-2}	0.16
(6,5)	1.1×10^{0}	3.30
(8,6)	3.3×10^{-1}	0.99

* The concentrations of these semiconducting species are estimated based on absorption cross section values from ref [59].

8.4.3 Single-chirality SWCNT separation by ATPE

8.4.3.1 TTA(TAT)$_2$ATT

As shown in Figure 8.3, the parent suspension contains a wide distribution of SWCNT species while the major species is (6,5). After the first step of separation (TTA(TAT)$_2$ATT-SWCNTs (SG 65i)), as shown in Figure 8.3 (a), the 1T fraction was highly enriched with (6,5) while the majority of the SWCNTs were in the PAM-rich bottom phase (The labelling system of the fractions is referred to section 2.3.1.3 and Figure 2.1). With the repetitive addition of DX and the blank bottom phase, (6,5) from 1T was further purified with other species moving to the bottom phase. The absorbance peak position for E_{11} and E_{22} are at 993 and 575 nm, which is

slightly red-shifted compared to the surfactant dispersed SWCNTs due to the differences in dielectric environment.[54] This red shift is widely observed in all DNA-wrapped SWCNT samples. In addition, after the multistep separation of 1B, another (6,5) fraction was collected at 4B, as shown in Figure 8.3 (b). Both two fractions (1TTT and 4B) were enriched with (6,5) but they were two different enantiomers, (-) (6,5) at 1TTT and (+) (6,5) at 4B.[60] The current understanding of the handedness selectivity is that DNA sequences adopt two different wrapping manners on a pair of enantiomers, resulting in large difference in the chemical reactivity and the intensity of the fluorescence.[60]

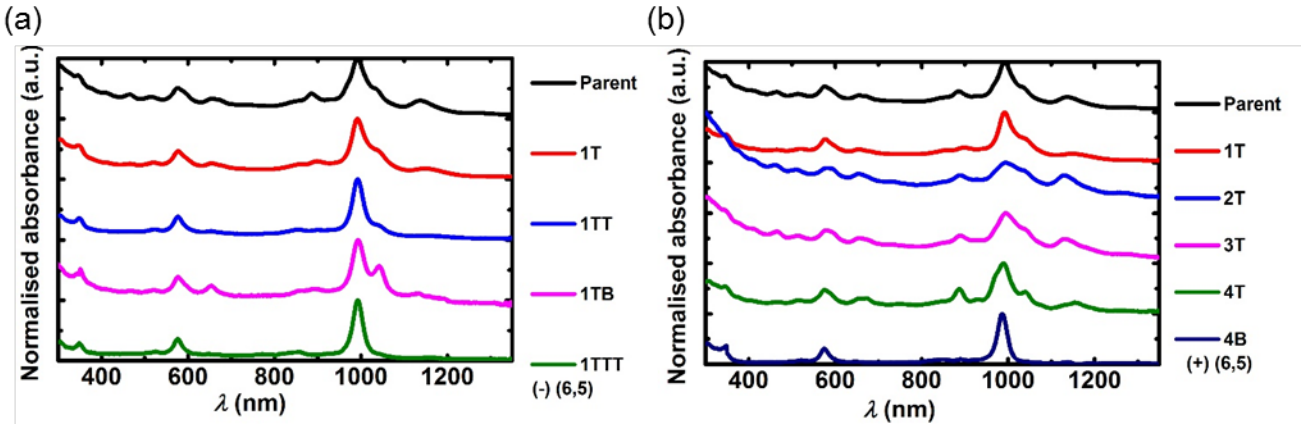

Figure 8.3 ATPE of SWCNTs (SG 65i) with ssDNA (TTA(TAT)$_2$ATT) in PEG/PAM system. UV-Vis-NIR spectra of the fractions from the purification of (a) PEG rich top and (b) PAM rich bottom phases. The spectra are normalised at the maximum of E_{11}.

The same SWCNT dispersion was also separated in PEG/DX system, as shown in Figure 8.4. Noticeably, in most cases of PEG/DX separation, 1T does not contain any SWCNTs due to their strong affinity to DX enriched bottom phase. With the addition of modulating agent (the modulators are extremely useful in SWCNT separation though the exact reason why is still unknown), PVP, SWCNTs are partitioned into the top phase step by step. In this case, 2T was highly enriched with (6,5) and was purified 2 more steps to 2TTT with the removal of (7,6) and (7,5) (as shown in Figure 8.4, trace 2TB). The multi-step purification of 1B was also performed but there was no interesting fraction observed (not shown). In addition, PEG/DX does not have any selectivity to different enantiomers.

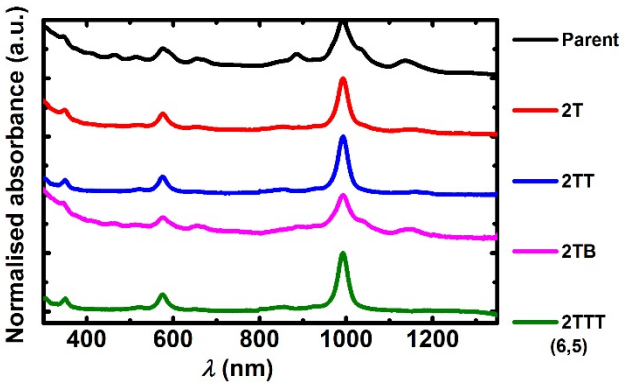

Figure 8.4 ATPE of SWCNTs (SG 65i) with ssDNA (TTA(TAT)$_2$ATT) in PEG/DX system. UV-Vis-NIR spectra of the fraction from the purification of (a) PEG rich top phases. The spectra are normalised at the maximum of E_{11}.

8.4.3.2 CTCCCTC

As shown in Figure 8.5, the parent suspension contains a wide distribution of chiral species with (7,6) the majority species. After the first step separation of CTCCCTC-SWCNTs in the PEG/PAM system, (7,6) partitioned into the top phase (1T) with a small amount of (7,5) while other species were in the bottom phase (1B, not shown). With the addition of DX and blank bottom phase of PEG/PAM system, the impurities were removed and 1TTT was highly enriched with (7,6).

In addition, the separation of the same parent dispersion was performed in a PEG/DX system, as shown in Figure 8.6. Similarly, 1T did not have any SWCNTs (not shown), which was normally observed in the separation with PEG/DX system. 2T was highly enriched with (7,6) while the majority of 3T is (7,6) with some (8,6) (S_{11} = ~1185 nm and S_{22} = ~730 nm) as the impurities. A metallic species, (8,5), was collected at 6B with the addition of PVP after the multi-step separation, as shown in Figure 8.6. Since the enrichment of (7,6) at 3T, further purification was conducted with the addition of NaSCN acting as the modulator. After 1 more step, the impurity was removed from the top phase (3T) to the bottom fraction (3TB, as shown in Figure 8.6 (b)). It is worth noting that there is a trade-off between the yield and the purity. Specifically, though the impurities were removed from (7,6) fraction, some (7,6) partitioned into the bottom phase as well.

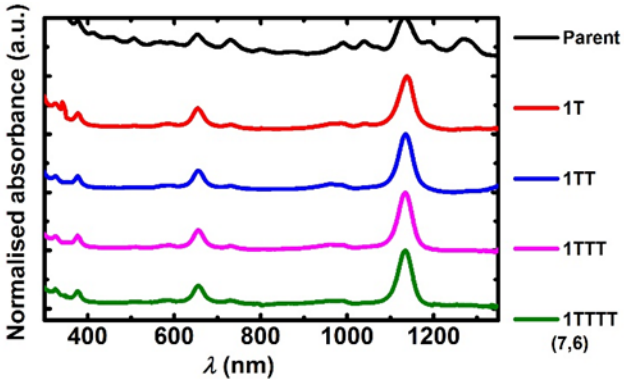

Figure 8.5 ATPE of SWCNTs (EG 150X) with ssDNA (CTCCCTC) in PEG/PAM system. UV-Vis-NIR spectra of the fraction from the purification of PEG rich top phase. The spectra are normalised at the maximum of S_{11}.

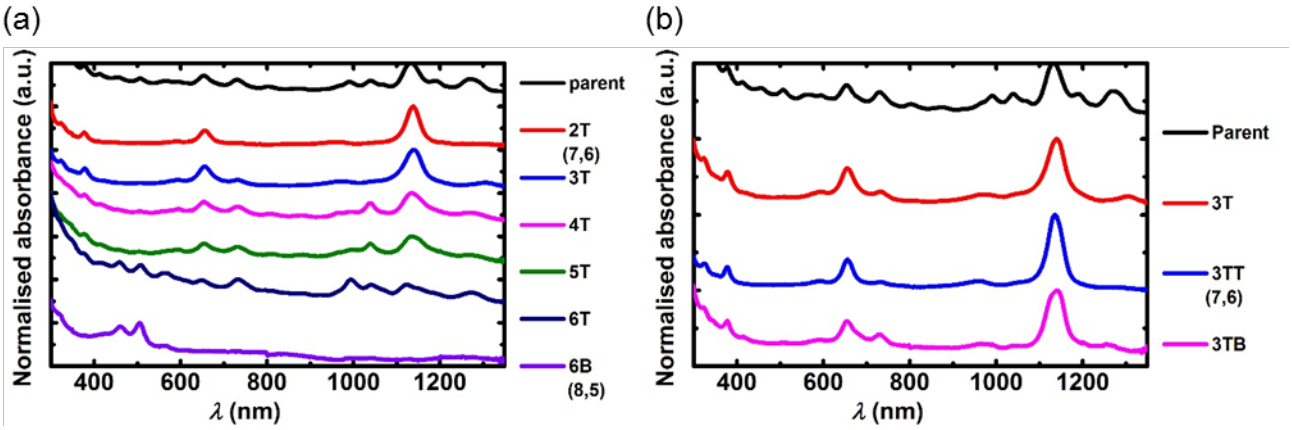

Figure 8.6 ATPE of SWCNTs (EG 150X) with ssDNA (CTCCCTC) in PEG/DX system. UV-Vis-NIR spectra of the fraction from the purification of (a) DX rich bottom and (b) PEG rich top phases. The spectra are normalised at the maximum of E_{11}.

It has been shown that some ssDNA-SWCNT hybrids can be purified in both PEG/PAM and PEG/DX systems. However, for most of ssDNA sequences, the purification of the single-chirality species did not occur.[54,60] In the following sections, two ssDNA libraries are tested in order to find some rules between the selectivity of single-chiral species and the ssDNA sequences.

8.4.3.3 Sequences based on TTT and CCC blocks

A library of ssDNA sequences based on TTT and CCC blocks were tested in this section. As shown in Table 8.3, there are in total 32 different types of ssDNA sequences build by TTT and CCC blocks in this library when the length of the sequences is determined to be 15-mer. After the preparation of the SWCNTs dispersion, separations were performed in both PEG/PAM and PEG/DX systems to test the selectivity of the single-chiral species.

Table 8.3 ssDNA sequences of the TTT and CCC block library.

T_{15}	$T_{12}C_3$	$T_9C_3T_3$	T_9C_6
$T_6C_3T_6$	$T_6C_3T_3C_3$	$T_6C_6T_3$	T_6C_9
$T_3C_3T_9$	$T_3C_3T_6C_3$	$T_3C_3T_3C_3T_3$	$T_3C_3T_3C_6$
$T_3C_6T_6$	$T_3C_6T_3C_3$	$T_3C_9T_3$	T_3C_{12}
C_3T_{12}	$C_3T_9C_3$	$C_3T_6C_3T_3$	$C_3T_6C_6$
$C_3T_3C_3T_6$	$C_3T_3C_3T_3C_3$	$C_3T_3C_6T_3$	$C_3T_3C_9$
C_6T_9	$C_6T_6C_3$	$C_6T_3C_3T_3$	$C_6T_3C_6$
C_9T_6	$C_9T_3C_3$	$C_{12}T_3$	C_{15}

As shown in Figure 8.7, 7 different SWCNT chiral species were purified by 7 ssDNA sequences in the entire library with 32 ssDNA sequences in total. In previous study, by scanning more than 300 random ssDNA sequences, 23 types of SWCNT species were purified. The successful rate of this TTT/CCC-block library is 21.9 % (7/32), which is two times higher than that in the literature, 7.7 % (23/300). This suggests that TTT and CCC blocks have better chirality selectivity than a random library. It is worth noting that the particular sequence, $T_3C_9T_3$, has the ability to purify 3 different species ((11,1), (8,5) and (6,5)) from 2 ATPE systems, and one of them, the metallic species (8,5), is achieved from a middle fraction, which indicates that the wrapping of ssDNA on (8,5) is unique enough to be discriminated from others. The basic understanding of ssDNA sorting is that an ordered ssDNA-SWCNT hybrid is formed only for a certain match between the sequence and the structure of CNTs, which results in the differentiation of the specific ssDNA-wrapped SWCNTs from all other hybrids.[38-39] In the case of $T_3C_9T_3$, it seems to be able to form 3 types of well-ordered structure with two ATPE systems. In addition, it was reported that $T_nC_mT_n$ can separate metal (9,9), quasi-metal (9,6) and semiconductor (11,1).[60] Thus, in the next section, a library based on $T_nC_mT_n$ sequence is tested.

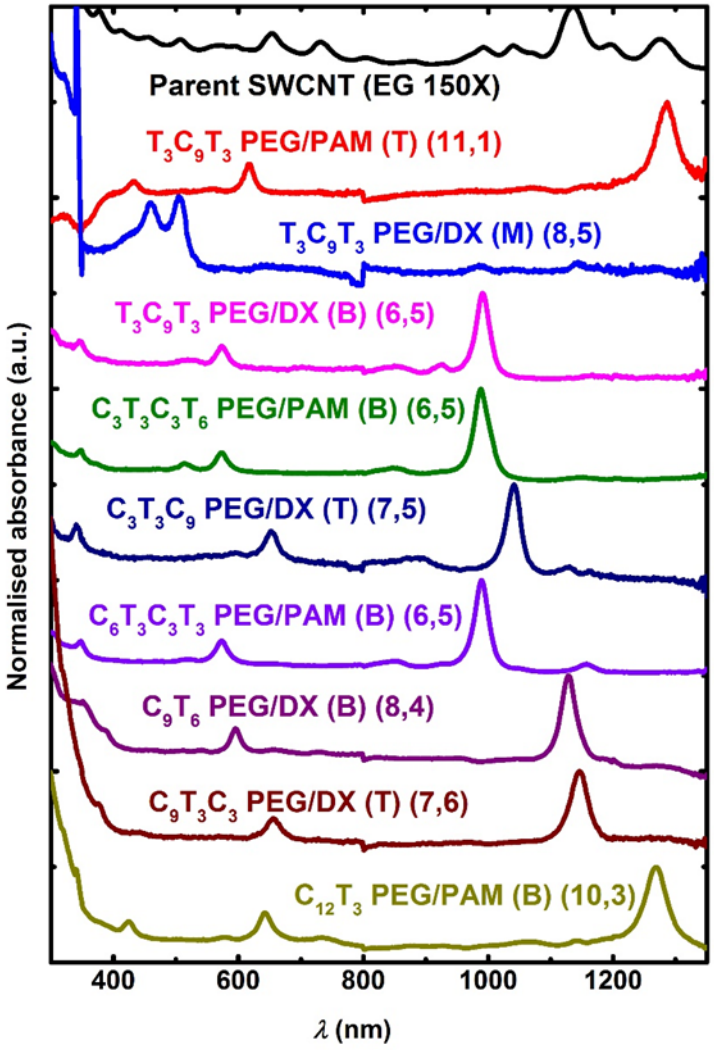

Figure 8.7 UV-Vis-NIR spectra of separated single-chirality SWCNTs by the ssDNA sequences from the library based on TTT and CCC blocks. T, M and B in the legend indicate where the specific species was separated (top, middle and bottom fraction during the separation process based on a specific ssDNA). The spectra are normalised at the maximum of E_{11}.

8.4.3.4 Sequences based on $T_nC_mT_n$

Several sets of ssDNA sequences based on $T_nC_mT_n$ are scanned in this section, as shown in Table 8.4 and the UV-Vis-NIR spectra of the successfully separated species are shown in

Figure 8.8, Figure 8.9 and Figure 8.10. Overall, among these 21 sequences, 16 of them can purify 12 different species in total by 2 different ATPE systems, PEG/PAM and PEG/DX.

Table 8.4 ssDNA sequences in the library of $T_nC_mT_n$.

$T_3C_mT_3$	$T_4C_mT_4$	$T_5C_mT_5$
$T_3C_5T_3$	$T_4C_4T_4$	$T_5C_4T_5$
$T_3C_7T_3$	$T_4C_6T_4$	$T_5C_5T_5$
$T_3C_8T_3$	$T_4C_7T_4$	$T_5C_6T_5$
$T_3C_9T_3$	$T_4C_8T_4$	$T_5C_7T_5$
$T_3C_{10}T_3$	$T_4C_9T_4$	$T_5C_8T_5$
$T_3C_{11}T_3$	$T_4C_{10}T_4$	$T_5C_9T_5$
$T_3C_{12}T_3$	$T_4C_{11}T_4$	$T_5C_{10}T_5$

As shown in Figure 8.8, several chiral species with different electronic species (semiconductor ((7,6), (11,1), (6,5), (8,4) and (10,3)), metal ((6,6)) and quasi-metal ((8,5) and (11,2))) are purified with the help of $T_3C_mT_3$. 5 sequences have some positive results, and more interestingly, some of these sequences can purify more than 1 species in different ATPE system, such as $T_3C_5T_3$, $T_3C_9T_3$, $T_3C_{10}T_3$ and $T_3C_{11}T_3$. Although the yield of the metal and quasi-metals is not high (as shown in Table 8.5), the overall ability of chirality separation of $T_3C_mT_3$ is much better than that of a random ssDNA library.[60]

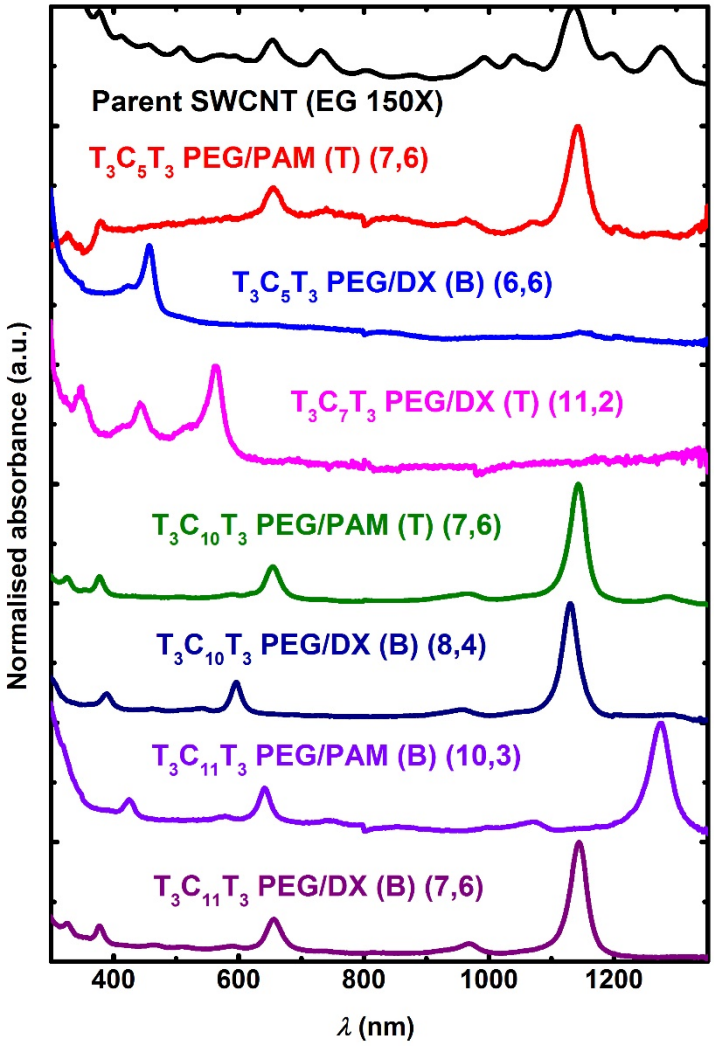

Figure 8.8 The UV-Vis-NIR spectra of separated chiral species with ssDNA sequences based on $T_3C_mT_3$. T (Top) and B (Bot) indicate where the species are separated. (11,1), (8,5) and (6,5) separated by $T_3C_9T_3$ are shown in Figure 8.7 previously.

$T_4C_mT_4$ sequences can purify several semiconducting species, including (11,1), (9,2), (10,3) and (7,5), as shown in Figure 8.9. Most of these species are purified in PEG/PAM system with the exception of (7,5) separated by PEG/DX. Among the tested 7 sequences, $T_4C_8T_4$ can purify two species. The yield of the species separated by $T_4C_mT_4$ seems to be lower than that of $T_3C_mT_3$, as shown in Table 8.5, but the separation ability is slightly higher than that of $T_3C_mT_3$ (6/7 versus 5/7).

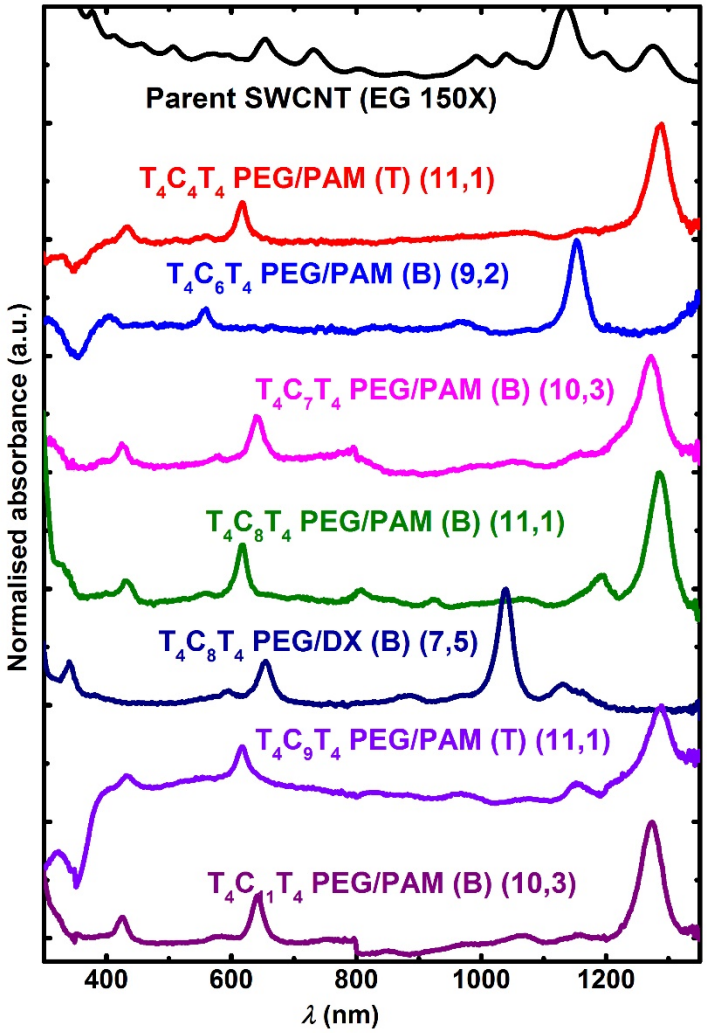

Figure 8.9 The UV-Vis-NIR spectra of separated chiral species with ssDNA sequences based on $T_4C_mT_4$. T (Top) and B (Bot) indicate where the species are separated.

Similar to $T_4C_mT_4$ sequences, $T_5C_mT_5$ sequences have the ability to purify several semiconducting species, including (6,5), (8,6), (7,5), (10,3), (11,1), (11,0) and (7,6), as shown in Figure 8.10. Noticeably, 2 sequences ($T_5C_9T_5$ and $T_5C_{10}T_5$) can purify 3 different species by 2 ATPE systems. The yield of the species separated by this system is similar to that of $T_4C_mT_4$ sequences, but it can purify more species than $T_4C_mT_4$ sequences (7 versus 4).

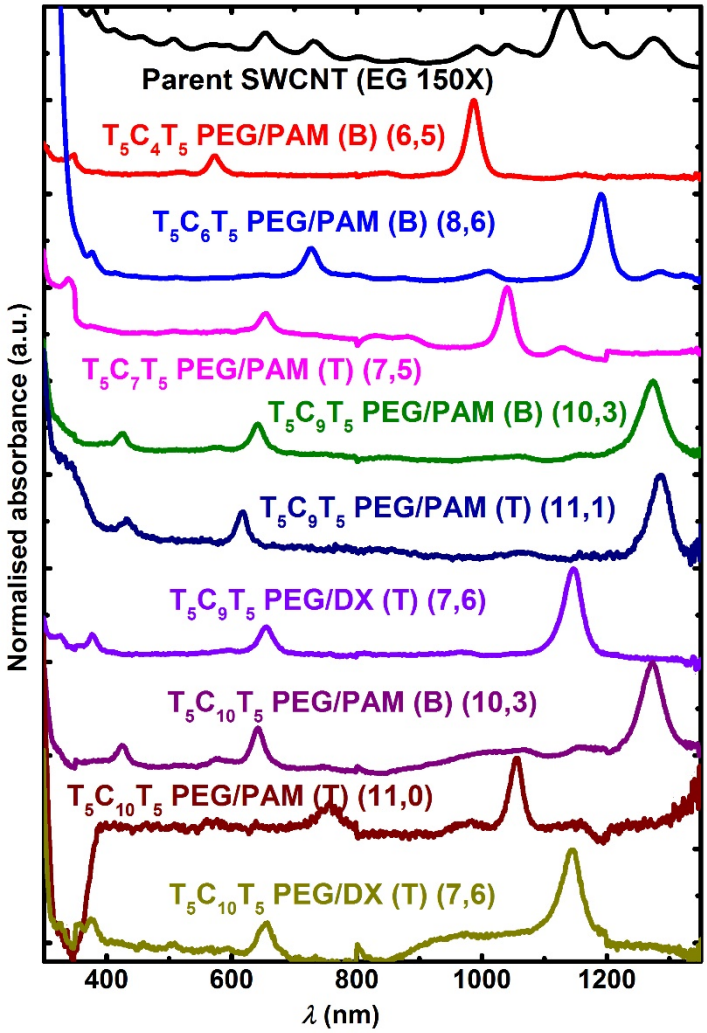

Figure 8.10 The UV-Vis-NIR spectra of separated chiral species with ssDNA sequences based on $T_5C_mT_5$. T (Top) and B (Bot) indicate where the species are separated.

In summary, $T_3C_mT_3$ sequences can separate chiral species with three different electronic properties while $T_4C_mT_4$ sequences have the highest successful rate (6/7) and the only zig-zag structure (11,0) is purified from $T_5C_mT_5$ sequences library. In terms of the yield, as shown in Table 8.5, $T_3C_mT_3$ has the highest yield and $T_4C_mT_4$ and $T_5C_mT_5$ are in a similar level. The overall yield of ATPE is higher than that of gel chromatography separation, as shown in Table 8.2 and Table 8.5.

Table 8.5 Estimated concentration and yield based on UV-Vis-NIR spectra of the single-chirality species separated by ATPE (about 1.2 mL of each species can be collected from 1 mL SWCNT parent suspension).

Species	DNA sequence	ATPE system*	Estimated concentration** ($\mu g\ mL^{-1}$)	Mass (μg)
(6,5)	$TTA(TAT)_2ATT$	**PEG**/PAM	6.0×10^{0}	7.20
(6,5)	$TTA(TAT)_2ATT$	PEG/**PAM**	6.2×10^{0}	7.44
(6,5)	$TTA(TAT)_2ATT$	**PEG**/DX	7.4×10^{0}	8.88
(7,6)	CTC_3TC	**PEG**/PAM	4.8×10^{0}	5.76
(7,6)	CTC_3TC	**PEG**/DX	1.39×10^{1}***	16.72***
(8,5)	CTC_3TC	PEG/**DX**	8.3×10^{-2}	0.10
(11,1)	$T_3C_9T_3$	**PEG**/PAM	4.2×10^{-1}	0.50
(8,5)	$T_3C_9T_3$	PEG/DX(M)****	4.5×10^{-3}	0.0054
(6,5)	$T_3C_9T_3$	PEG/**DX**	4.4×10^{-1}	0.53
(6,5)	$C_3T_3C_3T_6$	PEG/**PAM**	1.1×10^{0}	1.32
(7,5)	$C_3T_3C_9$	**PEG**/DX	3.2×10^{-1}	0.38
(6,5)	$C_6T_3C_3T_3$	PEG/**PAM**	1.8×10^{0}	2.16
(8,4)	C_9T_6	PEG/**DX**	1.8×10^{0}	2.16
(7,6)	$C_9T_3C_3$	**PEG**/DX	4.0×10^{-1}	0.48
(10,3)	$C_{12}T_3$	PEG/**PAM**	3.1×10^{0}	3.72
(7,6)	$T_3C_5T_3$	**PEG**/PAM	3.4×10^{-1}	0.41
(6,6)	$T_3C_5T_3$	PEG/**DX**	2.5×10^{-2}	0.03
(11,2)	$T_3C_7T_3$	**PEG**/DX	5.7×10^{-3}	0.0069
(7,6)	$T_3C_{10}T_3$	**PEG**/PAM	4.5×10^{0}	5.43
(8,4)	$T_3C_{10}T_3$	PEG/**DX**	2.7×10^{0}	3.24
(10,3)	$T_3C_{11}T_3$	PEG/**PAM**	1.9×10^{0}	2.28
(7,6)	$T_3C_{11}T_3$	PEG/**DX**	2.4×10^{0}	2.88
(11,1)	$T_4C_4T_4$	**PEG**/PAM	5.3×10^{-1}	0.64
(9,2)	$T_4C_6T_4$	PEG/**PAM**	3.0×10^{-1}	0.36
(10,3)	$T_4C_7T_4$	PEG/**PAM**	4.3×10^{-1}	0.52
(11,1)	$T_4C_8T_4$	PEG/**PAM**	5.6×10^{-1}	0.67
(7,5)	$T_4C_8T_4$	PEG/**DX**	5.4×10^{-1}	0.65
(11,1)	$T_4C_9T_4$	**PEG**/PAM	5.7×10^{-1}	0.68
(10,3)	$T_4C_{11}T_4$	PEG/**PAM**	6.9×10^{-1}	0.83
(6,5)	$T_5C_4T_5$	PEG/**PAM**	5.9×10^{-1}	0.71
(8,6)	$T_5C_6T_5$	PEG/**PAM**	1.7×10^{0}	2.04
(7,5)	$T_5C_7T_5$	**PEG**/DX	1.2×10^{0}	1.44
(10,3)	$T_5C_9T_5$	PEG/**PAM**	7.5×10^{-1}	0.90
(11,1)	$T_5C_9T_5$	**PEG**/PAM	2.9×10^{-1}	0.35
(7,6)	$T_5C_9T_5$	**PEG**/DX	4.2×10^{-1}	0.50
(10,3)	$T_5C_{10}T_5$	PEG/**PAM**	6.7×10^{-1}	0.80
(11,0)	$T_5C_{10}T_5$	**PEG**/PAM	1.3×10^{-1}	0.16
(7,6)	$T_5C_{10}T_5$	**PEG**/DX	1.7×10^{-1}	0.20

* The polymer phases in bold in ATPE system column indicates where the final purified species were collected. For example, **PEG**/PAM in the first line means that the separated (6,5) was collected from the purification of SWCNTs in the very beginning top phase (1T, for PEG/DX system, it is normally 2T) enriched in PEG. Similarly, PEG/**PAM** in the second line means that (6,5) was collected from the very last bottom phase enriched with PAM.

** The concentrations of these semiconducting and metallic species are estimated using absorption cross section values from ref [59] and ref [54].

*** The estimated concentration and the yield of CTCCCTC separated (7,6) in **PEG**/DX system is the sum of SWCNTs from both 2T and 3TT.

**** The fraction of (8,5) is a middle fraction.

8.5 Conclusions

SWCNT separation can be achieved via both gel chromatography and ATPE approach. The separation of SWCNTs into metal and semiconducting species were achieved with high purity and yield by gel chromatography with the help of surfactants. 6 semiconducting species were purified by gel chromatography while single chiral species including metals, quasi-metals and semiconductors were purified by ATPE. ATPE seems to have higher yield and purity at the same time, but gel chromatography is a potentially more economical method for separating SWCNTs.

REFERENCES:

(1) Iijima, S.; Ichihashi, T., SINGLE-SHELL CARBON NANOTUBES OF 1-NM DIAMETER. *Nature* 1993, *363*, 603-605.

(2) Iijima, S., Helical Microtubules of Graphitic Carbon. *Nature* 1991, *354*, 56-58.

(3) Bethune, D. S.; Kiang, C. H.; Devries, M. S.; Gorman, G.; Savoy, R.; Vazquez, J.; Beyers, R., COBALT-CATALYZED GROWTH OF CARBON NANOTUBES WITH SINGLE-ATOMIC-LAYERWALLS. *Nature* 1993, *363*, 605-607.

(4) Dal, H. J.; Rinzler, A. G.; Nikolaev, P.; Thess, A.; Colbert, D. T.; Smalley, R. E., Single-wall nanotubes produced by metal-catalyzed disproportionation of carbon monoxide. *Chem. Phys. Lett.* 1996, *260*, 471-475.

(5) Jones, D. E. H., Science of fullerenes and carbon nanotubes - Dresselhaus,MS, Dresselhaus,G, Eklund,PC. *Nature* 1996, *381*, 384-384.

(6) Bronikowski, M. J.; Willis, P. A.; Colbert, D. T.; Smith, K. A.; Smalley, R. E., Gas-phase production of carbon single-walled nanotubes from carbon monoxide via the HiPco process: A parametric study. *J. Vac. Sci. Technol., B* **2001**, *19*, 1800-1805.
(7) Bachilo, S. M.; Balzano, L.; Herrera, J. E.; Pompeo, F.; Resasco, D. E.; Weisman, R. B., Narrow (n,m)-distribution of single-walled carbon nanotubes grown using a solid supported catalyst. *J. Am. Chem. Soc.* **2003**, *125*, 11186-11187.
(8) Wang, Y.; Wei, F.; Luo, G. H.; Yu, H.; Gu, G. S., The large-scale production of carbon nanotubes in a nano-agglomerate fluidized-bed reactor. *Chem. Phys. Lett.* **2002**, *364*, 568-572.
(9) Cheng, H. M.; Li, F.; Su, G.; Pan, H. Y.; He, L. L.; Sun, X.; Dresselhaus, M. S., Large-scale and low-cost synthesis of single-walled carbon nanotubes by the catalytic pyrolysis of hydrocarbons. *Appl. Phys. Lett.* **1998**, *72*, 3282-3284.
(10) Fan, S. S.; Chapline, M. G.; Franklin, N. R.; Tombler, T. W.; Cassell, A. M.; Dai, H. J., Self-oriented regular arrays of carbon nanotubes and their field emission properties. *Science* **1999**, *283*, 512-514.
(11) Ma, W. J.; Song, L.; Yang, R.; Zhang, T. H.; Zhao, Y. C.; Sun, L. F.; Ren, Y.; Liu, D. F.; Liu, L. F.; Shen, J.; Zhang, Z. X.; Xiang, Y. J.; Zhou, W. Y.; Xie, S. S., Directly synthesized strong, highly conducting, transparent single-walled carbon nanotube films. *Nano Lett.* **2007**, *7*, 2307-2311.
(12) De Volder, M. F. L.; Tawfick, S. H.; Baughman, R. H.; Hart, A. J., Carbon Nanotubes: Present and Future Commercial Applications. *Science* **2013**, *339*, 535-539.
(13) Wang, H.; Yuan, Y.; Wei, L.; Goh, K.; Yu, D. S.; Chen, Y., Catalysts for chirality selective synthesis of single-walled carbon nanotubes. *Carbon* **2015**, *81*, 1-19.
(14) Zhang, Y. N.; Zheng, L. X., Towards chirality-pure carbon nanotubes. *Nanoscale* **2010**, *2*, 1919-1929.
(15) Liu, B. L.; Wu, F. Q.; Gui, H.; Zheng, M.; Zhou, C. W., Chirality-Controlled Synthesis and Applications of Single-Wall Carbon Nanotubes. *ACS Nano* **2017**, *11*, 31-53.
(16) Green, A. A.; Hersam, M. C., Nearly Single-Chirality Single-Walled Carbon Nanotubes Produced via Orthogonal Iterative Density Gradient Ultracentrifugation. *Adv. Mater.* **2011**, *23*, 2185-2190.
(17) Jain, R. M.; Howden, R.; Tvrdy, K.; Shimizu, S.; Hilmer, A. J.; McNicholas, T. P.; Gleason, K. K.; Strano, M. S., Polymer-Free Near-Infrared Photovoltaics with Single Chirality (6,5) Semiconducting Carbon Nanotube Active Layers. *Adv. Mater.* **2012**, *24*, 4436-4439.
(18) Robinson, J. T.; Welsher, K.; Tabakman, S. M.; Sherlock, S. P.; Wang, H. L.; Luong, R.; Dai, H. J., High Performance In Vivo Near-IR (> 1 mu m) Imaging and Photothermal Cancer Therapy with Carbon Nanotubes. *Nano Res.* **2010**, *3*, 779-793.
(19) Hong, G. S.; Lee, J. C.; Robinson, J. T.; Raaz, U.; Xie, L. M.; Huang, N. F.; Cooke, J. P.; Dai, H. J., Multifunctional in vivo vascular imaging using near-infrared II fluorescence. *Nat. Med.* **2012**, *18*, 1841-1846.
(20) Nikolaev, P.; Bronikowski, M. J.; Bradley, R. K.; Rohmund, F.; Colbert, D. T.; Smith, K. A.; Smalley, R. E., Gas-phase catalytic growth of single-walled carbon nanotubes from carbon monoxide. *Chem. Phys. Lett.* **1999**, *313*, 91-97.
(21) Diao, S.; Hong, G. S.; Robinson, J. T.; Jiao, L. Y.; Antaris, A. L.; Wu, J. Z.; Choi, C. L.; Dai, H. J., Chirality Enriched (12,1) and (11,3) Single-Walled Carbon Nanotubes for Biological Imaging. *J. Am. Chem. Soc.* **2012**, *134*, 16971-16974.
(22) Hong, G. S.; Diao, S.; Chang, J. L.; Antaris, A. L.; Chen, C. X.; Zhang, B.; Zhao, S.; Atochin, D. N.; Huang, P. L.; Andreasson, K. I.; Kuo, C. J.; Dai, H. J., Through-skull fluorescence imaging of the brain in a new near-infrared window. *Nat. Photonics* **2014**, *8*, 723-730.
(23) Liu, J.; Wang, C.; Tu, X. M.; Liu, B. L.; Chen, L.; Zheng, M.; Zhou, C. W., Chirality-controlled synthesis of single-wall carbon nanotubes using vapour-phase epitaxy. *Nat. Commun.* **2012**, *3*.
(24) Yang, F.; Wang, X.; Zhang, D. Q.; Yang, J.; Luo, D.; Xu, Z. W.; Wei, J. K.; Wang, J. Q.; Xu, Z.; Peng, F.; Li, X. M.; Li, R. M.; Li, Y. L.; Li, M. H.; Bai, X. D.; Ding, F.; Li, Y., Chirality-specific growth of single-walled carbon nanotubes on solid alloy catalysts. *Nature* **2014**, *510*, 522-524.

(25) Sanchez-Valencia, J. R.; Dienel, T.; Groning, O.; Shorubalko, I.; Mueller, A.; Jansen, M.; Amsharov, K.; Ruffieux, P.; Fasel, R., Controlled synthesis of single-chirality carbon nanotubes. *Nature* **2014**, *512*, 61-64.
(26) Chiang, W. H.; Sankaran, R. M., Linking catalyst composition to chirality distributions of as-grown single-walled carbon nanotubes by tuning NixFe1-x nanoparticles. *Nat. Mater.* **2009**, *8*, 882-886.
(27) Wang, H.; Wei, L.; Ren, F.; Wang, Q.; Pfefferle, L. D.; Haller, G. L.; Chen, Y., Chiral-Selective CoSO4/SiO2 Catalyst for (9,8) Single-Walled Carbon Nanotube Growth. *ACS Nano* **2013**, *7*, 614-626.
(28) Lolli, G.; Zhang, L. A.; Balzano, L.; Sakulchaicharoen, N.; Tan, Y. Q.; Resasco, D. E., Tailoring (n,m) structure of single-walled carbon nanotubes by modifying reaction conditions and the nature of the support of CoMo catalysts. *J. Phys. Chem. B* **2006**, *110*, 2108-2115.
(29) Che, Y. C.; Wang, C.; Liu, J.; Liu, B. L.; Lin, X.; Parker, J.; Beasley, C.; Wong, H. S. P.; Zhou, C. W., Selective Synthesis and Device Applications of Semiconducting Single-Walled Carbon Nanotubes Using Isopropyl Alcohol as Feedstock. *ACS Nano* **2012**, *6*, 7454-7462.
(30) Fouquet, M.; Bayer, B. C.; Esconjauregui, S.; Blume, R.; Warner, J. H.; Hofmann, S.; Schlogl, R.; Thomsen, C.; Robertson, J., Highly chiral-selective growth of single-walled carbon nanotubes with a simple monometallic Co catalyst. *Phys. Rev. B* **2012**, *85*, 235411.
(31) He, M.; Chernov, A. I.; Fedotov, P. V.; Obraztsova, E. D.; Sainio, J.; Rikkinen, E.; Jiang, H.; Zhu, Z.; Tian, Y.; Kauppinen, E. I.; Niemela, M.; Krauset, A. O. I., Predominant (6,5) Single-Walled Carbon Nanotube Growth on a Copper-Promoted Iron Catalyst. *J. Am. Chem. Soc.* **2010**, *132*, 13994-13996.
(32) Liu, B. L.; Ren, W. C.; Li, S. S.; Liu, C.; Cheng, H. M., High temperature selective growth of single-walled carbon nanotubes with a narrow chirality distribution from a CoPt bimetallic catalyst. *Chem. Commun.* **2012**, *48*, 2409-2411.
(33) Li, X. L.; Tu, X. M.; Zaric, S.; Welsher, K.; Seo, W. S.; Zhao, W.; Dai, H. J., Selective synthesis combined with chemical separation of single-walled carbon nanotubes for chirality selection. *J. Am. Chem. Soc.* **2007**, *129*, 15770-15771.
(34) Zhao, Q. C.; Xu, Z. W.; Hu, Y.; Ding, F.; Zhang, J., Chemical vapor deposition synthesis of near-zigzag single-walled carbon nanotubes with stable tube-catalyst interface. *Sci. Adv.* **2016**, *2*, e1507129.
(35) Zhu, Z.; Jiang, H.; Susi, T.; Nasibulin, A. G.; Kauppinen, E. I., The Use of NH3 to Promote the Production of Large-Diameter Single-Walled Carbon Nanotubes with a Narrow (n,m) Distribution. *J. Am. Chem. Soc.* **2011**, *133*, 1224-1227.
(36) Harutyunyan, A. R.; Chen, G. G.; Paronyan, T. M.; Pigos, E. M.; Kuznetsov, O. A.; Hewaparakrama, K.; Kim, S. M.; Zakharov, D.; Stach, E. A.; Sumanasekera, G. U., Preferential Growth of Single-Walled Carbon Nanotubes with Metallic Conductivity. *Science* **2009**, *326*, 116-120.
(37) Yang, F.; Wang, X.; Zhang, D. Q.; Qi, K.; Yang, J.; Xu, Z.; Li, M. H.; Zhao, X. L.; Bai, X. D.; Li, Y., Growing Zigzag (16,0) Carbon Nanotubes with Structure-Defined Catalysts. *J. Am. Chem. Soc.* **2015**, *137*, 8688-8691.
(38) Tu, X. M.; Manohar, S.; Jagota, A.; Zheng, M., DNA sequence motifs for structure-specific recognition and separation of carbon nanotubes. *Nature* **2009**, *460*, 250-253.
(39) Tu, X. M.; Walker, A. R. H.; Khripin, C. Y.; Zheng, M., Evolution of DNA Sequences Toward Recognition of Metallic Armchair Carbon Nanotubes. *J. Am. Chem. Soc.* **2011**, *133*, 12998-13001.
(40) Ming, Z.; Diner, B. A., Solution redox chemistry of carbon nanotubes. *J. Am. Chem. Soc.* **2004**, *126*, 15490-15494.
(41) Zheng, M.; Semke, E. D., Enrichment of single chirality carbon nanotubes. *J. Am. Chem. Soc.* **2007**, *129*, 6084-6085.
(42) Arnold, M. S.; Green, A. A.; Hulvat, J. F.; Stupp, S. I.; Hersam, M. C., Sorting carbon nanotubes by electronic structure using density differentiation. *Nat. Nanotechnol.* **2006**, *1*, 60-65.
(43) Ha, M. J.; Xia, Y.; Green, A. A.; Zhang, W.; Renn, M. J.; Kim, C. H.; Hersam, M. C.; Frisbie, C. D., Printed, Sub-3V Digital Circuits on Plastic from Aqueous Carbon Nanotube Inks. *ACS Nano* **2010**, *4*, 4388-4395.
(44) Ghosh, S.; Bachilo, S. M.; Weisman, R. B., Advanced sorting of single-walled carbon nanotubes by nonlinear density-gradient ultracentrifugation. *Nat. Nanotechnol.* **2010**, *5*, 443-450.

(45) Liu, H. P.; Nishide, D.; Tanaka, T.; Kataura, H., Large-scale single-chirality separation of single-wall carbon nanotubes by simple gel chromatography. *Nat. Commun.* 2011, *2*, 309.
(46) Gui, H.; Li, H. B.; Tan, F. R.; Jin, H. H.; Zhang, J.; Li, Q. W., Binary gradient elution of semiconducting single-walled carbon nanotubes by gel chromatography for their separation according to chirality. *Carbon* 2012, *50*, 332-335.
(47) Liu, H. P.; Tanaka, T.; Urabe, Y.; Kataura, H., High-Efficiency Single-Chirality Separation of Carbon Nanotubes Using Temperature-Controlled Gel Chromatography. *Nano Lett.* 2013, *13*, 1996-2003.
(48) Tanaka, T.; Urabe, Y.; Hirakawa, T.; Kataura, H., Simultaneous Chirality and Enantiomer Separation of Metallic Single-Wall Carbon Nanotubes by Gel Column Chromatography. *Anal. Chem.* 2015, *87*, 9467-9472.
(49) Yomogida, Y.; Tanaka, T.; Zhang, M. F.; Yudasaka, M.; Wei, X. J.; Kataura, H., Industrial-scale separation of high-purity single-chirality single-wall carbon nanotubes for biological imaging. *Nat. Commun.* 2016, *7*, 12056.
(50) Khripin, C. Y.; Fagan, J. A.; Zheng, M., Spontaneous Partition of Carbon Nanotubes in Polymer-Modified Aqueous Phases. *J. Am. Chem. Soc.* 2013, *135*, 6822-6825.
(51) Zhang, M.; Khripin, C. Y.; Fagan, J. A.; McPhie, P.; Ito, Y.; Zheng, M., Single-Step Total Fractionation of Single-Wall Carbon Nanotubes by Countercurrent Chromatography. *Anal. Chem.* 2014, *86*, 3980-3984.
(52) Fagan, J. A.; Khripin, C. Y.; Batista, C. A. S.; Simpson, J. R.; Haroz, E. H.; Walker, A. R. H.; Zheng, M., Isolation of Specific Small-Diameter Single-Wall Carbon Nanotube Species via Aqueous Two-Phase Extraction. *Adv. Mater.* 2014, *26*, 2800-2804.
(53) Fagan, J. A.; Haroz, E. H.; Ihly, R.; Gui, H.; Blackburn, J. L.; Simpson, J. R.; Lam, S.; Walker, A. R. H.; Doorn, S. K.; Zheng, M., Isolation of > 1 nm Diameter Single-Wall Carbon Nanotube Species Using Aqueous Two-Phase Extraction. *ACS Nano* 2015, *9*, 5377-5390.
(54) Ao, G. Y.; Khripin, C. Y.; Zheng, M., DNA-Controlled Partition of Carbon Nanotubes in Polymer Aqueous Two-Phase Systems. *J. Am. Chem. Soc.* 2014, *136*, 10383-10392.
(55) Liu, H.; Feng, Y.; Tanaka, T.; Urabe, Y.; Kataura, H., Diameter-Selective Metal/Semiconductor Separation of Single-wall Carbon Nanotubes by Agarose Gel. *J. Phys. Chem. C* 2010, *114*, 9270-9276.
(56) Zhao, P.; Einarsson, E.; Lagoudas, G.; Shiomi, J.; Chiashi, S.; Maruyama, S., Tunable separation of single-walled carbon nanotubes by dual-surfactant density gradient ultracentrifugation. *Nano Res.* 2011, *4*, 623-634.
(57) Weisman, R. B.; Bachilo, S. M., Dependence of Optical Transition Energies on Structure for Single-Walled Carbon Nanotubes in Aqueous Suspension: An Empirical Kataura Plot. *Nano Lett.* 2003, *3*, 1235-1238.
(58) Maultzsch, J.; Telg, H.; Reich, S.; Thomsen, C., Radial breathing mode of single-walled carbon nanotubes: Optical transition energies and chiral-index assignment. *Phys. Rev. B* 2005, *72*, 205438.
(59) Sanchez, S. R.; Bachilo, S. M.; Kadria-Vili, Y.; Lin, C. W.; Weisman, R. B., (n,m)-Specific Absorption Cross Sections of Single-Walled Carbon Nanotubes Measured by Variance Spectroscopy. *Nano Lett.* 2016, *16*, 6903-6909.
(60) Ao, G. Y.; Streit, J. K.; Fagan, J. A.; Zheng, M., Differentiating Left- and Right-Handed Carbon Nanotubes by DNA. *J. Am. Chem. Soc.* 2016, *138*, 16677-16685.

Chapter 9 Conclusions

9.1 Conclusions

In this Thesis, it has been shown that heterojunction solar cells based on carbon nanotubes and Si are one of the potential alternatives to the current semiconductor photovoltaics. Several strategies were developed to enhance the performance these devices, including the application of CNT hybrid films with conductive polymers, the introduction of grid design of the front metal electrodes, the application of conducting organic hole transporting materials as the interlayer, the optimal p-type dopants and the formation of the surface structures on Si. The best efficiency in the Thesis is above 13 %, which is one of the highest efficiencies in this type of solar cells. The highest efficiency of CNT/Si based photovoltaics reported in the literature by Wang et al. is about 17 %,[1] which involves the application of metal oxide (MoO_x) as (a) an antireflection layer to improve the absorption of incident light, (b) a dopant in order to decrease the series resistance as well as the Schottky barrier. However, the active area of their device (0.0079 cm^2) is much smaller than the one in this Thesis (0.087 cm^2). The influence of the size of the active area of the devices has been described in Chapter 4 and smaller active area generally results in higher photovoltaic performance. Thus, the highest efficiency of solar cells in this Thesis (13 %) is competitive among this type of devices, though it is still much lower than that of traditional semiconductor based solar cells (about 20 %). It would be possible to combine some of the techniques listed in this Thesis to further pursue a high performance CNT/Si device. For example, devices with efficiency of more than 13 % can probably be produced when a PANI-CNT composite is placed on top of a spiro-OMeTAD coated silicon substrate. However, applying a conformal thin organic/polymeric film (< 50 nm) on a textured silicon surface would be highly challenging. In this case, the antireflective effect can be achieved by adding a transparent film on top of CNT layer. Additionally, the work in this thesis was certainly focussed exploring different approaches to construct the CNT/Si solar cells as a means to understand their operation and the underlying mechanisms at play. Achieving the maximum efficiency will arise from this work but it is not core to the goal of the Thesis. Overall, the heterojunction solar cells based on Si and CNTs have a bright prospect considering that the first device was produced in 2007 and the efficiency has been improved for more than 10 times from 1.3 %.[2]

However, there are still several issues to be addressed before any practical applications. One of the main challenge widely reported is the long-term stability of the solar cells. The major source for the instability is the growth of the silicon dioxide layer when the device is exposed to the atmosphere, which can be suppressed by the application of polymer encapsulation layers to some degree.[3] However, the best way to solve the issue is probably to replace the Si layer with a different material with long-term chemical stability in atmosphere. Specifically, the alternative structure of the solar cell we propose could be devices containing two layers of carbon nanotube of different chirality, in which each particular CNT chiral species acts as a semiconducting material layer (refer to section 9.2.2). In this Thesis, two different methods are used to separate a mixture of CNT soot containing a number of different chiralities into individual chiral species with high purity in Chapter 8, which paves the way to fabricate solar cells with specific absorption features by choosing different chiral species with various absorption wavelengths, as shown in Figure 9.1.

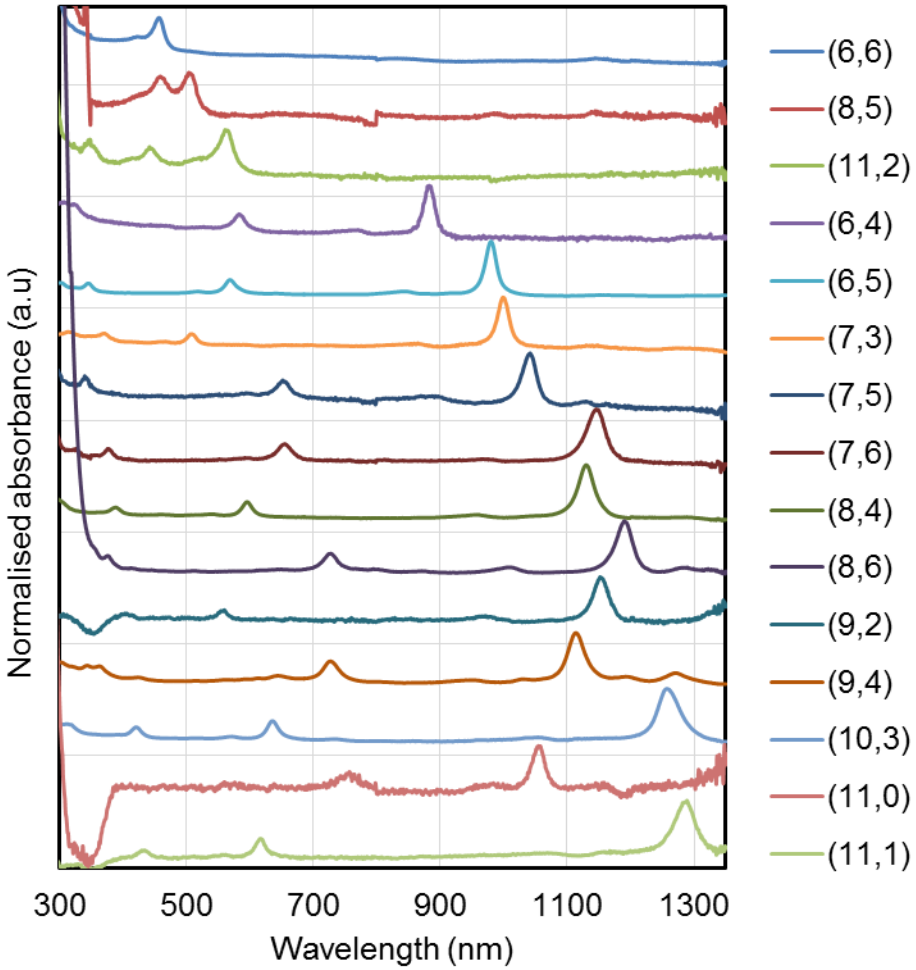

Figure 9.1 Purified SWCNTs in this Thesis by both gel chromatography and ATPE. The spectra are normalised at E_{11} peak.

The other difficulty in commercial application is how to maintain the performance of the solar cells with the increase in the active area of the devices. In this Thesis, it has been proved that an optimal front metal contact could significantly improve the efficiency of a solar cell with large active area (about 0.09 cm^2) to above 10 %.[4] However, this approach including the application of photolithography in the definition of the delicate front metal structure (the optimal distance between each line is 0.5 mm and the width of the line is 0.01 mm) which is very difficult to be applied in large scale manufacturing. Some traditional approaches in printing industry, such as screen printing, might need to be considered to solve this practical problem. Additionally, the preparation and processing of large CNT-based thin electrodes are challenging as well. Spray

coating and rod coating might the alternatives to vacuum-transfer method on an industrial scale.

It is clear that CNTs are one of the best materials for the application of transparent conducting films due to their excellent chemical stability, mechanical and optoelectronic properties. Several novel techniques listed in this Thesis (including applying CNT hybrid films with conductive polymers, introducing grid design of the front metal electrodes, the addition of conducting organic hole transporting materials as the interlayer, optimisation of p-type dopants and etching of Si surface) have been proved to effectively enhance the performance of CNT/Si devices and were all novel when first reported. As many of these methods can be applied to other photovoltaic devices, such as replacing the expensive Au layer with a high quality CNT based TCF in perovskite solar cells, this Thesis will provide some new thoughts in the fabrication of a high performance solar cell. In addition, the interesting selectivity of TnCmTn sequences to specific chiral SWCNTs would potentially benefit both the separation of target SWCNT and its further application in other fields. Overall, this Thesis indicates the promising future of CNT-based transparent films to be applied in the industry of photovoltaics.

9.2 Future directions

9.2.1 Application of other 2D materials

In the last 10 years, there was an impressive development in the synthesis, characterisation, and application of a large number of novel 2D materials, including MXenes, metal-organic frameworks, and transition metal dichalcogenides. It has already been proved that the application of graphene oxide in the CNT network can effectively enhance the optoelectronic as well as the mechanical properties.[5] Thus, it is possible that many of the recently developed 2D materials can be applied into the well-established heterojunction solar cell structure.

One of the latest reports in this field is about the application of a composite transparent conducting thin electrode by adding few-layer black phosphorus into CNT network.[6] Heterojunction solar cells formed with such a composite film and silicon have been successfully fabricated with the efficiency approaching to 10 % after optimisation while the

efficiency of the control device without few-layer black phosphorus is about 7.5 %. Such improvement is attributed to the enhancement of charge transport due to unique electronic structure of the added 2D material which is related to the decrease in the orbital localised on few-layer black phosphorus from highest occupied molecular orbital to lowest unoccupied molecular orbital transition. Therefore, one can imagine that there is a great potential for other 2D materials to be applied in such PV devices with the careful selection of their electronic properties.

9.2.2 Solar cells purely based on CNTs

As mentioned previously in section 9.1, one effective way to extend the lifetime of the solar cell is to replace the silicon layer with other materials and the proposed candidate is a layer of CNTs, which results in a devices entirely based on CNTs, as shown in Figure 9.2 (a).

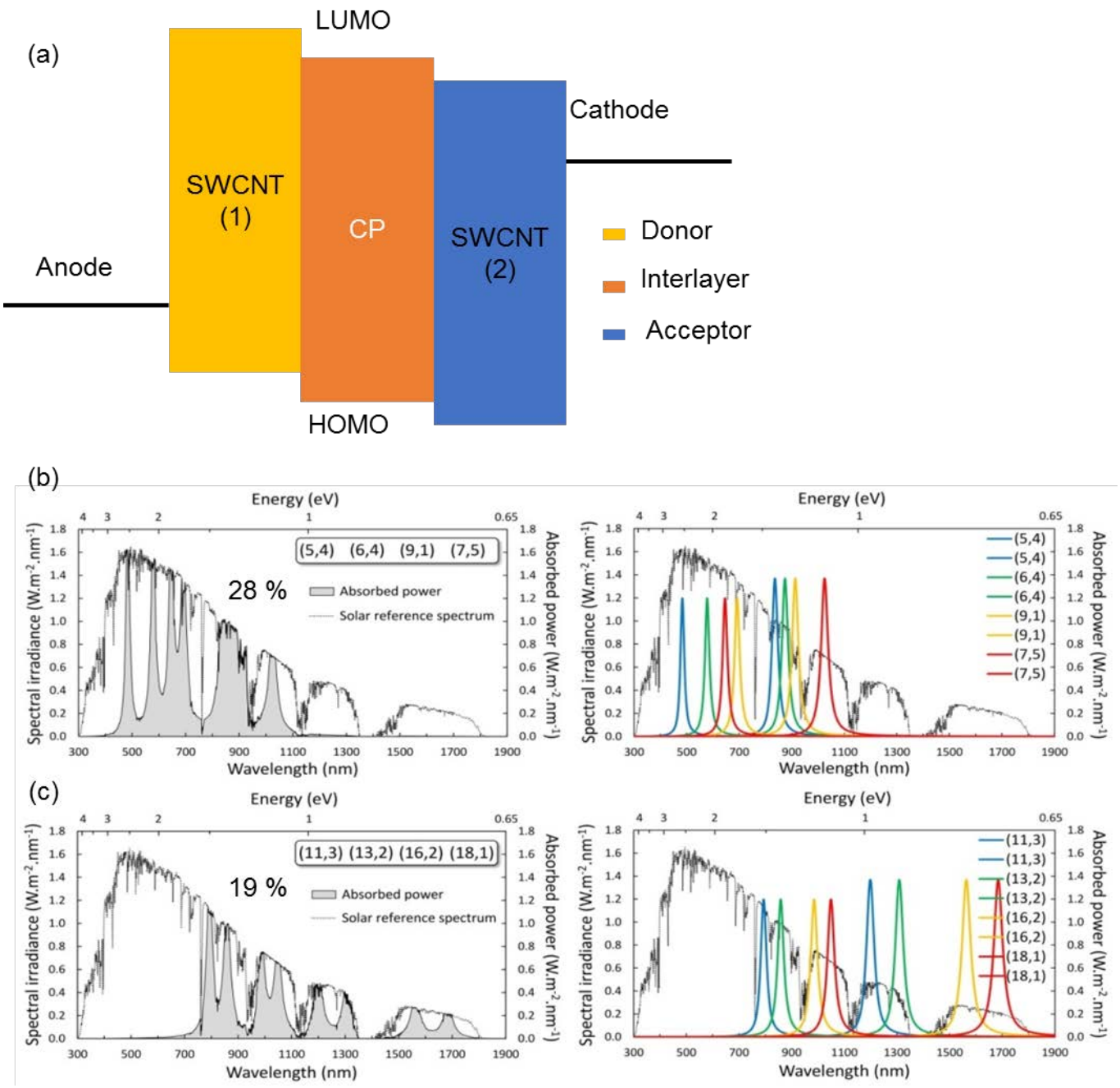

Figure 9.2 (a) Schematic structure of photovoltaic device based on 2 different kinds of SWCNTs with different work functions and van Hove optical transitions (Purple rectangle: SWCNT (1) which acts as the electron donor and is connected to anode; Blue rectangle: SWCNT (2) which act as electron acceptor and is connected to cathode; Red rectangle: conductive polymer (CP) interlayer which helps to form a conformal contact between SWCNT (1) and SWCNT (2)). Not to scale. The simulation output of a SWCNT-

based four junction tandem solar cell optimised for (b) maximum power absorption and (c) IR absorption. Reprinted with permission from ref 9. Copyright 2013 Royal Society of Chemistry.

Since SWCNTs with different diameters have various work functions and van Hove optical transition energies, it is possible to build a photovoltaic system which is based on gradual change of the optical transition energy level.[7-8]. Figure 9.2 (a) shows the schematic structure of the target carbon based device. There are 3 main parts, 2 different kinds of SWCNTs with various work function and van Hove optical transition energy and a conductive polymer interlayer which is used to form a conformal junction between 2 sparse SWCNT networks. SWCNTs could absorb energy from the incident light and produce electron-hole pairs which are separated later, and electrons and holes transport along LUMO (lowest unoccupied molecular orbital) and HOMO (highest occupied molecular orbital) levels are collected by cathode and anode. There is no limitation to the number of SWCNTs that could be used in such a structure as for chirally pure layers only one specific wavelength is harvested at a time. Calculations have shown that with just 4 SWCNTs, about 28 % of the solar spectrum can be harvested, as shown in Figure 9.2 (b) and (c).[9]

The key point of this type device is the correct selection of the SWCNT species as well as the conducting polymers which enable the electron flow of the solar cell. The potential advantages of this new type of devices are more than the extended lifetime. The added benefits with this new design include improved flexibility compared to rigid silicon substrate, selectivity of the incident light with a certain type of SWCNT species. However, the main drawback of this solar cell might be its low efficiency compared to that of traditional silicon based solar cells due to the limited ability in absorbing light when a thin film is applied (less than 100 nm generally) although application of thicker films will solve this issue.

Overall, due to the attractive benefits of this proposed new design, it is worth placing continuous effort in exploring and developing some devices based on these new concepts. At that time, CNT based photovoltaics will certainly have a welcome prospect.

REFERENCES:

(1) Wang, F. J.; Kozawa, D.; Miyauchi, Y.; Hiraoka, K.; Mouri, S.; Ohno, Y.; Matsuda, K., Considerably Improved Photovoltaic Performance of Carbon Nanotube-Based Solar Cells Using Metal Oxide Layers. *Nat. Commun.* 2015, *6*, 6305.
(2) Wei, J. Q.; Jia, Y.; Shu, Q. K.; Gu, Z. Y.; Wang, K. L.; Zhuang, D. M.; Zhang, G.; Wang, Z. C.; Luo, J. B.; Cao, A. Y.; Wu, D. H., Double-walled carbon nanotube solar cells. *Nano Lett.* 2007, *7*, 2317-2321.
(3) Yu, L. P.; Tune, D. D.; Shearer, C. J.; Shapter, J. G., Implementation of Antireflection Layers for Improved Efficiency of Carbon Nanotube-Silicon Heterojunction Solar Cells. *Sol. Energy* 2015, *118*, 592-599.
(4) Yu, L.; Grace, T.; Dadkhah, M.; Shearer, C.; Shapter, J., Optimization of the Metal Front Contact Design for Single-walled Carbon Nanotube Silicon Heterojunction Solar Cells. *Solar RRL* 2017 1600026.
(5) Yu, L.; Tune, D.; Shearer, C.; Shapter, J., Heterojunction Solar Cells Based on Silicon and Composite Films of Graphene Oxide and Carbon Nanotubes. *ChemSusChem* 2015, *8*, 2940-2947.
(6) Bat-Erdene, M.; Batmunkh, M.; Tawfik, S. A.; Fronzi, M.; Ford, M. J.; Shearer, C. J.; Yu, L. P.; Dadkhah, M.; Gascooke, J. R.; Gibson, C. T.; Shapter, J. G., Efficiency Enhancement of Single-Walled Carbon Nanotube-Silicon Heterojunction Solar Cells Using Microwave-Exfoliated Few-Layer Black Phosphorus. *Adv. Funct. Mater.* 2017, *27*.
(7) Su, W. S.; Leung, T. C.; Chan, C. T., Work function of single-walled and multiwalled carbon nanotubes: First-principles study. *Phys. Rev. B* 2007, *76*.
(8) Weisman, R. B.; Bachilo, S. M., Dependence of Optical Transition Energies on Structure for Single-Walled Carbon Nanotubes in Aqueous Suspension: An Empirical Kataura Plot. *Nano Lett.* 2003, *3*, 1235-1238.
(9) Tune, D. D.; Shapter, J. G., The Potential Sunlight Harvesting Efficiency of Carbon Nanotube Solar Cells. *Energy Environ. Sci.* 2013, *6*, 2572-2577.